UNIVERSITÀ
DEGLI STUDI
FIRENZE

DOTTORATO DI RICERCA IN
Fisica e Astronomia

CICLO XXXVI

Extending the physics reach of the fixed-target programme at the LHCb experiment

Settore Scientifico Disciplinare FIS/04

Dottorando
Lucarelli Chiara

Supervisore
Dott. Graziani Giacomo

Supervisore
Prof. Adriani Oscar

Coordinatore
Prof. Modugno Giovanni

Anni 2020/2023

Preface

The last century of research in high energy physics has been marked by the birth and affirmation of the Standard Model of Particle Physics, to date the most complete description of the fundamental constituents of the matter and their interactions. The Standard Model has proven to be extremely robust against tests of increasing accuracy over the years, with its predictions always confirmed by the experiments. The most recent success has been the Higgs boson discovery in 2012 by the CMS and ATLAS collaborations at the LHC accelerator at CERN. Nevertheless, numerous questions remain unanswered and push the research to look for phenomena beyond the Standard Model. One of the most compelling open problems is the evidence, from astrophysical and cosmological observations, that more than 85% of the mass in the Universe is of unknown nature and it is visible only through its gravitational interaction. The discovery of the so-called Dark Matter is the target of numerous experiments that look for its creation in high-energy collisions at particle accelerators or search for signals of its interaction with the baryonic matter. Experiments in space measuring charged particles emitted by astrophysical sources, known as Cosmic Rays, on the other hand, are trying to identify and characterise its nature looking for signatures of its annihilation and decay processes. The fraction of antinuclei in Cosmic Rays is considered to be the golden channel: the absence of known primary sources and the low production cross-section in secondary collisions of Cosmic Rays with the interstellar medium offers a channel with a limited background for the detection of exotic sources in the Universe. Recently, the AMS-02 collaboration claimed to have observed both antideuterium and antihelium candidates in their data sample. However, the antinuclei production can not be predicted from first principles and to constraint it, measurements in different collisions systems and at different energies must be provided. It is of the upmost importance thus to measure the production cross-section for light antinuclei in the relevant collision systems, in order to reduce the uncertainties on the theoretical models describing the secondary antinuclei flux and be able to isolate exotic signals.

Research at the accelerators has proven to be instrumental in constraining the uncertainties on the production mechanism observed in space. The LHC accelerator can play a major role in the field. The ALICE collaboration has provided many results on light nuclei and antinuclei production, contributing to increase the understanding of the production mechanism. Nevertheless, there is still a lack of results in the intermediate energy range, between the GeV energies at the fixed-target experiments at the SpS and the TeV energies of the LHC. The LHCb experiment, thanks to the forward geometry of its spectrometer and the possibility to inject noble gas targets in the LHC beam pipe, is ideal to fill this gap. The SMOG injection apparatus, originally intended for precise luminosity measurements, has been exploited since 2015 in a pioneering fixed-target physics programme studying collisions between the LHC beams and gaseous targets. By injecting helium, one of the main constituents of the interstellar medium, it has been possible to reproduce collisions of primary Cosmic Rays at the energy scale relevant to the AMS-02 physics. In 2018 and 2022 the first measurements of prompt and detached antiproton production in pHe collisions at $\sqrt{s_{\mathrm{NN}}} = 110$ GeV have been published and contributed to improve the precision of the modelling for secondary antiproton production in space. The expansion of such measurements towards light antinuclei production is one

of the subjects of this thesis.

In view of the increased luminosity expected during the LHC Run3 data-taking period, the LHCb experiment underwent a radical detector and data-taking strategy upgrade. In this context, the SMOG fixed-target system has been renovated. During Run2, limited samples of beam-gas collisions were acquired, mostly during brief special runs of the LHC, due to the overlap between the beam-gas and beam-beam interaction regions. Moreover, the system was not equipped with precise gauges to directly measure the fixed-target luminosity. A 20 cm-long storage cell, SMOG2, has hence been installed upstream of the LHCb interaction point and it will allow the gas to be confined within a limited well-defined region. This will enable to reach a density up to two orders of magnitude higher than in Run2 for the same gas flow rate. At the same time, a simultaneous data-taking both in collider and fixed-target configuration will be possible without introducing significant background to the main LHCb programme with beam-beam collisions. Finally, the possibility to inject non-noble gases, such as hydrogen, deuterium, nitrogen, and oxygen, will further enrich the fixed-target physics programme, from Quark-Gluon Plasma studies to the extension of the programme of Cosmic Ray interest.

In this thesis, I present my contributions to the extension of the LHCb fixed-target physics programme through the development of a particle identification technique based on the time-of-flight for light antinuclei, not originally foreseen in the LHCb detector. I also contributed to the feasibility studies for the injection of non-noble gases in the SMOG2 storage cell and to its commissioning and integration in the LHCb control system.

The theoretical and experimental context of this work is introduced in Part I. A general introduction of the Standard Model of Particle Physics and of the Dark Matter is covered in Chapter I.1, while Chapter I.2 introduces the experimental searches for Dark Matter signals through the measurements of the antimatter fraction in Cosmic Rays, with a particular focus on the antinuclei and their production mechanisms. The LHCb experiment and its fixed-target programme SMOG are presented in Chapter I.3 and Chapter I.4, where their recent upgrades are discussed in detail.

The original contribution of my work to the Run2 fixed-target physics programme extension and to the preparation and operation of the newly installed SMOG2 system is presented in Part II and Part III, respectively. Chapter II.1 presents the motivations to perform the light antinuclei production cross-section measurement in the pHe data sample at $\sqrt{s_{\mathrm{NN}}} = 110$ GeV, collected during 2016. The preliminary studies needed to assess the expected statistics in the available data sample are also presented, as well as the available tools to perform light nuclei identification. The time-of-flight technique is identified as the optimal choice to discriminate between particle species in the low momentum region ($p < 10$ GeV). With the standard LHCb reconstruction software, a large inefficiency in the track reconstruction for heavy particles, such as deuterons, is discovered, as well as a bias in the reconstructed time-of-flight that would impact the particle identification performance. A modified reconstruction algorithm is thus presented in Chapter II.2, which takes into consideration the speed of the particle in order to recover for the observed inefficiencies. A newly developed tool is then used to precisely measure the speed of the particle. Its implementation and performance evaluated on simulation are described in Chapter II.3. The first results on part of the pHe data sample, reconstructed with the new algorithm, are presented.

The work I have done in the context of the SMOG2 system, operating since 2022, is presented in Part III. After a brief introduction to the basic principles of vacuum systems, coating technologies and operation of a storage cell in Chapter III.1, Chapter III.2 is dedicated to the studies performed to assess the impact on the LHC machine of the injection of non-noble gases into the storage cell. The NEG coating, which helps in reducing the emission effects induced by the beam, can undergo degradation processes if exposed to a significant flow of non-getterable gases. In order to evaluate the time evolution of the degradation that can be expected during one year of SMOG2 operation in nominal conditions, I developed a new dynamic time-dependent simulation algorithm, whose results are presented. In Chapter III.3 the work I have done during the commissioning of the SMOG2 system is detailed. The simulations of the gas density profile both in the longitudinal and transverse direction are presented, as well as their impact on the luminosity and ghost charge measurements. Their results are then compared with the first data collected during 2022 in order to identify and evaluate possible discrepancies in the description of the system. The Supervisory Control And Data Acquisition system for the SMOG2 injection system that I developed for its integration in the LHCb control system is also described.

The conclusions of this work are finally drawn in Part IV.

Contents

Part I

Introduction

I.1 Elements of theory

In this introductory chapter, a brief presentation of the theoretical context for the research activities documented in this thesis is provided. A general review of the basic elements of the Standard Model of Particle Physics is given in Section I.1.1, while Section I.1.2 delves into Quantum ChromoDynamics (QCD), describing the strong nuclear forces that bind quarks into hadrons. Finally, the available evidences for Dark Matter and the experimental strategies employed for its study are outlined in Section I.1.3.

I.1.1 The Standard Model of particle physics

The Standard Model of Particle Physics (SM) is a coherent description of the fundamental constituents of matter and their interactions using the quantum field formalism. It is a renormalisable theory based on the $\mathrm{SU}(3) \otimes \mathrm{SU}(2) \otimes \mathrm{U}(1)$ algebra, from which the fundamental interactions, except for the gravitational force, arise. The symmetry $\mathrm{SU}(3)$ is associated to the strong force, which describes the interaction of the constituents of nuclei, the nucleons and quarks, through the theory known as Quantum ChromoDynamics (QCD). The $\mathrm{SU}(2) \otimes \mathrm{U}(1)$ symmetry, on the other hand, is associated with the so-called electroweak theory, which describes both the electromagnetic phenomena through the Quantum ElectroDynamics (QED) and the weak interaction governing the nuclear beta decay. Each of these interactions is mediated through fields, which are associated to particle characterised by unitary spin called bosons. The electroweak field is carried by the photon γ and the $W^{\pm}$ and Z, while the strong force is mediated through 8 bosons called gluons g. An additional boson H, characterised by spin=0, mediates the Brout-Hengler-Higgs field [1–3] and its interaction with the particles gives rise to their mass. Expected in the SM since the 1960s, it was observed for the first time in 2012 [4,5] at the LHC accelerator at CERN.

The fundamental constituents of matter are also described by fields associated with particles, in this case of half-integer spin. They are organised in two groups, leptons and quarks, based on the interactions that they are subjected to. Each interaction is associated with conserved currents and their related charges. Since leptons carry only the electroweak charges, they can only interact through weak and electromagnetic forces. The quarks, on the other hand, also carry the so-called colour charge associated with the strong force and thus they are subjected to all the fundamental interactions. Both groups are organised in three generations, identified by a unique quantum number called

Standard Model of Elementary Particles
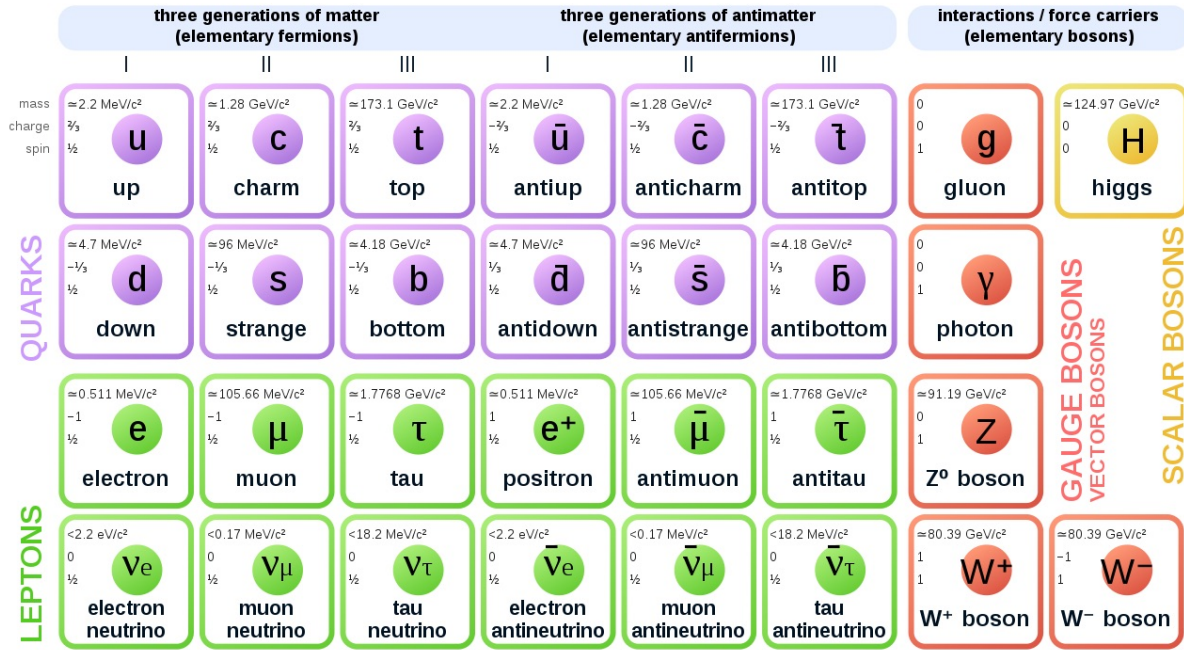
Figure I.1.1: Schematic representation of the fundamental particles described by the Standard Model of Particle Physics; their associated antiparticles are also reported. For all particles, the mass, electric charge and spin are shown.

flavour. Each lepton generation is formed by a pair of a negative particle and a neutral particle, called neutrino. The electron e^- is the lightest charged lepton and the only stable one, while muon μ^- and tauon τ^- follow at an increasing mass. The quarks generations, on the other hand, are formed by a negatively $-1/3\,e$ charged and a positively $+2/3\,e$ charged quark. In an increasing mass order, the quarks families are the down (d) and up (u), the strange (s) and charm (c), and the bottom (b) and top (t). Particles with additive quantum numbers, like the electric charge, have a corresponding antiparticle with opposite quantum numbers which is denoted by a bar over the particle symbol: $\bar{q}$.

A schematic representation of the SM, including the fundamental antiparticles, is given in Fig. I.1.1, where the mass, the electric charge and the spin are indicated.

I.1.2   Quantum ChromoDynamics

The Quantum ChromoDynamics (QCD) is the section of the SM describing the interactions between gluons and quarks through the strong interaction. As already introduced in the previous section, the strong interaction, through its symmetry group SU(3), is associated to charges called colours. The colour charge can assume three values, commonly referred to as red, blue and green, antired, antiblue and antigreen in case of antiparticles. Similarly to colour theory, the combination of the three values is neutral or colourless. Both quarks and gluons carry colour charges, which, in the case of gluons is a mix of colour and anticolour charges. Since free particles must be colourless, quarks are never observed as singlets, even

though they are fundamental constituents of matter. They group together to form colour-neutral particles known as hadrons. An additive quantum number $B = (n_q - n_{\bar{q}})/3$, where n_q and $n_{\bar{q}}$ are the number of constituent quarks and antiquarks, distinguishes between different hadrons families:

- mesons, which are composed by a quark-antiquark pair, such as the pions π (d and u) and kaons K (d or u, and s), are a combination of quark and antiquark with same, but opposite, colour. They have the baryon number $B = 0$;

- baryons, which are composed by three quarks, carry all the three colour charges and have $B = 1$. Protons and neutrons, which compose the ordinary matter, are baryons formed by the first generation of quarks, *uud* and *udd*, respectively;

- exotics, which are composition of four (tetraquarks) or five (pentaquarks) quarks, as two pairs of quark-antiquarks (*i.e.* colour+anticolour) or a pair of quark-antiquark (*i.e.* colour+anticolour) and a quark triplet (*i.e.* all three colours), can have both $B = 0$ and $B = 1$.

While for the electromagnetic force the mediator, γ, is chargeless, the gluons carry a non-neutral charge and, as such, they can interact between themselves. This self-interaction is at the origin of the dependence of the QCD coupling constant α_{QCD} on the squared quadrimomentum transferred during the interaction Q^2. Since gluons can self-interact, at small Q^2, or equivalently long distances, the virtually produced gluons around a quark increase the effective colour charge, enhancing the strength of the interaction, in an effect called antiscreening. When the exchanged energy increases and the distance decreases, the virtually produced gluons are less effective and the coupling constant decreases, generating the effect known as asymptotic freedom. As a consequence, if quarks and gluons experiment no strong interaction in the limit of infinite Q^2, the separation of quarks requires infinite energy, given that the interaction strength increase with the distance, and it brings to the production of hadronic jets whenever single quarks are produced. A perturbative approach can be used to describe QCD phenomena when the energy exchange exceed a reference energy scale Λ_{QCD}. On the contrary, processes at relatively low energies with respect to Λ_{QCD} are in the non-perturbative regime and thus their description is left to computational methods, such as lattice QCD, or to effective theories modelled on experimental data (*e.g.* the Gribov-Regge field theory [6]). The energy dependence of the strong interactions coupling, shown in Fig. I.1.2, is given by:

$$\alpha_{QCD}(Q^2) \simeq \left[\frac{33 - 2n_f}{12\pi} ln(\frac{Q^2}{\Lambda_{QCD}^2}) \right]^{-1}. \tag{I.1.1}$$

where n_f is the number of active quark flavours at the Q^2 energy scale.

While hadrons can be identified by their constituent quarks, called valence quarks, their internal structure contains constantly virtually produced gluons and quark-antiquark pairs of all families, which contribute to the final mass of the particle. The inelastic scattering of an elementary particle with a hadron can thus be described by its interaction with the different components, known as partons in a model firstly introduced by Feynman in the 1970s. The momentum of a hadron is carried by its constituent partons, which take part
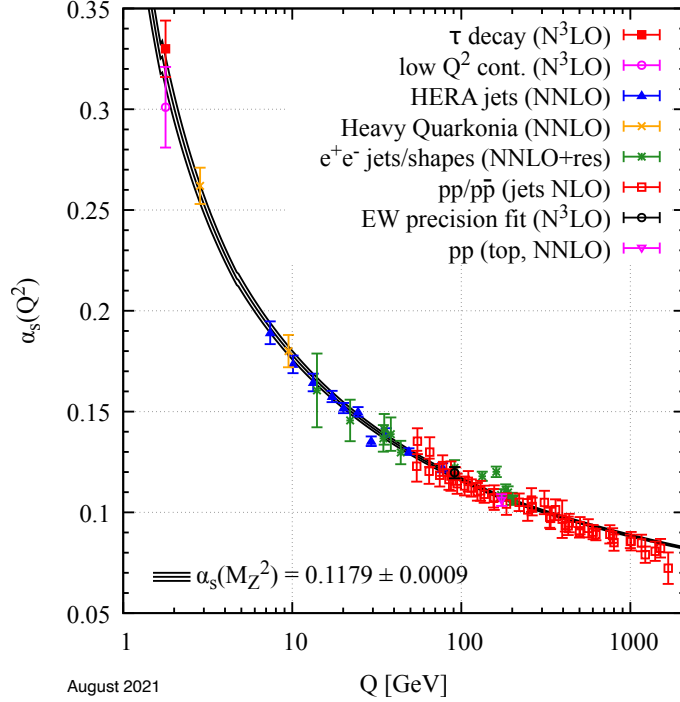
Figure I.1.2: Dependence on Q^2 of the QCD, as obtained from data. Figure taken from Ref [7].

in the interaction. The variable called Bjorken-x [8] is thus defined to describe the fraction of the total momentum that each parton carries. It can be measured in lepton-nucleon deep inelastic scatterings:

$$x = \frac{Q^2}{2Mc^2\nu}, \tag{I.1.2}$$

where ν represents the lepton energy loss and M the proton mass. The Parton Distribution Functions (PDFs) $f_i(x, \sqrt{s})$ describe the nucleon parton composition as a function of the Bjorken-x and Q^2. Even though they are non-perturbative objects, their dependence on Q^2 can be calculated perturbatively using the DGLAP equations [9]. They are thus obtained fitting data from deep inelastic scattering experiments and their value is rescaled to be applied at high energy colliders such as LHC. Figure I.1.3 shows the PDFs at two energy scales.

In hadronic colliders, both particles are composed by partons, therefore a variable taking into account the fraction carried by both interactive partons must be defined. The Feynman-x represents the difference of the Bjorken-x $x_{1,2}$ of the partons involved in the interaction:

$$x_F = x_1 - x_2 = \frac{p_L^*}{|\max(p_L^*)|}, \tag{I.1.3}$$

where p_L^* and $\max(p_L^*)$ are the longitudinal momentum of the observed produced particle and its maximum value in the centre-of-mass frame.

The energy available during a collision will be given by the quadrimomentum carried by the interacting partons $p_{1,2}$, which can be expressed as a function of the collision
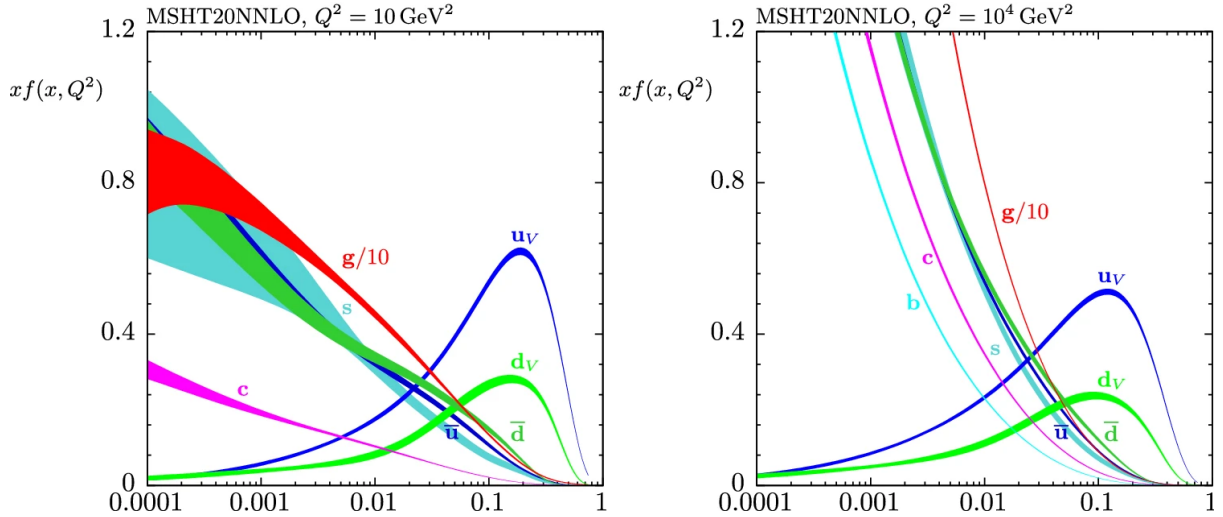
Figure I.1.3: Unpolarised parton distribution functions multiplied by x at two energy scales ($Q^2 = 10$ GeV^2 left, $Q^2 = 10^4$ GeV^2 right); the coloured bands represent the 68% confidence-level theoretical uncertainty. Figure taken from Ref. [10].

centre-of-mass energy $\sqrt{s}$ and of the Bjorken-x $x_{1,2}$:

$$\sqrt{s_{\mathrm{coll}}} = c\sqrt{(p_1 + p_2)^2} = c\sqrt{(x_1 P_1 + x_2 P_2)^2} \simeq \sqrt{x_1 x_2}\sqrt{s}, \qquad (\mathrm{I.1.4})$$

where $P_{1,2}$ are the hadrons quadrimomenta. The Lorentz boost from the centre-of-mass frame to the laboratory frame is different and unknown for every interaction. Some invariant quantities are thus defined to describe and classify the interactions. In particular, the transverse momentum p_{T} with respect to the direction of the collision is considered to distinguish between soft interactions (*i.e.* low $\sqrt{s}$) and hard interactions (*i.e.* high $\sqrt{s}$). The interactions can also be classified between inelastic interactions, when new particles are produces in the final state, and elastic interactions, if the interaction produces only a redistribution of the energy between the interacting particles.

I.1.3 The Dark Matter

Even though the SM have proven to be extremely robust against tests of increasing accuracy, having all its predictions experimentally confirmed, numerous questions remain unanswered and phenomena can not be explained in the framework of the SM. Between the open problems that push towards its extension, cosmological and astrophysical observations indicate that 84.4% [7] of the mass in the Universe is of unknown nature and it is visible only through its gravitational interaction, thus being called Dark Matter (DM). The first evidence of missing mass in the Universe came from studies of the motion of the stars and galaxies in clusters. First observations in the early 1930s [11–13], later confirmed in the 1970s [14], arrived at the conclusion that the galactic mass should exceed what was observed through photometry in order to explain the velocities obtained. In particular, the constant rotational curve observed outside the luminous radius of the galaxy (Fig. I.1.4) could be explained only including a non-visible mass contribution, distributed in a spherically symmetric halo extending beyond the visible border of the galaxy.
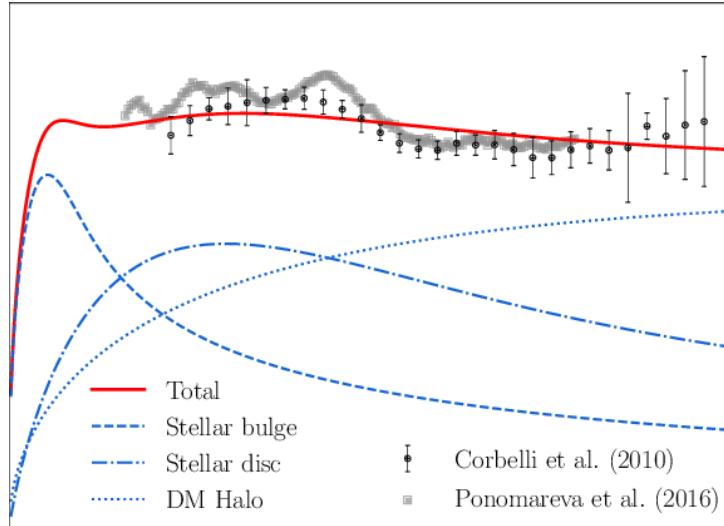
Figure I.1.4: Galaxy rotational curve as a function of the distance from the centre of the M31 galaxy. The dashed and dotted-dashed lines show rotational curves expected from the visible stars mass in the bulge and disc, respectively; the dotted line corresponds to the contribution from the Dark Matter halo. The red curve shows the total rotational speed obtained, in agreement with the observations.

Today, together with the measurements of the dynamic of stars inside the galaxy and of galaxies in clusters, the main observations that support the DM hypothesis come from cosmological measurements and gravitational lensing:

Gravitational lensing The gravitational lensing is a phenomenon predicted by the general relativity. The gravitational field produced by a mass induces a curvature in the space-time, which will bend the trajectory of light. Luminous bodies can thus be visible even when they are obscured in the line of sight if a massive body generates enough curvature. Measuring the curvature of the light is an indirect way to determine the mass that generates the gravitational field. Since this technique is independent of the dynamic of the system, it provides an independent cross-check to the DM measurements from the rotational curves. Numerous studies have compared mass measurements obtained through gravitational lensing with the amount of luminous matter calculated through various methods. These analyses have consistently revealed that a significant portion of matter in galaxies and galaxy clusters is indeed dark in nature (Fig. I.1.5, left). In recent years, a classic example of gravitational lensing applied to DM studies is provided by the bullet cluster collision [15]. The collision of two clusters is studied considering the gravitational lensing effect to understand the distribution of the mass (Fig. I.1.5, right, blue areas) and the X-rays emissions to detect the region where most of the baryonic matter, composed by hot gas, is distributed (Fig. I.1.5, right, pink areas). As it can be seen, most of the mass is distributed in regions where no baryonic mass is detected, and thus it is attributed to DM. Moreover, while hot gas, which experiences electromagnetic forces, is concentrated in the middle where the collision took place, the mass is distributed far from the collision site, strongly constraining interactions beyond the gravitational one for Dark Matter.

7
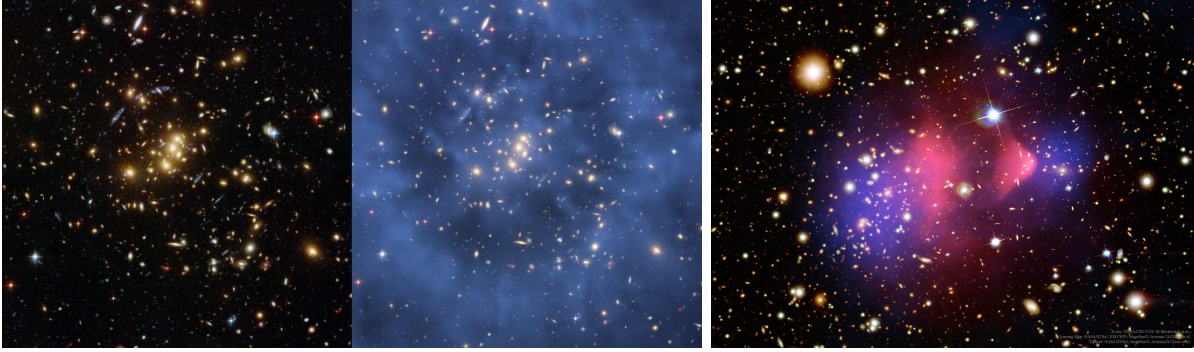
Figure I.1.5: Two examples of gravitational lensing techniques used to identify Dark Matter distribution. Left: gravitational lensing effect in the galaxy cluster CL0024+17 (repeated blue galaxies around the centre of the cluster), observed in the visible wavelength on the left and with the expected Dark Matter distribution superimposed on the right [16]. Right: composite image for the observation of the bullet cluster [15]. The hot gas distribution measured from its X-ray emission with the Chandra telescope is shown in pink; the mass distribution, as measured with the gravitational lensing effect, is represented in blue.

Cosmological evidence The anisotropies in the Cosmic Microwave Background (CMB) [17], observed by experiments like WMAP [18] and Planck [19, 20], are originated by the gravitational interaction of the matter during the photon decoupling phase of the early Universe. The magnitude of the temperature anisotropies and their angular power spectrum, known as acoustic oscillation, allows to estimate the contribution of gravitationally-interacting matter to the energy distribution in the Universe. At the same time, the measured primordial abundance of deuterium constrains the baryonic matter fraction. These studies suggest a baryonic contribution of around 4.5% to the total energy distribution of the Universe, while DM contributes to around 27%.

From the available data, a DM candidate must be a non-baryonic primarily gravitationally-interacting stable in the cosmological time-scale particle. While no definitive solution has been found so far, different candidates have been proposed, typically organised in three categories based on their expected velocity:

Hot DM Hot Dark Matter are ultrarelativistic particles. The main candidates have been neutrinos from the SM, given their weakly interacting nature. They are nevertheless excluded because their relic density is much lower than the one measured from acoustic oscillations [21]. A class of candidates beyond the Standard Model, on the other hand, is the axion, introduced in the context of the QCD to explain the expected strong Charge-Parity (CP) violation not observed experimentally [7]. The expected relic fraction from cosmological measurements limits the maximum mass of axion candidates to less then 1 eV.

Cold DM Cold Dark Matter are particles characterised by an expected speed in space lower than the speed of light. They typically are massive particles (*i.e.* GeV- TeV energy range), in agreement with the expected relic density, that can be framed in natural SM extensions such as SuperSymmetry (SUSY) and extra-dimensions models (ED). They are collectively known as Weakly-Interacting Massive Particles (WIMP).

Although favoured because of their natural integration within the SM extensions, no candidate has yet been observed at collider experiments in the expected energy range. At a higher mass range, large dense objects like primordial black holes, neutron stars, or non-luminous celestial objects such as planets have been suggested but are currently disfavoured due to cosmological constraints [22].

Warm DM Warm Dark Matter has intermediate properties between hot and cold DM. The most prominent candidates are the sterile neutrinos [23].

The favoured candidates are WIMPs because they are able to justify the current astrophysical and cosmological observations, as well as some of the open questions on the SM. For this reason, the search for signals concentrates on these candidates. Three experimental approaches, schematised in Fig. I.1.6, are followed:

Direct searches Direct experiments aim to detect potential elastic and inelastic scattering of DM particles on the detector material (*i.e.* nuclei and atomic electrons). In the interaction, energy on the order of 1 to 100 keV would be released in the detector. The signature is thus characterised by a low-energy recoils in ordinary particles accompanied by light, ionisation or heat as a consequence of the released energy. Given that the expected rate of interaction is at most 1 event per day per kilogram of detector, direct experiment are typically situated deep underground to suppress background from Cosmic Rays and they employ large volumes of active materials. They also need advanced techniques and materials to shield or veto background from natural radiation. A famous example is the DAMA/LIBRA experiment [24, 25], located at the Gran Sasso INFN national laboratories and employing approximately 250 kg of NaI(Tl) scintillators. They claimed to have observed an annual modulation in the signal that could be compatible with the motion of the Earth relative to the DM halo. The claim, however, has yet to be independently confirmed.

Colliders searches While direct searches look for interaction with ordinary matter, colliders such as the LHC at CERN aim to produce DM particles exploiting their high energy collisions. In the hypothesis that the particles would escape detection without leaving a direct signal, the production would then be identified by a significant amount of missing energy and momentum. No signal from DM has yet been observed. An alternative approach is to look for the decays or interactions of long-living DM particles [26].

Indirect searches Indirect searches focus on identify the possible SM products of the annihilation or decay of DM candidates in space. Measuring the composition of the Cosmic Ray (CR)s and comparing them to the expectations from ordinary sources, the signal would be identified as an excess. A particularly sensitive probe is the antimatter fraction in the Cosmic Ray flux, which will be presented in detail in the next chapter.
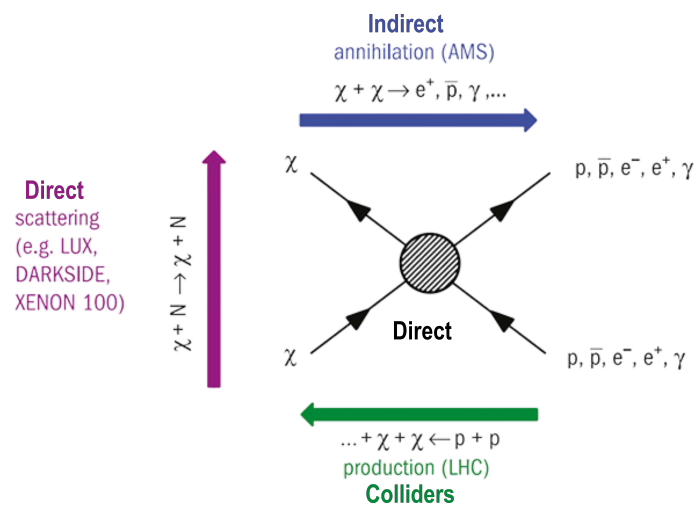
Figure I.1.6: Schematic representation of the detection techniques employed for Dark Matter identification.

I.2 Cosmic antinuclei

In this chapter, the key elements of indirect Dark Matter searches are outlined. After an overview of the fundamental properties of Cosmic Rays in Section I.2.1, Section I.2.2 presents the theoretical and experimental advances for the measurement of antimatter in Cosmic Rays as an indirect probe for Dark Matter. Section I.2.3 finally concentrates on the importance of the light (anti)nuclei searches, in particular focussing on the (anti)deuterium presenting its production mechanism and the expected flux from standard and exotic sources

I.2.1 Introduction to Cosmic Rays

The Cosmic Rays (CRs) are highly energetic charged particles that reach the Earth from the interstellar space. While they are primarily composed of protons and helium nuclei, almost all the elements of the periodic table can be found.

The CRs can be classified based on their production mechanism. Those that are directly produced and accelerated in astrophysical sources are called primary CRs. They are composed by electrons, photons, neutrinos, as well as stable nuclei synthesized in stars,
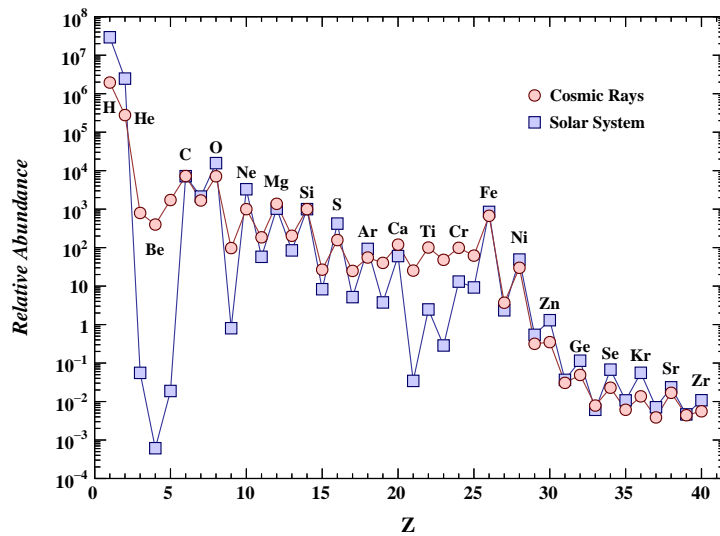
Figure I.2.1: Relative elemental abundances in Cosmic Rays (red) compared to the solar system (blue). Figure taken from Ref. [7].

11
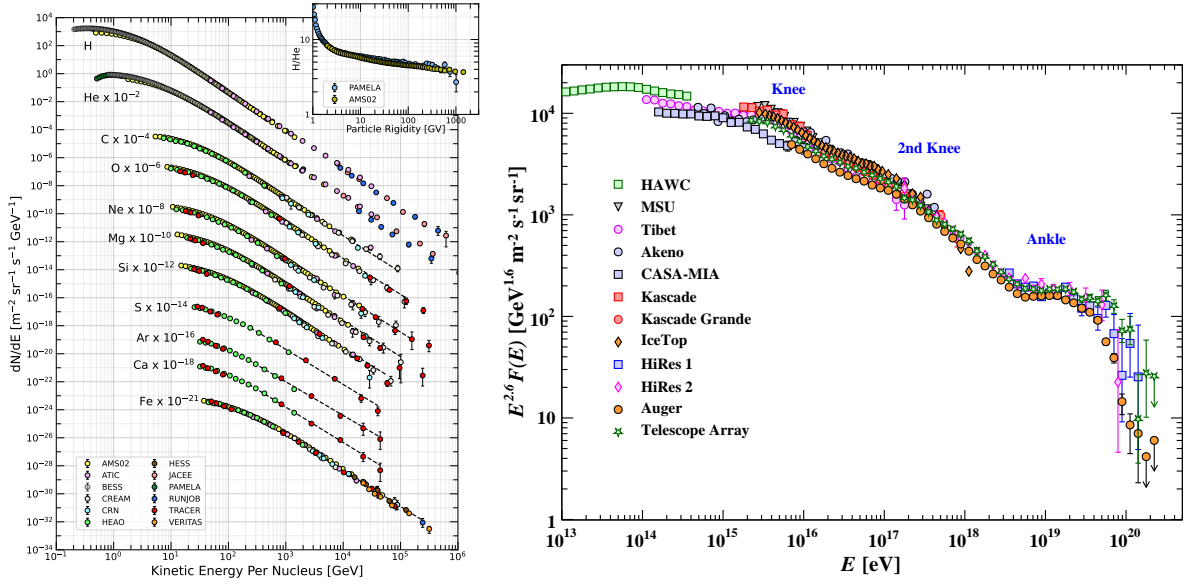
Figure I.2.2: Cosmic Rays energy spectrum for the different nuclear species (left) and for all the particles (right), drawn multiplied by $E^{2.6}$ to highlight the changes in slope; the inset at the top right of the left figure shows the H/He ratio as a function of the rigidity. Figures taken from Ref. [7].

and in particular protons and helium nuclei, which represent the 74% and 18% of the observed particles. Comparing the nuclear abundances in CRs and in the Solar System, as it is shown in Fig. I.2.1, a good agreement is found, which suggests the primary origin of most cosmic nuclei. However, in addition to the see-saw evolution caused by the weaker binding energies of odd-Z nuclei, the Li-Be-B and Sc-V-Mn groups result to be more abundant in CRs. These nuclei are mainly produced in the fragmentation of primary CRs when they collide with the InterStellar Medium (ISM), or by the decay of unstable nuclei. For this reason, they are called secondary CRs.

Cosmic Rays up to 10^{11} GeV have been observed, giving the unique opportunity to access energies unavailable in ground-based experiments. The spectrum follows a steeply falling near-power law:

$$\frac{dN}{dE} \propto E^{-\alpha}, \tag{I.2.1}$$

where the spectral index α ranges between 2.5 and 3.1, depending on the energy range. As shown in Fig. I.2.2, left, the most abundant CR particles are found in the lower energy region of the spectrum, with kinetic energy less than 1 GeV per nucleon. Considering the spectrum for all the particles (Fig. I.2.2, right), three variations in the spectral index can be identified. A so-called knee, around $\mathcal{O}(10^{15})$ eV, corresponds to an increase of α from 2.7 to 3.1. It indicates that the galactic accelerators mechanisms have reached their maximum energy. A second knee can be also identified around $\mathcal{O}(10^{17})$ eV, corresponding to a similar effect on the heavier components. At the opposite, an ankle around $\mathcal{O}(10^{18})$ eV is formed by the flattening of α around 2.7, suggesting a higher-energy flux of extra-galactic particles dominating over the galactic components. A final sharp cut-off has been observed above 10^{20} eV. This is explained as the onset of inelastic interactions of the

ultra-high energy CRs with the CMB photons, in a process known as the GZK effect [27,28].

The characterisation of the CRs flux is reached employing complementaries strategies based on the energy range under study.

Low-energy CRs (below the knee), thanks to their high flux ($\sim 6 \ km^{-2} \cdot srad^{-1} \cdot min^{-1}$ at the knee), can be measured using long-term spacecraft missions equipped with high-resolution detectors. Indeed, due to the limited size of the detector allowed to be installed in space, not enough statistics would be collected for energy over the knee. The component below $\mathcal{O}(10)$ GeV is significantly influenced by the magnetic field carried by the solar wind, which experiences fluctuations following the 11-year solar cycle, and by the geomagnetic field. Its intensity is thus dependent on both the location and time of the measurement. These experiments can employ a magnetic spectrometer coupled with a particle identification system to distinguish the different species and measure their direction and momentum, like the PAMELA [29] and AMS-02 [30] detectors. Otherwise, they can exploit a segmented calorimetric system to reach the same target, like the CALET [31] experiment.

Cosmic Rays with energies greater than the knee are more effectively measured indirectly through the air showers that they produce in the atmosphere. In particular, the particles in the showers, the air fluorescence or the atmospheric air Cherenkov light are detected. They are therefore observed by ground-based experiments employing a similar principle to that of a calorimeter: deploying a matrix of detectors across a large area, the core of the shower, correlated to the point in the atmosphere hit by the primary CR, is reconstructed as well as its lateral distribution. An example is the Pierre Auger observatory [32] covers a vast region of 3000 km^2 in Argentina and has measured CRs with energies up to 10^{20} eV. Finally, balloon-flight-based experiments lie between ground-based and space experiments. They have to take into account the interactions of the CRs with the atmosphere, which may modify the observed spectrum, yet they are significantly more cost-effective and easier to design and operate compared to space experiments. An example of such experiments is GAPS [33].

The region of interest for the measurements related to this work is the one between 1 GeV and the first knee, where increasing precision allows for a good discrimination between the CRs species. They are expected to be produced by supernovae explosions in the galaxy and accelerated by the supernovae remnants.

The galactic CRs are believed to be accelerated in a process called diffusive shock acceleration, where the impulse given to charged particles by the shock waves of the supernovae remnants is sufficient to accelerate them to the energies observed. This mechanism was firstly proposed by Enrico Fermi during the 1950s [34]. A shockwave in a supernova remnant is formed when the speed of the ejected material V_{ej} is much higher than the speed of sound c_s in the ISM. It thus forms a discontinuity in the gas flow between the upstream undisturbed ISM and the downstream region moving at V_{ej}. In the reference frame of the shock front, the ISM gas moves at a speed $u_1 = V_{ej}$, leaving the front with a smaller speed u_2. Both in the upstream and in the downstream reference frame, the matter behind the shock moves to the front with a speed $u_1 - u_2 = 3V_{ej}/4$. Charged particles moving towards the shock front thus can be reflected by the moving magnetic inhomogeneities in the shock wave with an increased speed $u_1 - u_2$, in a process that is repeated every time the particles cross the front. The average energy gain in a

round trip is:

$$\left\langle \frac{\Delta E}{E} \right\rangle = \frac{4}{3} \frac{(u_1 - u_2)}{c}. \tag{I.2.2}$$

Given the first order dependence to the speed, the mechanism is known as first-order Fermi acceleration [35] and it can be demonstrated to give a power-law energy spectrum for the CR particles with a spectral index $\alpha = 2$. A second contribution to the acceleration in supernovae remnants arise from the so-called second-order Fermi acceleration mechanism [35]. The main idea of this theory is that charged particles in CRs are iteratively accelerated due to scatterings with randomly-distributed magnetic fields in interstellar clouds. Unlike the first-order Fermi mechanism, in this process, the particle may lose energy depending on the speed direction with respect to the magnetic cloud. The resulting energy gain is related to the cloud speed V_{cl} as

$$\left\langle \frac{\Delta E}{E} \right\rangle = \frac{8}{3} V_{cl}^2. \tag{I.2.3}$$

This stochastic acceleration produces a power law spectrum with an index that depends on the speed of the cloud. However, given the small speeds of the clouds compared to c, the energy gained by the particles is rather small, therefore this mechanism is relevant only for a second acceleration of the particles coming from the shock waves.

Given the production, acceleration and all loss effects occurring during the propagation, the evolution of the CR density $\psi_i(\vec{r}, p, t)$ for the species i with the position $\vec{r}$, momentum p and time t is described by the propagation equation [36]:

$$\begin{aligned}
\frac{\partial \psi_i(\vec{r}, p, t)}{\partial t} =& \vec{\nabla} \cdot (D_{xx} \vec{\nabla} \psi_i - \vec{v}_c \psi_i) + \frac{\partial}{\partial p} \left[p^2 D_{pp} \frac{\partial}{\partial p} \left(\frac{\psi_i}{p^2} \right) \right] \\
& - \frac{\partial}{\partial p} \left[\dot{p} \psi_i - \frac{p}{3} (\vec{\nabla} \cdot \vec{v}_c) \psi_i \right] - \frac{\psi_i}{\tau_{i, frag}} - \frac{\psi_i}{\tau_{i, decay}} + q_i(\vec{r}, p, t),
\end{aligned} \tag{I.2.4}$$

being $q_i(\vec{r}, p, t)$ the total local production rate, called source term, D_{xx} and D_{pp} the space and momentum diffusion tensor terms, τ_{frag} and τ_{decay} the timescales for the CR nuclear fragmentation or radiative decay losses, $\vec{v}_c$ the convection velocity, describing the CR interaction with the galactic winds and, finally, $\dot{p}$ the time derivative of the momentum, which describes the momentum losses caused by interaction with the ISM and the galactic magnetic field or caused by radiative processes, especially important for electrons and positrons.

The use of a diffusion model to describe the CRs propagation in the Galaxy is justified by the structure of the galactic magnetic field B. It exhibits a large-scale symmetry aligned with the spiral arms of the Galaxy (Fig. I.2.3), along with lower-scale irregularities that function as scattering centres and induce stochastic and isotropic propagation of the particles, which justify the diffusive description. The motion of a particle with speed $\vec{v}$ within a magnetic field is described by the Lorentz equation:

$$m\gamma \frac{d\vec{v}}{dt} = Ze \, (\vec{v} \times \vec{B}). \tag{I.2.5}$$

where Ze is the particle charge and m the particle mass. The curvature of the trajectory is determined only by the transverse speed component $v_\perp = v \sin\theta$ where θ denotes the
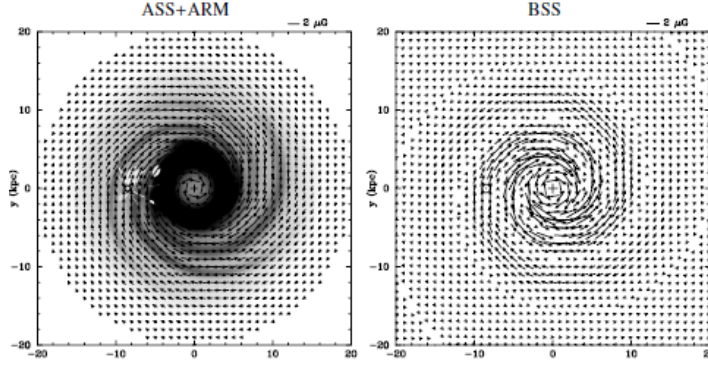
Figure I.2.3: Galactic magnetic field model with an axissymmetric configuration (*i.e.* 2π symmetry) (left) and a bisymmetric configuration (*i.e.* π symmetry) (right). Figure taken from Ref. [37].

angle between the speed and the magnetic field vectors. As a consequence, the resulting circular motion has a radius given by:

$$ r = \frac{m\gamma v}{Ze}\frac{\sin\theta}{B} = \frac{pc}{Ze}\frac{\sin\theta}{Bc} = \frac{R}{Bc}\sin\theta. \tag{I.2.6} $$

being $R = pc/Ze$ the particle rigidity. Cosmic Rays with rigidity below 10 GV are affected both by the galactic magnetic field and by solar and geomagnetic effect before detection. The relative elemental or isotope abundances are fundamental to characterise CR propagation. The ratio of stable and unstable isotopes of the same secondary element in the low energy range is used to determine the propagation time in the Galaxy (*i.e.* ^{9}Be/^{10}Be [38]). The secondary-to-primary ratios for light elements, instead, is used to quantify the thickness of the ISM traversed by the CRs in their propagation [39], which is related to the time required for a charged particle to leave the Galaxy τ_{esc}. Assuming a simplified model where no energy loss-and-gain effects and a uniform and constant density of CRs in the Galaxy are considered, the diffusion can be described by:

$$ \frac{\partial\psi_i}{\partial t} \simeq -\frac{\psi_i}{\tau_{esc}} - \frac{\psi_i}{\tau_{frag}} + \sum_j \frac{\psi_j}{\tau_{frag,j\to i}} + q_i = 0, \tag{I.2.7} $$

where $\sum_j \frac{\psi_j}{\tau_{frag,j\to i}}$ represent the sum of the contribution to the production of the nucleus i by the fragmentation of the higher mass nucleus j. For secondary CRs, the source term is 0. Considering a secondary nucleus S produced by fragmentation of a primary P, their flux ratio will be given by:

$$ \frac{N_S}{N_P} \simeq \frac{\frac{1}{\tau_{frag,P\to S}}}{\frac{1}{\tau_{esc}} + \frac{1}{\tau_{frag,S}}} \qquad \Longrightarrow \qquad \frac{N_S}{N_P} \simeq \frac{\frac{1}{\tau_{frag,P\to S}}}{\frac{1}{\tau_{esc}}} \quad \text{for } \tau_{esc} \ll \tau_{frag,S}, \tag{I.2.8} $$

where the last equation is valid for rigidities higher than 100 GV. The secondary-to-primary ratio, therefore, depends on the escape time and on the fragmentation timescale. Cosmic Ray fragmentation in the ISM can be described by the equation:

$$ \frac{\partial\psi_i}{\partial t} = -\frac{\psi_i}{\tau_{frag}} = -n_{ISM}v\sigma_i\psi_i, \tag{I.2.9} $$

15
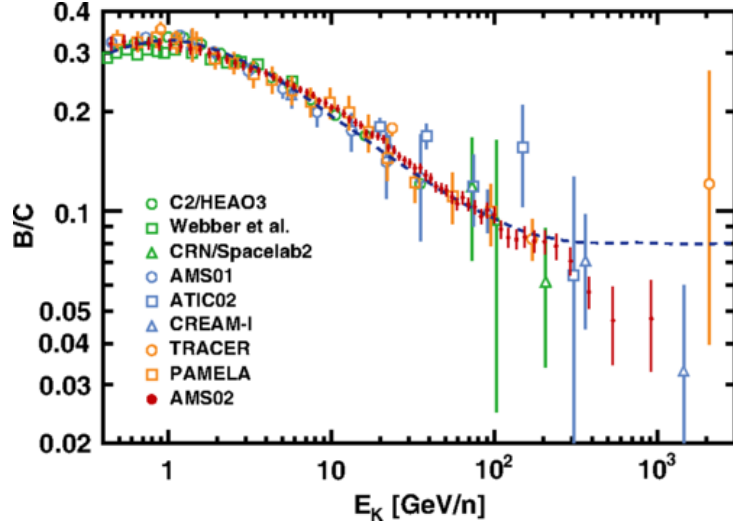
Figure I.2.4: Boron-to-carbon ratio measured by the AMS-02 collaboration, compared with previous experiments. Figure taken from Ref. [39].

where n_{ISM} is the ISM particle density and σ_i the interaction cross-section. The particle density is estimated to be $n_{ISM,H} \simeq 1$ cm^{-3} for hydrogen and $n_{ISM,He} \sim 0.1 \cdot n_{ISM,H}$ for helium, while heavier elements are only present in traces [40].

The typically considered ratio is the boron-to-carbon ratio. Indeed, the boron is essentially only produced in nuclear interactions of carbon with the ISM, while the carbon is a highly abundant primary nucleus, after helium and hydrogen. Applying the propagation equation to boron and carbon, the secondary-to-primary ratio can be expressed as a function of the carbon-to-boron fragmentation cross-section $\sigma_{C \to B}$:

$$\frac{N_B}{N_C} \simeq n_{ISM} v \sigma_{C \to B} \tau_{esc}. \tag{I.2.10}$$

From the experimental data available, shown in Fig. I.2.4, the boron-to-carbon ratio decreases with the energy without any distinct structure and it is used to extrapolate the τ_{esc} energy dependence.

I.2.2 Antimatter in Cosmic Rays

As for standard particles, also antimatter is expected to be observed in the CR flux measured by the experiment. Nevertheless, it is expected to be produced only by the primary CRs interactions with the ISM, and therefore it is rare. Its flux is thus considered to be a particularly sensitive indirect probe for contributions from exotic sources, such as DM annihilation and decay processes. While the measurements of antimatter flux in CRs are being carried out since the 1980s, the improvement in the detector technologies allowed only recently to reach a level of experimental precision that outmatches the uncertainties on the models. The major experiments that contributed in recent years are:

PAMELA The Payload for Antimatter Matter Exploration and Light-nuclei Astrophysics (PAMELA) experiment [41] has been a satellite-installed detector dedicated to the measurement of the charge component of the CRs. The core of the detector
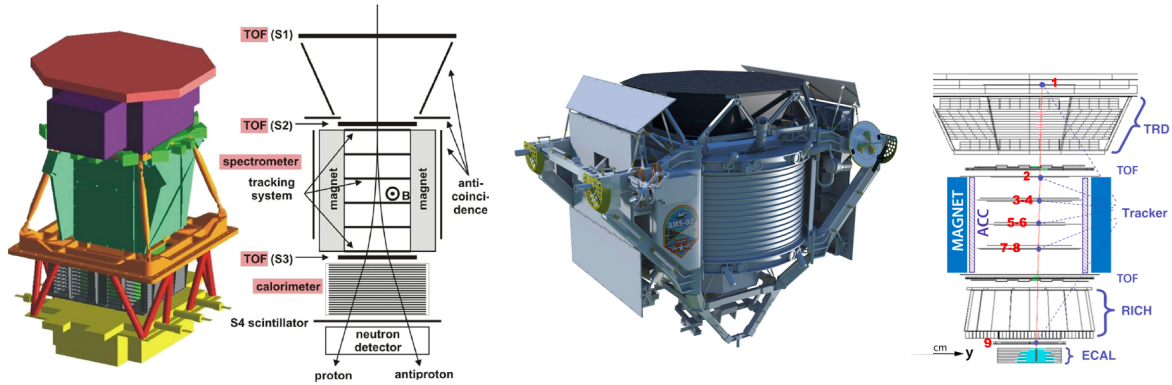
Figure I.2.5: Schematic representation of the PAMELA (left) and AMS-02 (right) detectors. Figures taken from Ref. [42] and Ref. [43], respectively.

(Fig. I.2.5, left), 1.3 m high and weighting 470 kg, was a spectrometer composed by a permanent 0.43 T magnet and six silicon-based tracking stations to reconstruct the trajectories of the charged particles and extract their charge and rigidity. The particle identification was then performed with two time-of-flight scintillator planes, providing also the trigger for the acquisition, and a calorimeter. Operating between 2006 and 2016 on a satellite, it provided precise measurements on the positron and antiproton fractions in the CRs, with a sensitivity ranging in 50 MeV −270 GeV and 80 MeV −190 GeV, respectively. It also measured the effect of the solar modulation on low-energy CRs. While it was designed to be sensitive to the antihelium-to-helium ratio up to 10^{-7}, it did not observe any signal.

AMS-02 The Alpha Magnetic Spectrometer (AMS-02) experiment [30] is the scientific heir of PAMELA, sharing the same physics targets and detection idea, but it provides an improved detector design, dimensions and operational duration thanks to its installation on the International Space Station in 2011. The AMS-02 detector (Fig. I.2.5, right) consists of a spectrometer to measure the rigidity of the particles coupled with a heterogeneous particle identification system. The spectrometer is composed by nine silicon tracking planes disposed within a permanent magnet of 0.15 T over a ~ 3 m arm. Two time-of-flight stations provide the trigger for the data acquisition, as well as the particle identification together with the electromagnetic calorimeter. The additional Transition Radiation Detector (TRD), which improve the electrons/positrons and (anti)protons discrimination, and Ring Imaging CHerenkov detector (RICH) guarantee a redundancy in the particle identification technique, improving its performance. While it is still taking data, it already proved to be able to increase the measurement precision pushing the boundaries of the observable energy (up to $\mathcal{O}(TV)$ rigidities) and charge (up to Z=26).

These experiments are instrumental in advancing the understanding of CR antimatter fluxes and they are fundamental in the search for DM signatures within CR data. In particular, the fraction of positrons, antiprotons and light antinuclei is being investigated.
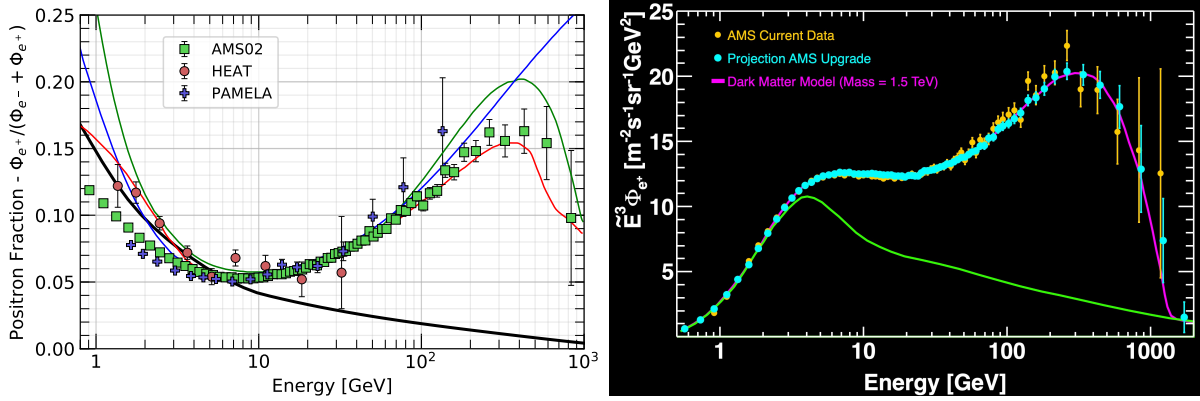
Figure I.2.6: Left: measurement of the positron fraction in CRs by the PAMELA (blue cross), HEAT (red circle) and AMS-02 (green square) collaborations compared to predictions from a pure secondary origin (black line), with a DM decay (green line), with a different propagation description (blue line) and with the emission from pulsars (red line). Right: positron flux as a function of the energy, as measured by the AMS-02 experiment. Current data (yellow dot) are compared to the projection of the expected results in 2030 (light blue dot); the expected flux from secondary CRs (light green line) and from a DM candidate annihilation (pink line) are also shown. Figure taken from Ref. [7] and Ref. [47].

I.2.2.1   Positron fraction in Cosmic Rays

Positrons in CRs are expected to be produced only in collisions with the ISM via π^+ and K^+ decay, and, as such, their expected fraction compared to the electrons should be decreasing with the energy. Both PAMELA and AMS-02, though, observed a clear rise in the spectrum of the ratio for energy above 10 GeV, which is in clear disagreement with the secondary production hypothesis (black line in Fig. I.2.6, left). Different hypotheses have been proposed to explain the excess observed in the CR positrons:

- exotic positron primary sources such as DM annihilation or decay [44] (green line on the Fig. I.2.6, left),

- nearby astrophysical positron primary sources, such as pulsars [45] (red line on the Fig. I.2.6, left),

- change in the spectrum due to propagation effects within the Galaxy, such as the non-uniform distribution of the sources indicated by astrophysical observations [46] (blue line on the Fig. I.2.6, left).

While the pulsar emission hypothesis provides the best description of the AMS-02 results at the moment, reducing uncertainties and extending the energy range of the data with further observations are necessary to confirm these findings. Figure I.2.6, right, shows the current data on the positron flux together with the projection of the expected results and uncertainties in the 2030. A precise measurement of the spectrum cut-off around the TeV would indeed confirm or exclude an exotic origin to the observed excess.

I.2.2.2 Antiproton fraction in Cosmic Rays

The antiproton-to-proton ratio represents a second possible channel for the indirect DM searches, which complements the searches in the positron channel and contribute to constrain the space of the DM candidates. In particular, if DM annihilation were the cause of the observed positron excess, an excess of antiprotons at higher energies would be anticipated and visible in the antiproton-to-proton ratio, which is expected to be around 10^{-4} for kinetic energies of 10 GeV. Any excess would be difficult to be explained with standard astrophysical sources given the difficulty in the antiproton production in the known processes. The antiproton-to-proton ratio has been measured firstly by PAMELA up to 100 GeV in kinematic energy [48], and later by AMS-02 up to 525 GV rigidity [49,50]. In both cases, a flattening around 2×10^{-4} for $E > 10$ GeV is observed (Fig. I.2.7, top). The expected antiproton production mechanism consists in the collisions of CRs on the ISM. Given that both in CRs and ISM the main components are protons and helium nuclei, the interesting reactions are:

$$p + \text{H} \to \bar{p} + X,$$
$$p + \text{He} \to \bar{p} + X,$$
$$\text{He} + \text{H} \to \bar{p} + X.$$
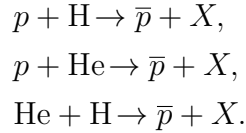
The expected flux is then obtained from the source terms related to the given reactions, applying the propagation equation Eq. I.2.4 and taking into account the effect of the solar modulation.

The theoretical model, with the different contribution to its uncertainty, as known in 2015, is compared to the experimental results of PAMELA and AMS-02 in Fig. I.2.7, top. For energies above 10 GeV, the data suggest a milder dependence on energy than expected, indicating a potential excess with respect to secondary antiproton production and the possible presence of an exotic primary source. The uncertainty associated with the model though does not allow to draw conclusive statements. While contribution from the primary CR spectrum, the CR propagation and the solar modulation are not negligible, the leading contribution to the uncertainty is given by the production cross-section. More precise experimental measurements of relevant cross-sections within a wide range of energy are thus essential.

In 2017 and 2018 the NA61/SHINE and LHCb collaborations performed the prompt antiproton production measurements in pp collisions at $\sqrt{s_\text{NN}} = 6.3, 7.7, 8.8, 12.3$ and 17.3 GeV [53] and in pHe at $\sqrt{s_\text{NN}} = 110$ GeV [54]. The latter represented the first determination of antiproton production in the pHe system. Prior to it, no data on interactions involving helium were available and a phenomenological extrapolation was performed from pp, pC or pA. Both results had a major impact in reducing the model uncertainties, as they tested a wide and previously unexplored energy range. In particular, the measurement of antiproton production at an intermediate energy range between traditional fixed-target experiments ($\mathcal{O}(10$ GeV$)$) and collider experiments ($\mathcal{O}($ TeV$)$) allowed to constrain the cross-section scaling violation models, for which no accurate predictions were available before. An updated evaluation of the antiproton abundance in CRs [52] is shown in Fig. I.2.7, bottom. A better agreement with respect to the AMS-02 data is found, thus disfavouring the hypothesis of a primary contribution to the antiproton flux. However, it is crucial to note that the knowledge of the antiproton production
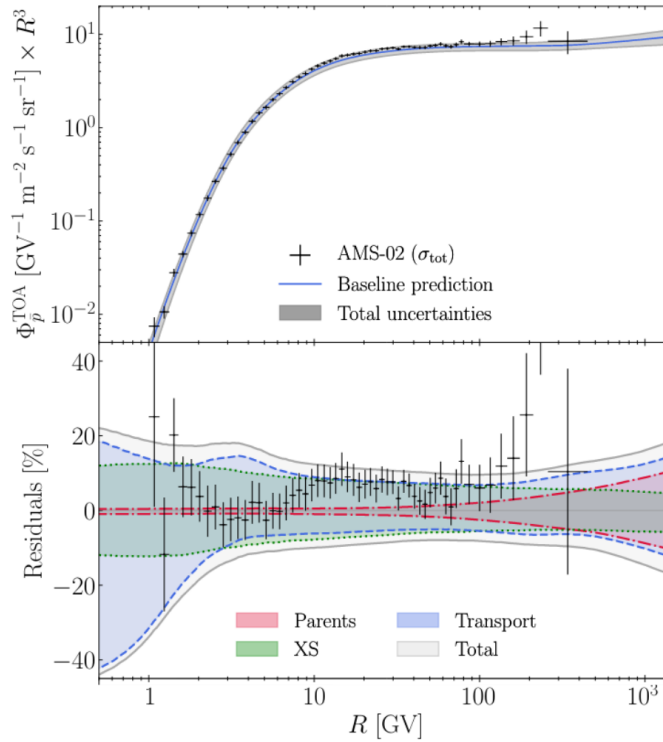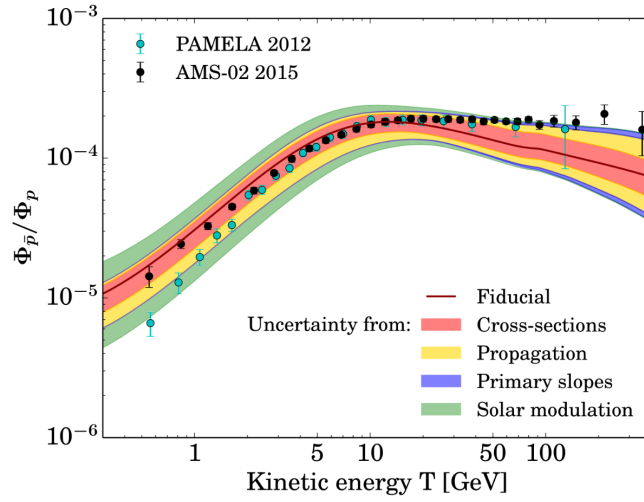
Figure I.2.7: Top: measurement of the antiproton-to-proton flux as a function of the energy by the PAMELA (blue circle) and AMS-02 (black circle) collaborations in the 2015; the theoretical model (red line) with the related uncertainties is reported as well. Bottom: measurement of the antiproton-to-proton flux as a function of the rigidity by the AMS-02 collaborations in the 2019; the updated theoretical prediction (black line) with the related uncertainty (grey area) is reported as well. In the bottom panel, the residuals of the model and the different contributions to the uncertainty are reported. Figure taken from Ref. [51] and Ref. [52], respectively.
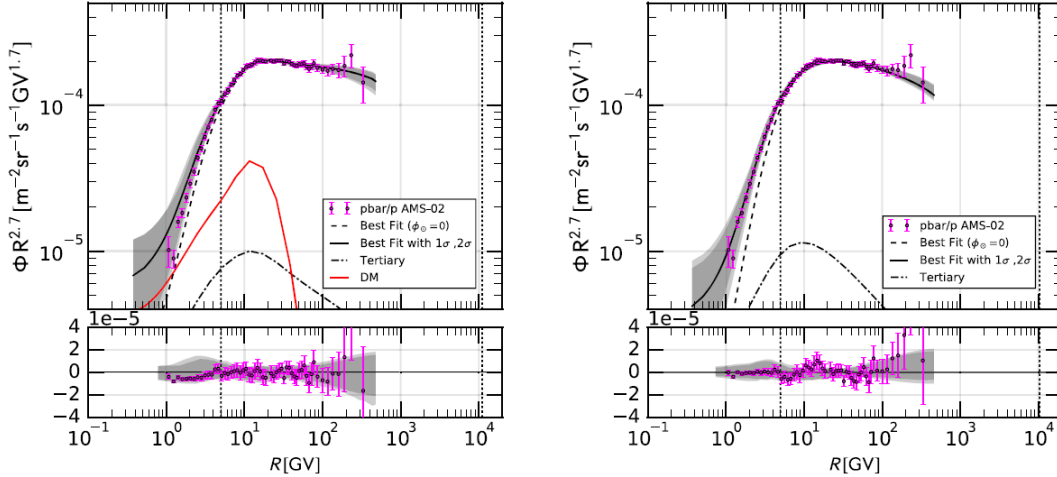
Figure I.2.8: Comparison of the best fit of the antiproton-to-proton ratio to the AMS-02 data, with a DM component (left) and without DM contributions (right). The lower panels show the corresponding residuals. Figure taken from Ref. [55].

cross-section remains one of the leading sources of uncertainty. Indeed, comparing the most recent antiproton-to-proton ratio results with theoretical models, both including and excluding a DM contribution, a similar level of agreement is found [55] (Fig. I.2.8), highlighting the need for further experimental data and to expand the searching channels considered.

I.2.2.3 Antinuclei fraction in Cosmic Rays

As it is made clear by the two channels considered in the previous paragraphs, the search for exotic sources is favoured in channels where low background from standard astrophysical sources is expected. Light antinuclei are thus golden channels for these searches since their primary production from astrophysical sources or secondary production in CRs is extremely suppressed. At the same time, multiple exotic models expect the production of antinuclei, with precise scaling laws depending on their mass number A, therefore their observation in the CR flux, or lack thereof, can contribute to constrain the space of DM candidates. The current expectations of the peak antideuterium flux from secondary production is at the limit of the sensitivity of the AMS-02 detector after 15 years of operation ($\sim 5 \times 10^{-7}$ $(s \cdot m \cdot srad \cdot \mathrm{GeV}/n)^{-1}$) [56], while the sensitivity up to 10^{-9} $(s \cdot m \cdot srad \cdot \mathrm{GeV}/n)^{-1}$ for antihelium is not expected to be enough to detect any secondary signals [56]. Nevertheless, the predictions are strongly dependent on the production mechanism considered.

In recent years, the AMS-02 collaboration has reported the observation of few antideuteron and antihelium candidates [47], yet to be confirmed, and in 2024 the novel balloon experiment General AntiParticle Spectrometer (GAPS) [33] is expected to undertake its first flight, paving the way for a new high precision era for the antinuclei search in CR. In this context, studying and understanding the mechanisms, both exotic and standard, involved in the production of antinuclei is crucial to clearly discriminate and identify the origin of possible signals.

The expected antinuclei flux model can be derived from the propagation model of Eq. I.2.4

21
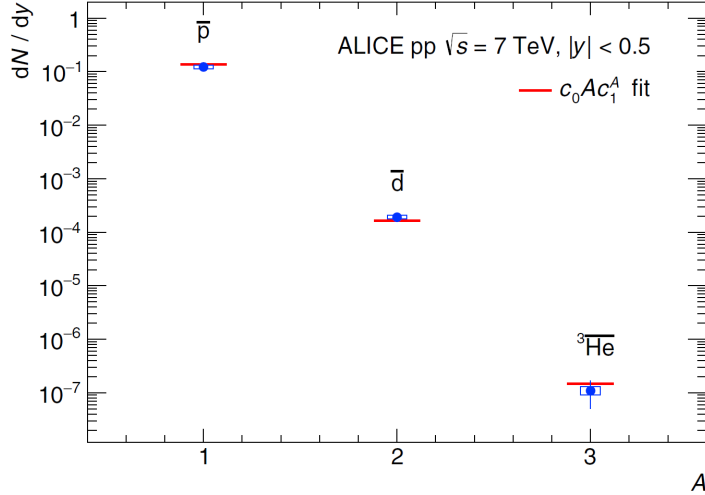
Figure I.2.9: Integrated yields of antiprotons, antideuterons and antihelium-3 nuclei as a function of the mass number A in elastic pp collisions at $\sqrt{s} = 7$ TeV. Figure taken from Ref. [57].

where the propagation mechanism and the source term q are crucial elements. The latter in particular requires the knowledge of the mechanisms governing the antinuclei production both from exotic sources and from the interactions of the primary CRs with the ISM. Given the experimental data reported, the channels of greatest interest are the (anti)deuterium and the (anti)helium. In the following sections, the antinuclei production mechanisms are presented focussing on the (anti)deuterium as an example case.

I.2.3   Light (anti)nuclei production models

In hadron collisions, antinuclei production can occur only through the formation of nucleon-antinucleon pairs, in order to ensure the conservation of the baryonic number. As a consequence, the elevated energy threshold required for their production limits the achievable production rates. Given that any additional antinucleon in the final antinucleus state requires the production of an additional pair, the production of light antinuclei gets strongly suppressed as a function of the mass number A. Production studies in pp collisions at the LHC showed that the production yield of antinuclei decreases as $(\mathcal{O}(10^{-3}))^{A-1}$ with respect to the antiproton yield [57] (Fig. I.2.9).

Considering the minimal reaction to produce an antideuterium in pp collisions:

$$p + p \rightarrow p + p + p + n + \overline{\text{d}}, \tag{I.2.12}$$

the threshold energy in the centre-of-mass system is 6 GeV, which corresponds to a projectile energy of 17 GeV in the ISM system. The collision products are therefore boosted in the direction of the projectile, as a consequence of the elevated threshold energy. The expected antideuteron energy distribution associated to secondary production (*i.e. pp*, pHe and Hep) is thus concentrated in the $E > 1$ GeV region. Similar results are expected for antihelium-3 and antihelium-4, given the respective projectile energy thresholds in the ISM system of 31 GeV and 49 GeV.

Possible DM signals, on the other hand, are expected to show a different energy distribution. Considering the cold DM hypothesis, due to the very low-speed distribution of DM in the

Galaxy, antiprotons and antinuclei produced in annihilation or decay events are at rest with respect to the Galaxy, leading to a flux highly concentrated at low energies (~ 1 GeV). Indirect searches thus exploit the kinematic differences between DM production and standard astrophysical production to identify DM signals.

Regardless of the origin, antinuclei production proceeds through the formation of its constituent nucleons and their subsequent aggregation. The underlying mechanism has thus to be understood so that accurate predictions can be made on the expected primary and secondary fluxes.

I.2.3.1 Coalescence model

No comprehensive theoretical model available at the moment is able to explain and predict the mechanism of production of nuclei and antinuclei in hadronic interactions from first principles. Different phenomenological models, tuned on data, have been tested and resulted more or less able to predict the experimental yield and spectra observed. To date, the model that has proven to be the most successful is the coalescence model [58, 59], which states that an (anti)nucleus is formed when the (anti)nucleons are sufficiently close in phase space. Throughout the rest of this section, the nucleon notation will be used for readability, although the equations are equally applicable for antinucleons. Moreover, the explicit derivation of the coalescence distribution [60–62] will be performed in the case of deuterons, considering the case of higher mass nuclei as an extension of the described approach.

The coalescence function $C\left(\sqrt{s}, \vec{p}_p, \vec{p}_n\right)$, describing the probability of deuteron formation, is a function of the nucleons momentum difference $2\Delta\vec{p} = \vec{p}_p - \vec{p}_n$ and of the total energy of the system. The momentum distribution of deuterons is thus given by:

$$\frac{dN_{\mathrm{d}}}{d\vec{p}_{\mathrm{d}}^3}\left(\sqrt{s}, \vec{p}_{\mathrm{d}}\right) = \int d^3\vec{p}_p d^3\vec{p}_n \left(\frac{dN_{pn}}{d\vec{p}_p^3 d\vec{p}_n^3}\left(\sqrt{s}, \vec{p}_p, \vec{p}_n\right)\right) C\left(\sqrt{s}, \vec{p}_p, \vec{p}_n\right). \qquad (I.2.13)$$

dN_i with $i = \mathrm{d}, pn$ is the number of deuterons or nucleons pair produced in the collisions and they depend on the ratio between the differential and the total cross-section based on the following relations:

$$\frac{dN_{\mathrm{d}}}{d\vec{p}_{\mathrm{d}}^3}\left(\sqrt{s}, \vec{p}_{\mathrm{d}}\right) = \frac{1}{\sigma_{\mathrm{d}}^{tot}}\frac{d\sigma_{\mathrm{d}}}{d\vec{p}_{\mathrm{d}}^3}\left(\sqrt{s}, \vec{p}_{\mathrm{d}}\right),$$
$$\frac{dN_{pn}}{d\vec{p}_p^3 d\vec{p}_n^3}\left(\sqrt{s}, \vec{p}_p, \vec{p}_n\right) = \frac{1}{\sigma_{pn}^{tot}}\frac{d\sigma_{pn}}{d\vec{p}_p^3 d\vec{p}_n^3}\left(\sqrt{s}, \vec{p}_p, \vec{p}_n\right). \qquad (I.2.14)$$

In first approximation, the coalescence function is expected to be independent of the collision energy. The expression can thus be transformed applying the momentum conservation and, changing the integration variables to the deuteron momentum and the nucleons relative momentum:

$$\frac{dN_{\mathrm{d}}}{d\vec{p}_{\mathrm{d}}^3}\left(\sqrt{s}, \vec{p}_{\mathrm{d}}\right) = \int d^3\vec{p}_{\mathrm{d}} d^3\Delta\vec{p}\left(\frac{dN_{pn}}{d\vec{p}_p^3 d\vec{p}_n^3}\left(\sqrt{s}, \vec{p}_{\mathrm{d}}/2 + \Delta\vec{p}, \vec{p}_{\mathrm{d}}/2 - \Delta\vec{p}\right)\right)$$
$$C\left(\Delta\vec{p}\right)\delta\left(\vec{p}_d - \vec{p}_p - \vec{p}_n\right). \qquad (I.2.15)$$

Integrating over the deuteron momenta, the expression simplifies to:

$$\frac{dN_{\mathrm{d}}}{d\vec{p}_{\mathrm{d}}^{\,3}}\left(\sqrt{s},\vec{p}_{\mathrm{d}}\right) = \int d^3\Delta\vec{p}\left(\frac{dN_{pn}}{d\vec{p}_p^{\,3}d\vec{p}_n^{\,3}}\left(\sqrt{s},\vec{p}_{\mathrm{d}}/2+\Delta\vec{p},\vec{p}_{\mathrm{d}}/2-\Delta\vec{p}\right)\right)C\left(\Delta\vec{p}\right). \qquad (I.2.16)$$

Given that the energy required to form a deuteron is around 3.7 GeV and its binding energy is ~ 2.2 MeV, the coalescence function must be strongly peaked around 0, so the expression can be rewritten in the limit of $|\Delta\vec{p}| \ll |\vec{p}_{\mathrm{d}}|$:

$$\frac{dN_{\mathrm{d}}}{d\vec{p}_{\mathrm{d}}^{\,3}}\left(\sqrt{s},\vec{p}_{\mathrm{d}}\right) = \frac{dN_{pn}}{d\vec{p}_p^{\,3}d\vec{p}_n^{\,3}}\left(\sqrt{s},\vec{p}_{\mathrm{d}}/2,\vec{p}_{\mathrm{d}}/2\right)\int d^3\Delta\vec{p}\,C\left(\Delta\vec{p}\right). \qquad (I.2.17)$$

It is convenient to define the deuteron momentum distribution in its Lorentz-invariant form:

$$E_{\mathrm{d}}\frac{dN_{\mathrm{d}}}{d\vec{p}_{\mathrm{d}}^{\,3}}\left(\sqrt{s},\vec{p}_{\mathrm{d}}\right) = \frac{m_{\mathrm{d}}}{m_p m_n}\int d^3\Delta\vec{p}\,C\left(\Delta\vec{p}\right)\times\left(E_{pn}\frac{dN_{pn}}{d\vec{p}_p^{\,3}d\vec{p}_n^{\,3}}\left(\sqrt{s},\vec{p}_{\mathrm{d}}/2,\vec{p}_{\mathrm{d}}/2\right)\right)$$

$$\Rightarrow \quad E_{\mathrm{d}}\frac{dN_{\mathrm{d}}}{d\vec{p}_{\mathrm{d}}^{\,3}}\left(\sqrt{s},\vec{p}_{\mathrm{d}}\right) = B_2\left(E_{pn}\frac{dN_{pn}}{d\vec{p}_p^{\,3}d\vec{p}_n^{\,3}}\left(\sqrt{s},\vec{p}_{\mathrm{d}}/2,\vec{p}_{\mathrm{d}}/2\right)\right), \qquad (I.2.18)$$

where B_2 is the coalescence probability for a pn pair which can be measured experimentally. Nevertheless, commonly the coalescence is described through the so-called coalescence momentum p_0, which represents the maximal distance between nucleons in the momentum space that allows deuteron formation. When assuming that the coalescence function can be approximated as a step function $\Theta\left(\Delta p^2 - p_0^2\right)$, the deuteron momentum distribution becomes:

$$E_{\mathrm{d}}\frac{dN_{\mathrm{d}}}{d\vec{p}_{\mathrm{d}}^{\,3}}\left(\sqrt{s},\vec{p}_{\mathrm{d}}\right) = \frac{m_{\mathrm{d}}}{m_p m_n}\left(\frac{4\pi}{3}p_0^3\right)\left(E_{pn}\frac{dN_{pn}}{d\vec{p}_p^{\,3}d\vec{p}_n^{\,3}}\left(\sqrt{s},\vec{p}_{\mathrm{d}}/2,\vec{p}_{\mathrm{d}}/2\right)\right). \qquad (I.2.19)$$

The coalescence probability B_2 and the coalescence momentum p_0 are related by:

$$B_2 = \frac{m_{\mathrm{d}}}{m_p m_n}\left(\frac{4\pi}{3}p_0^3\right). \qquad (I.2.20)$$

When the production of a pn pair can be factorised as the product of the single nucleons production:

$$E_{\mathrm{d}}\frac{dN_{\mathrm{d}}}{d\vec{p}_{\mathrm{d}}^{\,3}}\left(\sqrt{s},\vec{p}_{\mathrm{d}}\right) = B_2\left(E_p\frac{dN_p}{d\vec{p}_p^{\,3}}\left(\sqrt{s},\vec{p}_{\mathrm{d}}/2\right)\right)\left(E_n\frac{dN_n}{d\vec{p}_n^{\,3}}\left(\sqrt{s},\vec{p}_{\mathrm{d}}/2\right)\right). \qquad (I.2.21)$$

This hypothesis is not true when the interaction energy is close to the mass of the product, as it is the case for deuterons. A multiplicative correction factor $R_n\left(\sqrt{s+m_{\mathrm{d}}^2-2\sqrt{s}E_{\mathrm{d}}}\right)$ can be applied to take into account the reduction of the phase space due to the production of the first nucleon. In this case, the coalescence probability measured in data would contain also the correction factor.

Following similar assumption as for the deuteron, the factorised coalescence model for a nucleus of mass number A and charge Z is given by:

$$E_A \frac{dN_A}{d\vec{p}_A^3}\left(\sqrt{s}, \vec{p}_A\right) = B_A \left(E_p \frac{dN_p}{d\vec{p}_p^3}\left(\sqrt{s}, \vec{p}_A/A\right)\right)^Z \left(E_n \frac{dN_n}{d\vec{p}_n^3}\left(\sqrt{s}, \vec{p}_A/A\right)\right)^{A-Z}, \quad \text{(I.2.22)}$$

where the coalescence probability B_A is related to the coalescence momentum as:

$$B_A = \frac{m_A}{m_p^z m_n^{A-Z}} \left(\frac{4\pi}{3} p_0^3\right)^{A-1}. \quad \text{(I.2.23)}$$

Finally, assuming isospin invariance, the neutron production cross-section is equal to the proton production cross-section. This simplified model is known as the analytical coalescence model, which is commonly applied to extract the coalescence probability from experimental data:

$$\begin{aligned} E_A \frac{dN_A}{d\vec{p}_A^3}\left(\sqrt{s}, \vec{p}_A\right) &= B_A \left(E_p \frac{dN_p}{d\vec{p}_p^3}\left(\sqrt{s}, \vec{p}_A/A\right)\right)^A = \\ &= \frac{m_A}{m_p^A}\left(\frac{4\pi}{3}p_0^3\right)^{A-1}\left(E_p \frac{dN_p}{d\vec{p}_p^3}\left(\sqrt{s}, \vec{p}_A/A\right)\right)^A. \end{aligned} \quad \text{(I.2.24)}$$

The nuclei production yields and their spectra are thus dependent on the nucleons production cross-section in the relevant systems (*i.e.* pp, pHe, Hep for secondary CRs), and on the coalescence momentum p_0 that is measured on data.

In recent years, in order to take into account correlations involved in the nuclei production, Monte Carlo (MC) generators have been applied to derive the coalescence momentum instead of the traditional analytical model [61,62], since they allow to apply the coalescence condition on an event-by-event basis. The coalescence momentum is favoured over the coalescence probability because of its physical meaning, which can be easily implemented in numerical simulations. MC models solve Eq. I.2.13 without simplifying assumptions and considering the coalescence function as a step function around the coalescence momentum, as the only free parameter of the system. The value for the coalescence momentum is then derived fitting the resulting distribution on data. This effective model describes the physics coalescence through a single parameter, which could depend on the interaction energy, collision system and final product. For this reason, it is of pivotal importance to perform (anti)nuclei production measurements in multiple systems and interaction energies.

The data currently available on the production of light (anti)nuclei are concentrated in two energy ranges. For projectile energies lower than the TeV scale, the most recent results come from the NA49 collaboration, which measured the deuterium, tritium and helium-3 production in fixed-target PbPb collisions for beam energies ranging from 20 to 158 GeV [63]. The study highlighted a rising trend in the coalescence probability as a function of the transverse momentum. In the same energy range, the data available in pp interactions date back to 1970s and 1980s and are affected by strong uncertainties, but new results are foreseen from the NA61/SHINE collaboration in the near future [64].
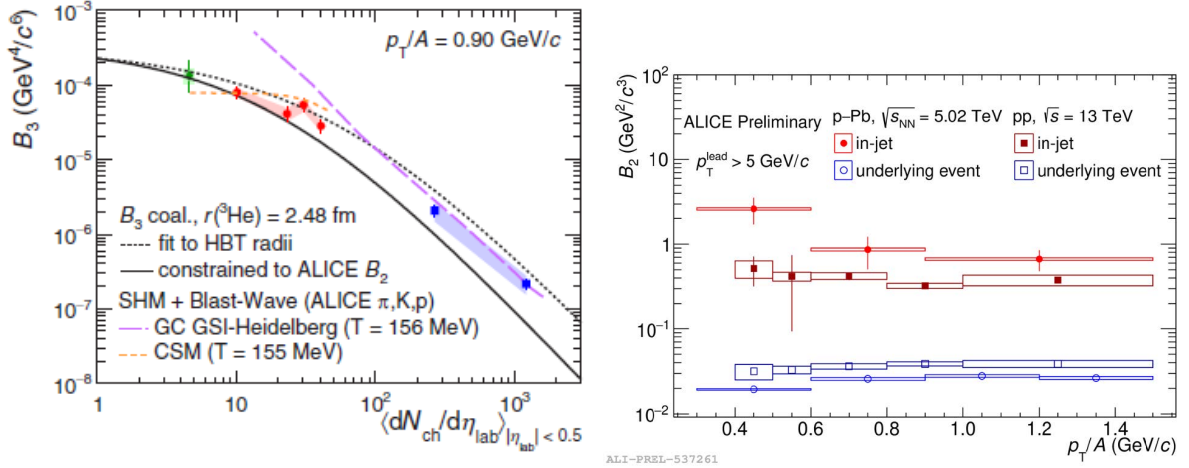
Figure I.2.10: Left: helium-3 coalescence probability B_3 as a function of the mean charged-particle multiplicity density for pp (green), pPb (red) and PbPb (blue) interactions. The expected values for different parametrisation models for the source radius are also shown. Right: deuteron coalescence probability B_2 as a function of the transverse momentum per nucleon p_T/A in pp (square) and pPb (dot) within the jet (full red marker) and in the underlying event (empty blue marker). Figure taken from Ref. [66] and Ref. [68].

Colliders data cover the range higher than 100 TeV for the projectile energy. The most interesting results come from the ALICE collaboration at CERN, which exploits both the proton and the lead LHC beam collisions. The projectile energy range spans from 400 TeV to 2^4 TeV. A systematic study of the coalescence dependence on the collision system and kinematic parameters has been performed.

Considering the dependence on the collision system, the production of (anti)deuterium and (anti)helium has been studied in pp, pPb and PbPb collisions. While in the first two cases the nucleons are expected to be always produced close in space, in the so-called large systems, such as the latter, both momentum and space correlations impact the nucleus production and a smaller B_A is expected compared to pp. The latest results [65, 66] shows a smooth evolution with multiplicity and size of the system, in agreement with the advanced coalescence models taking into account the size of the nucleus and of the emitting source (Fig. I.2.10, left). The dependence of B_A on the phase-space has also been highlighted in the study of the deuteron production in and out of jets in pp and pPb collisions. The nucleons produced within the jets are created close in phase-space between each other and an enhancement of B_2 is expected. Indeed, an enhancement is observed both in pp and pPb [67, 68] in agreement with the expectations (Fig. I.2.10, right).

The light (anti)nuclei production has finally been studied as a function of p_T [57] and of the rapidity y [68] of the interaction. Even though the rapidity coverage is limited to the midrapidity region ($-0.5 < y < 0.5$), the results are used to extrapolate the model to the forward region, which is of interest for the astrophysical models.

At the moment, no data are available for projectile energies in the TeV range.
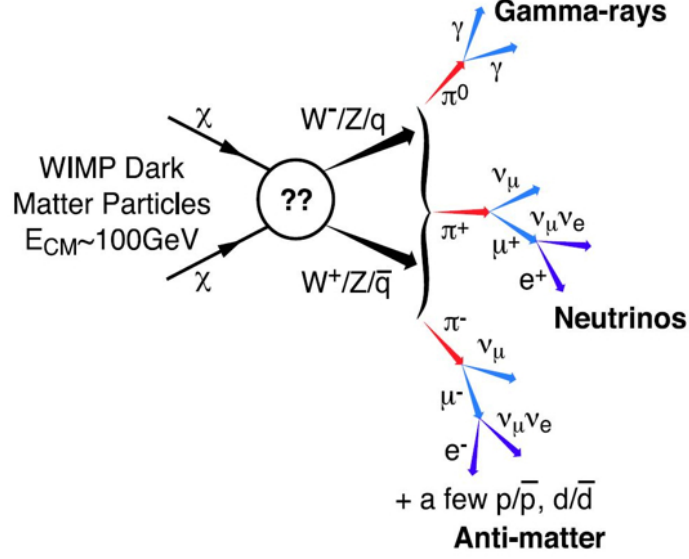
Figure I.2.11: Schematic representation of the annihilation of a WIMP DM candidate into SM particles.

I.2.3.2 Antinuclei as a signature of Dark Matter

When calculating the expected antinuclei flux from exotic sources, the source term in the propagation equation Eq. I.2.4 strongly depends on the candidate source considered. In the case of DM annihilation processes, for instance, the source term for the antinuclei flux is highly influenced by the DM model considered, which is characterised by a specific DM candidate with its mass m_{DM} and characteristic annihilation cross-sections, and by the DM density distribution in the galaxy $\rho_{DM}(\vec{x})$. A general expression is given by:

$$q(T, \vec{x}) = \langle \sigma_{ann} v \rangle \left(\frac{\rho_{DM}(\vec{x})}{m_{DM}} \right)^2 \frac{dN_{\bar{A}}}{dT}, \tag{I.2.25}$$

where $\langle \sigma_{ann} v \rangle$ is the thermally averaged DM candidate annihilation cross-section and $\frac{dN_{\bar{A}}}{dT}$ is the differential energy spectrum of the antinucleus. As already shown in the previous section, the antinucleus is not directly formed but it is the consequence of the coalescence of the antinucleons produced by the DM annihilation (Fig. I.2.11). Its differential energy spectrum is thus calculated considering the coalescence model. For antideuterons, this is given by:

$$\frac{dN_{\bar{d}}}{dT} = B_2 \frac{1}{p} \sum_F \mathcal{B}^F \{ \frac{dN_{\bar{p}}}{dT_{\bar{p}}} \frac{dN_{\bar{n}}}{dT_{\bar{n}}} \} \tag{I.2.26}$$

where $\mathcal{B}^F$ are the branching ratios for all the annihilation final states F which produce antiprotons and antineutrons, and $\frac{dN_{\bar{p}, \bar{n}}}{dT_{\bar{p}, \bar{n}}}$ the differential energy spectrum of the antinucleons. Considering a spherically symmetric density distribution for the DM, the source term can be applied to the propagation equation Eq. I.2.4, to obtain the expected flux observed at Earth.

In Fig. I.2.12 the antideuteron expected flux is reported for different DM candidates, comparing it with the expected secondary background flux and the sensitivities of AMS-02 after 8 years and GAPS. The exclusion limit defined by previous experiments is also shown
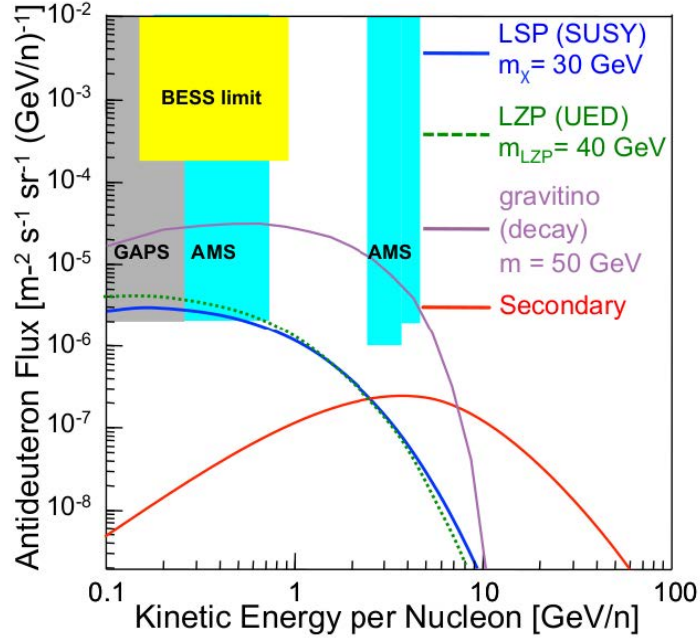
Figure I.2.12: Expected antideuteron flux from three DM candidates (blue, green, pink) compared to the expected secondary flux (red) and the detector sensitivity limits for GAPS (grey) and AMS-02 (light blue). Figure taken from Ref. [62].

as a yellow band at the top of the plots. For all the candidates considered, the expected signals are at least one orders of magnitude higher than the secondary production for kinetic energies per nucleon below 1 GeV/n.

Nevertheless, it must be taken into consideration that ionization losses and inelastic non-annihilation scatterings on the ISM can cause a redistribution in the energy, increasing the low-energy tail of the secondary antinuclei flux; additionally, solar modulation shifts the energy spectrum toward lower energies, resulting in a secondary antinuclei contribution that could overlap with a possible exotic signal. Therefore, it is imperative to enhance the precision of calculations for secondary antinuclei flux, minimizing both propagation and production uncertainties and taking into consideration all potential sources of contamination to the exotic signals.

I.3 The LHCb experiment

The experimental context for the activities presented in this thesis is described in this chapter. After a general introduction to the LHC accelerator facility in Section I.3.1, the LHCb experiment in its Run2 configuration is presented in Section I.3.2, focussing on the detector configuration and data processing strategy. Finally, Section I.3.3 is dedicated to the presentation of the upgraded detector that will operate for the next data-taking campaigns.

I.3.1 The LHC accelerator

The Large Hadron Collider (LHC) [69] is the main accelerator currently operating at *le Conseil europèen pour la recherche nuclèaire* (CERN). Approved by the CERN council in 1994, it is located in the same tunnel used for the Large Electron-Positron (LEP) collider, with a 27 km-long circumference and an average depth of 100 m underground. After the first proton-proton collision at a $\sqrt{s} = 7$ TeV was delivered in 2009, it has collected data during a first data-taking period, the Run1 from 2009 to 2012, reaching a peak energy of $\sqrt{s} =$ 8 TeV and then during a second data-taking period, Run2 from 2015 to 2018, with a collision energy of $\sqrt{s} = 13$ TeV, 1 TeV below the design energy, alternating protons and ions, mainly lead, beams. After the conclusion of the second long shutdown in 2022, the Run3 data-taking is now taking place, operating with 6.8 TeV beams, and it is foreseen to conclude in 2025 to allow the upgrade of the LHC machine in order to provide higher intensity beams (Fig. I.3.1).

Four main experiments are located along the LHC ring. The Compact Muon Solenoid (CMS) experiment [70] is a general purpose experiment designed to search and study the Higgs boson, the top quark physics and to explore the physics beyond the Standard Model. Its geometry is thus optimised to cover the largest fraction of solid angle thanks to a central barrel-shaped section and two end-caps instrumenting the large pseudorapidity region. It features a superconducting solenoidal magnet producing a magnetic field of 3.8 T, enabling a highly compact design that inspired the experiment's name.

The A Toroidal LHC ApparatuS (ATLAS) experiment [71] shares the same aims, therefore following similar conceptual design choices. In this case, though, the magnetic field employed is provided by both a toroidal and a solenoid magnet. The final detector spans 46 m in length, it has a diameter of 25 m, and weighs 7000 tons, making it the largest collider experiment ever built.
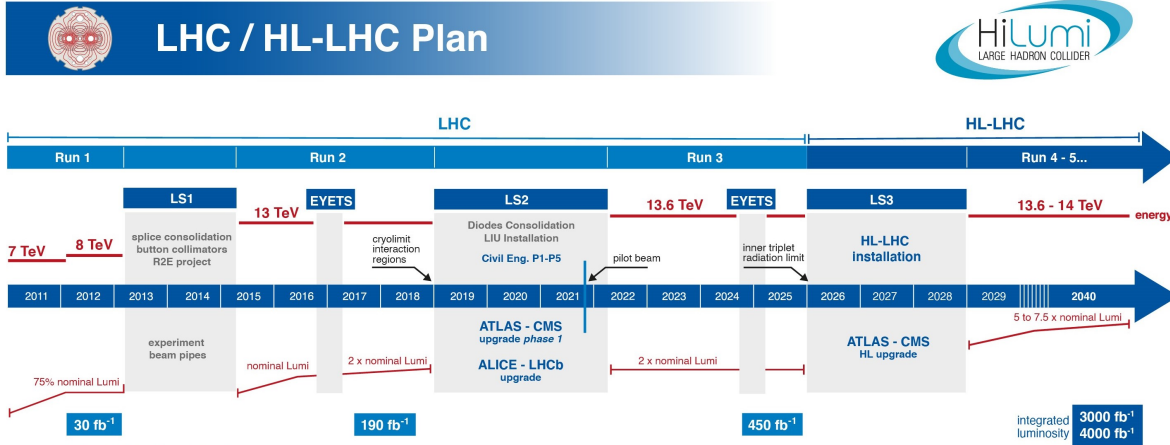
Figure I.3.1: Schematic representation of the operation time schedule of LHC.

The A Large Ion Collider Experiment (ALICE) detector [72] is designed to investigate nuclear matter under extreme temperature and pressure conditions, leading to the formation of Quark-Gluon Plasma (QGP), a state where quarks are deconfined from within the hadrons. It is thus optimised to study heavy-ion collisions, where the QGP formation is expected.

Finally, the Large Hadron Collider beauty (LHCb) detector [73], as described in details in Sec. I.3.2, is a forward spectrometer that has been originally designed as a dedicated flavour physics experiment, aiming at precision measurements of b- and $c-$ quark decays in order to indirectly highlight physics beyond the Standard Model. Thanks to its outstanding vertex and mass resolution, particle identification and the flexibility of its data-taking strategy, it is now viewed as a general purpose detector covering the forward region.

I.3.1.1 The LHC accelerator system

The LHC ring is supported by a system of smaller and less powerful particle accelerators that gradually increase the energy of the beam up to 450 GeV before injecting them into the LHC ring. Protons for the beams are obtained stripping hydrogen molecules with an electric field. As illustrated in Fig. I.3.2, left, particles are initially accelerated in the linear accelerator LINAC2, from where they are moved to the Proton Synchrotron Booster that injects them in the Proto-Synchrotron (pS). After they reach the energy of 25 GeV, they can move to the Super Proto-Synchrotron (SpS), which accelerates the particles up to 450 GeV and feeds them to the storage rings. The SpS accelerator is also used to provide beam to a fixed-target facility, where proton, pion and muon beams are distributed to multiple experiments. Particles in the LHC storage rings take around 20 minutes to reach the operational energy, when they can be collided to collect data. A complex system of magnets is used to bend and squeeze the beams. Superconducting NbTi dipole magnets, cooled with liquid helium to reach intensities up to 8 T, are employed to guide the beam along the beam pipe, while multi-poles magnets are used to compress the beam dimensions near the four collision points, where the main experiments are located. Unlike SpS, no extracted beams are provided for a high-energy fixed-target facility.

Contrary to LEP that delivered electron-positron collisions, the usage of hadron beams allows LHC to reach higher collision energies thanks to the reduced bremsstrahlung
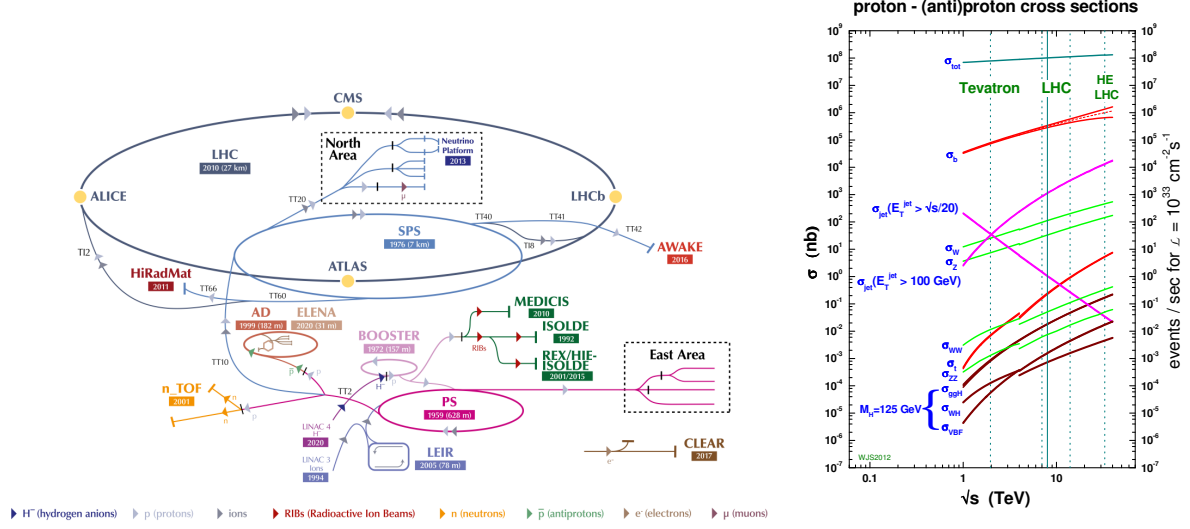
Figure I.3.2: Left: schematic representation of the CERN accelerator complex. Right: cross-sections of selected proton-(anti)proton processes as a function of centre-of-mass energy. The discontinuity around $\sqrt{s} = 4$ TeV is from the transition from proton-antiproton (left) to proton-proton (right) colliders. Figure taken from Ref. [74] and Ref. [75], respectively.

emissions. As shown in Fig. I.3.2, right, the cross-section for relevant processes, such as the H production, as a function of the centre-of-mass energy is higher in proton-antiproton collisions. However, the production, accumulation and uniform squeezing of the antiprotons pose significant challenges. For this reason, it has been chosen to use protons in both beams allowing to increase the number of delivered collisions. This compensates the lower cross-section and allows to study rare processes or search for physics beyond the Standard Model.

In the system of reference of the LHC accelerator, the beam axis is aligned with the z axis of the Cartesian coordinate system. The transverse momentum is thus defined as $p_\mathrm{T} = \sqrt{p_x^2 + p_y^2}$, where x points towards the centre of the LHC ring and y is directed upwards. Considering the equivalent polar system, the polar θ and azimuthal ϕ angles can be defined as $\theta = \arctan \sqrt{x^2 + y^2}/z$ and $\phi = \arctan y/x$. The pseudorapidity is then defined as a function of θ, as $\eta = -\ln(\tan \theta/2)$, which coincides with the rapidity y, defined as $y = \frac{1}{2} \ln \left(\frac{E+p_z}{E-p_z} \right)$, in the ultra-relativistic limit.

I.3.1.2 The beam structure and the luminosity

The particles in the LHC beams are organised in separated bunches, typically spaced by 25 ns. They contain around 10^{11} protons each, squeezed at the interaction point in a transverse size of the order of the μm. During Run2, in order to guarantee safe beam injection and dumping procedures, the LHC ring was filled with up to 2800 bunches. At the crossing of two bunches, the average number of visible interactions is denoted with μ. It is the mean value of the Poisson distribution $P(n) = \mu^n e^{-\mu}/n!$ of the actual number n of visible interactions. The value of μ is proportional to the pile-up, which denotes the number of overlapping interactions in the same event. A rise in the pile-up is associated with an increase in the radiation level and occupancy in the detector, therefore requiring
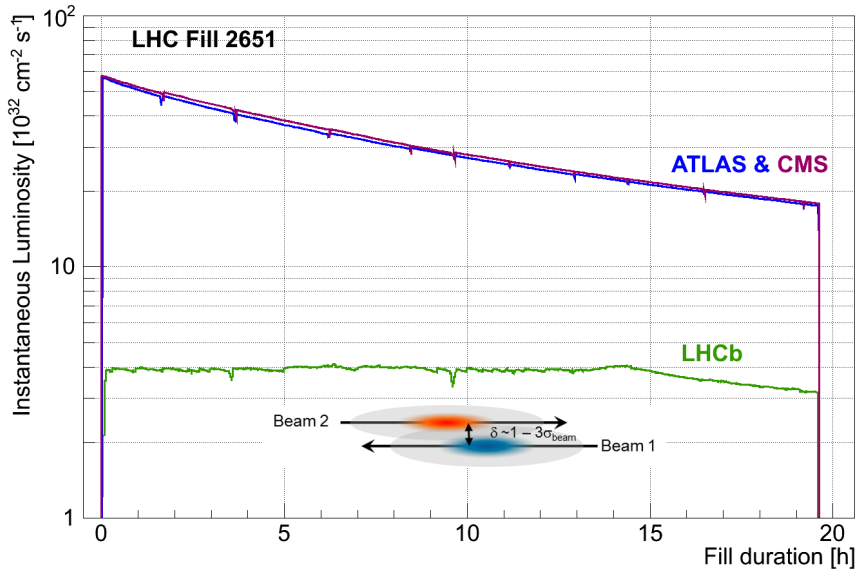
Figure I.3.3: Evolution of the instantaneous luminosity delivered at ATLAS (blue), CMS (red) and LHCb (green) in a typical fill (Fill 2651 in the figure). Figure taken from Ref. [78].

more stringent trigger strategies.

An alternative way to measure the number of interactions produced in the collision of the beams is the instantaneous luminosity $\mathcal{L}$. While μ indicates the number of visible interactions, the instantaneous luminosity $\mathcal{L}$ is the proportionality factor between the rate of events measured dN/dt and the event cross-section $\sigma(\sqrt{s})$, which depends on the energy scale $\sqrt{s}$:

$$\frac{dN}{dt} = \mathcal{L}\sigma(\sqrt{s}), \tag{I.3.1}$$

The luminosity is proportional to the density distribution of the particles in the colliding systems $\rho_{1,2}$ and to their overlap, roughly proportional to the beams crossing angle α. When considering high energy colliders like LHC, it can be expressed as a function of the number of circulating bunches n_b, the number of particles per-bunches $N_{1,2}$ and the revolution frequency ν_{rev} [76]:

$$\mathcal{L} \simeq n_b N_1 N_2 \nu_{rev} \times 2c \times cos^2\alpha \int \rho_1(x,y,z,t)\rho_2(x,y,z,t)\,dxdydzdt \equiv n_b N_1 N_2 \nu_{rev}\Omega, \tag{I.3.2}$$

where Ω is called the beam overlap factor.

The typical particle density distribution of the bunches in the transverse plane follows a bivariate distribution. Assuming that the distributions in the two transverse directions are not correlated [77]:

$$\mathcal{L} \simeq n_b \nu_{rev} \frac{N_1 N_2}{4\pi\sigma_x\sigma_y}, \tag{I.3.3}$$

where σ_x and σ_y are the width in the two directions and the crossing angle has been neglected.
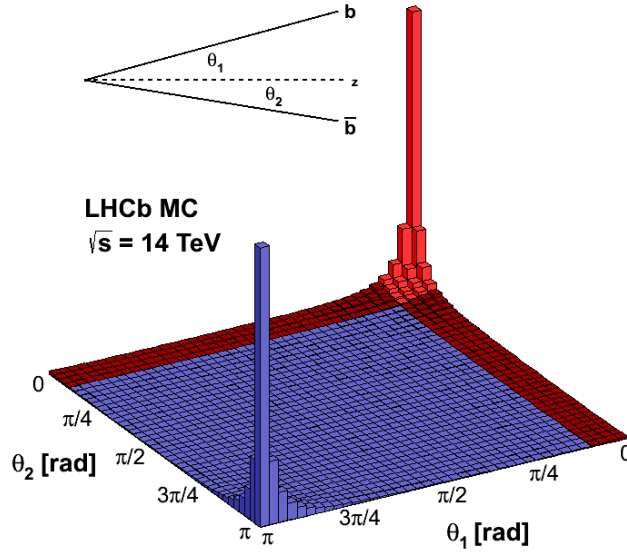
Figure I.3.4: Polar angle distribution with respect to the beam axis for the $b\bar{b}$ pairs production cross-section at an energy of $\sqrt{s} = 14$ TeV, according to the PYTHIA generator [79]. Figure taken from Ref. [80].

The instantaneous luminosity is maximal at the beginning of the fill, and then decreases because of several factors including beam warming and proton losses, as illustrated in Fig. I.3.3. It is however possible to operate at a lower but constant instantaneous luminosity employing a levelling technique (Fig. I.3.3, green line): the two beams near the interaction point are initially displaced and then they are progressively realigned to counteract the decreasing luminosity trend. This is the case for the LHCb experiment, where the luminosity required is around one order of magnitude lower than the peak luminosity that the LHC can provide. The value has been chosen based on the maximum occupancy, radiation tolerance, and manageable pile-up for the study of b-quark physics. During Run2, it was $2 \cdot 10^{32}\,\mathrm{cm}^{-2}s^{-1}$, corresponding to around $\mu = 1.1$. The total quantity of collected data is typically indicated with the integrated luminosity $\int \mathcal{L}\,dt$.

I.3.2   The LHCb detector

The LHCb detector, contrary to the other three experiments at the LHC characterised by a cylindrical symmetry that allows them to cover almost 4π srad of solid angle, has been developed as a single-arm forward spectrometer, as a trade-off between the physics acceptance and the budget and space constraints. The instrumented region covers the interval $\theta \in [10, 300]$ mrad in the horizontal plane and $\theta \in [10, 250]$ mrad in the vertical plane relative to the beam axis, corresponding to a pseudorapidity coverage of $\eta \in [2, 5]$. This configuration allows maximising the acceptance of $b\bar{b}$ pairs up to 24%, as illustrated by Fig. I.3.4 where the production cross-section of such pairs is shown as a function of the emission angles of the two quarks with respect to the beam axis. The forward
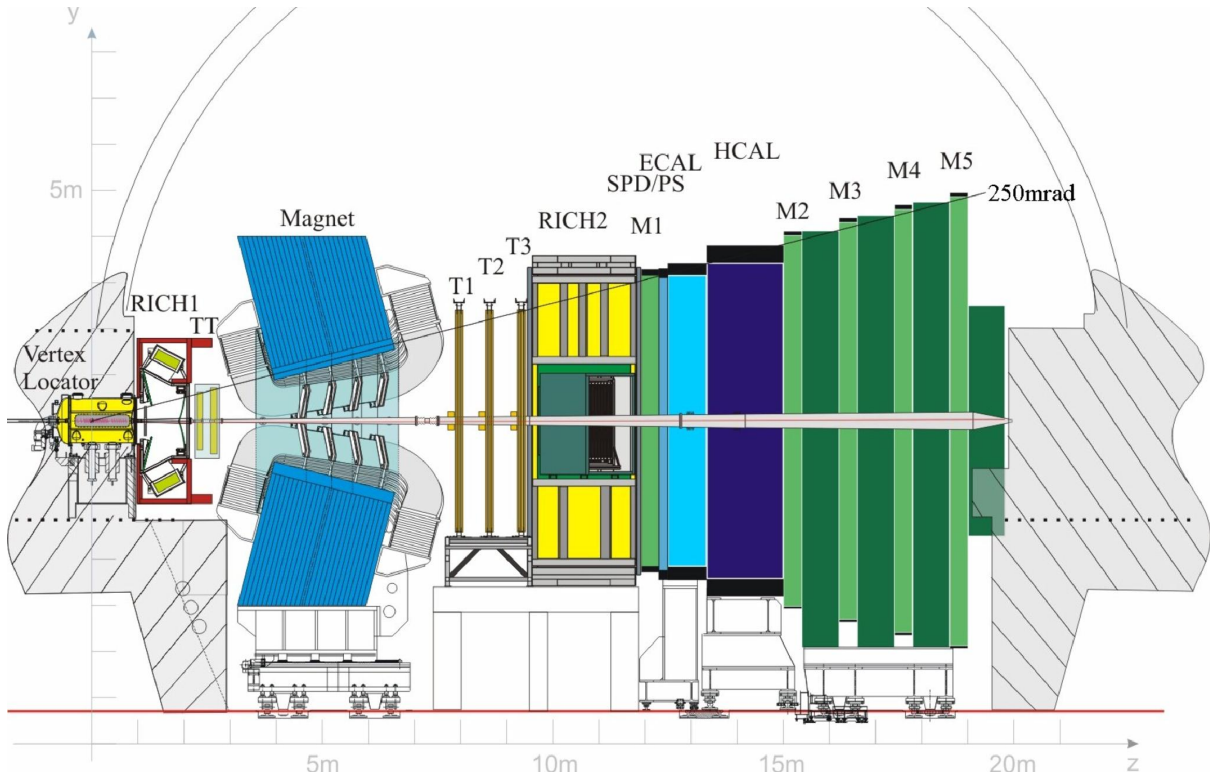
Figure I.3.5: Schematic representation of the LHCb spectrometer. Figure taken from Ref. [78].

configuration is well suited for fixed-target measurements, where the particles produced are expected to be boosted in the forward direction. The LHCb fixed-target system and physics programme is presented in details in Ch. I.4. The detector has been designed to be projective, in order to reduce dead zones for particle detection. Figure I.3.5 shows a schematic representation of the detector layout, where the main subdetectors are indicated. They can be grouped based on their target as:

Tracking system The tracking system measures the charge particle momenta and identifies the collision and decay vertices. In order to efficiently perform heavy flavour measurements, an excellent vertex and proper time resolution is required, as well as a precise invariant mass reconstruction.

Particle IDentification (PID) system The Particle IDentification (PID) system provides the information on the speed and/or the energy of the particles that, combined with the momentum information, allows identifying the different charged particle species and some neutral particles, such as the photons and the neutral pions. In particular, an excellent π-K-p separation is required to separate the rare b-physics signal events from the background.

A versatile and high-bandwidth trigger system was designed to efficiently collect high statistic samples for the study of varied and rare physics channels.
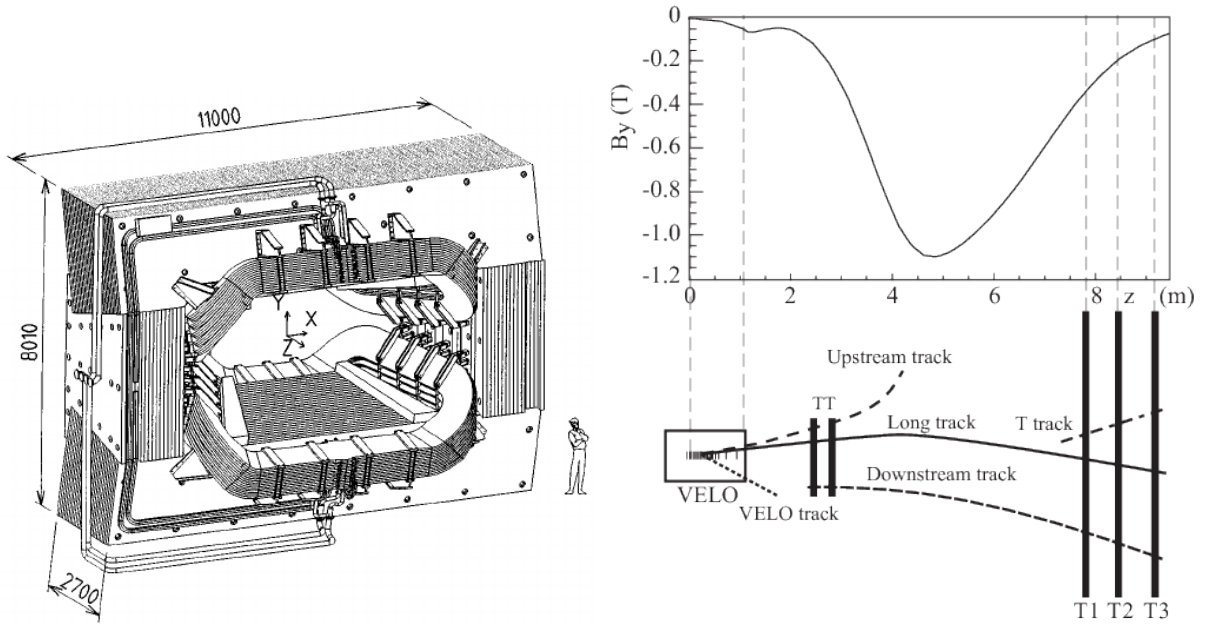
Figure I.3.6: Representation of the LHCb magnet (left) and evolution of the magnetic field strength in the y direction as a function of the z coordinate (right, top); the position in the z direction of the subdetectors in the tracker system is also shown (right, bottom). Figures taken from Ref. [73] and Ref. [78], respectively.

I.3.2.1 The LHCb tracking system

The aim of the tracking system is to precisely reconstruct the interaction and decay vertices, measure the particle momenta and combine them to determine the decaying particles mass. This can be achieved measuring the bending trajectories of the charged particles inside a magnetic field. At LHCb the magnetic field is provided by a warm dipole magnet. The magnetic field as a function of the z coordinate is shown in Fig. I.3.6, together with an illustration of the magnet. It is formed by two saddle-shaped coils, inclined to match the LHCb detector acceptance, and it provides a bending power of 4 Tm [81], with a maximum peak of 1.1 T in the y direction. Its direction is periodically inverted during the data-taking in order to reduce the charge-dependent detection asymmetries associated with disuniformities in the detector, which could impact the measurements of charge conjugation and parity symmetry violation.

The tracking system combines the information coming from three subdetectors (Fig. I.3.6, bottom right) to reconstruct the trajectory of the particles: the VELO detector, the TT stations and the main tracker T.

I.3.2.1.1 The VELO detector

The VErtex LOcator (VELO) [83], the first detector encountered by the particles produced in the LHC collisions, is a silicon strip detector surrounding the pp interaction region. It is designed to offer accurate measurement of the track coordinates in proximity to the interaction region. The detector has been optimised to separate the interaction vertices (primary) to the displaced secondary vertices, a distinctive feature of b- and c- hadron decays.
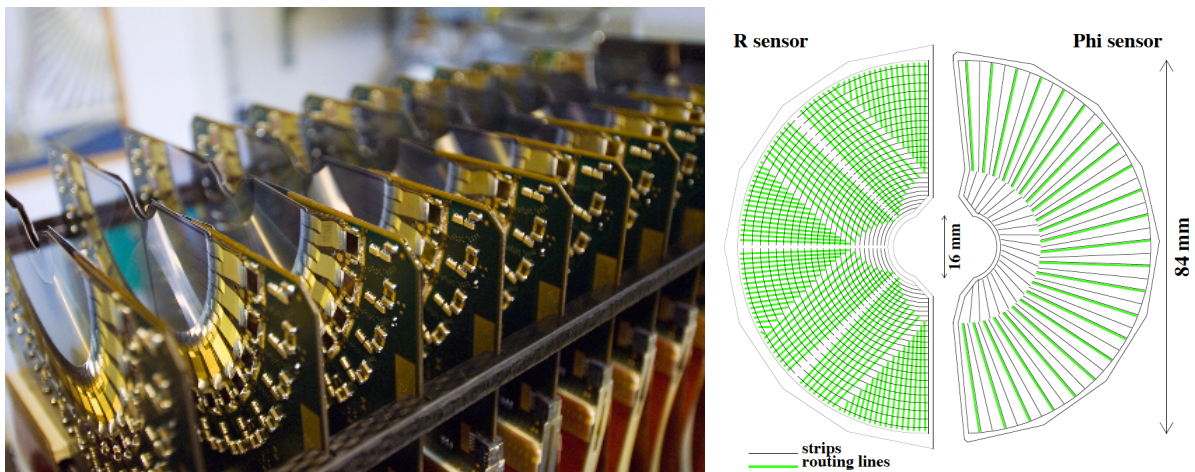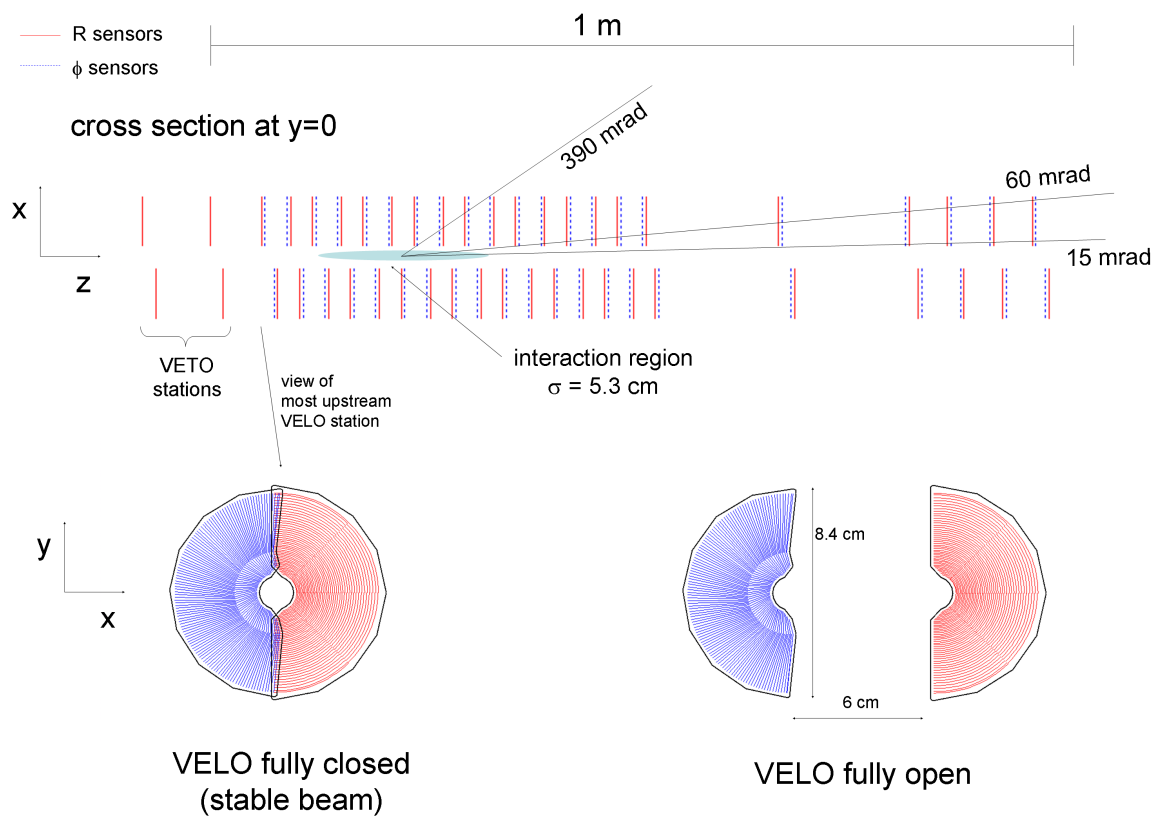
Figure I.3.7: Modules of the VELO detector. Top: modules position along the beam axis. Middle: comparison of the open and closed configuration for the VELO modules. Bottom: picture (left) and schematic representation of a VELO module, with the radial and azimuthal strips indicated. Figures taken from Ref. [82].
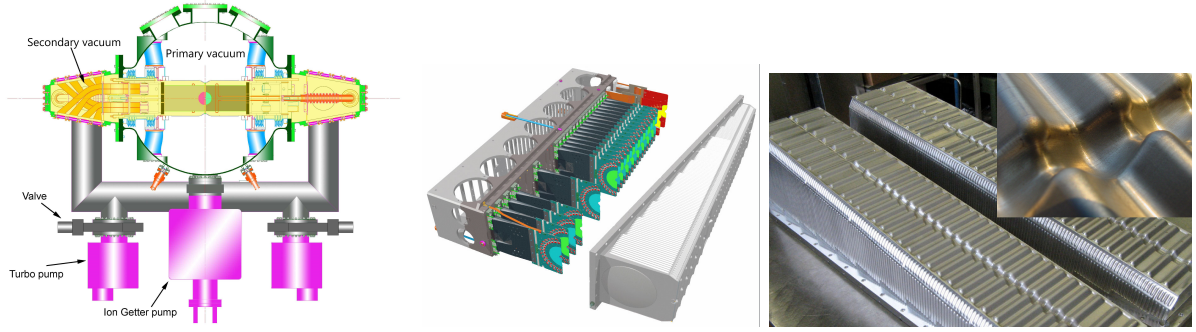
Figure I.3.8: Left: vacuum configuration in the VELO vessel; the primary LHC vacuum (white) and secondary VELO vacuum (yellow) are shown. Middle and right: scheme and picture of the RF foil box. Figures taken from Ref. [73] and Ref. [84].

The detector is composed by 23 silicon-strip tracking stations positioned orthogonally to the beam axis and covering 1-m wide region in the z direction (Fig. I.3.7, top). Each station alternates modules measuring the radial distance r from the origin and the azimuthal angle ϕ (Fig. I.3.7, bottom). The cylindrical coordinate system facilitates rapid and efficient online reconstruction of the tracks. The pitch of the strips in each module increases from a minimum 32 µm pitch up to around 100 µm moving towards the outer region. This configuration optimises the resolution of the vertex and of the Impact Parameter IP (*i.e.* the distance between the linearly-extrapolated track and the reconstructed vertex position).

The first four modules, upstream of the interaction point, are called veto or pile-up and are radial modules. They provide an estimate of the number of particles produced in each bunch-bunch collisions, which is used for the luminosity measurement. They also improve the reconstruction efficiency for particle with negative pseudorapidity, which contribute to improve the determination of the position of the primary vertices.

The detector has been designed to operate at a minimum distance from the beam of 8.2 mm. Outside of stable conditions, however, the beam is expected to be unstable and characterised by a radial aperture higher than the distance of the modules. For these reasons, each station is composed by two movables halves that can be retracted during the beam injection and technical development periods. A mechanical system moves the module 3 cm out to protect them from radiation and instabilities. When stable conditions are restored, the VELO modules are closed again around the measured beam-beam interaction point in the xy plane, which can vary up to ± 5 mm from fill to fill. The modules are mounted in a box that maintains the vacuum around the sensors, called secondary vacuum, separated from the machine vacuum, called primary vacuum. The surface facing the beam is a 300 µm thin corrugated aluminium foil, named RF foil, which provides to the sensors shielding from the radiofrequency effects induced by the LHC circulating beam. Its shape is designed to minimise the material that charged particles traverse before crossing the sensors and it allows for the two halves of the detector to overlap when they are in closed position (Fig. I.3.8).

Thanks to the position of the sensors, the VELO covers a larger angular acceptance than the nominal one, detecting particles within the pseudorapidity range of $1.6 < \eta < 5$.
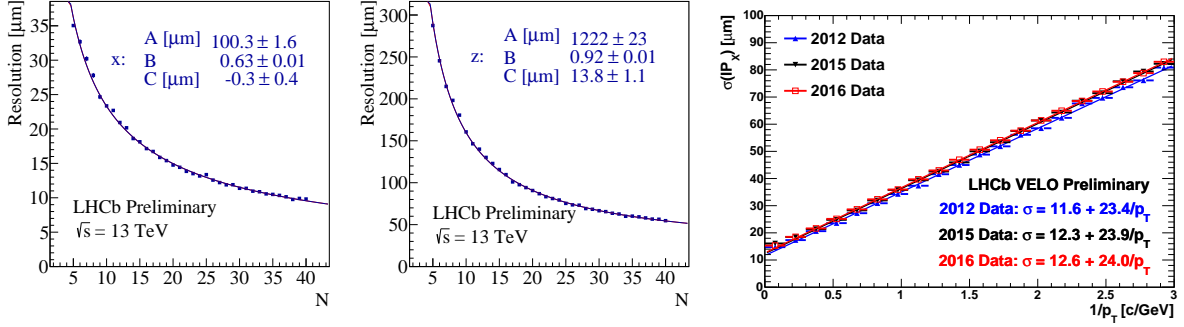
Figure I.3.9: Performance of the VELO detector on Run2 data. Left and middle: primary vertex resolution as a function of the number of particles originating the vertex in the x (left) and z (middle) direction. Right: impact parameter resolution measured on 2012 (blue), 2015 (black) and 2016 (red) data as a function of $1/p_T$. Figures taken from Ref. [85].

Figure I.3.9 shows the performance obtained on data during Run1 and Run2 [82]. On the left and middle, the primary vertex resolution in x and in z is presented as a function of the number of tracks associated to the reconstructed vertex for 2015 data. A typical 25-track primary vertex can be reconstructed with ~ 13 μm resolution for the x and y coordinate and ~ 71 μm resolution in z. On the right, the IP resolution is shown as a function of the inverse transverse momentum $1/p_T$. The dominant uncertainty is the multiple scattering of tracks passing through the VELO stations, therefore an inverse relation with the transverse momentum of the track is expected. Thanks to the proximity to the beam, though, values ranging between 10 μm and 80 μm are reached, the highest resolution among the main LHC experiments.

I.3.2.1.2 The trigger tracker detector

The Trigger Tracker (TT) [73] is positioned upstream of the magnet and comprises two stations separated by 27 cm, each composed by two layers of silicon strip detectors that cover the entire acceptance range. The four layers are arranged in a *xuvx* configuration, where u and v denotes non-orthogonal axes set at a 5-degree angle, clockwise and counterclockwise, respectively, with respect to x. This configuration provides a spatial resolution of approximately 50 μm in the x coordinate. The enhanced resolution in the bending plane is required for a high resolution momentum measurement. Moreover, the *xuvx* configuration offers a significant improvement in the resolution of ambiguities in cases involving two or more tracks with respect to a classic orthogonal reference system. A schematic illustration of the TT detector is shown in Fig. I.3.10, left. Each layer is composed by a set of half-modules, composed by a column of 7 silicon detectors, covering half of the height of the LHCb acceptance. In this way, all the front-end electronics and cooling infrastructure are positioned outside the detector acceptance, either above or below the detector active area, ensuring optimal performance thanks to the reduction of the dead space.

The TT tracker is used to set a reference for charged particle trajectories prior to their deflection, enhance the momentum resolution and enables the reconstruction of long-lived particles like Λ or K_S^0 that decay outside the VELO detector [89]. It is also used to reduce the number of fake tracks, which are the tracks obtained connecting energy deposits from
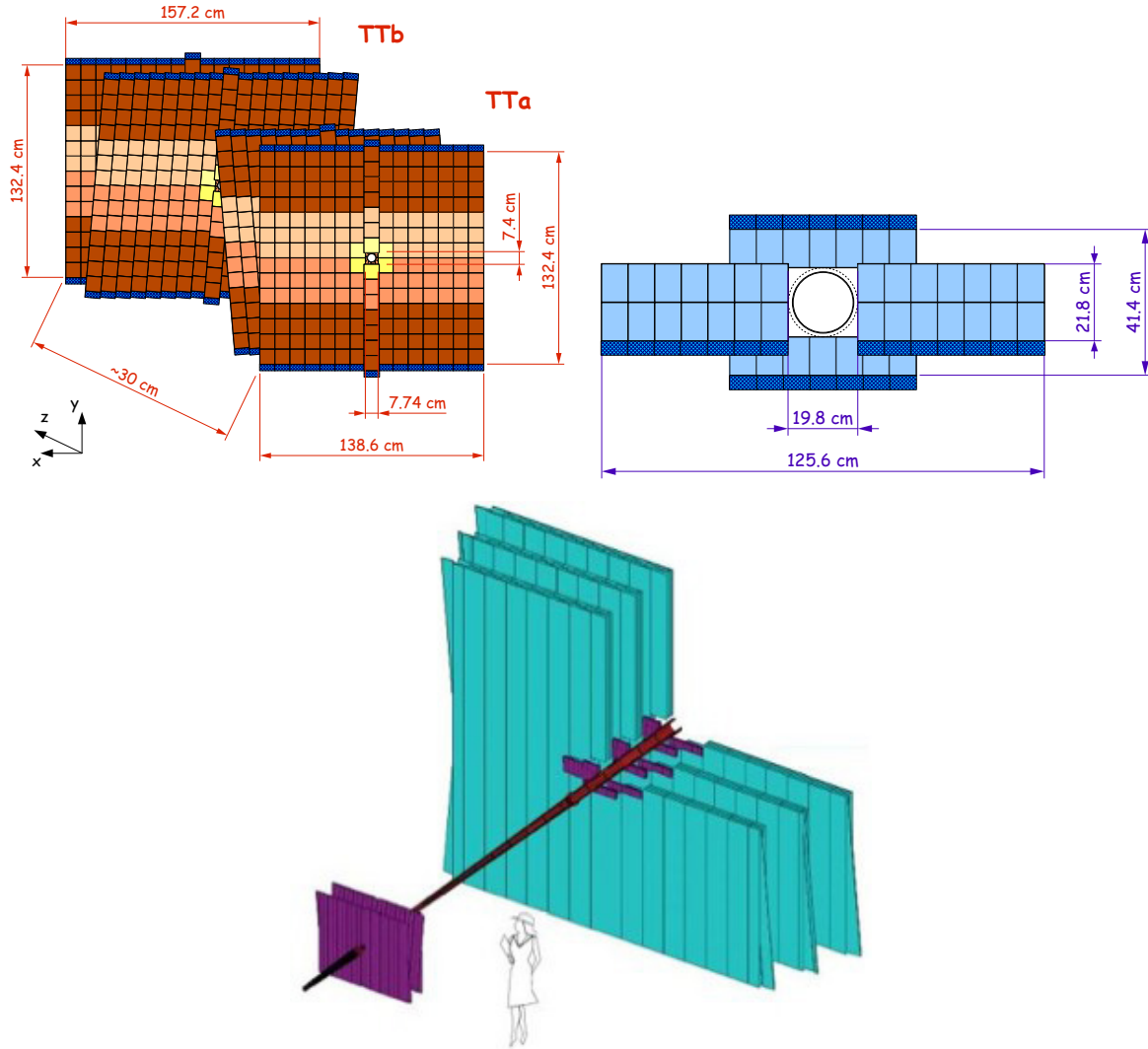
Figure I.3.10: Schematic representation of the TT (top, left) stations, IT (top, right) x station and complete tracker (bottom). Figures taken from Ref. [86], Ref. [87] and Ref. [88].

different particles. Moreover, since the TT detector is positioned within the magnetic field, extrapolating the track from the VELO detector to the associated energy deposit in the TT stations allows to give a first estimation of the particle momentum, which can be used to reduce the searching window for compatible hits in the downstream detectors and improve the reconstruction algorithm performance [90].

I.3.2.1.3 The main tracker detector

Three additional tracking stations, constituting the main tracker T, are positioned downstream of the magnet to reconstruct the particle trajectory after being bent in the magnetic field and to measure their momenta (Fig. I.3.10, bottom). Each station is formed by four layers, in the same $xuvx$ configuration used in the TT stations, that in turn employ two different techniques in the inner and outer region: the Inner Tracker (IT) [87] and Outer Tracker (OT) [91–93].

Inner Tracker (IT) The inner region of the main tracker is exposed to a challenging radiation level and larger detector occupancy. For this reason, silicon strip detectors are employed, thanks to their high radiation resistance, granularity, and spatial resolution. While the IT covers around 2% (120 cm wide and 40 cm high cross-shaped region) of the total area of the tracking station, it is exposed to about 20% of the particle flux due to the increased track density at high pseudorapidities. Employing the same strip silicon sensors used in the TT stations, they are disposed in four seven-modules boxes distributed in a cross shape around the beam pipe (Fig. I.3.10, right). The achieved spatial hit resolution, as for the TT sensors, is 50 μm.

Outer Tracker (OT) The OT detector occupies the radial position where the detector occupancy decreases below 10%. It employs straw tubes drift chambers, covering the largest fraction of the tracker sensitive area and with a maximum extension of 6×4.9 m. The detector is designed to minimise the material budget before the calorimeters. Each of the four layers in a station is composed by two staggered mono-layers of straw tubes filled with a gas mixture of $Ar/CO_2/O_2$ (70:28.5:1.5), which ensure a drift time below 50 ns and good ageing properties (Fig. I.3.11, left).

The straw tubes, 2.4 m long with a 4.9 mm inner diameter, are constructed from two layers of foil material. The inner layer, composed of carbon-doped Kapton, serves as a cathode for collecting positive ions. The outer layer, made of a polyimide-aluminium laminate, acts as a shield and, together with the anode wire, forms a transmission line to transport the high-frequency signals. The tubes are affixed to carbon-fiber panels, forming gas-tight boxes containing standalone detector modules. Each module consists of two mono-layers of 64 drift tubes each. In the longest modules, the straw tubes are divided in the middle into two independent readouts.

While the OT aims at determining the spatial position of the energy deposit, the detector measures the arrival time on the wire of the ionisation clusters, called t_{drift}. Calibrating on data a curve describing the relation between the measured t_{drift} and the energy deposit distance from the wire, the hit position to be used in the tracking reconstruction can be extracted [93]. Such relation, called TR-relation, is obtained from good quality reconstructed tracks, selected requiring $p > 10$ GeV/c and the track-fit $\chi^2/\text{ndf} < 2$. The distribution of the measured t_{drift} as a function of the reconstructed radial position r of the track (Fig. I.3.11, right) is fitted using a second order polynomial of the normalised radial distance $|r|/R$, being R the radius of the straw tube:

$$t_{drift}(r) = \left(21.3 \frac{|r|}{R} + 14.4 \frac{|r|^2}{R^2} \right) \text{ ns} \tag{I.3.4}$$

From the same fit, the time resolution on the hit is related to the distance from the wire $|r|$:

$$t_{drift}(r) = \left(2.25 + 0.3 \frac{|r|}{R} \right) \text{ ns} \tag{I.3.5}$$

Given a t_{drift} resolution of 2.4 ns, obtained through a thorough time alignment and calibration of each front-end, the achieved spatial hit resolution is around 171 μm.
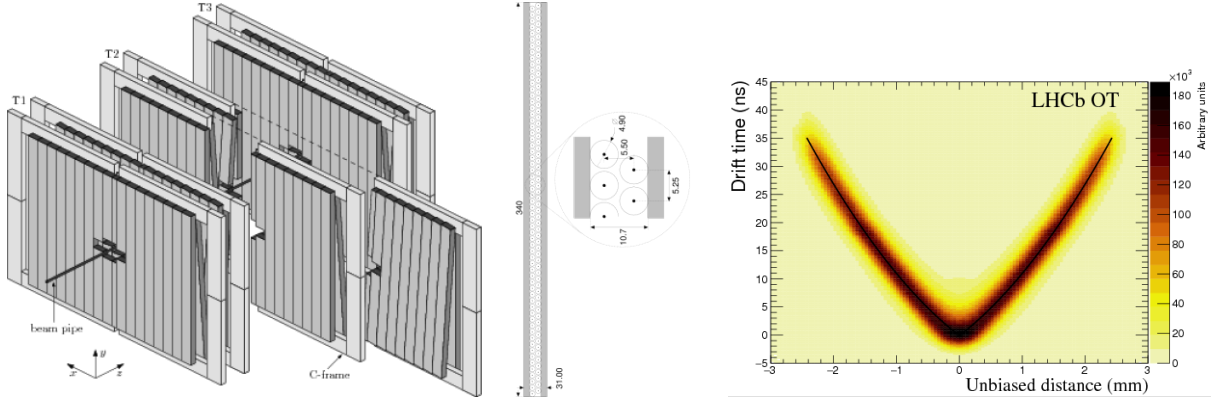
Figure I.3.11: Left: schematic representation of the OT stations cross-section; the straw-tubes disposition within each layer as double mono-layers is also shown. Right: t_{drift} as a function of the reconstructed radial position r of the track; the TR-relation curve obtained from the fit is overlayed in black. Figures taken from Ref. [93].
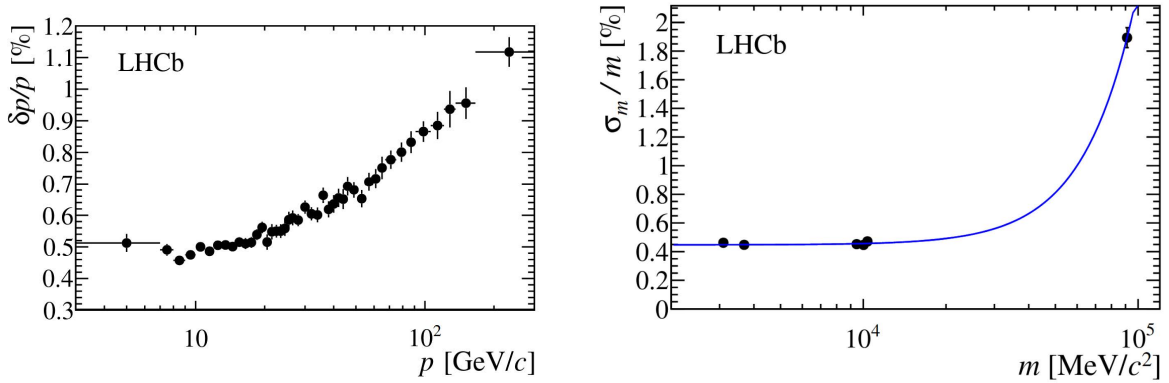
Figure I.3.12: Relative momentum resolution (left) and mass resolution for di-muon resonances (right) of the LHCb tracking system. Figures taken from Ref. [82].

Given the complete tracking system, the achievable momentum resolution varies between 0.5% and 2% for $p \in [5, 200]$ GeV/c, as it can be seen in Fig. I.3.12, left. While at high momentum the resolution is dominated by the hit position resolution in the spectrometer, for momenta lower than 20 GeV/c the multiple scattering becomes the leading contribution, generating the saturation of the resolution at 0.5%. Given tracks originating from the same vertex, their invariant mass is obtained as:

$$Mc^2 = \sqrt{\left(\sum_i E_i\right)^2 - \left(\sum_i p_i c\right)^2} \tag{I.3.6}$$

where E_i and p_i denote the energy and momentum of the $i - th$ particle. The right plot of Fig. I.3.12 shows the invariant mass resolution for di-muon resonances, which ranges from $\sim 0.5\%$ to $\sim 2\%$ for $M \in [3, 100]$ GeV/c^2.

I.3.2.2   The LHCb particle identification system

In order to determine the mass of a charged particle, its speed or energy must be known in addition to its momentum, measured by the tracking system. Discriminating
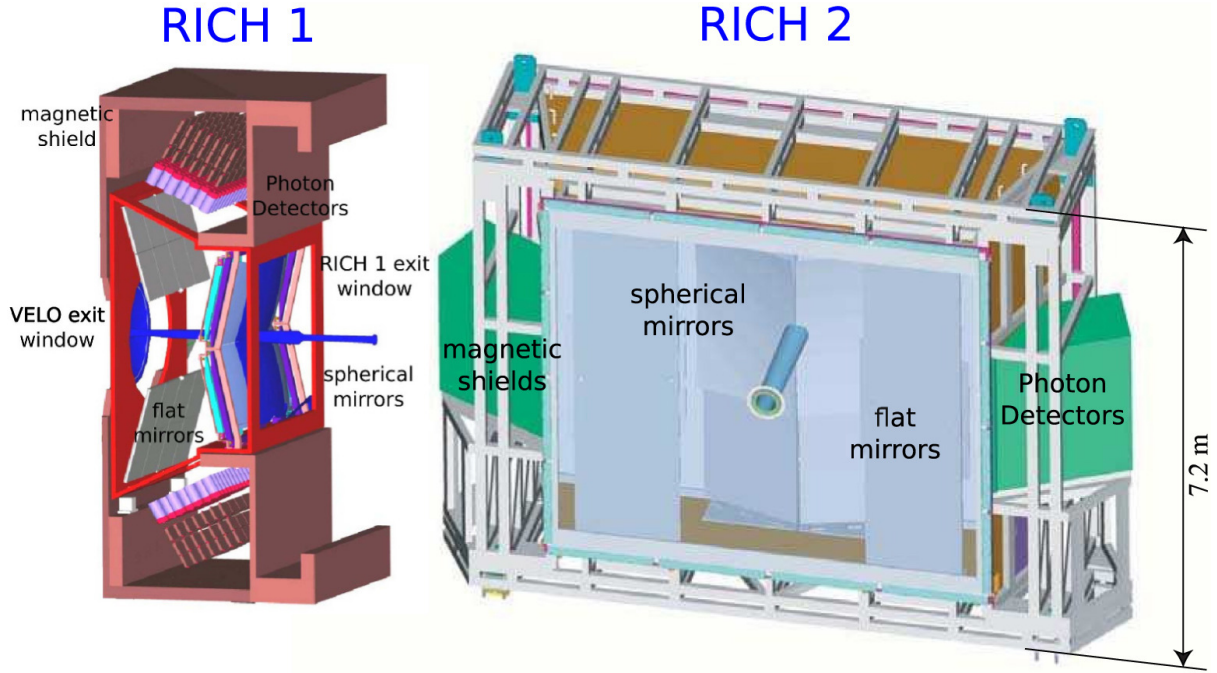
Figure I.3.13: Schematic representation of the RICH1 (left) and RICH2 (right) detectors. Figure taken from Ref. [95].

between different particle species in the whole momentum range of the LHCb detector (approximately $1-150$ GeV/c) requires employing complementary experimental techniques, which can be grouped in three detector families: the Ring Imaging CHerenkov detector (RICH) detectors, the calorimeter system and the muon stations. The overall system allows for an efficient discrimination between protons, kaons, pions, muons and electrons, as well as photons.

I.3.2.2.1 The RICH system

The RICH detector [94] is composed by two separated measuring stations, RICH1 and RICH2 (Fig. I.3.13), positioned respectively upstream and downstream of the magnet, allowing to efficiently identify charged particles both at low and high momentum. They exploit the Cherenkov effect to measure the particle speed that, coupled with the momentum information, gives the particle mass.

A charged particle travelling through a dielectric medium with a refractive index n and speed $\beta > 1/n$ emits Cherenkov photons at a characteristic angle θ_c, dependent on its speed β or, equivalently, its mass m and momentum p, as described in Eq. I.3.7 [96]:

$$cos\theta_c = \frac{1}{n\beta} = \frac{1}{n}\sqrt{1 + \left(\frac{mc^2}{pc}\right)^2}. \qquad (I.3.7)$$

Through a system of spherical and planar mirrors, the photons produced at different points along the trajectory are all concentrated in characteristic rings on the focal plane, with aperture θ_c and centre associated with the particle trajectory.

The refractive index of the medium determines the minimum speed required to produce Cherenkov photons. This requirement translates into a minimum p for each particle species
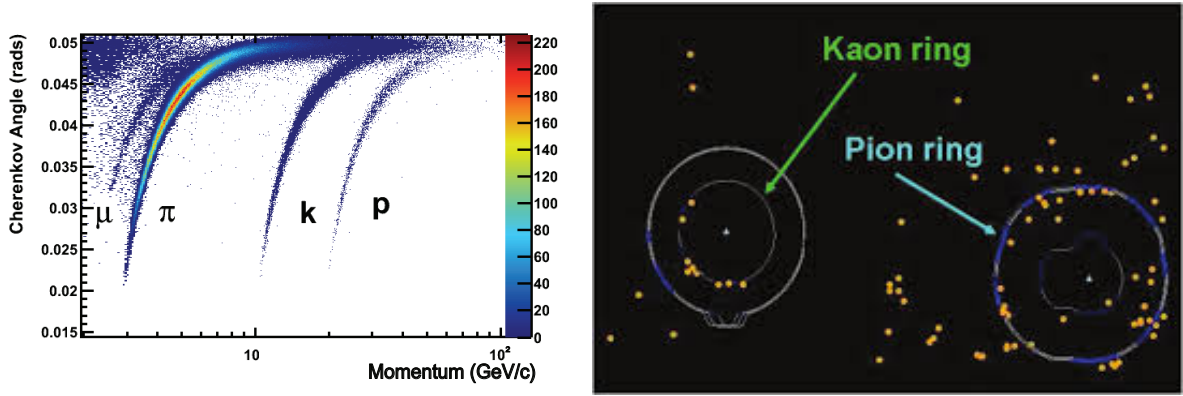
Figure I.3.14: Left: measured Cherenkov angle as a function of the momentum in the RICH1 detector in 2010 and 2011 data. Right: Examples of test rings for the hypotheses of kaon and pion mass compared to the photon hits in the PMTs. Figures taken from Ref. [97] and Ref. [98].

Table I.3.1: Particle momentum thresholds in GeV/c for light emission in RICH1 (middle column) and RICH2 (left column).

Particle	RICH1	RICH2
e	0.01	0.02
μ	2	3.3
π	2.6	4.4
K	9.3	15.6
p	17.7	29.7
d	35.4	59.3
^{3}He	53.1	88.8

to generate a Cherenkov ring. RICH1 and RICH2 are thus optimised to cover different momentum intervals. In particular, RICH1 is optimised for particle with $p < 60$ GeV/c, which could exit the detector acceptance due to magnetic deflection. It is filled with fluorobutane (C_4F_{10}, $n = 1.0014$ at a wavelength $\lambda = 400$ nm) and it covers the full LHCb acceptance. RICH2, on the other hand, identifies particles with $p \in [15, 110]$ GeV/c thanks to the tetrafluoromethane (CF_4, $n = 1.0005$), covering the acceptance region $[15, 120]$ mrad. In Tab. I.3.14 the momentum thresholds for different particles are reported, for both RICH detectors. Figure. I.3.14, left, shows the reconstructed Cherenkov angle as a function of the momentum in the RICH1 detector for the same particles.

In both cases, the focal plane where the Cherenkov photons are reflected is instrumented with PhotoMultiplier Tubes (PMT), conserving the information on the emission angles. The PMTs are placed outside the geometrical acceptance of the detector, in order not to generate dead regions, and a magnetic shield is provided.

Starting from the information on the direction and momentum of the particle, taken from the tracking system, a test ring is constructed for each mass hypothesis and it is compared against the positions of the activated PMT channels (Fig. I.3.14, right). A RICH likelihood function is defined by considering the varying resolution of the hits available in different regions of PMT plane. Its value, combined with information from the
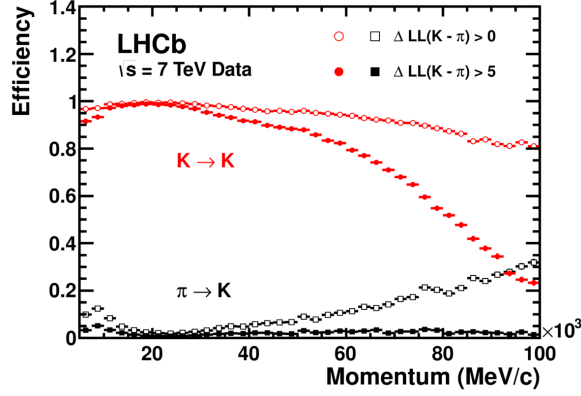
Figure I.3.15: PID efficiency (red) and misidentification rates (black) for the discrimination of kaons from pions; two possible threshold on the $\mathrm{DLL}_{K,\pi}$ are considered (empty markers: loose cuts; full markers: tight cuts). Figures taken from Ref. [97].

calorimeters and the muon system, is associated with each track to define PID classifier to be used in physics analyses, typically expressed as a log-likelihood difference between two hypotheses h_1 and h_2:

$$\mathrm{DLL}_{h1,h2} = log\left(\frac{\text{h1 likelihood}}{\text{h2 likelihood}}\right). \tag{I.3.8}$$

Given that the pions are the most abundant species produced at hadron colliders, it is common practice to use the variables $\mathrm{DLL}_{K,\pi}$ and $\mathrm{DLL}_{p,\pi}$ to discriminate against pions when selecting kaons and protons, and the variable $\mathrm{DLL}_{p,K}$ when discriminating against kaons in a proton selection. The PID efficiency, defined as the fraction of particles correctly identified, and the misidentification rate, which is the number of particles assigned to the wrong mass hypothesis, is shown in Fig. I.3.15 for the $\mathrm{DLL}_{K,\pi}$ classifier, considering two possible cuts. An integrated PID efficiency of 95% can be obtained with the loose cuts at the expense of a pion misidentification rate of about 10%. With the tighter threshold, the efficiency drops to around 85% with a pion misidentification rate of about 3% [97].

I.3.2.2.2 The calorimeter system

The calorimeter system [100] is responsible for the identification and reconstruction of the energy of neutral particles. It also contributes to the identification of charged particles, notably electrons, complementing the information coming from the RICH detector. The different particle species are distinguished by the characteristic showers that they produce when they are absorbed by the detector material (Fig. I.3.16). It is composed by an Electromagnetic Calorimeter (ECAL), preceded by two polystyrene-based scintillator planes separated by a lead converter, the Scintillating Pad Detector (SPD) and PreShower (PS), and by a Hadronic Calorimeter (HCAL). While the ECAL is designed to identify electromagnetic showers generated by $e^{\pm}$ and γ, the HCAL is dedicated to the energy deposits from hadrons. Overall, they provide the particle transverse energy measurement, used in the hardware level trigger, and they allow to efficiently reconstruct and distinguish the π^0 and γ particles, as well as providing information on their position and energy.
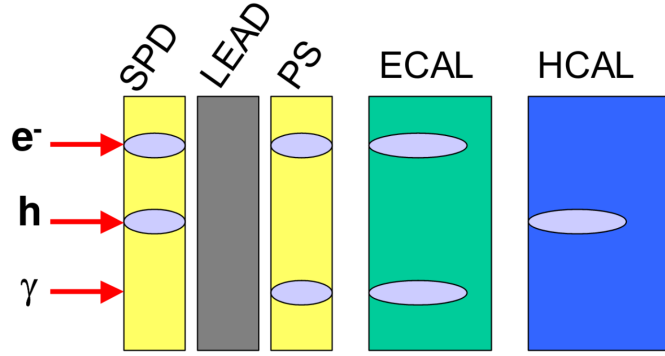
Figure I.3.16: Schematic representation of the shower development in the LHCb calorimetric system for different particle species. Figures taken from Ref. [99].
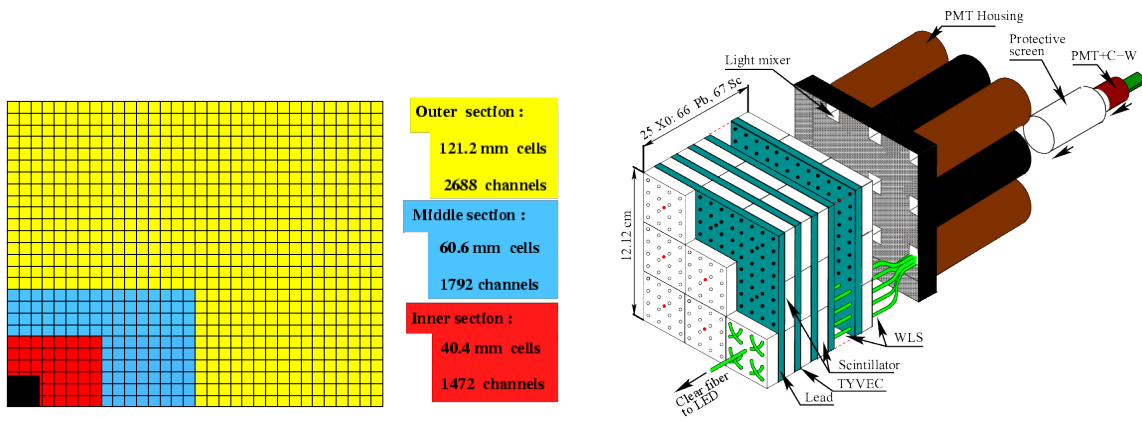
Figure I.3.17: ECAL transverse segmentation (left) and schematic representation of one cell. Figures taken from Ref. [101].

The SPD and PS [99] are the first two stations in the calorimeter system. The SPD detector is used to discriminate between neutral particles and photons coming from showers generated by charged particles. In the latter case, it also contributes to the matching between the track and the associated shower in the ECAL. The PS, on the other hand, discriminates between electromagnetic and hadronic showers and separate overlapping electromagnetic showers caused by different particles.

The ECAL (Fig. I.3.17) is a sampling calorimeter with a shashlik configuration: 4 mm of scintillator pads are alternated with 2 mm of lead, in layers oriented perpendicularly to the beam direction. The light from the scintillators is collected by plastic optical fibres arranged along the beam direction. The transverse segmentation allows to measure the longitudinal and transverse development of showers and optimise the separation between neighbouring showers. The cell size varies with the region in order to cope with the increasing occupancy in the inner section. The achieved resolution on the energy measurement is

$$\frac{\sigma_E}{E} = \frac{10\%}{\sqrt{E\,[\,\mathrm{GeV}\,]}} \oplus 1\%, \tag{I.3.9}$$

where $\oplus$ indicates the sum in quadrature $a \oplus b = \sqrt{a^2 + b^2}$.
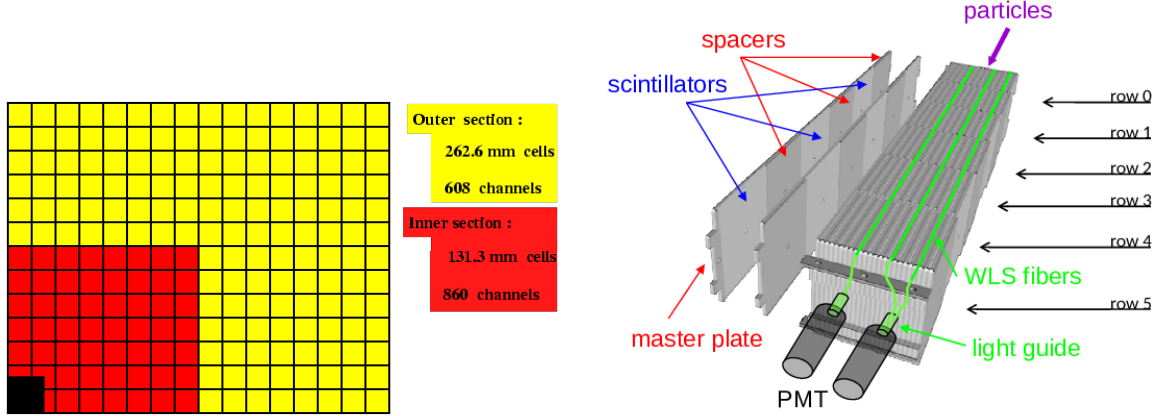
Figure I.3.18: HCAL transverse segmentation (left) and schematic representation of one cell. Figures taken from Ref. [101].

As the ECAL, the HCAL is a sampling colorimeter, but it employs iron as the absorber material and scintillating tiles as the active material, in layers oriented parallel to the beam direction (Fig. I.3.18). This orientation enhances the angular resolution of the calorimeter. Additionally, a transverse segmentation is provided with two different cell sizes for the inner and outer region. Similar to the shashlik design, the readout is accomplished through optical fibres running along the beam direction. The final achieved resolution is

$$\frac{\sigma_E}{E} = \frac{69\%}{\sqrt{E\,[\,\mathrm{GeV}]}} \oplus 9\%. \tag{I.3.10}$$

I.3.2.2.3   The muon system

Completing the PID system, the muon system [102] is composed by five stations (M1 to M5) that provide the identification and reconstruction of the muon tracks. Indeed, they are the only particles capable of penetrating past the calorimeters material and the muon filters.

M1 is positioned upstream of the PS, enhancing the early muon transverse momentum measurement, achieving alone approximately 20% resolution. This information is crucial for the hardware trigger, allowing to identify high-p_{T} muon at the earliest stage. The innermost region of the station, where a large occupancy is expected, employs Gas Electron Multipliers (GEM) chambers, characterised by an elevated radiation hardness coupled with a high granularity and spatial resolution. They are filled with a $\mathrm{Ar/CO_2/CF_4}$ (45:15:40) gas mixture. The outer region, on the other hand, is covered by MultiWire Proportional Chambers (MWPC) detectors filled with the same gas mixture in different proportions: $\mathrm{Ar/CO_2/CF_4}$ (40:55:5). The remaining four stations are positioned downstream of the HCAL and are interleaved with 80-cm thick iron layers, corresponding to 20 interaction lengths, to contain the hadronic showers. The stations are composed by the same MultiWire Proportional Chambers (MWPC) detectors used in the outer region of M1.
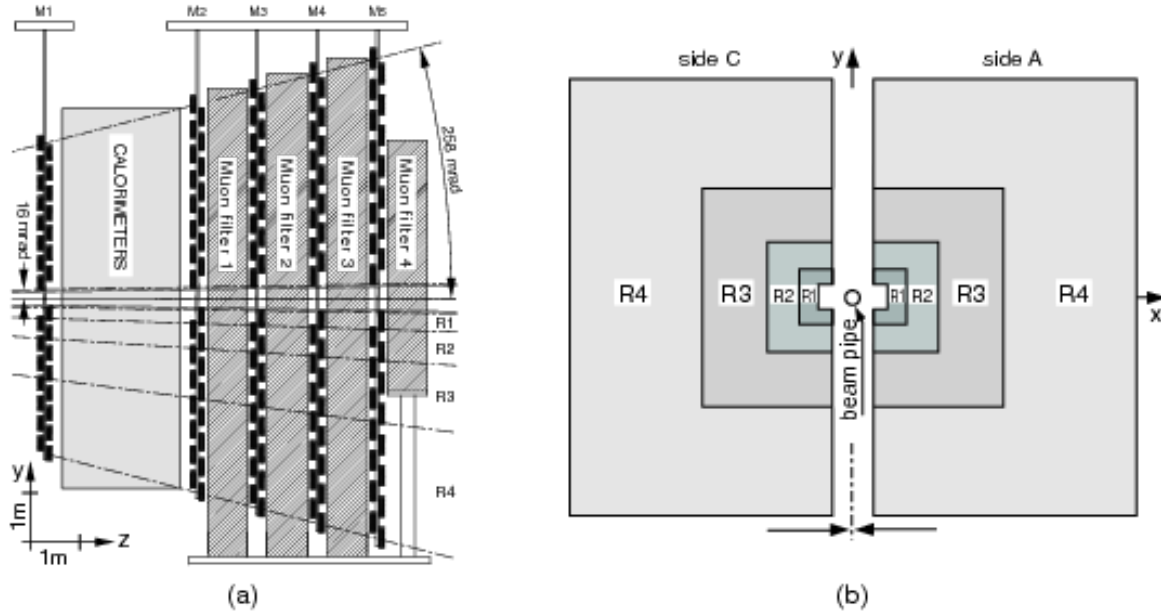
Figure I.3.19: Side view of the muon chambers disposition in the LHCb detector (left) and layout of the four regions R1-R4 of one station (right). Figures taken from Ref. [103].

The hardware trigger requires a signal from all the five stations. A hit efficiency higher than 99% is thus required in each station in order to guarantee a hardware trigger efficiency higher than 95% [103]. This is achieved through a redundancy design in the chambers spatial disposition. A time resolution on the hit < 4 ns is also required to guarantee the hit reconstruction within the 25 ns between two interactions. The excellent hit efficiency and time resolution are exploited in the PID technique presented in Ch. II.3 of this work.

Overall, the system presents an angular acceptance of $[20, 306]$ mrad in the horizontal plane and $[16, 258]$ mrad in the vertical plane. Only muons with a minimum momentum of 6 GeV/c are able to traverse all the chambers. Each muon chamber is divided into four regions (R1-R4), with dimensions increasing in a 1:2:4:8 ratio to achieve a roughly constant occupancy throughout them. A side view of the detector and an example of the transverse segmentation of one of the stations is shown in Fig. I.3.19.

Muon tracks are identified matching extrapolated tracks with energy deposits in all the stations [104]. The identification is initially performed with a binary classifier based on the particle penetration through the calorimeters and iron filters. Subsequently, a likelihood function is computed for both muon and non-muon hypotheses, considering the pattern of energy deposits in the muon stations along the track. Similarly to the RICH PID technique, the classifier $DLL_{\mu,h}$ is obtained combining the information from the logarithm of the likelihood ratio between the muon and non-muon hypotheses with information from the RICH and calorimeter systems. With this combined likelihood approach, average muon identification efficiencies of around 93% are achieved, with a hadron misidentification rate below 0.6% [104].
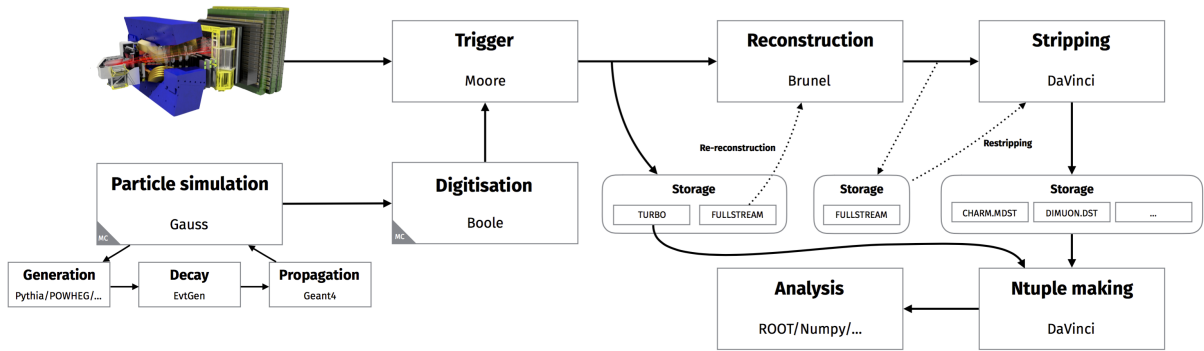
Figure I.3.20: Schematic representation of the LHCb data processing sequence. Figures taken from Ref. [108].

I.3.2.3   The LHCb data trigger and processing

The raw signals coming from the detectors must be processed to reconstruct high-level objects such as tracks, vertices, and particles, and to select events with interesting physics signatures [105–107]. The data processing sequence at LHCb involves several software applications dedicated to each step, as illustrated in Fig. I.3.20.

Events that lack signatures of interesting physics signals must be filtered out as early as possible in the reconstruction process. An online trigger system is thus employed to progressively reduce the throughput preserving only the events and information relevant for physics analysis. The system, shown in Fig. I.3.21, consists of three levels:

Level 0 (L0) The first level operates on dedicated custom Field Programmable Gate Array (FPGA) cards working synchronously with the LHC bunch-crossing rate. L0 reduces the data from the 1 Tb/s generated at the collisions to approximately ~ 1 MHz, selecting events based on the information from the calorimeter and the muon systems. A fraction of events is also selected requiring only minimal or none conditions, to study the experimental efficiency and for particular analysis, like the pHe fixed-target sample considered in this work.

High-Level Trigger (HLT) For the events accepted by at least one of the L0 lines, data from all detectors are merged and transferred to the software trigger. The software trigger, running on a large computing farm located at the experimental site, is divided in two separate stages [109]:

    HLT1 Firstly, a partial event reconstruction takes place, including tracks finding and the muon PID algorithm. Inclusive selection algorithms dedicated to generic one- or two-body signatures are defined based on these objects.

    HLT2 Finally, a complete event reconstruction with an offline-like quality is performed on the selected events and both inclusive and exclusive triggers lines are acquired.

The raw data of events that pass the trigger are distributed worldwide through the LHC computing grid [110] and reconstructed offline using the BRUNEL application. The reconstruction utilizes calibration and alignment constants that are continuously updated as the understanding of the detector improves. The reconstructed data contains all objects
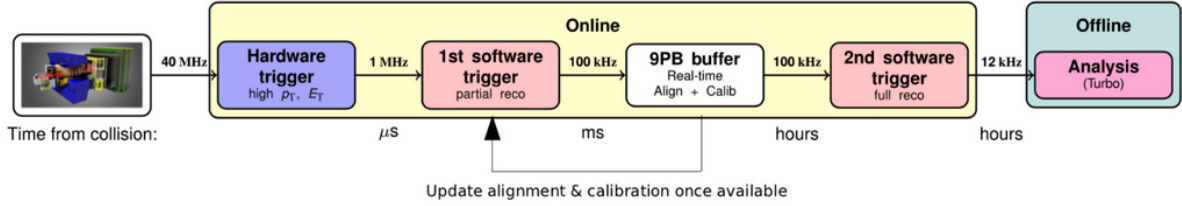
Figure I.3.21: Schematic representation of the LHCb trigger sequence employed during the LHC Run2 data-taking period.

describing the collision. The output is processed with the DAVINCI application, producing a final data format that is easily processed for the analysis.

In parallel to the real data processing, simulated samples are also produced to understand the detector response and to compare theoretical predictions with experimental observations. The simulation production [111] can be summarised in three steps:

Event generation Theoretical models are used to simulate the particles produced in the collisions. Input parameters such as the LHC beam characteristics are provided. For physics analyses of *pp* collisions at the LHCb detector, the PYTHIA generator [79] is commonly used. However, for the fixed-target program discussed in this document, the default generator is EPOS-LHC [112].

Decay simulation Unstable particles are decayed into their allowed final states based on available data for their decay probabilities. The software application employed at the LHCb experiment for this purpose is EvtGen [113].

Propagation through the detector The simulated particles are propagated through the detector material, accounting for their interactions and responses within the detector. This simulation is performed using the GEANT4 toolkit [114, 115].

After the production, the processing steps for simulated data are the same as those for real data. During the trigger selection steps, simulated data are typically not removed but are flagged as either kept or discarded based on the applied selection criteria. The generated particles distributions, before the interactions within the detector, are also separately saved. This allows to study selection efficiencies and unfold experimental effects from the measured quantities, providing a way to quantify and account for the detector-induced effects in the final analyses.

I.3.3 The LHCb Upgrade I

During the long shutdown 2, the LHCb detector has undergone a radical upgrade [116] to expand the reach of its physics programme. An increase in the luminosity by a factor five is expected during Run3 and Run4, up to $\mathcal{L} \simeq 2 \times 10^{33}$ cm$^{-2}s^{-1}$. The increased luminosity, with an expected $\mu \sim 5.5$, produces a higher pile-up and occupancy, as well as a harsher radiation environment. The upgraded detector has thus been designed aiming at a higher radiation hardness, a finer granularity and faster readout to cope with the increased complexity for the event reconstruction. Moreover, given the increase in the
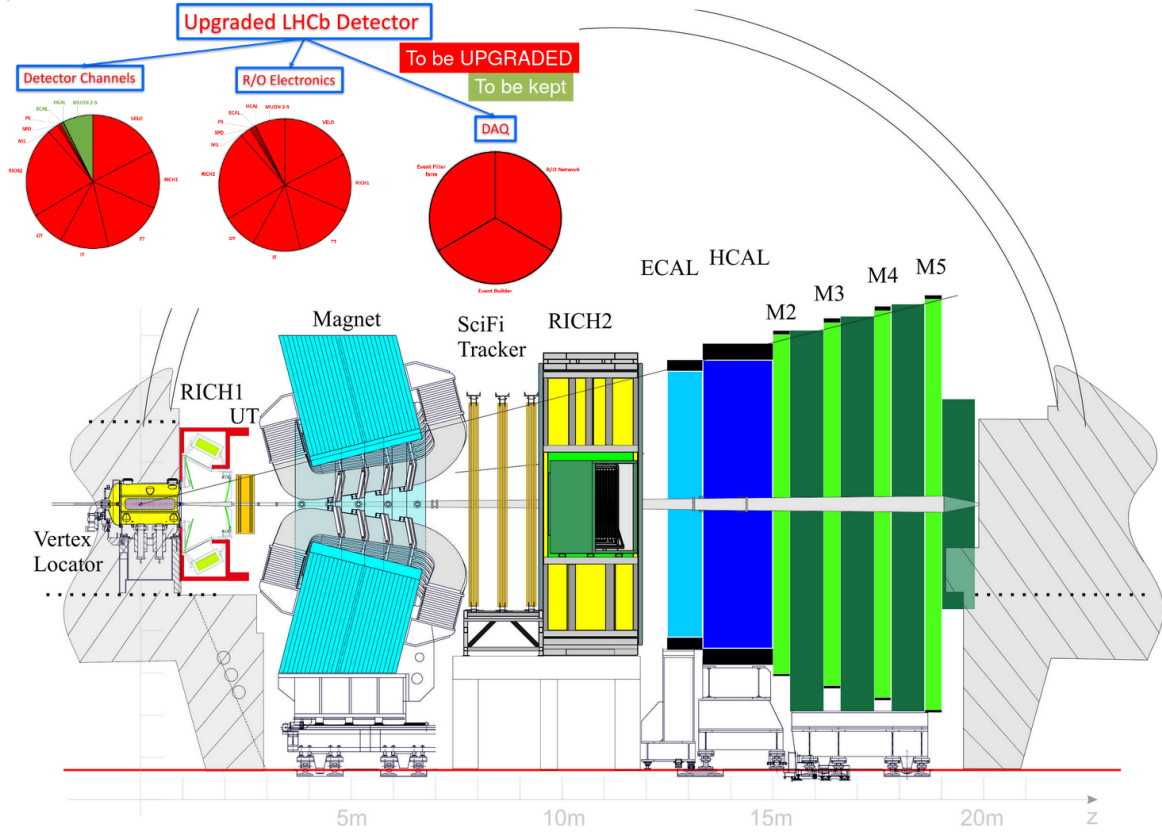
Figure I.3.22: Schematic representation of the upgraded LHCb spectrometer; the inset on top left of the figure shows the fraction of the detector (left), electronics (middle) and data acquisition channels (right) that have been maintained (green) or upgraded (red).

acquired data flow and in the complexity of the selection algorithm required right from the low-level trigger, a new selection strategy has been developed to sustain the ~ 40 MHz detector readout.

The upgraded detector is shown in Fig. I.3.22, top: the tracking system has been completely replaced, as well as the RICH optics and most of the readout electronics. The M1 muon station, SPD and PS have been removed, since they would not sustain the increased occupancy and no hardware trigger is foreseen. Indeed, the L0 trigger has been removed, as its efficiency for hadron and electromagnetic signatures could not withstand the luminosity upgrade (Fig. I.3.23), making the LHCb experiment the first one operating with a fully software-based detector readout, calibration, and alignment system, along with real-time event reconstruction and selection, designed to operate at the acquisition rate of 30 MHz.

I.3.3.1 The tracking system

While the general structure of the tracking system is maintained, all its detectors have been completely replaced. The VELO strip sensors have been substituted with pixels, which guarantee a higher granularity, and the TT and main tracker have been replaced with the Upstream Tracker (UT), a silicon detector, and with the Scintillating Fibre (SciFi), a scintillating fibres detector, respectively.
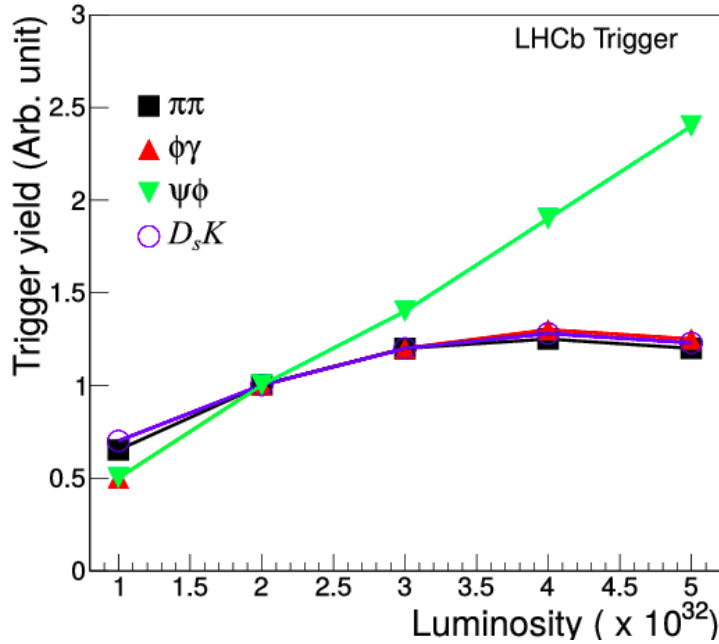
Figure I.3.23: L0 trigger yield for different decay channels of the *B* mesons as a function of the instantaneous luminosity, assuming constant output rate. Figures taken from Ref. [117].

VELO The general configuration of the detector is maintained: the modules are disposed on two separate moving halves, to safeguard their safety outside stable operation. However, their spatial distribution and the modules themselves have been changed [118].

The semi-circular strip modules used during Run2 have been replaced with L-shaped pixels detectors (Fig. I.3.24, top), to reduce the distance from the beam from 8.2 mm to 5.1 mm. The *z* position of the modules have been changed with respect to Run2 (Fig. I.3.24, bottom, Run2 in black and Run3 in red): given the absence of the L0 trigger, the pile-up modules have been removed and the new disposition is optimised to ensure that all particles in the detector acceptance traverse at least four modules. The pixels technology, coupled with the reduced distance, significantly enhances the reconstruction efficiency and the resolution on the IP determination (Fig. I.3.25).

In order to cope with the harsher radiation environment associated with the vicinity to the beam, an innovative micro-channel cooling system have been installed. It is based on evaporative CO_2 circulating in capillaries surrounding the sensors, maintaining them at a stable temperature of around $\sim$ -25°. The supporting structures have also been improved. In particular, the RF foil boxes housing the modules have been redesigned (Fig. I.3.26) ensuring a thickness of 150-200 μm, about half that of Run2.

Upstream Tracker (UT) The Upstream Tracker (UT) detector [119] is installed replacing the TT stations, sharing the same goals and structure with it. As represented in Fig. I.3.27, left, the UT comprises four stations of silicon microstrip detectors arranged in the *xuvx* configuration. The minimum distance from the beam is reduced by approximately $\sim$ 7 cm, while the strip pitch is maintained at 187.5 μm in the external region (indicated in green in the figure) and reduced to 93.5 μm in
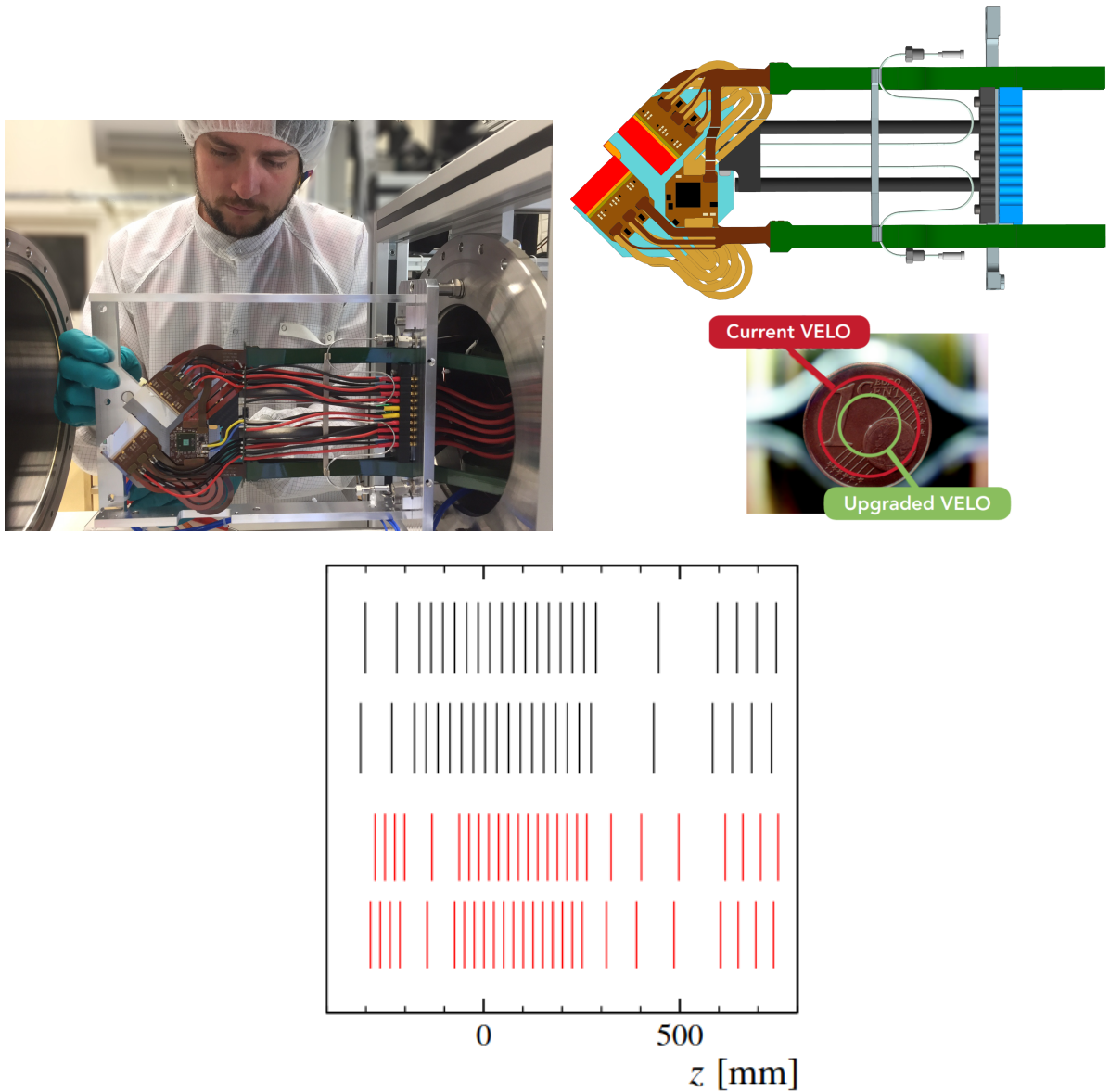
Figure I.3.24: Top: upgraded module of the VELO detector. Middle: comparison of the Run2 (black) and Run3 (red) module z positions.

the inner ones. An improved granularity and radiation resistance is thus achieved.

Scintillating Fibre (SciFi) During Run3 the Scintillating Fibre (SciFi) [119] constitutes the main tracker, downstream of the magnet. Employing a gaseous detector like the OT would result in poor track reconstruction efficiencies due to high detector occupancy expected in Run3. The scintillating fibres technology has thus been chosen for the SciFi detector. The detector (Fig. I.3.27, right) is composed by three stations made of four *xuvx* layers. Each layer is composed by 96 multi-layered mats of fibers, each 2.4 meters long and having a diameter of 250 μm, grouped in 12 modules. At the end of each module, 16 Silicon PhotoMultiplier (SiPM) collect the light produced in the fibres. They are kept at -40° to minimise noise and radiation damage. A resolution better than 100 μm over a total active area of 340 m² is
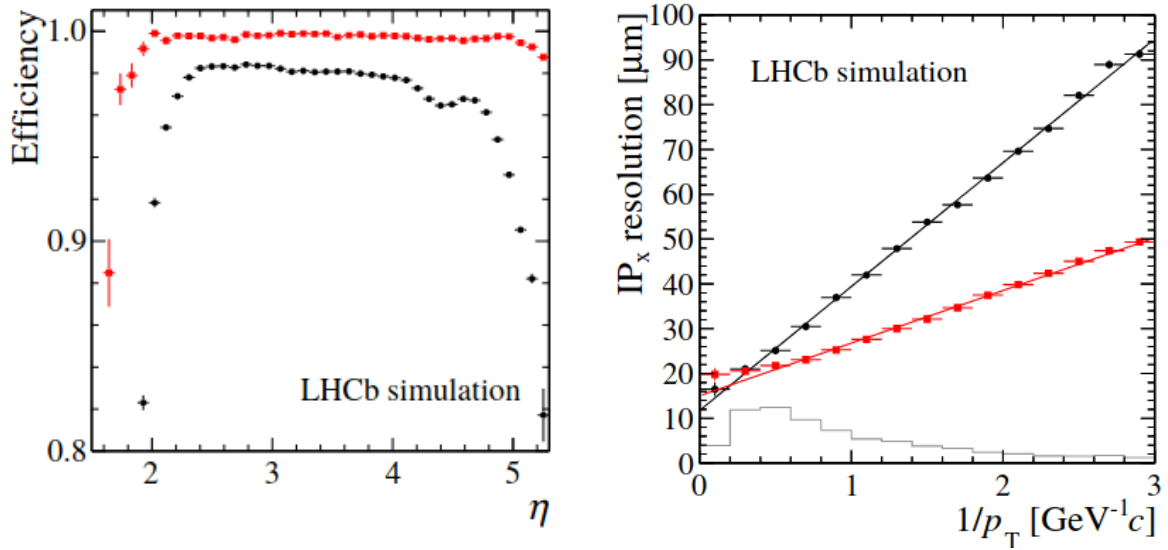
Figure I.3.25: Studies on simulations of the performance of the upgraded VELO detector (red) compared to the Run2 one (black) at the Run3 beam conditions ($\mu = 5.5$, $\sqrt{s} = 14$ TeV). Left: track reconstruction efficiency as a function of the pseudorapidity for particles leaving at least one hit in three VELO modules. Right: resolution on the impact parameter for reconstructed VELO segments as a function of $1/p_{\mathrm{T}}$. Figures taken from Ref. [118].
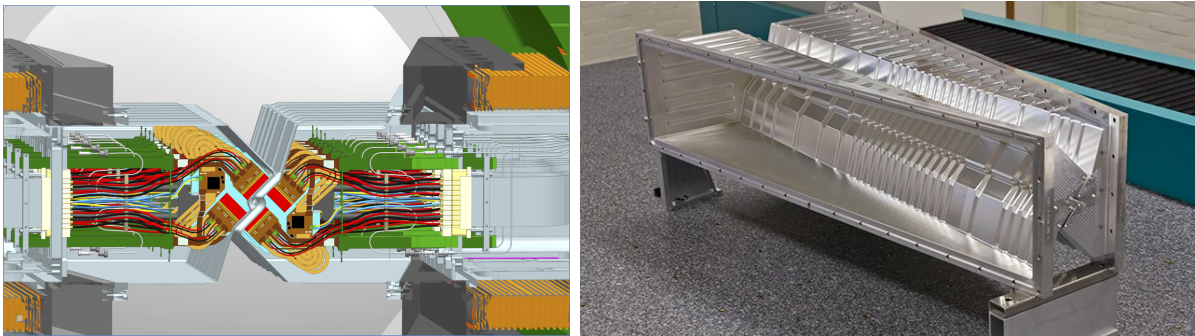
Figure I.3.26: Closed configuration of the VELO detector with the module disposition inside the upgraded RF foil boxes (right)

achieved.

I.3.3.2 The particle identification system

Following the removal of the hardware trigger level, the detectors feeding it, the PS, SPD and the M1 muon chamber, have been removed, also to reduce the material budget. The overall structure of the PID system has otherwise remained unchanged [120]. The optic system of the RICH detector has been significantly improved. The existing Hybrid PhotoDetectors (HPDs) with 1 MHz readout electronics encapsulated within the tube have been replaced by multianode photomultiplier tubes, designed to handle the higher data rate expected in the upgrade. Additionally, the optical system of RICH1 has been redesigned to reduce the high hit occupancy within the central regions of the detector. Increasing the spherical mirror focal lengths from 2.7 m to 3.7 m, the hit density results
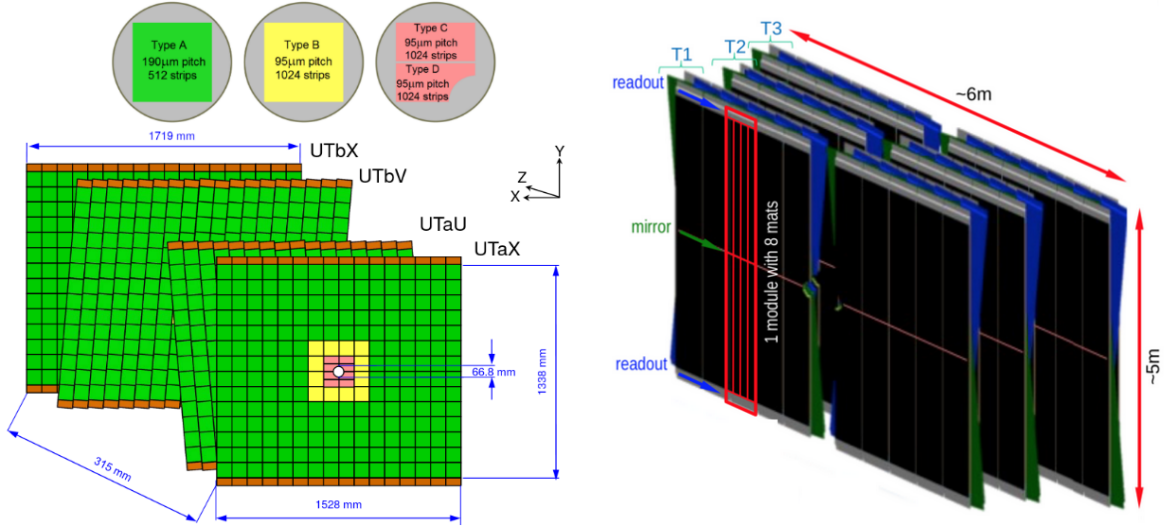
Figure I.3.27: Schematic representation of the UT detector (left) and SciFi detector. Figures taken from Ref. [119].
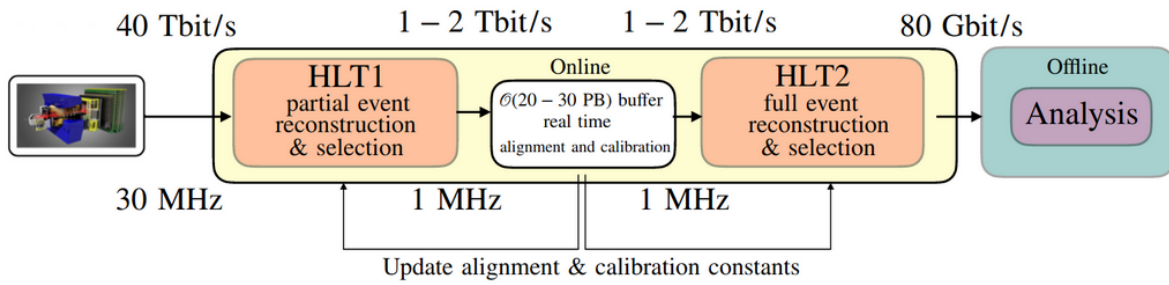
Figure I.3.28: Schematic representation of the LHCb trigger sequence that will be employed during the LHC Run3 data-taking period.

to be halved with respect to Run2.

The layout of the calorimeter and muon system remained unchanged, except the removed stations, but the read-out electronics has been substituted to adapt to the upgrade rate. At the same time, the gain of the photomultiplier tubes reading the calorimeter cells has been decreased by a factor of five to prevent rapid ageing.

I.3.3.3 The data acquisition strategy

During Run1 and Run2, the input event rate was reduced to 1 MHz based on the decision of the hardware L0 trigger. While the strategy was highly efficient for dimuon channels, half of the fully hadronic decays were removed and the performance would get worse with an increased luminosity (Fig. I.3.23). For this reason, a purely software-trigger solution was chosen [121–123] for Run3. At the luminosity expected for Run3, LHC collisions generates a data volume of 4 Tb/s, corresponding to unprecedented rate of heavy flavour production, with b quarks produced at a frequency of 200 kHz and c at 1 MHz.

Figure. I.3.28 outlines the trigger strategy implemented, running on a dedicated computing farm on the experimental site. The first level trigger, HLT1 [124, 125], runs completely on

54

Graphic Processing Unit (GPU) and performs the partial event reconstruction, including decoding and pattern recognition across all tracker detectors. Based on the reconstructed quantities, inclusive selection algorithms are defined to accept or reject events based on their general properties. The selections in HLT1 reduce the data rate from ~ 30 MHz to approximately ~ 1 MHz. Similarly to Run2 [126], dedicated HLT1 samples are employed for real-time alignment and calibration.

Events selected by the HLT1 trigger are then processed asynchronously by the HLT2 trigger. This allows to distribute the workflow even during periods when no data are acquired, like during machine development phases and non-stable beam. The HLT2 performs an offline-quality complete event reconstruction and reduces the data rate to approximately $\mathcal{O}$ (10 Gb/s).

I.4 The LHCb gas fixed-target

The implementation of the LHCb fixed-target programme is discussed in this chapter. After an overview of the luminosity measurement techniques employed in LHCb in Section I.4.1, the gas injection system known as SMOG is presented in Section I.4.2, describing its use as a target to study beam-gas collisions in the LHC Run 2 and outlining the obtained physics results. Section I.4.3 provides an overview of the limitations faced during the Run2 programme, motivating the installation of an upgraded system. Section I.4.3.1 describes the new confinement cell and the gas injection system constituting the SMOG2 system, while the related new physics opportunities are presented in Section I.4.3.2.

I.4.1 The luminosity measurement in the LHCb experiment

As shown in Eq. I.3.1, precise luminosity measurements are essential for all cross-section evaluations. Different methods have been used during the years, which can be grouped based on their approach as direct or indirect methods. While indirect measurements are based on the reconstruction and selection of a process with a well-known cross-section in order to invert Eq. I.3.1 to obtain the luminosity, the direct methods calculate the absolute luminosity calibration based on the geometric properties of the colliding beams. Both approaches are affected by systematics that limit their precision. Indirect measurements are affected by the theoretical uncertainties associated with the cross-section considered, as well as by the experimental reconstruction efficiency. The direct measurements, on the other hand, are affected by the systematics associated to the description of the beam properties. During Run2, the LHCb experiment employed two direct techniques [127] to reach the best level of precision on the luminosity measurement between the experiments on the LHC ring.

Van Der Meer scan The Van Der Meer (VDM) scan technique, firstly proposed at the Intersecting Ring Collider in 1968, has been widely adopted in the accelerator field and it is still the most frequently used technique at the LHC. One of the two circulating beams is displaced first in the x and then in the y directions. The rate of a defined observable process is measured as a function of the displacement to gain insights into the particle distribution within the bunch. In its original concept, it was performed only in the horizontal plane with non-bunched beams but

it has now been extended to pulsed accelerators and to two dimensions [128]. In the LHCb experiment, real-time control of the beam position is ensured through dedicated monitors. The counters considered for the luminosity measurement are those that were demonstrated to be proportional to the number of visible interactions over a wide range of luminosity (typically, the number of hits or tracks in certain subdetectors). During Run2, a precision within the 2%-3% has been achieved using the VDM scan. The main systematics came from the luminosity variation over time, LHC optical system operations, and the assumption that the x and y directions can be factorized. During Run3, the novel bidimensional scan [129] will allow to further improve the reachable precision: the luminosity will be measured considering Eq. I.3.2 without any assumption on the independence of the x and y particle density distributions.

Beam gas imaging Exploiting the residual gas in the LHC vacuum, an image of the transverse distribution of the particles in the beams can be obtained reconstructing the collision vertices between the particles and the gas. In this way, a direct measurement of the beam overlap factor Ω as defined in Eq.I.3.2 is obtained without the need to displace the beams. This technique heavily relies on the vertex resolution to reconstruct the beam-gas interactions, which in the case of the LHCb detector, as discussed in Sec. I.3.2.1.1, is exceptional due to the forward geometry and the high performance of VELO track reconstruction. During Run2, the LHCb experiment conducted parasitically Beam Gas Imaging (BGI) measurements [77, 130] (Fig. I.4.1) during the VDM scan of the other LHC experiments. The achieved luminosity uncertainty has been reduced to as low as $1.2 - 1.5\%$, the smallest among all LHC experiments. The BGI technique allows also to perform the ghost charge measurement. The ghost charges are the charges present outside the nominally filled bunch slots, which can contribute to the total measured bunch intensity without, on the other hand, contributing to the total luminosity. The VDM calibration requires to normalised the measured rates by the interacting bunch intensities, which are measured by dedicated beam current monitors. The ghost charge measurement allows to obtain the corrected values of intensities, further improving the accuracy of the luminosity measurement.

The two techniques are highly complementary thanks to the two completely different approaches, which are affected by different systematics.
In order to perform the BGI measurement, a sufficient level of contamination in the LHC vacuum is needed. Initially, when the method has been introduced, the pure residual gas in the LHC has been used, reaching a level of pressure around 10^{-9} mbar corresponding to a HLT trigger rate of about $0.5\,\mathrm{Hz}$ per 10^{11} protons. Switching off the ion pumps of the VELO detector, allowed to increase the rate by a factor four. Finally, a dedicated injection system called System for Measuring Overlap with Gas (SMOG) has been installed in 2011 to maximise the collected statistics. SMOG allows injecting small amount of noble gases inside the VELO vessel (*i.e.* 10^{-7} mbar) to create a local bump of density around the nominal LHCb interaction point. The pressure obtained with the new injection system is two order of magnitude higher than the nominal LHC contamination level, corresponding to approximately $100\,\mathrm{Hz}$ recorded rate of beam-gas per 10^{11} protons.
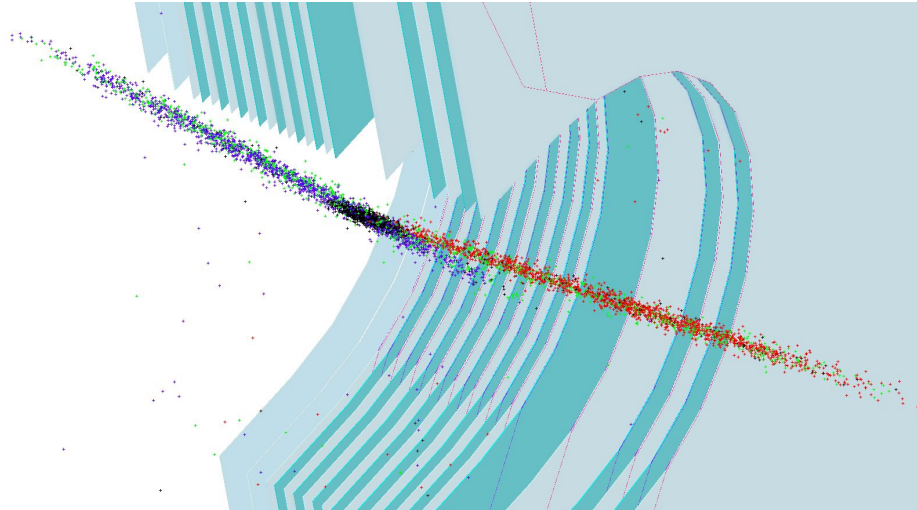
Figure I.4.1: Three dimensional reconstruction of the beam profiles through BGI technique, with 2013 data.
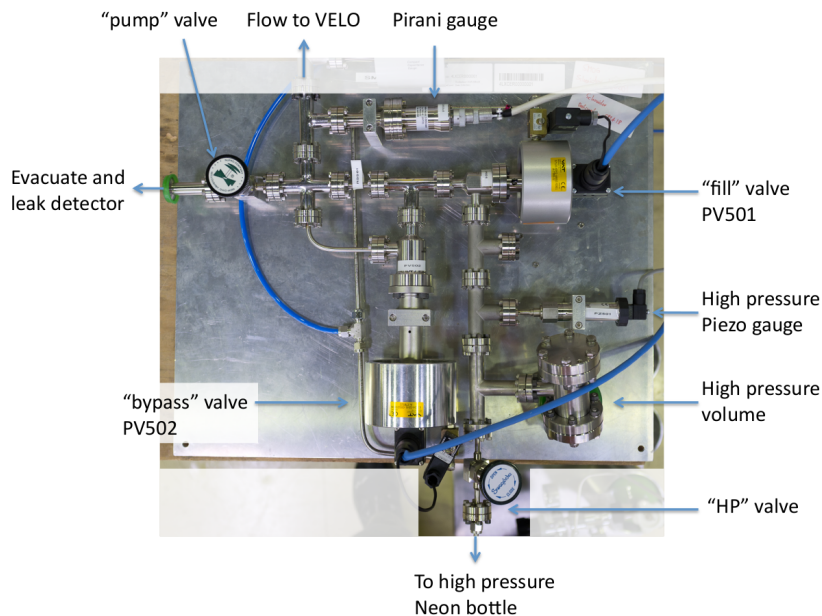
Figure I.4.2: Photo of the SMOG Gas Feed System main components. Figure taken from Ref. [77].

I.4.2 The SMOG gaseous target

The SMOG gas injection system with all its main components is shown in Fig. I.4.2. The gas is pressurized in a high-pressure reservoir and then directed toward the VELO detector through a 4 m-long tube at a flow rate of $3 \cdot 10^{-5}$ mbar·l/s. The injected pressure is monitored by three cold-cathode (Penning type) positioned around the VELO detector. The gauges, however, have an absolute calibration with a $\sim 50\%$ uncertainty, therefore only relative pressure variation is considered reliable. An additional hot filament ionization gauge (Bayard-Alpert type) has been installed in
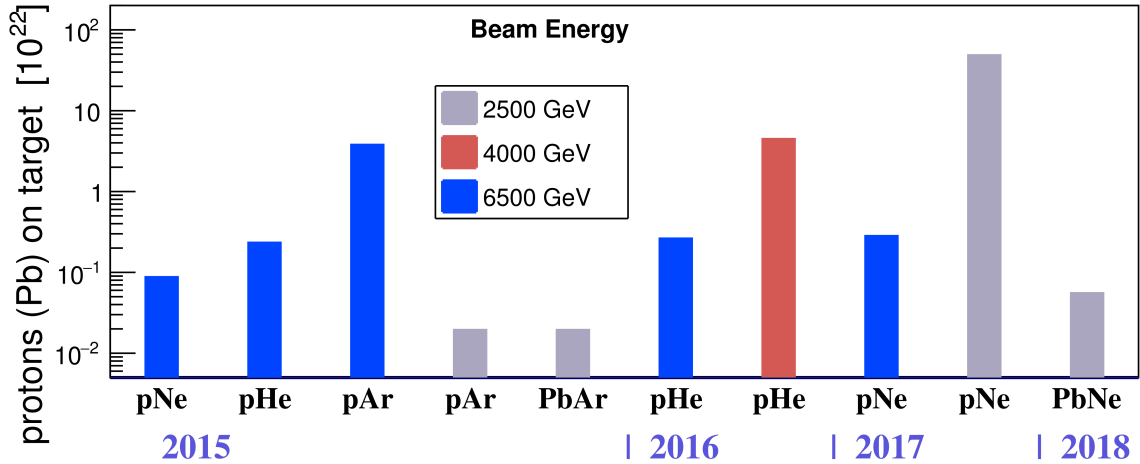
Figure I.4.3: Fixed-target samples collected in Run2 with SMOG; the collision system, the LHC beam energy and the statistics collected are indicated. Figure taken from Ref. [131].

2017 to measure the pressure in the beam pipe 7 m upstream of the injection point. Its calibration is expected to guarantee an accuracy below the 10%. Since the gas is injected only when the VELO ion pumps are switched off, the gas is extracted at the nearest LHC vacuum pumps, located $z = \pm 20$ m from the nominal interaction point.

Since 2015, the possibility to inject noble gases into the LHC accelerator vacuum coupled with a fully-instrumented detector geometry covering the forward direction has been exploited to start a pioneering fixed-target physics programme at the LHCb. During Run2, samples with different centre-of-mass energies and gas targets have been collected, both with proton and lead beams, as summarised in Fig. I.4.3. During both 2015 and 2016, fixed-target data were acquired in brief dedicated periods. First samples with helium, neon and argon were collected in 2015 to test the physics performance of the system under various conditions. In 2016, instead, the data-taking was exclusively focussed on pHe collisions, for antimatter production measurements of interest for CR physics (Sec. I.4.2.1). An improved data-taking strategy was developed for the 2017 in order to increase the statistics and allow for heavy particle measurements. Toward the end of 2017, a special pp run with $\sqrt{s} = 5$ TeV was collected simultaneously injecting neon with SMOG. The pNe collisions were recorded only for the bunches crossing the detector from the VELO side, not colliding within the LHCb detector. The LHCb detector thus demonstrated for the first time the feasibility of a simultaneous operation in both collider and fixed-target configuration. Due to the overlapping luminous regions between beam-beam and beam-gas interactions, the two programmes cross-contaminated each other: an additional background coming from the beam-gas programme had to be taken into consideration for pp physics, and a significant contamination of the pNe sample from pp collisions due to debunched beam2 protons was observed. Nevertheless, the recorded number of protons on target for the pNe sample, amounting to $\mathcal{O}(10^{23} \text{ nb}^{-1})$, was at least one orders of magnitude larger than previous fixed-target samples. A PbNe sample was collected in 2018 with the same energy as the pNe one to study nuclear effects in the two systems, providing valuable insights into the behaviour of particles in different collision scenarios.

For fixed-target samples, the luminosity is a function of the areal density θ of the gas target:

$$\mathcal{L} = \nu_{rev} n_b N_1 \theta \tag{I.4.1.a}$$

$$\theta = \frac{P_{gas}\Delta z}{k_B T} \tag{I.4.1.b}$$

where θ is expressed in terms of the gas pressure P_{gas}, its temperature T and the spread Δz over the longitudinal direction, following the perfect gas law, because a uniform distribution in z is expected. Due to the lack of precise gauges for the injected gas pressure, the luminosity cannot be directly measured. The number of protons on target (pot) is therefore used to quantify the collected statistics for all samples. Given a nominal pressure of $P_{gas} = 2 \cdot 10^{-7}$ mbar, the corresponding luminosity for 10^{22} pot is approximately 5 nb^{-1} per meter of gas.

I.4.2.1 Physics with SMOG

Fixed-target collisions of LHC proton or lead beams on gas atoms open unique opportunities. When collisions of nuclei are studied, the interaction energy in the centre-of-mass frame is provided per-nucleon $\sqrt{s_{NN}}$. In fixed-target configuration, this is given by:

$$\sqrt{s_{NN}} = \sqrt{2E_N M_N c^2}, \tag{I.4.2}$$

where E_N is the per-nucleon beam energy and M_N is the nucleon mass. At the LHC, $\sqrt{s_{NN}}$ ranges in $[29, 115]$ GeV when considering a beam energy spanning from the protons injection energy to the design circulating energy $E_N \in [0.45, 7]$ TeV. The corresponding boost of the centre-of-mass-frame with respect to the laboratory spans $y_{cm} \in [3.8, 4.8]$. This range covers an intermediate scale between fixed-target experiments conducted at the SpS and collider experiments at the LHC or RHIC accelerators, providing an additional test bench to study energy evolution in a region poorly constrained by experimental data. Given the pseudorapidity coverage in LHCb, the accessible rapidity in the centre-of-mass frame covers the backward to central region (from $y^* \in [-2.8, 0.2]$ at the highest beam energy, to $y^* \in [-1.8, 1.2]$ at the injection energy). SMOG opens the possibility to observe particles carrying a substantial fraction of the target nucleon momentum in the centre-of-mass reference. Indeed, the fraction of momentum carried by the produced particle is usually expressed in terms of Feynman-x, which is related to y^* according to:

$$x_F \simeq \frac{2}{\sqrt{s_{NN}}}\sqrt{(Mc^2)^2 + (p_{\mathrm{T}}c)^2} \cdot sinh(y^*) \simeq x_1 - x_2, \tag{I.4.3}$$

where M and p_{T} refer to the final particle.

The unique kinematic coverage of SMOG is clearly shown in Fig. I.4.4, where the fixed-target LHCb acceptance is shown. The smog configuration allows large values of the target Bjorken-x to be accessible at lower $\sqrt{s}$ if compared to other experiments (top) or beam-beam collisions at LHCb (bottom right).

The physics measurements achievable in the distinct LHCb fixed-target kinematic regime span various fields of interest, including [131]:
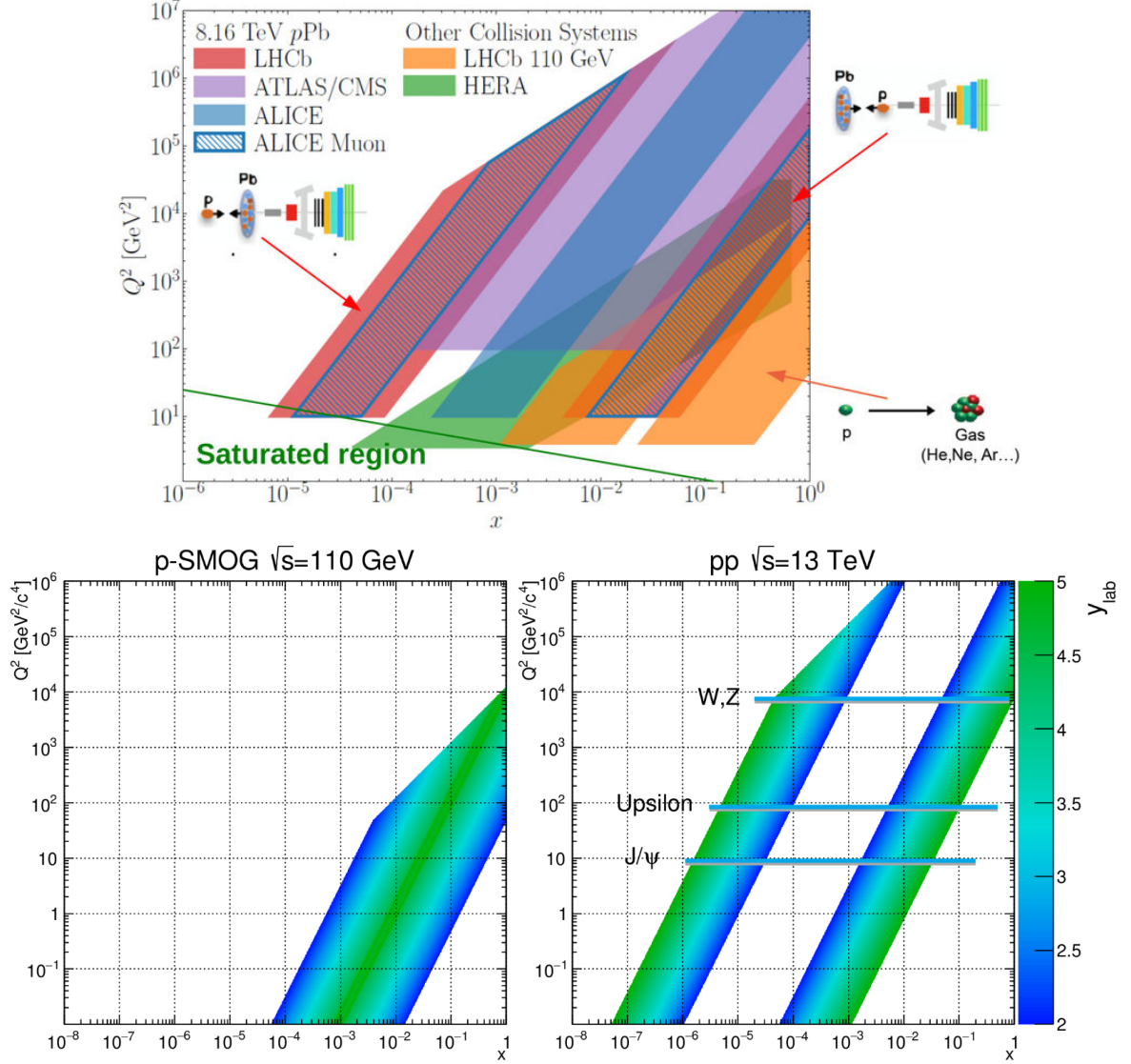
Figure I.4.4: Comparison between the accessible kinematic of the SMOG system with other experimental conditions. Top: accessible region in the Q^2−Bjorken-x phase space of different experiment, including LHCb pPb collisions (red) and fixed-target (orange) configuration. Bottom: comparison between the accessible region in the Q^2−Bjorken-x phase space of the LHCb pp collisions (right) and fixed-target (left) configuration. Figures taken from Ref. [132] and Ref. [131].

Final state effects The sequential suppression of quarkonia states is considered one of the key signature for QGP formation. Nevertheless, the production of quarkonia in nuclear collisions is influenced by several other effects, both in the initial and final state. Some examples are the interaction of the final state with the surrounding nuclear matter that can cause the break-up of the $c\bar{c}$ pair or, on the contrary, their secondary production. The study of cold nuclear-matter effects in heavy-flavour production, where no QGP formation is expected, is thus fundamental to disentangle the QGP signature from the underlying final state effects.

Nuclear PDFs at high-x Traditionally, the structure of the nucleon is described using

PDF, which, in the collinear form, are functions of the longitudinal momentum fraction of gluons and quarks, expressed by the Bjorken-x (Sec. I.1.2). Measurements of the nuclear PDF at high-x allows to constrain the theoretical models in a region where modifications due to the EMC[1] effect is expected and contributions from a nucleon intrinsic charm could be significant. These studies are also relevant for neutrino astronomy where the contribution from decays of charm hadrons produced in atmospheric showers, the main background, remains poorly constrained. A first measurement of charm production in fixed-target collisions at the LHC [133] has been published in 2018, based on the pHe and pAr samples at $\sqrt{s_{\text{NN}}} = 87$ and $\sqrt{s_{\text{NN}}} = 110$ GeV. It has been expanded in 2022 with the measurement in the PbNe and pNe samples at $\sqrt{s_{\text{NN}}} = 68.5$ GeV [134–136].

Cosmic Rays measurements The measurements of hadron production and spectra are crucial inputs for tuning theoretical models used in generators, especially where contributions from non-perturbative QCD become predominant. These measurements are in particular instrumental for CR physics to understand the production of secondary particles in their propagation in the ISM and the atmosphere. As presented in Sec. I.2.2, the antimatter fraction in CR is a sensitive indirect probe for exotic sources, but the clear interpretation of the results are mainly limited by the uncertainty on the secondary production in collisions between primary CRs and the ISM, which predominantly consists of hydrogen (90%) and helium (10%). The possibility to use He as a target allows to measure for the first time antimatter production cross-sections in the helium channels. The first measurement of prompt antiproton production in pHe collisions has been performed in 2018 using SMOG data sample at $\sqrt{s_{\text{NN}}} = 110$ GeV [54], contributing to significantly constrain the violation of cross-section scaling at high energies [137] (Fig. I.4.5). This result has been expanded in 2022 with the non-prompt production measurement [138, 139], which highlighted a larger contribution to the secondary antiproton production than the one expected from most models (Fig. I.4.6). Finally, the expansion towards the light antinuclei production cross-section is the focus of the work presented in this thesis.

I.4.3   The SMOG upgraded gaseous target

Even though the SMOG system has been exploited during Run2 to develop a rich and unique physics programme, it presents some limitations that hinder the achievable results:

Gas spread in a wide region The gas was injected directly in the VELO vessel and it was free to expand between ± 20 m around the LHCb nominal interaction point. The statistics of the collected sample was thus limited because

- to preserve the safety of the LHC operations and limit the contamination, only a maximum pressure of $\mathcal{O}(10^{-7})$ mbar could be reached due to the spread of the gas over 40 m;

---

[1]The EMC effect refers to the observation that the cross-section of deep inelastic scattering from an atomic nucleon is different from that of the free nucleons, thus implying that the parton momentum distributions are different for free or bound states.
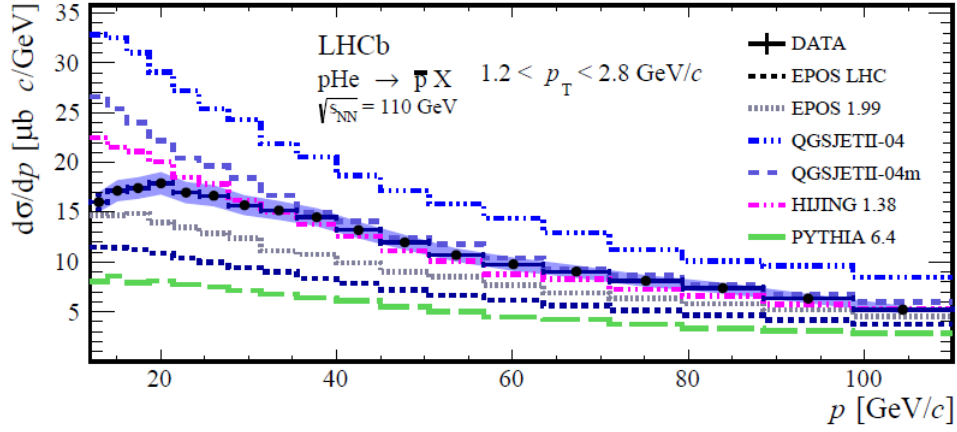
Figure I.4.5: Prompt antiproton production cross-section in pHe as a function of the momentum in one bin of transverse momentum; the data (black) are compared with different theoretical models. Figure taken from Ref. [54].
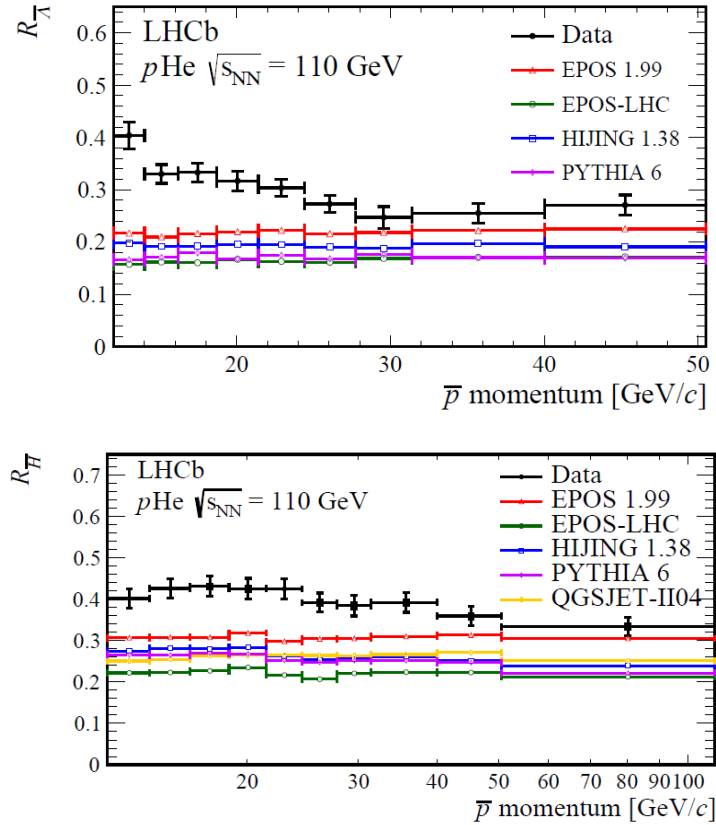
Figure I.4.6: Exlusive $\overline{\Lambda}$ (top) and inclusive (bottom) detached-to-prompt antiproton production cross-section in pHe as a function of the momentum; the data (black) are compared with different theoretical models. Figures taken from Ref. [138].
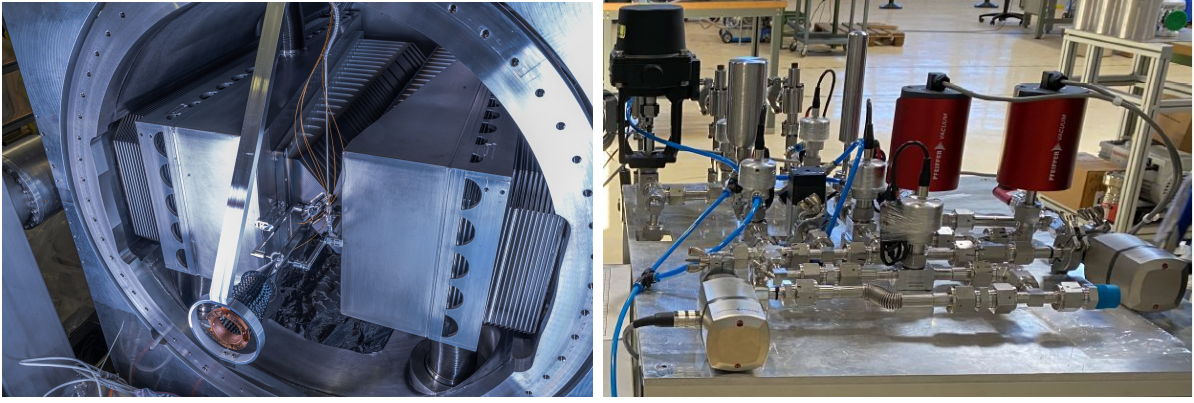
Figure I.4.7: Photos of the installed SMOG2 cell (left) and GFS (right). Figures taken from Ref. [140].

- the overlap with the beam-beam luminous region favoured limited and dedicated data collection periods for SMOG. A simultaneous data-taking with beam-beam was tested considering only the non colliding bunches entering the detector from the VELO side (10% of the total). Nevertheless, a significant interference between the two collision types was observed.

One gas reservoir The injection system was designed to accommodate only one gas reservoir, since it was developed for luminosity measurements where only Ne was expected to be injected. Changing the gas target, therefore, required an intervention in the experimental cavern that could be performed only during technical stops. It was thus impossible to acquire data with different targets during the same dedicated data-taking periods.

No direct pressure measurement SMOG was not equipped with precise gauges to measure the pressure of the injected gas. The luminosity was thus determined indirectly, measuring the elastic scattering of the beam particles on the atomic electrons:

$$\int \mathcal{L} \, dt = \frac{N_e}{Z_{He}\sigma_{pe}\varepsilon},\tag{I.4.4}$$

where N_e was the number of reconstructed and selected scattered electrons, Z_{He} the helium atomic number, σ_{pe} the pe^- elastic cross-section and ε the total experimental efficiency. Due to the limited reconstruction efficiency of soft electrons in the LHCb detector, the final systematic uncertainty associated to the luminosity, of the order of 6%, was the leading contribution limiting the cross-section measurements [54].

In the context of the upgrade of the LHCb detector after Run2, an improved gas injection system dedicated to the fixed-target programme has been designed and installed. The upgraded SMOG2 system [141] is composed by an open-ended 20 cm storage cell, installed between 34 and 54 cm upstream of the nominal LHCb interaction point (Fig. I.4.7, left). An advanced Gas Feed System (GFS) has also been installed, featuring four gas reservoirs and a precise control and measurement of the injected gas flow. The areal density in the cell can thus be directly measured (Fig. I.4.7, right).

The storage cell provides a reduced volume where the gas can flow with respect to the whole VELO vessel and beam pipe. As a consequence, the density profile along the LHCb longitudinal direction is characterised by a bump in correspondence of the cell, when the gas is injected in the middle of it. The density reached in the rest of the system (*i.e.* the VELO vessel and LHC beam pipe) is negligible compare to the values inside the cell. In this way, the beam-gas interaction region is essentially limited to the storage cell, well separated from the nominal LHCb interaction point, and an increase in the areal density up to two order of magnitude can be obtained with the same gas flow rate as used in SMOG. The system has been designed with the possibility to inject heavier noble gases like krypton and xenon and non-noble gases such as nitrogen, oxygen, hydrogen and deuterium. The four reservoirs in the GFS allows for a fast gas replacement ($\mathcal{O}$ (hour)), opening the possibility to change gas every fill. Detailed studies have been performed to evaluate the impact on the LHC machine of the injection of new gases, in order to determine the maximum integrated gas flow for each species. Indeed, heavy gases like krypton or xenon might be absorbed at the warm-to-cold transitions of the quadrupole magnets, leading to an increase in the local Secondary Emission Yield (SEY). Getterable gases like hydrogen, nitrogen and oxygen, on the other hand, can induce performance and mechanical degradation on the coating of the beam-line elements particularly close to the injection region. A detailed description of the simulation studies and their results performed for getterable gases is presented in Ch. III.2.

The new calibrated GFS has been equipped with multiple capacitance gauges and thermo-couples, installed on the storage cell, to precisely measure the injected gas flow rate and temperature. The new system allows an accurate measurement of the beam-gas collision luminosity and the associated systematic uncertainty is expected to be reduced to around 2-3% [142]. Finally, the separation between the beam-beam and beam-gas collision regions offers the unique opportunity at LHC to simultaneously collect data both in collider and fixed-target mode exploiting all the LHC bunches. LHCb will be the only experiment on the LHC ring able to operate at the same time at two different centre-of-mass energy.

I.4.3.1 The SMOG2 cell and the Gas Feed System

The gas storage cell, successfully installed in August 2020, consists of a 200 μm thin aluminium tube with a length of 20 cm and a diameter of 1 cm. Its alignment relative to the VELO RF foil is within 250 μm from the nominal position. Figure I.4.8 shows a sketch of its position within the VELO vessel (left) and its general design (right). The following requirements have been taken into consideration in the design of the cell:

- the dimensions have been chosen as a compromise between the available limited space upstream of the VELO detector (Fig. I.4.8, left) and the maximisation of the collectible luminosity. In particular, the diameter must be compatible with the radial aperture of the beam in correspondence of the cell $r(z)$. In Fig. I.4.9 the $r(z)$ upstream of the interaction point is shown for different beam scenarios. The cell radius is well within the safety limits;

- the cell must be composed by two opening halves (Fig. I.4.8, right) that follow the retraction of the two halves of the VELO detector. When the two halves are closed, they must guarantee enough gas tightness along the sides. In order to take into
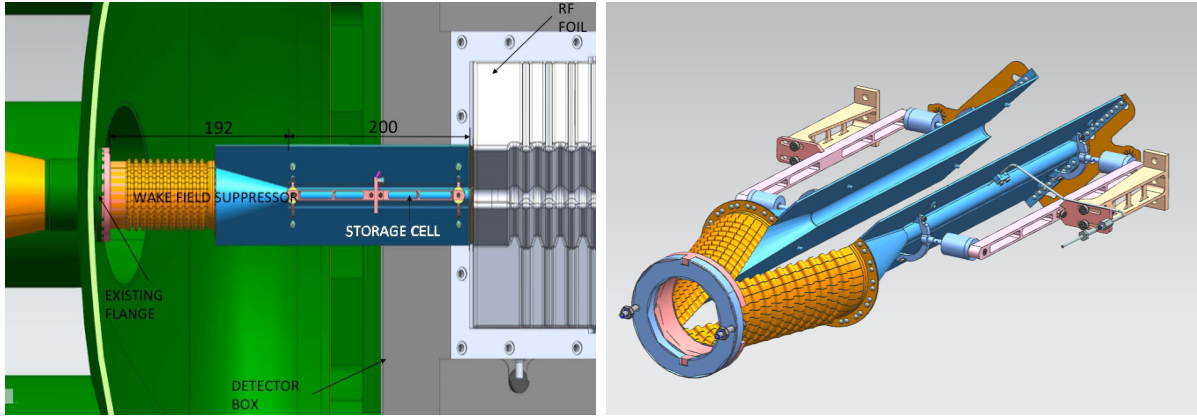
Figure I.4.8: SMOG2 cell position inside the VELO vessel (left) and its open configuration (right). Figures taken from Ref. [131] and Ref. [141].
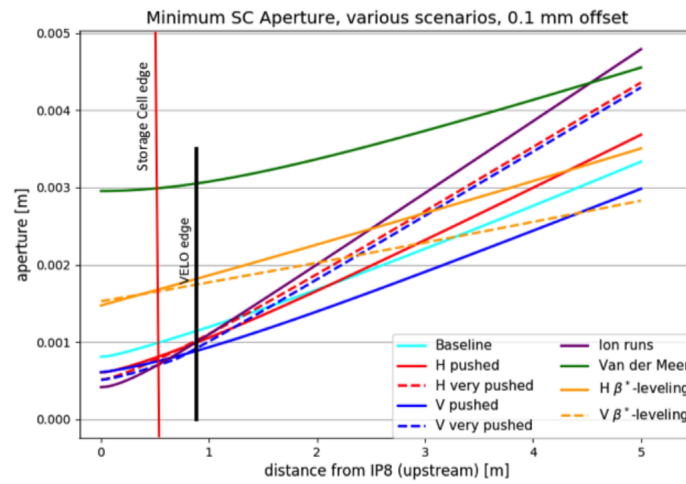
Figure I.4.9: Beam radial aperture as a function of the distance from the nominal LHCb interaction point in different beam configurations; the storage cell (red vertical line) and VELO vessel (black vertical line) position are also shown. Figure taken from Ref. [141].

account the variations in the exact VELO closed position, one half of the cell is rigidly fixed to the detector box, while the other half is equipped with a spring system that ensure enough movement flexibility. The cell reaches a complete closure 1 mm before the nominal VELO closure;

- in order to guarantee electrical continuity along the beam pipe and the suppression of the wake fields, an opening system of Wake Field Suppressor (WFS) has been installed at the upstream and downstream ends of the cell. In both cases, strips of CuBe foils are used to ensure excellent electrical and thermal conductivity as well as movement flexibility. The upstream WFS consists of a 56 mm diameter cylinder and it is connected to the cell via a conical transition (Fig. I.4.10, left). The downstream WFS, on the other hand, follows the profile of the RF foil, to which it is rigidly connected (Fig. I.4.10, right). The inner surface of the cell is smoothly milled in order to avoid cavity-like and resonance structures that could be sensitive to the radio-frequency fields generated by the bunched beam structure. In-depth
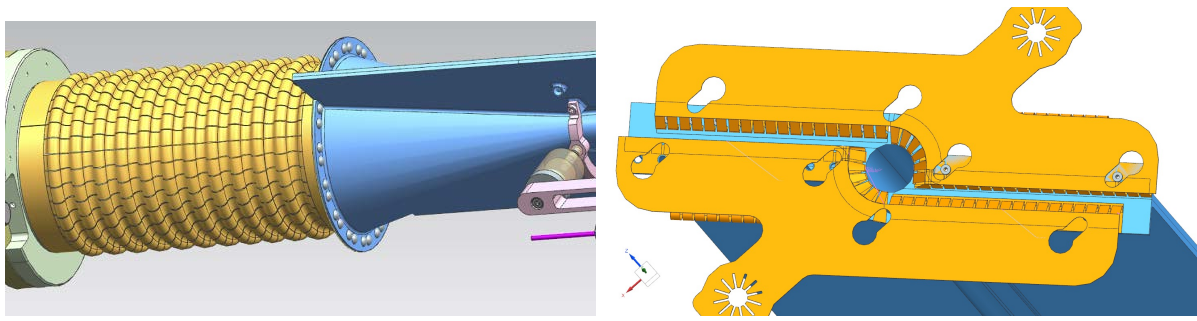
Figure I.4.10: Models of the upstream (left) and downstream (right) wake field suppressors. Figures taken from Ref. [141].

> studies on the cell impedance, dissipated power, and beam stability fluctuations have been conducted [141], revealing no signs of degradation effects;

- the cell must be coated with a low SEY thin film, in order to prevent the formation of Electron Clouds (ECs). Electron Clouds are produced when electrons generated by various ionization processes become trapped around a positively charged particle beam. They can cause avalanche effects and beam instabilities or losses. Amorphous carbon has been chosen because it is chemically less prone to ionization processes and it does not incur in deterioration following exposure to getterable gases;

- the material used for the cell must have a sufficiently low material budget to cause negligible additional Machine Induced Background (MIB). From simulation studies, it is demonstrated that the inclusion of the storage cell in front of the LHCb detector has no impact on the MIB, when properly compared to pp collisions. When the gas target is injected, an additional mechanism of beam loss arises due to beam-gas collisions. The expected beam lifetime amounts to 2060, 97, and 22 days for pH, pAr and PbAr, respectively, exceeding the typical duration of a LHC fill of 10-15 hours.

The gas is injected into the centre of the cell through a 0.72 mm inner diameter stainless steel capillary which is pushed into a 0.5 mm hole in the fixed half-side of the storage cell. On the other extremity, the capillary is connected to a flexible transition, which extends to the air side through a flange on the VELO vessel. The cell is equipped with five accurate K-Type twisted pair thermocouple wires that allows a precise monitoring of the temperature in the cell. They are distributed on the two sides of the cell, near the upstream and downstream WFS, and closed to the gas feed capillary on the fixed side. While the temperature profile of the gas in the cell is critical for the luminosity measurement, it also allows monitoring the heating effects associated with the beam, as it can be seen in Fig. I.4.11 where the temperature variations are clearly correlated with the beam status.

The GFS is schematically shown in Fig. I.4.12. It is equipped with two feed lines, connected to the VELO vessel and the storage cell, respectively, and filled using four gas reservoirs. It can be divided into four main parts:

GFS high pressure arm The high pressure arm of the GFS (orange) is composed by the four gas reservoirs of around 9 l supplying the feed lines. The reservoirs are
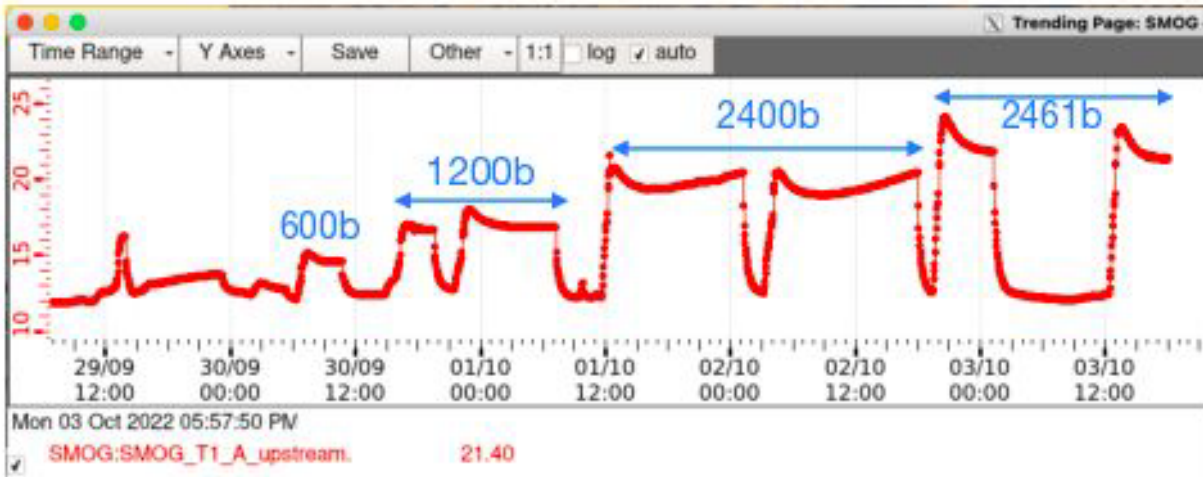
Figure I.4.11: Trend of the temperature readings from one of the thermocouples over four days during the 2022 run; the period of time corresponding to beam injection are reported, with the intensity indicated. A clear correlation between the temperature rising and fall and the presence of the beam can be observed.
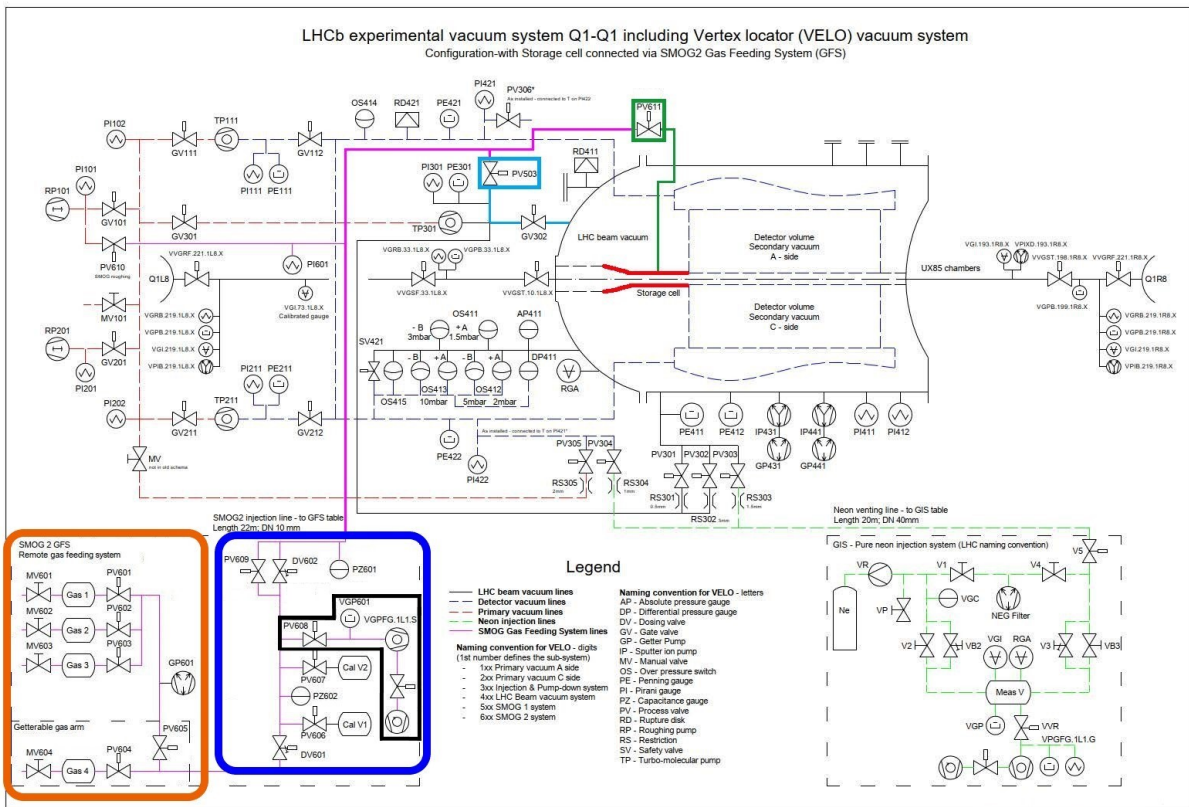
Figure I.4.12: Schematic representation of the LHC vacuum system around the LHCb interaction point. The SMOG2 GFS components are highlighted: high pressure arm (orange), low pressure arm (blue), pumping station (black), common feed line (pink), SMOG feed line (light blue) to the VELO vessel and SMOG2 feed line (green) to the storage cell (red).

68

filled at a pressure lower than 2500 mbar, the maximum value allowed on the DV601 dosing valve for stable pressure conditions. Three reservoirs are dedicated to noble gases and they are connected to a Non-Evaporable Getter (NEG) cartridge, which provides pumping of the background gases present on the arm. The fourth reservoir, filled with non-noble gases, is directly connected to the DV601 dosing valve. The separation from the noble gas side, provided by a dedicated valve, ensure the durability of the NEG cartridge. At a gas flow rate of 3.4×10^{-4} mbar·l/s, a reservoir can safely ensure a duration longer than the time between two LHC long technical stops, during which the reservoirs are refilled.

GFS low pressure arm The low pressure arm of the GFS (blue) is situated on the balcony in the LHCb cavern, approximately 17 m away from the VELO vessel. It hosts the main components for injecting calibrated gas flow, including the calibration volumes V1 and V2, the capacitance gauges PZ602 and PZ601 for the precise gas flow measurement, and the electro-pneumatic dosing valves DV601, connected to the high pressure arm, and DV602, which controls the flow in the feed lines.

Pumping station The GFS pumping station (black) consists of a 70 l/s turbo pump and a dry backing pump, connected to the low pressure arm through the PV608 valve.

Feed lines The GFS is equipped with two feed lines (pink). The first one is connected to the storage cell through the PV611 valve (green). The one feeding into the VELO vessel reuses the SMOG line (light blue). It is connected through the PV503 valve to the vessel, using the same injection point (GV302 valve) as the turbo-molecular pump TP301, which provides auxiliary pumping to the VELO vacuum.

Finally, the purity of the injected gas can be assessed using a Residual Gas Analiser (RGA), which employs mass spectrometer techniques to verify the absence of gas contaminations.

I.4.3.2 Physics opportunities with SMOG2

The enhanced capabilities of the upgraded LHCb detector coupled with the improvements in fixed-target data acquisition and the injection of new gases open a wide range of physics opportunities previously unexplored [131]. The possibility to inject hydrogen offers a reference for the measurements carried out with other gases, similarly to the *pp* reference runs for runs with circulating heavy ions. Comparing the results with injected deuterium, it allows highlighting possible isospin-violating effects. At the same time, during the lead ions data-taking, the improved LHCb upgraded reconstruction performance will allow the reconstruction of events in PbA collisions at an unprecedented centrality. The programme presented in Sec. I.4.2.1 will be improved and further expanded:

Cold nuclear-matter effects The underlying effects associated to the formation of the QGP will be better constrained thanks to the possibility to perform measurements with a wide range of collision systems and with an unprecedented statistics. Specifically, studying the charmonium production in proton-induced reactions across different nuclear targets, where QGP formation is not anticipated, is essential to establish a robust baseline against which to interpret the suppression patterns

observed in heavy-ion collisions. This research is also pivotal for comprehending the underlying physics mechanisms governing charmonium production.

Nuclear PDFs at high-x Expand the study of the high-x PDFs will be possible thanks to the enhanced statistics and the possibility to inject multiple gases, like hydrogen. The study of charm mesons and baryons production will shed light on the possible presence of intrinsic charm content within nucleons. Drell-Yan and inclusive quarkonia production measurements, instead, will contribute to reduce the uncertainties on the light quark and anti-quark PDFs in a wide kinematic region ($10^{-4} < x < 10^{-1}$), addressing their transverse momentum dependence.

Flow and fluctuation The hydrodynamic description of the QCD medium can help understand the QCD phase diagram and its critical points. This description has proven highly successful at the highest energies observed at RHIC and, with proper handling of the baryon density and a complete three-dimensional portrayal of the initial state, it remains applicable at the lower energies found at the LHC. Fixed-target data at energies around $\sqrt{s_{\mathrm{NN}}} = 70\,\mathrm{GeV}$ offers a valuable opportunity to test the hydrodynamic description up to the lower energy scale and over three fully-instrumented units of pseudorapidity for multiple collision systems.

Ultra-peripheral collisions Studying photon-induced processes in Ultra-Peripheral Collisions (UPC) between nuclei, where the impact parameter greatly exceeds the nuclear sizes, offers a unique testing ground for QCD. The LHC kinematic coverage allows investigating a regime where non-linear effects inherent to non-perturbative QCD might become apparent. Since the photon flux is directly proportional to the squared atomic number of the colliding nuclei, interesting measurements in UPC physics are possible with the fixed-target configuration. In particular, the heavy ion data-taking provides a complementary kinematic regime to the *pp* measurements. SMOG2 coupled with dedicated online selections will allow overcoming the statistics limitations encountered during Run2.

Cosmic Rays measurements The measurements of hadron production and spectra will be further expanded with SMOG2, in particular focussing on the completion of the measurements of interest for CR physics:

- exploiting the precise gauges and the rapid gas replacement system, it will be possible to improve the precision of the cross-section measurements. In particular, it will be possible to measure ratios of cross-sections from different injected gases collected under identical experimental conditions, like $\sigma(p\mathrm{He} \to \bar{p}X)/\sigma(p\mathrm{H} \to \bar{p}X)$;

- the antiproton production from antineutron decays can be constrained by measuring the isospin violation in the ratio $\sigma(p\mathrm{D} \to \bar{p}X)/\sigma(p\mathrm{H} \to \bar{p}X)$. Current data on antineutron-to-antiproton prompt production are limited and the theoretical models would benefit from a result in the SMOG2 kinematic region, as shown in Fig. ;

- the measurement of antiproton production cross-sections will be extended up to the LHC injection energy, where the positive Feynman-x range can be accessed, as shown in Fig. ;
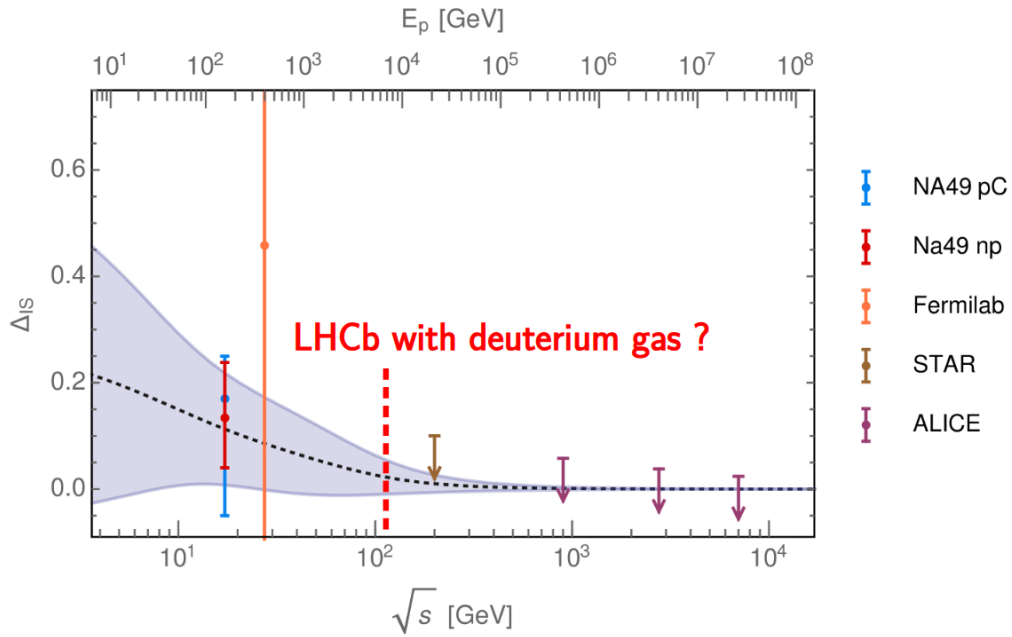
Figure I.4.13: Available data for the difference in the production cross-section for prompt antiprotons and antineutrons as a function of the centre-of-mass energy; the fitted trend with the associated uncertainty is also reported. Figure presented in Ref. [143] starting from Ref. [144].
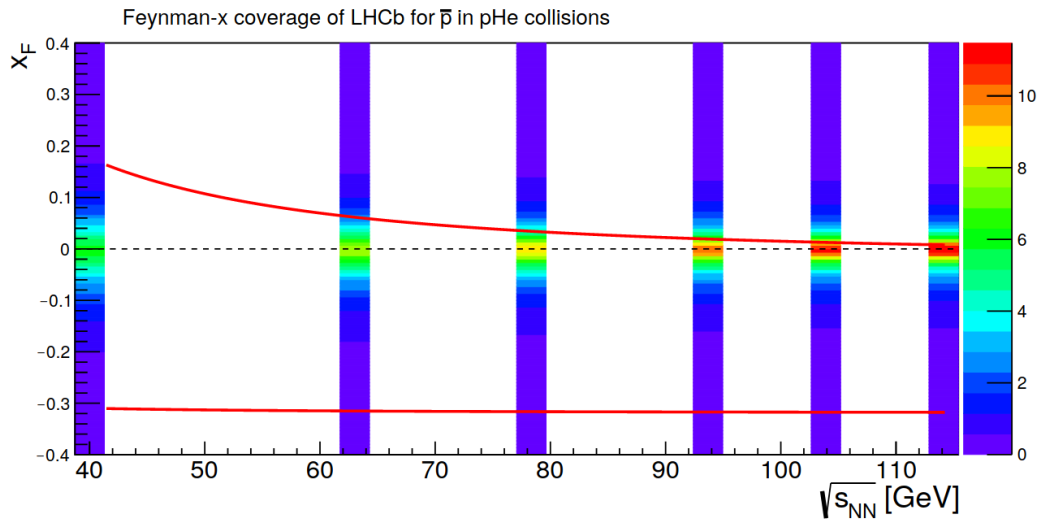
Figure I.4.14: Expected Feynman-x probability density function for antiprotons produced in pHe collisions at different centre-of-mass energies, according to QGSJETII04 model [145]; the red lines indicate the minimum and maximum values accessible at LHCb. Figure taken from Ref. [131].

Table I.4.1: Expected yields of reconstructed events for selected processes considering the largest collected data sample acquired in fixed-target configuration with the SMOG system and the expected statistics collected during Run3 with the SMOG2 system, considering a data-taking scenario with one third of the beam-time shared between beam-beam and beam-gas collisions. Table taken from Ref. [131].

	SMOG largest sample pNe @69 GeV	SMOG2 example pAr @115 GeV
Integrated luminosity	~ 100 nb^{-1}	~ 45 pb^{-1}
J/ψ yield	15k	15M
D_2^0 yield	100k	150M
Λ_c^+ yield	1k	1.5M
$\psi(2S)$ yield	150	150k
Υ (1S) yield	4	7k
Low-mass Drell-Yan yield	5	9k

- it will be possible to obtain data useful to improve the modelling of extensive cosmic air showers, injecting nitrogen and oxygen. These models require understanding of hadronic collisions in the atmosphere over a wide range of collision energy. SMOG2 data will cover the energy scale ~ 100 GeV for which little or no data exist. They are expected to provide a better understanding of deviations from predictions in the muon density in atmospheric showers, commonly referred to as the muon puzzle [146]. The run with circulating oxygen beams, expected in 2024, will allow extending the study to the very forward region (up to $\eta \simeq 7.6$) in the projectile rest frame thanks to the injection of hydrogen.

In Tab. I.4.1 the expected yields for some c- and b- hadrons are listed, considering a data-taking scenario with one third of the beam-time shared between beam-beam and beam-gas collisions. When compared to the highest-statistics sample collected in Run2, larger values by up to three orders of magnitude are found.

Part II

Deuterons and antideuterons identification

II.1 Analysis motivations and feasibility studies

After an introduction to the physical motivation for the measurement of antideuteron in the LHCb experiment (Section II.1.1), the feasibility studies for the antideuteron production cross-section in the pHe $\sqrt{s_{NN}}$ =110 GeV data sample are presented in Section II.1.2. Having demonstrated that a significant sample of antideuterons are expected to be within the LHCb detector acceptance, the particle identification techniques available are analysed demonstrating the need for an innovative approach to the problem.

II.1.1 Analysis motivations

As discussed in Chapter I.2, production of antinuclei is crucial for the understanding of their formation mechanism and the interpretation of the experimental data on the antinuclei abundance in CRs. In recent years, much progress has been made in the understanding of the antinuclei production mechanism, which is commonly described with the coalescence model (Sec. I.2.3.1):

- A systematic study of past and recent results in the antiproton and antinuclei production, coupled with the application of the novel MC approach to extract the coalescence momentum (Sec. I.2.3.1), demonstrated that the coalescence probability is not independent of the interaction energy [62] (Fig. II.1.1), but it can be parametrised as

$$p_0(T) = \frac{A}{1 + \exp B - \ln T/C} \tag{II.1.1}$$

  where T is the kinetic energy of the projectile in the ISM rest frame, and A, B and C are free parameters that depends on the MC generator considered.

- The traditional coalescence model disregards the dependences on the nucleon-emitting source (*i.e. pp*, *p*A, AA) and it applies a scaling law to the coalescence momentum p_0 obtained for the antideuteron (Eq. I.2.23) to extrapolate for higher mass antinuclei. This approach, though, ignores the internal structure of the nucleus and it is in tension with the most recent results [65–67] (Fig. II.1.2, left). A novel approach based on the Wigner formalism [148] has been proposed, where the volume of the interacting system and of the generated nucleus is taken into consideration, and it demonstrates to be able to reproduce the antideuteron distribution (Fig. II.1.2, right).
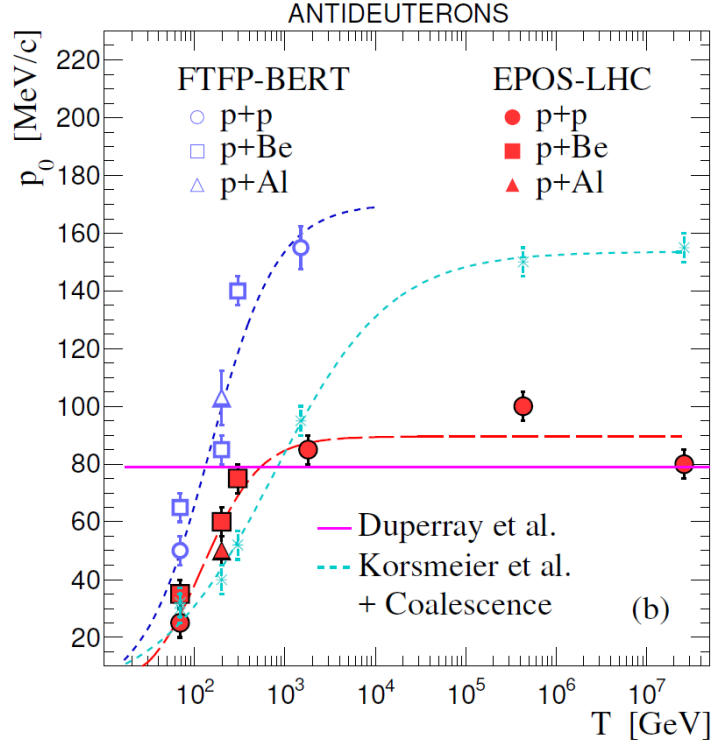
Figure II.1.1: Expected coalescence momentum p_0 for antideuterons as a function of the projectile kinetic energy T; the fit functions for the EPOS-LHC (dashed red) and Geant4 (dashed blue) event generators are shown. The p_0 value for two alternative parametrisation are also reported (dotted light blue and solid pink) [137, 147]. Figure taken from Ref. [62].
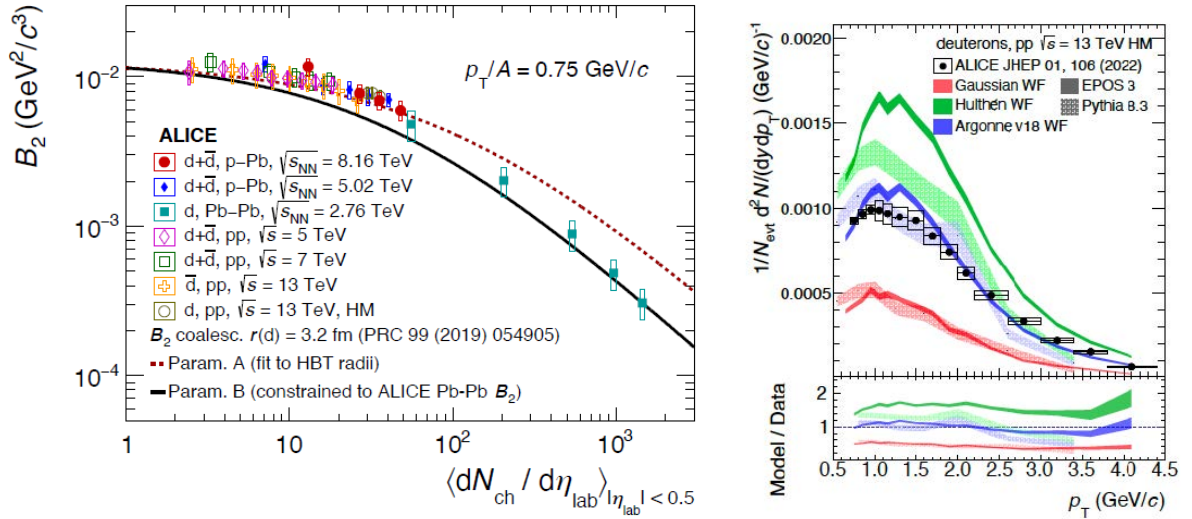
Figure II.1.2: Left: B_2 as a function of the multiplicity of the interaction; the results are compared with the coalescence calculations using two different parametrisations for the system size. Right: deuteron spectra obtained from EPOS3 and PYTHIA applying the coalescence model with different hypothesis for the deuteron wavefunction, compared to ALICE results. Figures taken from Ref. [65] and Ref. [148], respectively.
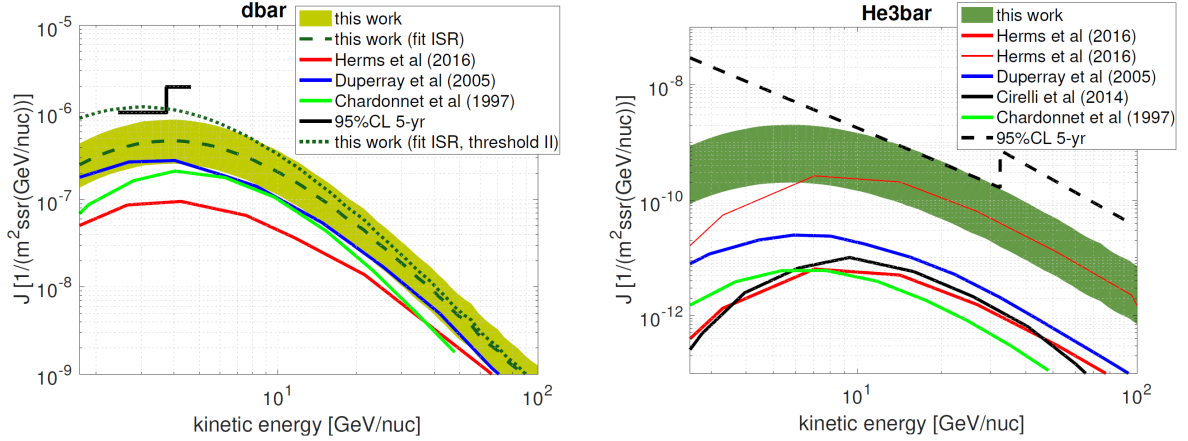
Figure II.1.3: Comparison of the expected antideuteron (left) and antihelium-3 (right) flux based on different models; the sensitivity limit for AMS-02 is also shown as a solid (dashed) black line for antideuterons (antihelium-3). Figures taken from Ref. [155].

Given that at the moment no comprehensive theoretical model is able to take into account all the physical effects and dependences in the coalescence process, direct measurements at the energy range and with the interaction systems most relevant for CRs physics are needed.

While ultra-high energy measurements from experiments operating at the TeV scale, such as the ALICE experiment at the LHC, and fixed-target measurements in $\sqrt{s_{NN}} < 30$ GeV energy range, such as NA49 and NA61/SHINE [63, 149, 150] at the SpS, have greatly enhanced the knowledge on antinuclei formation and interactions, less data on light antinuclei production are available in the intermediate energy range, where an increase in the coalescence probability is expected. The significant spread among the available theoretical models leads to order-of-magnitude uncertainties in the predicted antinuclei flux, thus limiting the interpretation of the space experiment results [147, 151–156] (Fig. II.1.3). Moreover, as it has already been highlighted, the formation of light antinuclei is tightly coupled with the production of antinucleons. Since almost no direct production measurements of antineutrons are available, the precise knowledge of the antiproton cross-section and its relation to the antineutron one is crucial. Current hadronic generators typically used for high-energy CRs predictions do not reproduce the measured antiproton production cross-sections with sufficient precision, both in terms of overall yield and spectral shape. Measurements of antiprotons production in the same experimental conditions as the antinuclei are thus beneficial to constrain the coalescence model.

The LHCb experiment with its fixed-target system SMOG is ideally suited to tackle these needs. Operating as a fixed-target experiment on the LHC ring, it covers an intermediate energy range between $\sqrt{s_{NN}} \in [69; 110]$ GeV. Moreover, the possibility to inject light noble gases allows to test different collision system, in particular pHe, reproducing the CRs-ISM interactions. After the measurements of the antiproton production cross-section described in Sec. I.4.2.1, a measurement of the antideuteron and antihelium-3 production cross-section using the Run2 data sample would provide a fundamental and unique input to the coalescence puzzle.

II.1.2   Estimation of antinuclei production yield in SMOG2 data

The identification of light nuclei can be performed combining the information on the particle momentum with a measurement of its speed. In high energy physics, the speed of the particle is measured using different detectors, whose operating principles can be broadly divided into three main approaches:

- the measurement of the time-of-flight of the particle, which is related to its speed, given the flight distance L as
$$t_{\mathrm{TOF}} = L/\beta c; \qquad\qquad (\mathrm{II.1.2})$$

- the measurement of the energy deposit, which is related to the particle speed and its charge by the Bethe-Bloch formula [157];

- the measurement of the Cherenkov radiation, as described in Sec. I.3.2.2.1

In the LHCb experiment the RICH system, based on the Cherenkov radiation, is dedicated to the PID. The OT detector, on the other hand, thanks to the time information associated with the hits could be exploited for a time-of-flight measurement in a complementary kinematic region.

II.1.2.1   Light nuclei identification using the RICH detector

As shown in Sec. I.3.2.2, the identification of the charged particles in the LHCb detector is performed using the RICH detectors. Given the RICH1 and RICH2 momentum thresholds for deuterons, respectively 35.4 GeV/c and 59.3 GeV/c, a production measurement based on this detector is possible only in the high momentum region.

Detailed studies have been performed [158, 159] in order to understand the RICH performance for deuteron identification. A neural network taking as input kinematic variables, tracking information and the response from the RICH detectors was optimised for the deuteron identification and a template fit, performed in bins of track momentum to take into account the RICH Cherenkov thresholds, was applied to extract the yields. Despite the optimisation of the background rejection maintaining high efficiency for the deuteron selection, the misidentification efficiency for pions remains at the level of 10^{-4}, giving similar expected levels for signal and background. Additional improvement are under study to increase the signal-background discrimination.

II.1.2.2   Light nuclei identification using a time-of-flight measurement

A different approach based on the time-of-flight measurement is possible for the low momentum deuteron that are below the RICH threshold [93]. The OT detector, as described in Sec. I.3.2.1.3, needs the drift time t_{drift} of the ionization cluster inside the straw to extract the position of the hit using the TR-relation defined in Eq. I.3.4. The quantity directly measured by the detector though is the arrival time t_{TDC} of the signal from the ionization cluster, and it includes contributions from the time-of-flight of the

Table II.1.1: Particle momentum that gives rise to a delay comparable with the track time resolution for different particle species.

Particle	Mass $[\text{MeV}/c^2]$	Momentum $[\text{MeV}/c]$
π	139.57	740
K	493.68	2616
p	938.27	4972
d	1875.61	9940
^3He	2808.39	14883
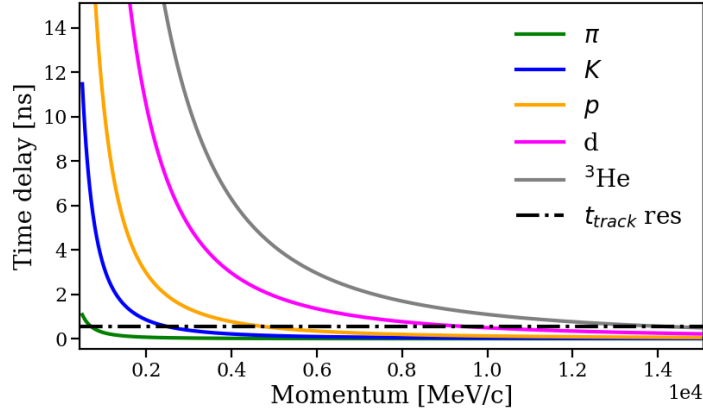
Figure II.1.4: Expected delay in arrival time at the centre of the OT detector, for different particle species.

particle between the interaction point and the detector t_{TOF}. The t_{drift} is therefore obtained correcting t_{TDC} for the time-of-flight in the hypothesis, generally true, that the particle moves at the speed of light.

When a track is reconstructed, the TR-relation can be used to define the expected arrival time $t(r)$ associated to every hits on the track and its value is compared to the corresponding t_{TDC}. The residual between the two is due to the approximation made considering $\beta = 1$ and it is proportional to the real β of the particle. In order to improve the time resolution, the track time can be defined as the sum of the residuals of the hits associated with the track, weighted by their errors. Given the hit time resolution of 2.4 ns and an average of 18 OT hits per track, the expected track time resolution is 0.57 ns. Tracks reconstructed from the combination of OT hits not produced by the same particle, called ghost tracks, show a larger track time distribution, confirming the discrimination power of the time information for PID.

Figure II.1.4 shows the expected delay in the arrival time at the centre of the OT detector, corresponding to a flight distance of 8 m, for different particles as a function of the particle momentum. In Tab. II.1.1, the momentum corresponding to a delay comparable with the track time resolution is reported for the same particle species. In principle, a time-of-flight measurement with this resolution can provide significant PID power for protons up to 5 GeV/c, while for deuterons the limit increases to 10 GeV/c, and it reaches even higher thresholds for heavier particles.
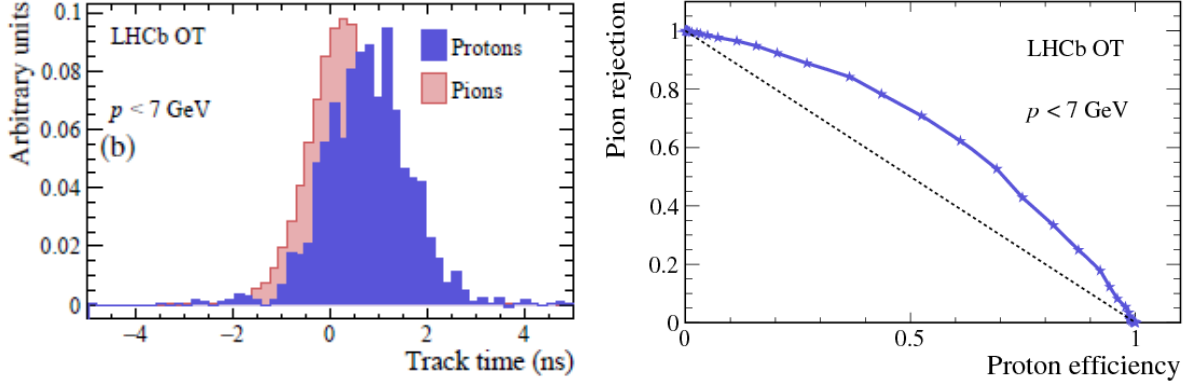
Figure II.1.5: Left: distribution of track times for protons and pions with $p < 7$ GeV/c in 2015 data. Right: pion rejection rate as a function of the proton efficiency in 2015 data. Figures taken from Ref. [93].

The track time π-p discrimination has been tested on LHCb data collected during 2015 [93]. A sample of D_2^* tagged $D_2^0 \to K^+\pi^+$ decays is used for the pion control sample, while semileptonic Λ_b^0 decays are considered for the proton control sample. The result for particles with momentum lower than 7 GeV/c is shown in Fig. II.1.5, where distribution of the track time for protons and pions (Fig. II.1.5, left) and its discrimination power (Fig. II.1.5, right) are presented. While the discrimination power confirms the PID capabilities of the technique, the track time distribution for protons shows a bias towards lower values decreasing the separation between the two distribution with respect to what expected from the time-of-flight.

The bias observed on the track time is associated to the approximations considered reconstructing the hits. The position of the hit is obtained from the TR-relation in the hypothesis that the reconstructed t_{drift} corresponds to the real one. When the hypothesis of $\beta = 1$ is applied, though, an overestimation of t_{drift} is performed, since the particles do not travel exactly at the speed of light. Through the TR-relation, the overestimation of t_{drift} translates into an error in the hit position r determination. While the correction is negligible for β values close to 1, it can bias the track reconstruction for slower particles. The error on r depends on t_{drift}, being higher for the hits closer to the wire. In Fig. II.1.6, the error on the hit position is showed as a function of t_{drift} for values of momentum in the range $[1; 10]$ GeV/c for a deuteron. As expected, the error increases for low t_{drift} and low momentum, being consistently higher than the OT spatial resolution (171 μm) for particles with momentum lower than 7 GeV/c, where the time-of-flight correction is expected to be more relevant, and reaching the order of the millimetres for particles with momentum lower than 2 GeV/c. This error on the hits positions impacts both the track reconstruction efficiency and it introduces a bias on the track time, impacting its performance in terms of PID power.

The performance of the LHCb track reconstruction algorithm must thus be carefully evaluated for light nuclei, and in particular for deuterons, and an alternative time-of-flight-based PID technique must be studied in order to successfully perform an antideuteron production measurement in the $p < 10$ GeV/c kinematic region.
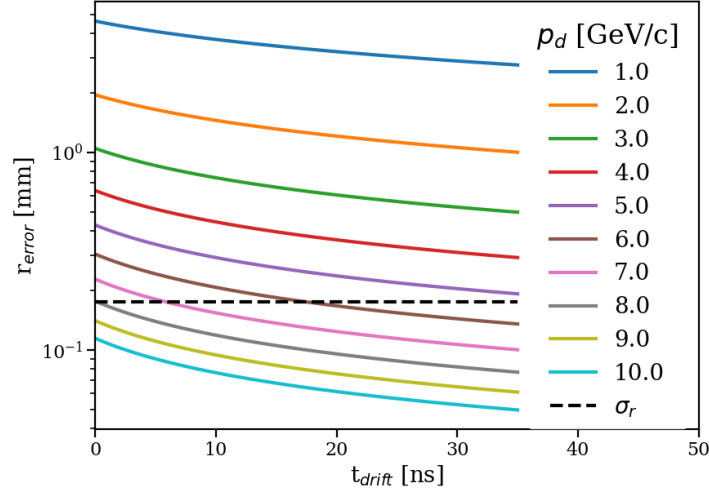
Figure II.1.6: Error on the reconstructed hit position as a function of t_{drift} for deuterons with momenta in the range $[1; 10]$ GeV/c.

II.1.2.3 Antinuclei production yield in SMOG

Considering the possible identification techniques available at the LHCb experiment, an evaluation of the expected antideuteron yield has been performed for the $p\text{He}$ $\sqrt{s_{\text{NN}}} = 110$ GeV data sample. A minimum bias simulated sample has been used for the study, generated using the EPOS-LHC model [112] within the CRMC [160] package v1.5.6. EPOS-LHC is a specialized event generator for soft hadronic production and nuclear effects, tuned to reproduce the most recent LHC data. While the EPOS-LHC simulation can generate antiprotons and antineutrons taking into account their correlation, no implementation for nuclei and antinuclei production is available. An afterburner must thus be created to generate antideuterons emulating the coalescence process. For every event, the afterburner identifies the antiproton-antineutron pairs and calculates their difference in momentum in the centre-of-mass frame. If the difference is lower than the coalescence momentum, an antideuteron with momentum equal to the sum of the antiproton and antineutron momenta is generated, while the corresponding antinucleons are deleted.

Since the focus of this study is to evaluate the expected yield in the data sample, a simplified approach is chosen. The antiproton spectra in bins of momentum p and transverse momentum p_{T} is obtained from the EPOS-LHC simulation and the analytical coalescence model is applied bin-by-bin in order to obtain the antideuteron distribution.

$$N_{\overline{\text{d}},i,j} = \frac{4}{2\pi} \text{B}_2 \frac{E_{\overline{p},i,j}}{p_{\text{T,j}}} \frac{N_{\overline{p},i,j}^2}{\Delta p_i \Delta p_{\text{T,j}}}, \tag{II.1.3}$$

where $N_{\overline{\text{d}},i,j}$ and $N_{\overline{p},i,j}$ are the number of antideuterons and antiprotons in the *i-th* p bin and *j-th* p_{T} bin, $E_{\overline{p},i,j}$ is the antiproton energy corresponding to the central value for the *i-th* p bin and *j-th* p_{T} bin, $p_{\text{T,j}}$ is the central value of the *j-th* p_{T} bin and Δp_i and $\Delta p_{\text{T,j}}$ are the width of the *i-th* p bin and *j-th* p_{T} bin. The coalescence probability B_2 has been taken from the latest available results from the ALICE collaboration [57]. In Fig. II.1.7 the expected ratio between antideuteron and antiproton is shown in bins of

Figure II.1.7: Expected ratio between antideuteron and antiproton in bins of momentum and transverse momentum per nucleon $p_A/A - p_{\mathrm{T,A}}/A$.

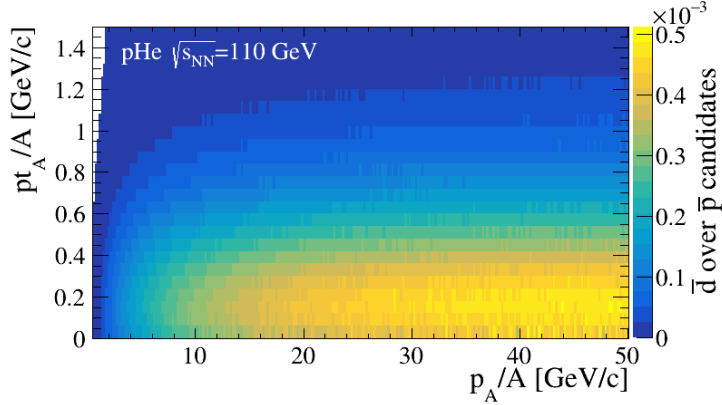momentum and transverse momentum per nucleon $p_A/A - p_{\mathrm{T,A}}/A$. Overall, 0.9×10^{-3} antideuterons are expected for every antiproton in the data sample, a result comparable with similar studies in literature [57]. Considering separately the time-of-flight kinematic region ($p \in [1; 10]$ GeV/c) and the RICH kinematic region ($p \in [35; 100]$ GeV/c), the ratio is 0.3×10^{-3} and 1×10^{-3}, respectively.

Given the number of antiprotons observed in the pHe $\sqrt{s_{\mathrm{NN}}}$ =110 GeV data sample [54], around 4500 antideuterons can be expected to be overall produced in the LHCb detector. Their distribution in bins of p and η (top) and their projections (p bottom left, η bottom right) are shown in Fig. II.1.8 for the kinematic region accessible, corresponding to $p \in [1; 100]$ GeV/c and $\eta \in [2; 5]$. The projected distributions both in p (left) and η (right) are reported in Fig. II.1.9 and Fig. II.1.10, for the time-of-flight and RICH kinematic regions, respectively. Around 300 antideuterons are expected to be reconstructed in the time-of-flight kinematic region, while 2000 can be found in the RICH kinematic region.

The same study has been performed considering $^3\overline{\mathrm{He}}$:

$$N_{^3\overline{\mathrm{He}},i,j} = \frac{9}{(2\pi)^2} B_3 \left(\frac{E_{\overline{p},i,j}}{p_{\mathrm{T,j}}} \right)^2 \frac{N^3_{\overline{p},i,j}}{(\Delta p_i \Delta p_{\mathrm{T,j}})^2}, \qquad (\text{II.1.4})$$

where $N_{^3\overline{\mathrm{He}},i,j}$ is the number of antihelium-3 in the *i-th* p bin and *j-th* p_{T} bin and the coalescence probability B_3 has been taken from the latest available results from the ALICE collaboration [57]. Since no studies on the ^{3}He identification using the RICH system have been performed, only the overall distribution and the one in the time-of-flight kinematic region ($p \in [1; 15]$ GeV/c) are considered. Figure. II.1.11 presents the expected ratio between antihelium-3 and antiproton in bins of momentum and transverse momentum per nucleon $p_A/A - p_{\mathrm{T,A}}/A$, while Fig. II.1.12 and Fig. II.1.13 show the distributions for $^3\overline{\mathrm{He}}$ as a function of p and η for the overall kinematic region covered by the LHCb detector and in the time-of-flight kinematic region, respectively. Overall, a ratio of 3×10^{-6} is obtained for antihelium-3, compatible with experimental results from ALICE, but it reduces to 4×10^{-7} in the time-of-flight kinematic region. No candidates are therefore expected in the time-of-flight kinematic region to perform a production measurement.

In the following sections, studies for the identification of deuterons and antideuterons are

Figure II.1.8: Expected antideuteron distribution in bins of p and η in the LHCb acceptance (top); the projections in momentum (left) and pseudorapidity (right) are also reported.

Figure II.1.9: Expected antideuteron momentum (left) and pseudorapidity (right) distribution in the time-of-flight reconstructable kinematic region ($p \in [1; 10]$ GeV/c).

going to be presented. For better readability, the particle name will be used to identify both the particle and the antiparticle, unless explicitly stated.

Figure II.1.10: Expected antideuteron momentum (left) and pseudorapidity (right) distribution in the RICH reconstructable kinematic region ($p \in [35; 100]$ GeV/c).
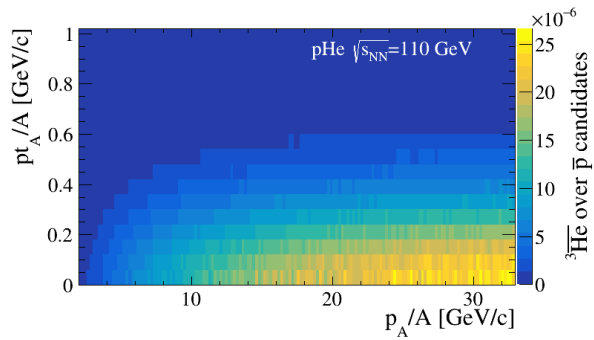
Figure II.1.11: Expected ratio between antihelium-3 and antiproton in bins of momentum and transverse momentum per nucleon $p_A/A - p_{T,A}/A$.
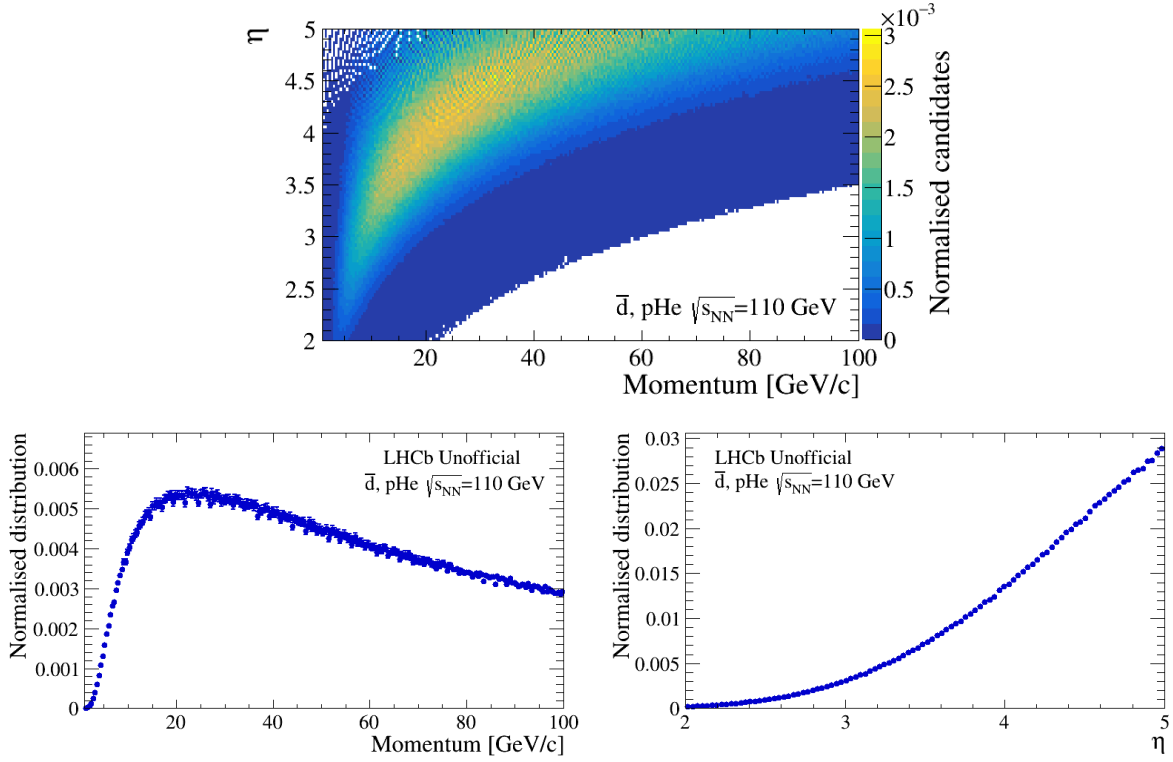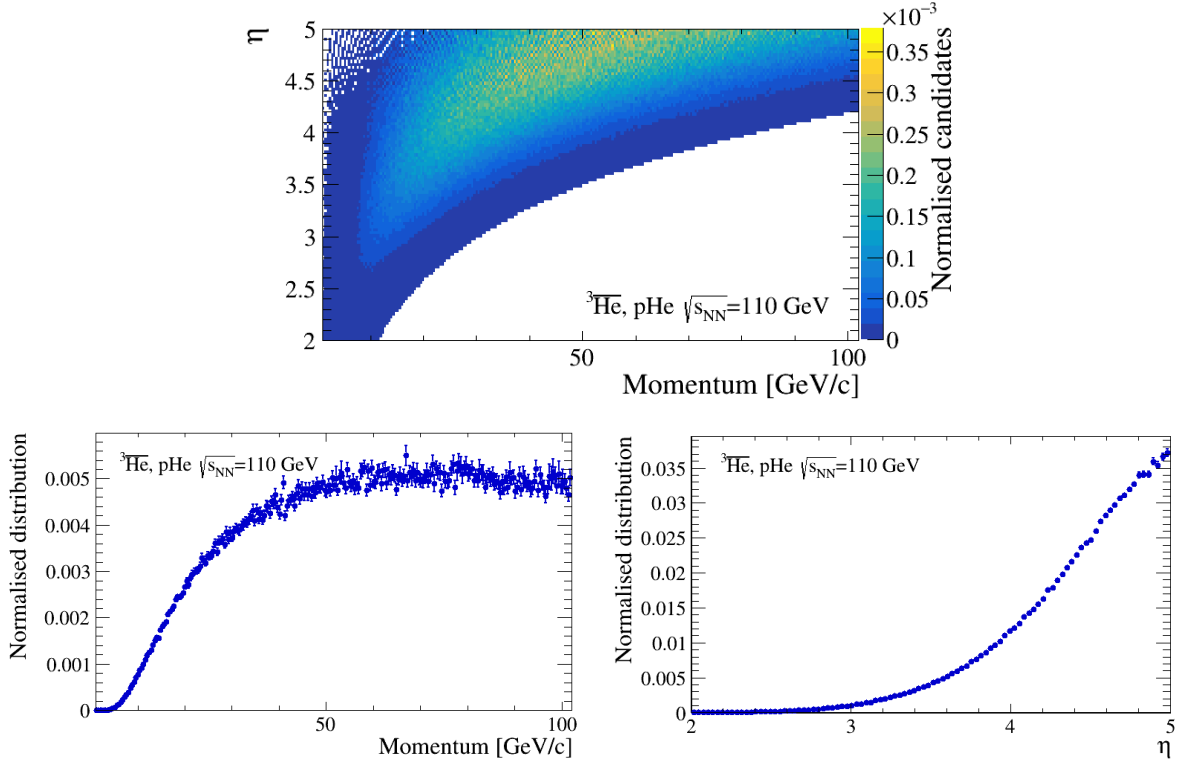
Figure II.1.12: Expected antihelium-3 distribution in bins of p and η in the LHCb acceptance (top); the projections in momentum (left) and pseudorapidity (right) are also reported.
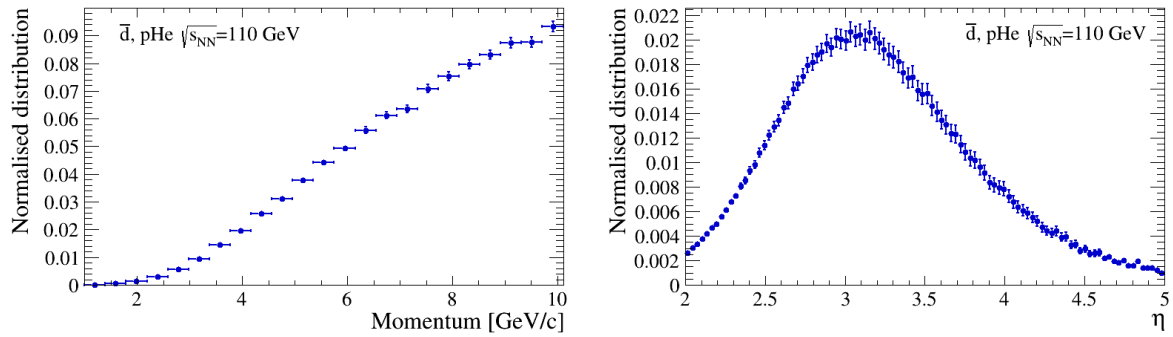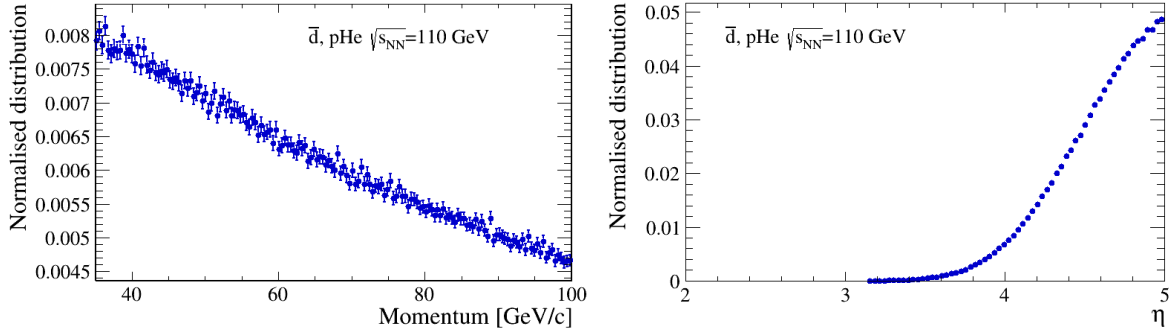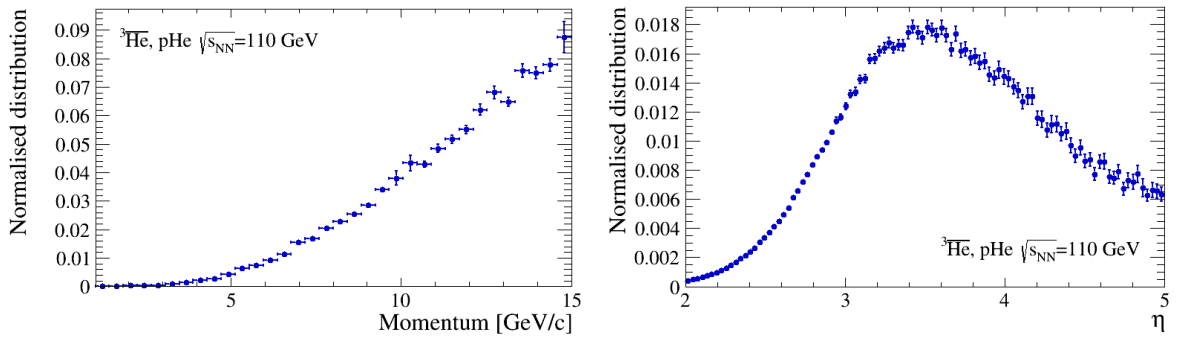

Figure II.1.13: Expected antihelium-3 momentum (left) and pseudorapidity (right) distribution in the time-of-flight reconstructable kinematic region ($p \in [1; 15]$ GeV/c).

II.2 Light nuclei reconstruction

This chapter is dedicated to the track reconstruction algorithm and its performance for light nuclei tracks. Section II.2.1 introduces the LHCb tracking strategy, focussing on the standard pattern recognition algorithm, PATFORWARD, and its limitations in the reconstruction of slow tracks. A newly developed alternative is presented in Section II.2.2 and its performance are shown in Section II.2.3, where they are compared to the PATFORWARD algorithm in particular in regard to the track reconstruction efficiency.

II.2.1   Track reconstruction in LHCb

The tracking strategy implemented in the LHCb software has been developed in order to maximise the physics output for decays of hadrons containing b quarks. As illustrated in Sec. I.3.2.3, the reconstruction quality reached at the output of the HLT2 trigger is required to be of the same level as offline reconstruction. As a consequence, the tracking strategy must be able to achieve an elevated reconstruction efficiency also when applied to highly selective triggers that exploit information coming from partially reconstructed events, working at the expected input rate of 1.1 MHz. This has been achieved through complementarity in the available patter recognition algorithms and flexibility in the reconstruction sequence, which allows running fast versions of the offline reconstruction algorithms in the trigger. The reconstruction sequence employed in LHCb software can be divided into three distinct steps [161]:

Patter recognition The first step requires identifying patterns in the detector signals (*e.g.* charge deposits over a defined threshold to be identified as hits) generally associated with the passage of a charged particle and associating them to form tracks.

Clone killer An additional step [162] is required in order to identify and discard the duplicate tracks, defined as candidate tracks that share more than 70% of hits. Between the clone tracks, the one with the highest number of hits is retained.

Track fit When a candidate track is available, a Kalman filter [163, 164] is applied to obtain the best estimation of the trajectory of the particle. During this step, correction for multiple scattering and energy loss effects are taken into account.
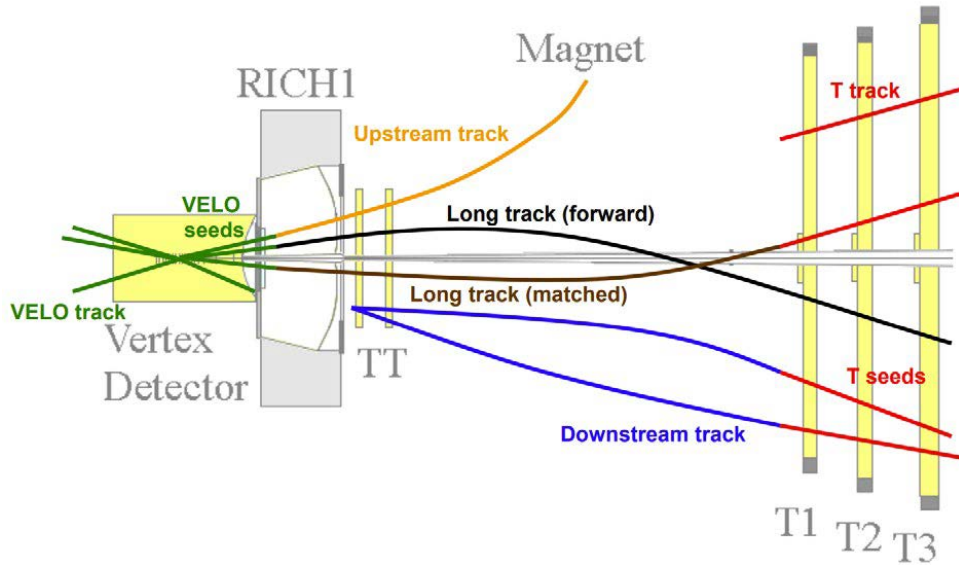
Figure II.2.1: Schematic representation of the track types reconstructable in the LHCb tracking system. Figure adapted from Ref. [166].

While the latter steps are the same for all the tracks, patter recognition algorithms are developed and defined for distinct track families, identified by common characteristics [165] as illustrated in Fig. II.2.1:

VELO tracks Tracks that use measurements from the VELO only. They can be used for vertexing and as starting seed to form longer tracks.

T tracks Tracks that use measurements from the T tracker stations only. They can be used as seed for tracks traversing the tracking stations.

Long tracks Tracks that go through the whole tracking system, most commonly used for physics analyses since they have the most accurate momentum reconstruction, having traversed the entire spectrometer. They can be reconstructed either starting from a VELO seed (forward tracking) or from a T track seed (track matching).

Upstream tracks Tracks that have hits only from the VELO and TT stations. Generally, they are tracks with momentum low enough to be bent out of the acceptance by the magnet.

Downstream tracks Tracks that have hits only in the TT and T tracker stations, generally associated with charged decay products from long-lived neutral resonances.

Each track, in the LHCb software, is represented by a set of state vectors $\vec{s}_i = (x, y, T_x, T_y, q/p)^T$, evaluated at key positions z_i along the trajectory [161] (*i.e.* at the beginning and at the end of each subdetector *competence* region). The state vector parameters consist of the x and y coordinates, the slopes in the $x - z$ and $y - z$ planes and the inverse of the rigidity. The state vectors paired with the covariance matrices from the fit represent the complete knowledge about both the particle trajectory and its uncertainty.

During the execution of the pattern recognition algorithm, a raw estimation of the track momentum, based on its inverse proportionality with respect to the track curvature, can be used to adjust the region to search for hits. While the calculation is extremely fast, it disregards any local field variations and energy loss or multiple scattering effects, giving a rather poor momentum resolution ($\sim 14\%$). The same estimation or, in case of long tracks, the parametrisation obtained from the forward tracking algorithm are used to obtain the starting parameters for the Kalman filter. The final value for the track momentum is obtained from the fit, using the full information from the magnetic field and correcting for material interactions, reaching a resolution from 0.5% to 2% for long tracks with $5 < p < 100$ GeV/c.

The performance of the different pattern recognition algorithms can be studied based on some indicators [165] evaluated on simulations. The indicators are based on the concepts of reconstructability and associated particle

Reconstructability The concept of reconstructability is related to tracks and it is associated to the existence of clusters of hits. A track is reconstructable as a defined type if its number of clusters exceeds the defined thresholds in all the tracking subsystems involved:

  VELO tracks: at least 3 r and 3 ϕ VELO sensors clusters.

  T tracks: at least 1 x and 1 *stereo* cluster in each T station.

  Long tracks: satisfy the VELO and T tracks reconstructibility.

  Upstream tracks: satisfy the VELO reconstructibility and at least 1 cluster in the first two and last two planes of the TT detector.

  Downstream tracks: satisfy the T tracks reconstructibility and at least 1 cluster in the first two and last two planes of the TT detector.

  The track is reconstructed if the corresponding reconstruction algorithm fit succeeds.

Associated particle MC particles and tracks are associated if at least 70% of the hits/clusters on the track are generated by the MC particle, independently for all the tracking subsystems involved. A track is defined as matched if it is associated with at least one MC particle, otherwise it is called a ghost track. In the same way, a MC particle is reconstructed if it is associated with at least one reconstructed track.

The indicators used in the following sections are reported:

Track reconstruction efficiency The track reconstruction efficiency $\varepsilon_{\text{reco}}$ is the fraction of reconstructable MC particle $N_{rec.ble}$ that are actually reconstructed $N_{rec.ble\&rec.ed}$

$$\varepsilon_{\text{reco}} = \frac{N_{rec.ble\&rec.ed}}{N_{rec.ble}}. \tag{II.2.1}$$

The general definition can be adapted to specific cases, where both the numerator and the denominator can be restricted to specific reference sets. An example relevant for the next sections is the track reconstruction efficiency for long tracks

$$\varepsilon_{\text{reco,Long}} = \frac{N_{rec.ble\&rec.ed,Long}}{N_{rec.ble,Long}}. \tag{II.2.2}$$
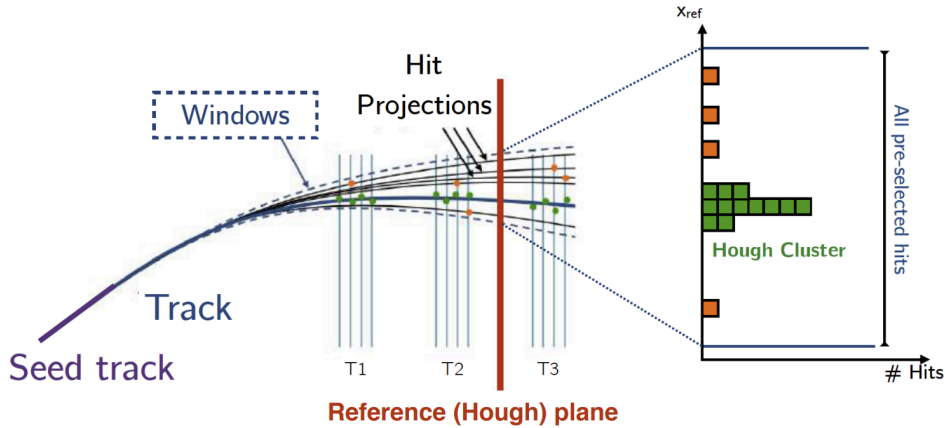
Figure II.2.2: Visual representation of the hit clustering algorithm based on the Hough transform.

The efficiency can be evaluated on data using *tag-and-probe* techniques, where the reconstructable sample is obtained using information from the subdetector not under study while the reconstructed one corresponds to the tracks actually reconstructed. This approach can be used both on data and simulation, allowing for checks on the agreement between the two.

Ghost rate The ghost rate r_{ghost} is the fraction of ghost tracks N_{ghost} among the reconstructed tracks $N_{rec.ed}$

$$r_{ghost} = \frac{N_{ghost}}{N_{rec.ed}}. \tag{II.2.3}$$

II.2.1.1 Standard PatForward algorithm in the OT detector

Given that deuterons are stable particles mainly promptly produced, only the reconstruction algorithms for long tracks have been considered and, in particular, the forward pattern recognition algorithm PATFORWARD [167] has been scrutinised.
Starting from a VELO track operating as seed, the PATFORWARD algorithm combines it with all the measurements obtained from the T stations using a Hough transform [168, 169]. The Hough transform consists in transforming the space of observables (*i.e.* the hits in the detector) to an abstract space, called Hough space, where their mutual distances are small when they are associated to the same particle. This approach exploits the fact that, discarding energy loss and multiple scattering effects, the trajectory of a particle in a magnetic field is completely determined. Knowing the particle direction at one position upstream and one downstream of the magnet, the particle trajectory can be calculated. Technically, for each combination of seed and hit, it calculates the coordinate x, the direction perpendicular to the magnetic field, of the candidate particle trajectory at a fixed $z = 8520$ mm, the Hough plane, and it projects the measurement along the trajectory on the plane. All the hits belonging to the same particle that originated the VELO seed will form a cluster around the same position while projections from random hits will distribute themselves uniformly in the space (Fig. II.2.2).
The focus of the algorithm is on the x component, where the most relevant deflection of the trajectory can be expected, but information from the y component is used to limit the

subdetector region under investigation and to finely tune the final fit. The PATFORWARD algorithm can be divided into four main steps:

Selection of potential x hits Starting from the x planes of the T stations(Sec. I.3.2.1.3), hits compatible with the VELO seed are selected applying loose cuts on the spatial information. In the hypothesis that the magnetic field component is zero in the direction perpendicular to the nominal magnet field, the search window Δy is centred around the intersection y_{centre} of the straight line extrapolation of the VELO seed to the central position $z_{0,\text{plane}}$ of the x plane

$$y_{centre} = y_{\text{VELO seed}} + T_{y,\text{ VELO seed}} \times z_{0,\text{plane}}. \qquad \text{(II.2.4)}$$

In case of OT hits, the t_{TDC} measured by the detector must be converted into a t_{drift} to obtain the hit positions, before performing the selection. Different components concur to the definition of t_{TDC} [93] (Fig. II.2.3):

- the time-of-flight of the particle between the interaction point and the detector t_{TOF};
- the drift time of the ionization cluster inside the straw t_{drift};
- the propagation time of the signal along the wire up to the readout electronics t_{prop};
- the bunch crossing time $T_{collison}$;
- the phase of the clock used by the OT front-end electronics T_{clk}^{FE};
- the delay induced by the front-end electronics t_{FE}.

$$t_{\text{TDC}} = \left(T_{collision} - T_{clk}^{FE} \right) + t_{\text{TOF}} + t_{\text{drift}} + t_{\text{prop}} + t_{FE}. \qquad \text{(II.2.5)}$$

The contributions coming from the electronics and the bunch crossing time can be rearranged as:

$$\left(T_{collision} - T_{clk}^{FE} \right) + t_{FE} = (T_{collision} - T_{clk}) + t_0, \qquad \text{(II.2.6)}$$

where T_{clk} represents the phase of the LHC clock received by the LHCb experiment and t_0 accounts for the drift of the global LHCb clock and for the delays of the front-end electronics. The offset t_0 is evaluated in real-time on data for the global drift contribution, while an offline analysis is performed to correct for the delays in the electronics, for each individual TDC chip. Once t_{TDC} is corrected for the offset and for the variations of the phase of the LHC clock, the reconstruction algorithms extract t_{drift} in the hypothesis, generally true, that the particle moves at the speed of light and considering a straight line trajectory from the interaction point to the middle of the straw

$$t_{\text{drift}} = t_{\text{TOF,corr}} - t_{\text{TOF}}(\beta = 1) - t_{\text{prop}}. \qquad \text{(II.2.7)}$$

The position of the hits are obtained using the TR-relation defined in Eq. I.3.4.

Only hits within the window are further considered, and their position is corrected for small y slopes of the planes using y_{centre}. The same value is also used to further correct t_{drift} for the t_{prop} contribution, in case of OT hits. The selected hits are then
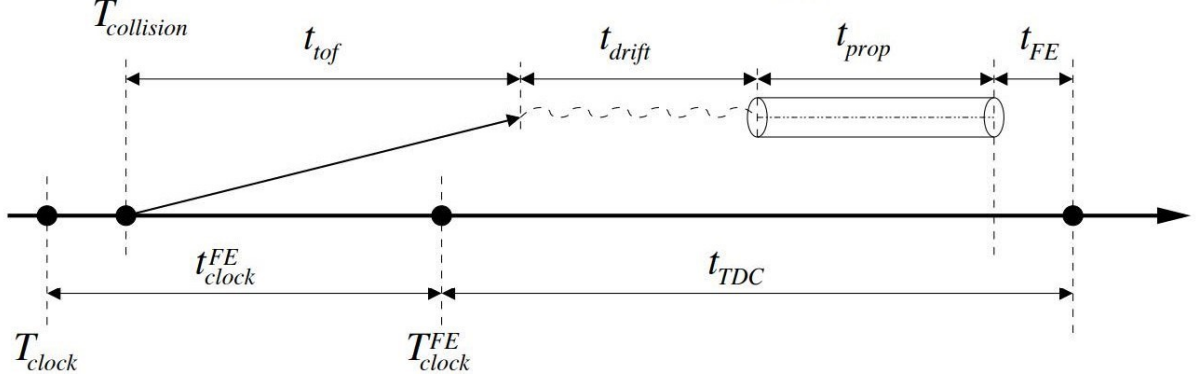
Figure II.2.3: Schematic representation of the contributions to the measured t_{TDC}. Figure adapted from Ref. [93].

projected on the Hough plane, positioned around the middle of the T stations at $z_{ref} = 8520$ mm, to form clusters.

The starting parameters are the state vector of the VELO seed $\vec{s}_V = (x_V, y_V, T_{x,V}, T_{y,V}, q/p_V)^T$ and the hit position (x_{meas}, z_{meas}). Since the first stations of the T tracker are inside the weak fringe field of the magnet, a cubical parametrisation is used to describe the track segment on the $x - z$ plane downstream of the magnet, while a linear one is retained for the $y - z$ plane:

$$
\begin{cases}
x(z) = x_{ref} + B_x \left(z - z_{ref}\right) + C_x \left(z - z_{ref}\right)^2 + D_x \left(z - z_{ref}\right)^3, & \text{(II.2.8.a)} \\
y(z) = y_{ref} + B_y \left(z - z_{ref}\right), & \text{(II.2.8.b)}
\end{cases}
$$

where (x_{ref}, y_{ref}) are the coordinates on the projection plane, to be computed. The parameter B_x correspond to the slope of the tangent to the track at z_{ref}. As shown in Fig. II.2.4, its intersection (x_M, z_M) with the VELO seed identifies the focal plane of the magnet:

$$
B_x = \frac{x_M - x_{ref}}{z_M - z_{ref}} \tag{II.2.9}
$$

An empirical parametrisation [167], based on fits to MC tracks, allows to express all the parameters in terms of z_M and Δ_{slope}, the angle between the VELO seed and the tangent to the track at z_{ref}.

$$
z_M = M_1 + M_2 \Delta_{slope}^2 + M_3 T_{x,V}^2 + M_4 x_{meas}^2 + M_5 T_{y,V}^2, \tag{II.2.10}
$$

$$
x_M = x_V + T_{x,V} z_M, \tag{II.2.11}
$$

$$
\Delta_{slope} = \frac{x_{meas} - x_M}{z_{meas} - z_M} - T_{x,V}, \tag{II.2.12}
$$

$$
C_x = X_1 \Delta_{slope}, \tag{II.2.13}
$$

$$
D_x = X_2 \Delta_{slope}, \tag{II.2.14}
$$

90
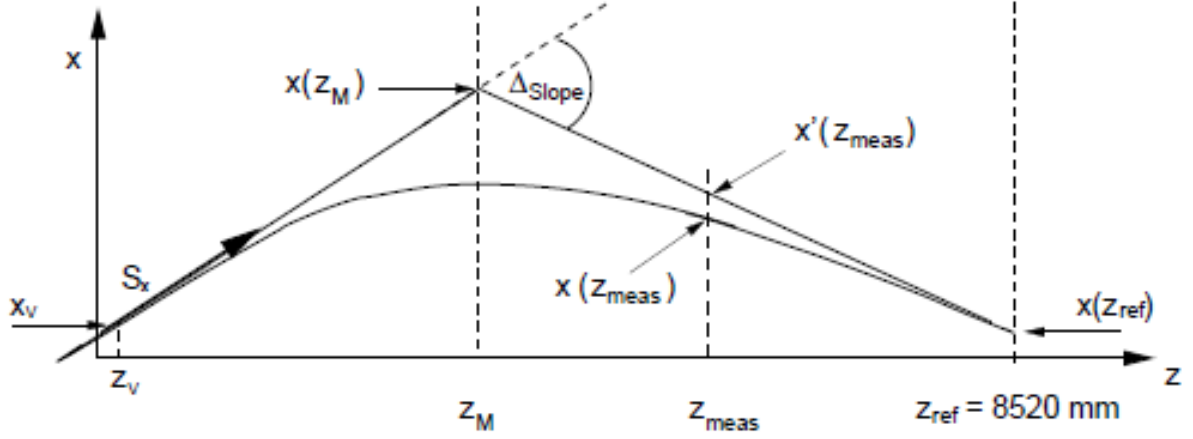
Figure II.2.4: Schematic representation of the relevant quantities used in the track parametrisation for the pattern recognition. Figure taken from Ref. [167].

$$x'_{meas} = x_{meas} - C_x \left(z_{meas} - z_{ref}\right)^2 - D_x \left(z_{meas} - z_{ref}\right)^3, \tag{II.2.15}$$

$$B_y = T_{y,V} + \Delta^2_{slope} T_{y,V} Y_2, \tag{II.2.16}$$

$$x_{ref} = x_M + \left(z_{ref} - z_M\right) \frac{x'_{meas} - x_M}{z_{meas} - z_M}, \tag{II.2.17}$$

$$y_{ref} = y_V + T_{y,V} z_{ref} + \Delta^2_{slope} T_{y,V} Y_1, \tag{II.2.18}$$

where M_1, M_2, M_3, M_4, M_5, X_1, X_2, Y_1 and Y_2 are all fixed from fits to MC tracks. Both z_M and Δ_{slope} depends on each other, thus computation of (x_{ref}, y_{ref}) is performed in two iterations:

$$z_M = M_1 + M_3 T^2_{x,V} + M_4 x^2_{meas} + M_5 T^2_{y,V}, \tag{II.2.19}$$

$$x_M = x_V + T_{x,V} z_M, \tag{II.2.20}$$

$$\Delta_{slope} = \frac{x_{meas} - x_M}{z_{meas} - z_M} - T_{x,V}, \tag{II.2.21}$$

$$z_M = z_M + M_2 \Delta^2_{slope}. \tag{II.2.22}$$

A correction to the hit position, both in terms of y slope of the measurement plane and in terms of t_{prop} when necessary, must be performed prior to the calculation of (x_{ref}, y_{ref}) in order to take into account the small residual component of the magnetic field perpendicular to y, which induce a change in $T_{y,V}$ downstream of the magnet and a consequent correction δy to the y position of the track at the measurement plane.

The search window in the Hough plane is defined to adjust for deviation from the straight line due to the magnetic field. The centre of the search window x_{extr} is the linear extrapolation of the VELO seed to z_{ref}

$$x_{extr} = x_{\text{VELO seed}} + T_{x, \text{ VELO seed}} \times z_{ref}. \tag{II.2.23}$$

Only hits within an aperture Δx around x_{extr} are considered in the clustering algorithm, where Δx is obtained considering the maximum deviation that can be expected from a track in acceptance of the LHCb detectors (*i.e.* with p_T =80 MeV/c and p =1 GeV/c).

Given the list of projected hits, clusters are formed considering all subgroups of hits within a distance $\Delta_{cluster}$

$$\Delta_{cluster} = A + B \left| x_{first} - x_{extr} \right| \tag{II.2.24}$$

where x_{first} is the first hit in the cluster, ordered by projection x_{ref}, and A and B are tunable parameters that take into account that the furtherest clusters from the straight line extrapolation are associated with low momentum tracks and they are expected to be broader. If two or more clusters are overlapping or they are within the distance $\Delta_{cluster}$, they are merged into one.

Fit on the x plane All the clusters found are considered as candidates tracks and they are fitted in an iterative procedure. A first parametrisation of the track, based on the VELO seed and the central hit of the cluster, is performed (Eq. II.2.8-II.2.22) and the hits are corrected accordingly. The fit is then carried out for the deviations $\delta A_x, \delta B_x, \delta C_x$ to the previous parametrisation $A_{x,0}, B_{x,0}, C_{x,0}, D_{x,0}$, considering all the hits in the cluster and x_M as additional constrain:

$$\begin{aligned} x(z) =& (A_{x,0} + \delta A_x) + (B_{x,0} + \delta B_x) (z - z_{ref}) \\ &+ (C_{x,0} + \delta C_x) (z - z_{ref})^2 + D_{0,x} (z - z_{ref})^3 . \end{aligned} \tag{II.2.25}$$

The fit procedure is iterated up to 10 times, updating the starting parameters after each iteration, until the fitted deviations drop below defined thresholds. The contribution of each hit to the χ^2 is then evaluated and, if any contribution exceed 20, the hit with the highest χ^2 contribution is removed and the fit procedure reiterated. When no contribution exceeds the limit on χ^2, the track candidate is accepted. If the number of hits in the cluster drops below a threshold during the outlier removal iterations, the candidate is discarded.

Selection of potential stereo hits The newly obtained track candidates are used as seeds to search for compatible hits in the stereo planes of the T stations (Sec. I.3.2.1.3), using a similar approach as for the x planes. The track parametrisation is firstly extrapolated to the u and v planes and the compatibilities in the y direction with the geometrical acceptance of the planes are checked. The stereo measurements are transformed in x information based on the track parametrisation:

$$\begin{cases} y = \dfrac{A_y - B_y (z_{ref} - z_{plane})}{1 - B_y dz/dy_{\text{plane}}}, & \text{(II.2.26.a)} \\[2ex] z_{meas} = z_{plane} + dz/dy_{\text{plane}} y, & \text{(II.2.26.b)} \\[1ex] x_{meas} = \text{stereo}_{meas} + \tan\left(\alpha_{tilt}\right) y. & \text{(II.2.26.c)} \end{cases}$$

The newly obtained x_{meas} are then selected if they are within a tolerance window Δx_{stereo} to x_{extr}, defined using the rigidity information p/q extracted from the track.

$$\Delta x_{stereo} = a + b \left(\frac{q}{p} \right)^2 \tag{II.2.27}$$

The clusters are then selected applying the same algorithm used for the x planes and the best candidate, in terms of number of hits in different planes, is selected.

Fit on the x and y plane As final step, a fit of the track considering the new cluster is performed, separately for the $x - z$ and $y - z$ planes. Firstly, the procedure described for the fit on the x plane is applied including the x information from the stereo hits. Then, the y components of the stereo hits are linearly fitted to update the y parametrisation. All the hits associated with the track are then updated and the fit procedure on the y plane is repeated up to 10 times, until the deviations between iterations are lower than the thresholds. Finally, the outlier removal step is applied to the stereo hits until the candidate track is discarded or the contribution to the χ^2 of all the hits are below the defined threshold.

The track candidates obtained are filtered based on a quality variable Q, defined combining the deviation Δy between the VELO seed and the track candidate in the T stations, the χ^2/ndf and the momentum of the track, using a neural network algorithm [170] tuned on good quality tracks in data.

Only tracks with $Q \in [Q_{min}; Q_{min} + 1]$ and a number of hits in the T station in $N_{\text{Thits}} \in [N_{\text{Thits; max}} - 2; N_{\text{Thits; max}}]$ are persisted in the track collection for the following step in the reconstruction, that is the association of the hits coming from the TT stations, performed with simplified procedure based on the one described above.

When all VELO seed have been investigated, the persisted tracks are filtered in the clone killer step and fitted with the Kalman filter procedure. If OT hits are associated with the track, before the fit their position is corrected for the time-of-flight along the track trajectory, in the hypothesis of $\beta = 1$.

II.2.1.2 PatForward algorithm performance

The performance of the PATFORWARD algorithm has been studied in terms of track reconstruction efficiency on a MC simulation. Since nuclei are not generated in the standard LHCb simulation, a privately produced sample consisting of 10 million simulated $p\text{He}$ collisions enriched with deuterons, both from spallation and from coalescence, has been used. Generated minimum-bias events ($p > 500$ MeV/c, $p_\text{T} > 100$ MeV/c, $\eta \in [1.5; 5.5]$) are used as input for a coalescence afterburner and only events with at least one coalesced light nucleus are accepted. The generator QGSJETII04 [145] has been favoured over EPOS-LHC [112] because it contains the spallation contribution and it better reproduces the antinucleons production spectra [171]. The deuteron-to-background in this simulated sample is enhanced with respect to an unbiased sample, but it gives enough statistics to test and understand the algorithm performance in realistic events. The generated particles are then decayed using EVTGEN and their interactions with the detector material are described using the GEANT4 toolkit [114, 115].

Figure II.2.5 shows the track reconstruction efficiency $\varepsilon_{\text{reco,Long}}$ of the PATFORWARD algorithm for long tracks in the low momentum region ($p < 8$ GeV/c), separately for π, K,
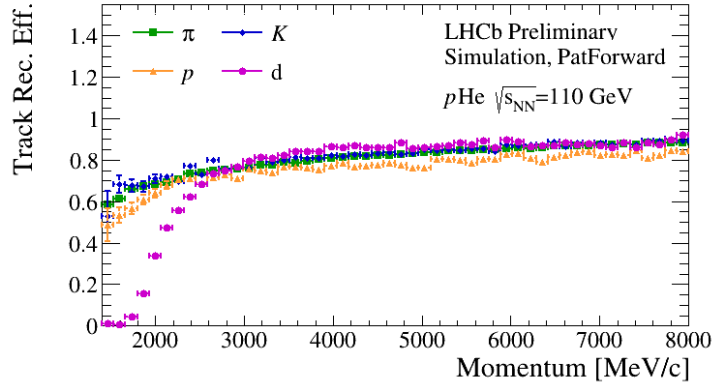
Figure II.2.5: Track reconstruction efficiency of the PATFORWARD pattern recognition algorithm as a function of the momentum for long reconstructible particles; the efficiencies for π (green square), K (blue diamond), p (yellow triangle) and d (purple dot) are reported separately.

p and d. While for p higher than 6 GeV/c a rather flat efficiency around 90% is reached by all particles, moving towards lower momenta a clear decreasing trend is observed, the worse the heavier the particle. Deuterons represent the extreme case, where a complete inefficiency is found for momenta lower than 2 GeV/c.

The inefficiency in the track reconstruction for low momentum deuterons can be explained because the hits, reconstructed in the wrong position as detailed in Sec. II.1.2, does not form a cluster to be associated to a VELO seed or they are excluded because of the high χ^2 contribution during the fit. The tracks are therefore discarded because they do not satisfy the quality checks required during the reconstruction.

A modified reconstruction algorithm is thus necessary in order to take into account and correct the hit positions for the right time-of-flight already from the pattern recognition step.

II.2.2 Time-of-flight based reconstruction algorithm

The PATFORWARD algorithm inefficiency at low momentum arises from two main effects:

- the tracks are not reconstructed because, due to the error in the hit position, there are not enough hits associated to them. These tracks can be lost as soon as the first step in the PATFORWARD algorithm;

- the tracks are discarded because, due to the error in the hit position, the χ^2 from the fit is too high. These tracks are discarder after the fit step or at the final quality selection in the PATFORWARD algorithm.

In order to recover the inefficiency, then, the reconstruction algorithm must be modified to correctly associate all the possible hits compatible with the track before the fit step and to correct the hit positions for the right time-of-flight to improve the χ^2 from the fit. While introducing β as a free parameter in the track fit would give the best estimate to the time-of-flight, it would require deep modification in the LHCb event model and it would not allow to recover the hits lost before the fit step. An iterative approach is therefore

chosen for the modified algorithm called TOFFORWARD, testing different β hypotheses and selecting the value providing the best track quality.

The correction of the time-of-flight considering the value of β under study is performed multiple time during the algorithm in order for it to be efficient. A first correction is applied during the selection of potential x hits. Since no parametrisation is available for the track, a straight line from the interaction point to the hit $(x_{hit}, y_{hit}, z_{hit})$ is considered:

$$t_{\text{TOF}} = \frac{\sqrt{x_{hit}^2 + y_{hit}^2 + z_{hit}^2}}{\beta c} \qquad \text{(II.2.28)}$$

When a parametrisation is available, an additional correction Δt_{TOF} is applied, in order to take into account the correction ΔL to the straight line L_0 due to magnetic field kick:

$$L_0 = \sqrt{x_{hit}^2 + y_{hit}^2 + z_{hit}^2}, \qquad \text{(II.2.29.a)}$$

$$\Delta L = \frac{z_{hit} - z_{M,0}}{2 z_{M,0}} \left(T_{x,\text{hit}} - x_{hit}/z_{hit}\right)^2 L_0, \qquad \text{(II.2.29.b)}$$

$$\Delta t_{\text{TOF}} = \frac{\Delta L}{\beta c}, \qquad \text{(II.2.29.c)}$$

where $z_{M,0}$ is the nominal position of the centre of the magnet along the longitudinal direction and $T_{x,\text{hit}}$ is the slope of the track at the hit position. The correction Δt_{TOF} is re-evaluated whenever a new parametrisation is available, in particular before and after each fit step.

Finally, the PATFORWARD algorithm quality variable has been tuned and optimise for the original physics case of the LHCb experiment, thus the quality is maximised for high momentum tracks. A simple selection based on the χ^2 is thus preferred for the TOFFORWARD algorithm, in order not to bias the track selection towards high β candidates. The value of β obtained from this procedure is propagated to the track fit step in the reconstruction, where the position of the hits is corrected a final time for the time-of-flight along the trajectory.

Technically, the execution of the iteration in the TOFFORWARD algorithm is preceded by an initial step, called *pre-loop*, where the PATFORWARD algorithm is performed without using information from the t_{drift} for the hits in the OT detector: the hit position along the x direction are associated with the centre of the straw with an uncertainty equal to the radius. In this way, no bias due to the imprecise time-of-flight correction is introduced and all the possible hits associated with VELO seed are identified if present. As a consequence, a first selection on the VELO seeds can be performed, identifying the ones that can be reasonably associated with at least one cluster. Moreover, for the VELO seeds associated with clusters without any OT hits, the standard PATFORWARD algorithm can be run.

For the VELO seeds that passed the *pre-loop* selection, the TOFFORWARD algorithm is iterated multiple times testing β values from $\beta = 1$, corresponding to the standard reconstruction, down to a minimum value β_{min} corresponding to the maximum mass M_{max} hypothesis considered for the candidate track:

$$\beta_{min} = \frac{1}{\sqrt{1 + \frac{M_{max}^2}{p^2}}} \qquad \text{(II.2.30)}$$

Table II.2.1: Parameters uesed for the TOFFORWARD algorithm, reconstructing isolated deuterons (left) and the QGSJETII04 simulated sample (right).

	Isolated deuterons MC	QGSJETII04 MC
M_{max}	3727 MeV/c^2	3727 MeV/c^2
β_{step}	0.01, 0.05 and 0.1	0.05

Figure II.2.6: Comparison of the track reconstruction efficiency of the PATFORWARD pattern recognition algorithm (blue) and of the TOFFORWARD pattern recognition algorithm without the *pre-loop* step (orange) and with the *pre-loop* step (green) as a function of the momentum for long reconstructible isolated deuterons.

The value of momentum p is obtained as the average of the momentum of the candidate tracks obtained during the *pre-loop*. The granularity of the steps with which the β range is tested is chosen by the user. The loop is stopped when the best χ^2 obtained at the end of each iteration does not improve for two consecutive steps.

II.2.3   Results

The TOFFORWARD algorithm has been first tested on a simulation sample consisting of 275 thousand isolated deuterons generated with a flat distribution both in momentum and in pseudorapidity, in the intervals $p \in [1.5, 15]$ GeV/c, $\eta \in [2; 5]$. The sample allows to perform a first level optimisation of the algorithm, working in a background-free environment to easily identify and solve the main problems. The parameters used for TOFFORWARD are summarised in Tab. II.2.1, left column.

The main metric considered for performance evaluation is the track reconstruction efficiency, as defined in II.2.2. In Fig. II.2.6 the reconstruction efficiency of the PATFORWARD algorithm is compared to the one for TOFFORWARD, considering an implementation with and without the *pre-loop* step. A clear improvement in the track reconstruction efficiency is obtained with the implementation of the correction of the time-of-flight. The introduction of the *pre-loop* does not affect the reached reconstruction efficiency, but it allows to reduce the execution time of the TOFFORWARD algorithm by a factor 3. Considering the impact of the granularity of the β steps, a comparison
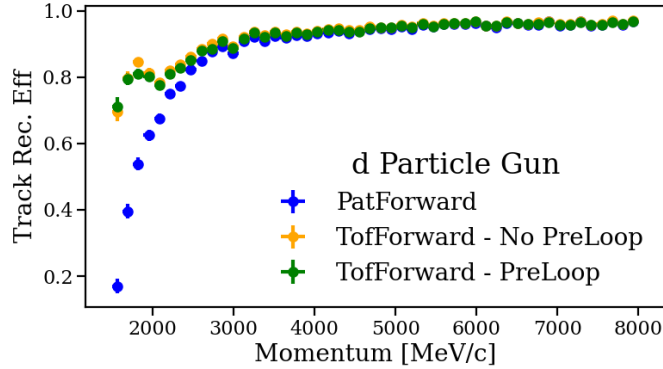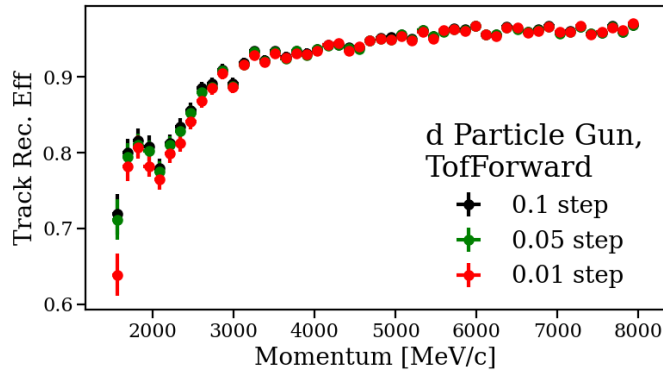
Figure II.2.7: Comparison of the track reconstruction efficiency of the TofForward pattern recognition algorithm for three dimensions for the step in the β loop (0.1 in black, 0.05 in green and 0.01 in red) as a function of the momentum for long reconstructible isolated deuterons.

Figure II.2.8: Comparison of the β resolution of the TofForward pattern recognition algorithm for three dimensions for the step in the β loop (0.1 in black, 0.05 in green and 0.01 in red) as a function of the momentum for long reconstructible isolated deuterons.

Figure II.2.9: Comparison of the number of iterations required to reconstruct a long isolated deuteron track with the TofForward pattern recognition algorithm for three dimensions for the step in the β loop (0.1 in black, 0.05 in green and 0.01 in red).
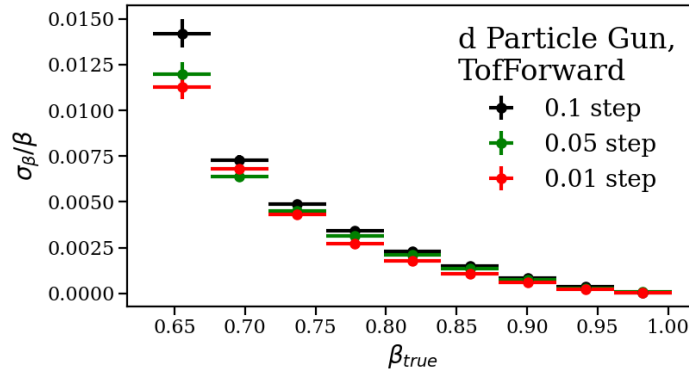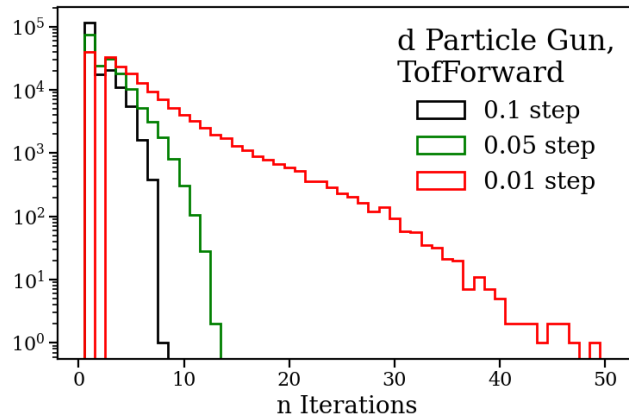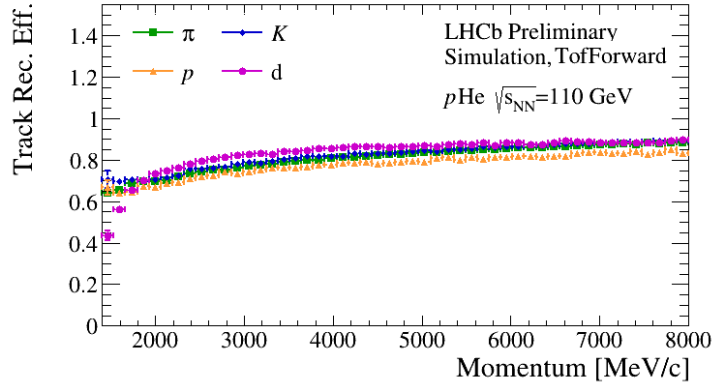
Figure II.2.10: Track reconstruction efficiency of the TofForward pattern recognition algorithm as a function of the momentum for long reconstructible particles; the efficiencies for π (green square), K (blue diamond), p (yellow triangle) and d (purple dot) are reported separately.

between three possible step dimensions (0.1, 0.05, 0.01) is shown in Fig. II.2.7. No significant difference is observed. As can be seen in Fig. II.2.8, an improvement in the performance in terms of β resolution is obtained from a finer granularity but at the cost of a much higher execution time, as can be seen from Fig. II.2.9, where the number of iterations needed to reconstruct the tracks is reported for the different step dimensions. Considering that the focus of the algorithm is on the reconstruction and not on the PID, an intermediate step is chosen as a compromise between timing and resolution.

Finally, the same MC simulation described in II.2.1 has been used to compare the performance of the PatForward and the TofForward algorithms on realistic events. The parameters used for TofForward are reported in Tab. II.2.1, right column. In Fig. II.2.10 the track reconstruction efficiency as a function of the momentum is shown for π, K, p and d for the TofForward algorithm, and in Fig. II.2.11 the comparison between the two algorithm is presented separately for each species. While for pions and kaons no difference in the efficiency is observed, as it was expected since in both cases their speed is close to c even for low momenta, the efficiency is clearly improved for both low-momentum protons and deuterons with the TofForward algorithm, in the region where a time-of-flight based identification is expected to be more performing. In particular, deuterons with momentum lower than 2 GeV/c, previously not reconstructed, are recovered. The performance in terms of momentum resolution and ghost rate are also considered. From Fig. II.2.12 it is clear that the momentum resolution remains unchanged for all the particle species. Indeed, at momenta lower than 6 GeV/c, where the correction due to the time-of-flight begins to be relevant for deuterons, the multiple scattering dominates the momentum resolution and no improvement can be expected from a more precise determination of the track absolute position. The uncertainty on β, which is driven by the alignment of OT hits rather than their absolute position, is found to be uncorrelated with the momentum uncertainty. In the same way, considering the ghost rate as a function of the multiplicity, measured using the number of primary vertices (Fig. II.2.13, left) or the number of reconstructed tracks (Fig. II.2.13, right), no significant increase in the ghost rate is observed. The improvement in reconstruction efficiency, therefore, does not imply a poorer reconstruction quality.
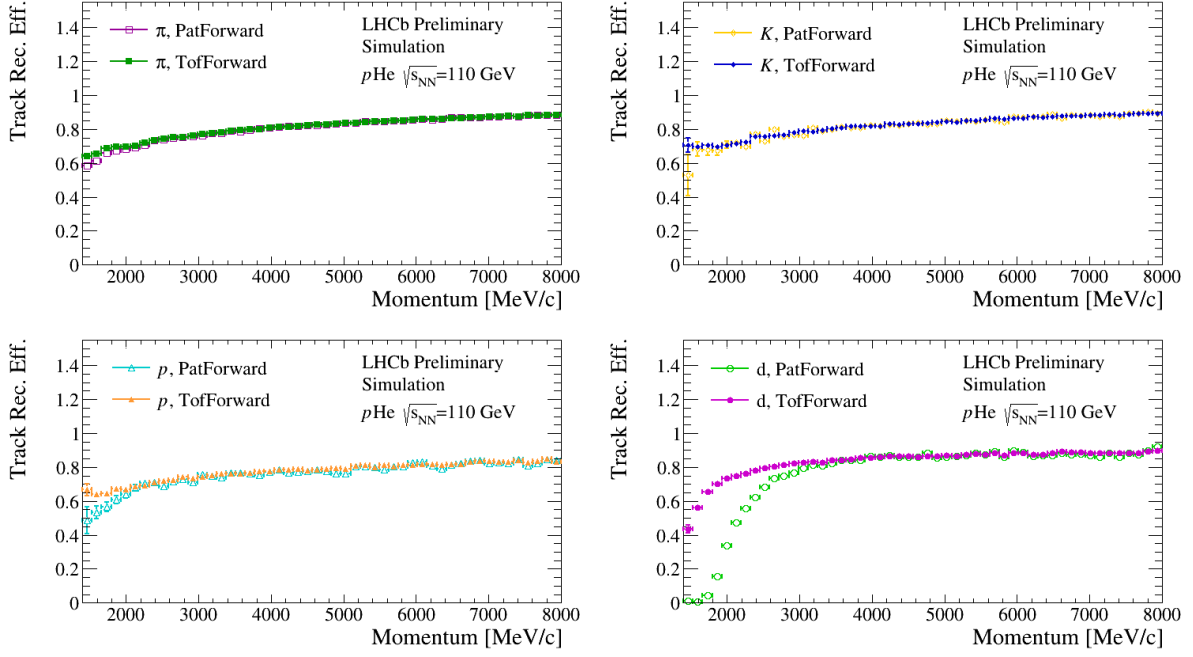
Figure II.2.11: Track reconstruction efficiency as a function of the momentum for pions (top left), kaons (top right), protons (bottom left) and deuterons (bottom right); the efficiencies of the TOFFORWARD pattern recognition algorithm (full markers) and of the PATFORWARD pattern recognition algorithm (empty markers) are compared.
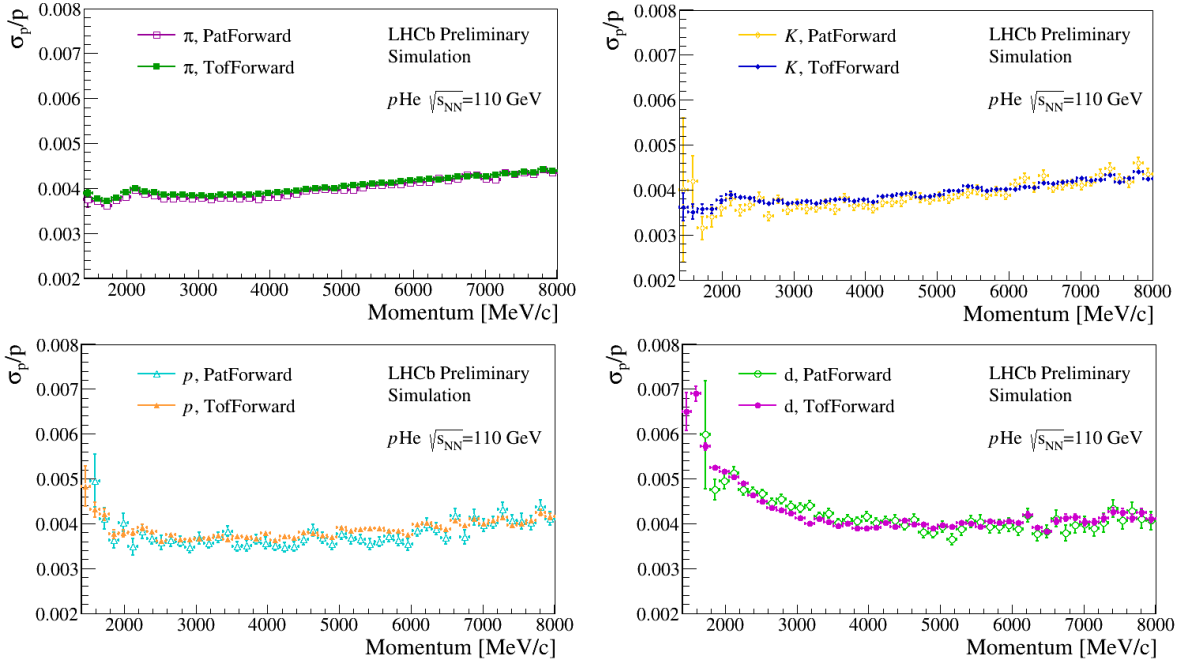
Figure II.2.12: Momentum resolution as a function of the momentum for pions (top left), kaons (top right), protons (bottom left) and deuterons (bottom right); the resolution of the TOFFORWARD pattern recognition algorithm (full markers) and of the PATFORWARD pattern recognition algorithm (empty markers) are compared.
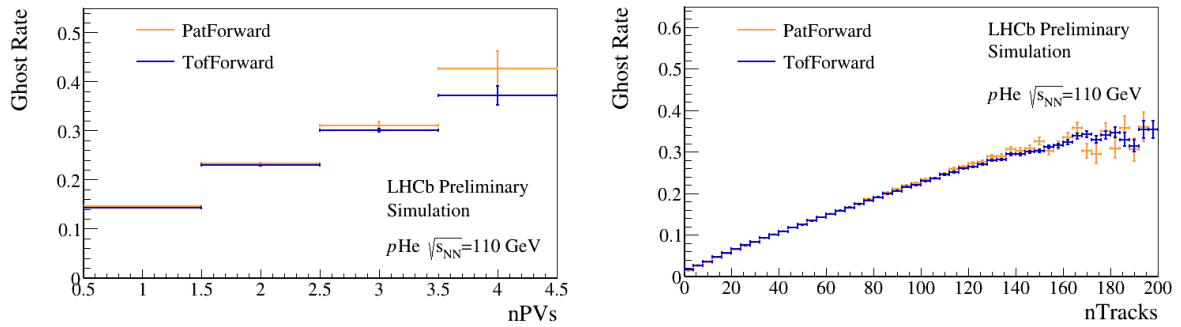
Figure II.2.13: Comparison of the track ghost rate as a function of the multiplicity, evaluated considering the number of primary vertices (left) or reconstructed tracks (right) in the event, for the TOFFORWARD pattern recognition algorithm (blue markers) and the PATFORWARD pattern recognition algorithm (orange markers).

II.3 Time of Flight particle identification

The time-of-flight based particle identification technique is presented in this chapter. After a detailed description of the algorithm employed to reconstruct the β of the candidate tracks in Section II.3.1, the performance is studied both on MC simulation and on data, in Section II.3.2.1 and Section II.3.2.2, respectively. Finally, the results are shown in Section II.3.3 for 10% of the pHe $\sqrt{s_{NN}}$ =110 GeV data sample.

II.3.1 Time-of-flight based particle identification

The particle identification technique used at the LHCb experiment mostly relies on the RICH system. Although a certain degree of discrimination to identify deuterons is in principle available, it is still not sufficient to separate the signal from the background of misidentified lighter particles. The available tool to perform a time-of-flight-based identification, on the other hands, shows good potentialities but it is biased by the error made in the hit position determination. A new tool, called TRACKBETATOOL, has thus been developed to reconstruct the β of the particle candidates and perform the PID combining it with the reconstructed momentum.

Each track candidate obtained from the reconstruction algorithm contains the raw information of the hits associated to it. It is thus possible to perform again the Kalman fit step to optimise the track parametrisation. In the TRACKBETATOOL the β is introduced as an additional fixed parameter in the Kalman fit: an iterative procedure is implemented to test different β hypotheses, recomputing the hits radial distance at each step for the time-of-flight along the trajectory (Eq. II.2.29).

Since the β reconstruction heavily relies on the time information coming from the OT hits, a first quality filter is applied, selecting only tracks with a minimum number of OT hits $nOT_{hit,min} = 15$. The candidates for which no reliable information on the time-of-flight can be extracted are excluded. Tracks with momentum higher than $p_{max} = 10$ GeV/c are also discarded because no mass discrimination is expected for the particle species of interest.

The iterative procedure is initialised in the hypothesis of a kaon track. The choice is made because it is the lighter particle for which effects from the time-of-flight correction could be expected in the track fit. The Kalman fit is then performed correcting the hits position for the time-of-flight along the trajectory for the β under study. No outlier removal is performed in order to evaluate the quality of the fit for different β hypotheses

considering the same hits every time. The additional timing information coming from the M1 muon station is added to the track with the purpose to increase the PID discrimination. Positioned between RICH2 and the calorimeters, it is expected to give a signal with all the reconstructed tracks with a time resolution σ_{M1}^2 between 3 and 4 ns. The track is extrapolated to the M1 station and the time residuals between the expected arrival time $t_{\text{TOF,M1}}$, evaluated for the β under study, and the time t_{M1} of the hits geometrically compatible with it are calculated and added to the χ_{Kalman}^2 from the Kalman fit:

$$\chi_{\text{fit}}^2 = \chi_{\text{Kalman}}^2 + \frac{(t_{\text{M1}} - t_{\text{TOF,M1}})^2}{\sigma_{\text{M1}}^2} \qquad (\text{II.3.1})$$

At the end of every step the new β to be tested is determined through a gradient descend algorithm based on the χ_{fit}^2 change. Given $\left(\beta_{old}; \chi_{\text{fit, old}}^2\right)$ and $(\beta; \chi_{\text{fit}}^2)$, respectively the previous and current step parameters, the β_{new} of the following step is defined for a learning rate γ as:

$$\beta_{\text{new}} = \beta - \gamma \frac{\chi_{\text{fit}}^2 - \chi_{\text{fit, old}}^2}{\beta - \beta_{\text{old}}} \qquad (\text{II.3.2})$$

The fit is performed up to 20 times, until the difference in the χ^2 or in the β between two consecutive steps decreases below defined thresholds value. The algorithm is also stopped if the β_{min} value, as defined in Eq. II.2.30, is reached. The convergence is usually reached within 5 to 10 steps.

Once the iterative procedure is finished, the best value of the speed β_{fit} and its uncertainty are obtained through a parabolic fit around the minimum of the χ^2 profile. Finally, the track is fitted again in the Kalman filter for the final value β_{fit}. Any remaining outliers are removed and the fit is reiterated, in order to eliminate possible ghost tracks.

II.3.2   Performance and systematic studies

II.3.2.1   Performance on MC simulation

The PID performance has been studied on events from the QGSJETII04 simulation reconstructed using the TofForward algorithm. All tracks for which the iterative fit converges with an the error σ_β on β_{fit} lower than 0.06 are selected.

Figure II.3.1 shows the difference with respect to 1 of β_{fit}, multiplied by the track charge q, as a function of the reconstructed momentum for different particle species. The distributions follow the expected relations (Eq. II.3.3), overlaid as solid curves, for all the species considered.

$$q * (1 - \beta) = 1 - \frac{p}{\sqrt{p^2 + M^2}} \qquad (\text{II.3.3})$$

The production of particle at low momenta from spallation of the helium target is also clearly distinguished as an asymmetry between particle and antiparticle population in the proton and deuteron distributions. Combining β_{fit} with the momentum of the track, the
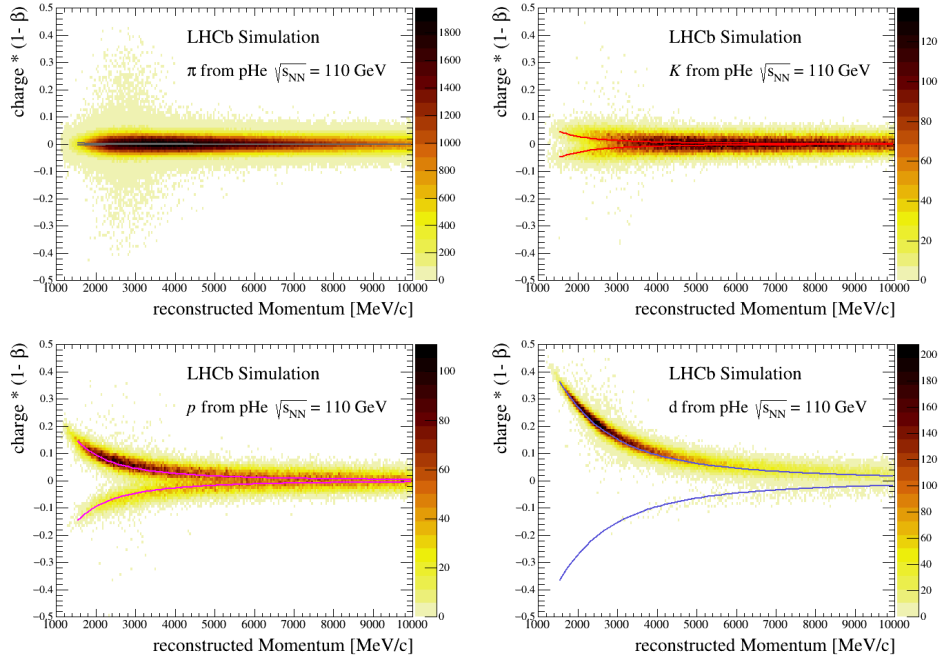
Figure II.3.1: Difference with respect to 1 of the reconstructed β_{fit}, multiplied by the particle charge, as a function of the reconstructed momentum for four particle species in the simulated sample: pions (top left), kaons (top right), protons (bottom left) and deuterons (bottom right). The overlaid curves show the expected relations. Production of low-momentum protons and deuterons is dominated by spallation of the He target.

reconstructed mass M_{rec} is obtained as

$$M_{\mathrm{rec}} = p_{\mathrm{rec}}\sqrt{\frac{1}{\beta_{fit}^2} - 1} \qquad (\text{II.3.4})$$

A comparison between the TRACKBETATOOL and the track time technique is performed considering candidates with $p < 3$ GeV/c. The peak corresponding to the deuteron candidates is well separated from the background population in the distribution of M_{rec} (Fig. II.3.2, left). In the track time tool (Fig. II.3.2, right), on the other hands, the distributions are more overlapped preventing an efficient separation, even though an increasing trend can be distinguished for the centroids of the different species.

As it is expected, the precision on the β determination increases for slow tracks. In Fig. II.3.3, the error σ_β on β_{fit} is reported as a function of the real β of the particle, where the difference in the covered region in β is due to the fact that the same momentum range is considered for particles with different masses. The same trend is observed for all the species. When the distribution is considered as a function of the particle momentum p (Fig. II.3.4), σ_β shows a certain separation power between deuterons and lighter particles, in particular in the low momentum region, which can be exploited for a cut-based selection. Since in real data deuterons are expected to be suppressed by a factor 10^{-3} with respect to the enriched simulation sample, tighter cuts are applied and, in particular, only tracks with $\sigma_\beta < 0.02$ and $\chi^2_{\mathrm{OT\ hits}}/\mathrm{ndf} < 2$ are selected. In Fig. II.3.5, top, a comparison of the efficiency on the deuteron signal of the loose and tight cuts is reported as a function of the candidate momentum. The efficiency for the tight cut is also shown for the different
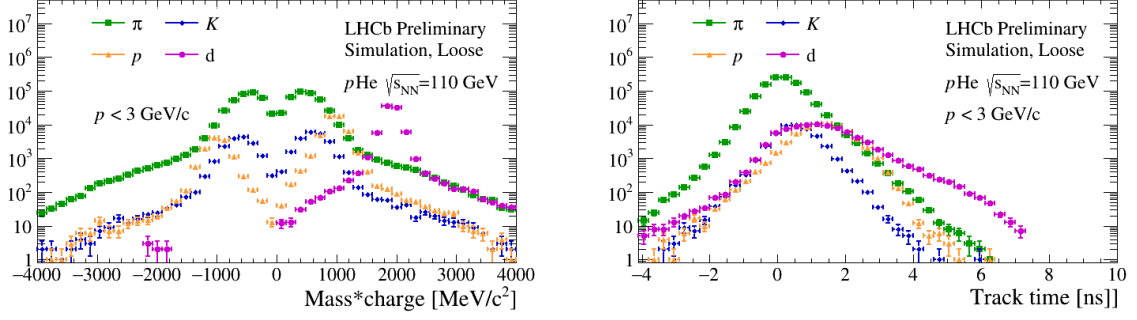
Figure II.3.2: Left: distribution of the reconstructed mass, multiplied by the particle charge, for four particle species in the simulated sample. Right: distribution of track time (as defined in Sec. II.1.1) for four particle species. The particle species considered are pions (green square), kaons (blue diamond), protons (yellow triangle) and deuterons (purple dot).

Figure II.3.3: Profile distribution of σ_β as a function of the particle β for four species in the simulated sample: pions (green square), kaons (blue diamond), protons (yellow triangle) and deuterons (purple dot).

species as a function of the reconstructed mass in Fig. II.3.5, bottom. While the tighter cut presents a lower efficiency compared to the loose cut for deuterons especially for momenta higher than 3 GeV/c, it shows a good rejection power for lighter particles, in particular for pions and kaons, where the rejection is higher than 50% in most of the range. This allows to reject the main background, coming from the long non-Gaussian tails in the reconstructed β for pions and kaons at low momentum, probably due to the effect of multiple scattering. Overall, the selection allows suppressing light particles where the reconstructed β value is largely underestimated, isolating the signals of protons and deuterons.

Finally, the pulls on the reconstruction of β are studied to identify possible systematics. In Fig. II.3.6 the distribution of the pulls for π, K, p and d are shown in 4 bins of momentum, while Fig. II.3.7 reports the mean value (top) and the width (bottom) of the distributions as a function of the momentum. The distributions present a Gaussian shape and the widths are distributed around 1, confirming a correct estimation of the uncertainty on β. The mean values on the other hand show a clear bias in the estimation of β. The value is systematically underestimated, in particular at high momentum ($p > 3$ GeV/c), and the
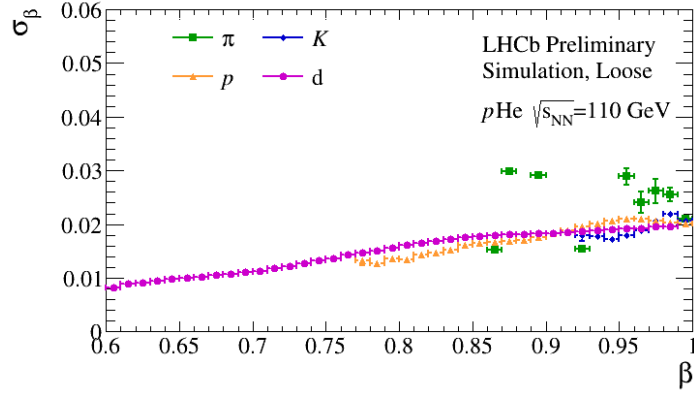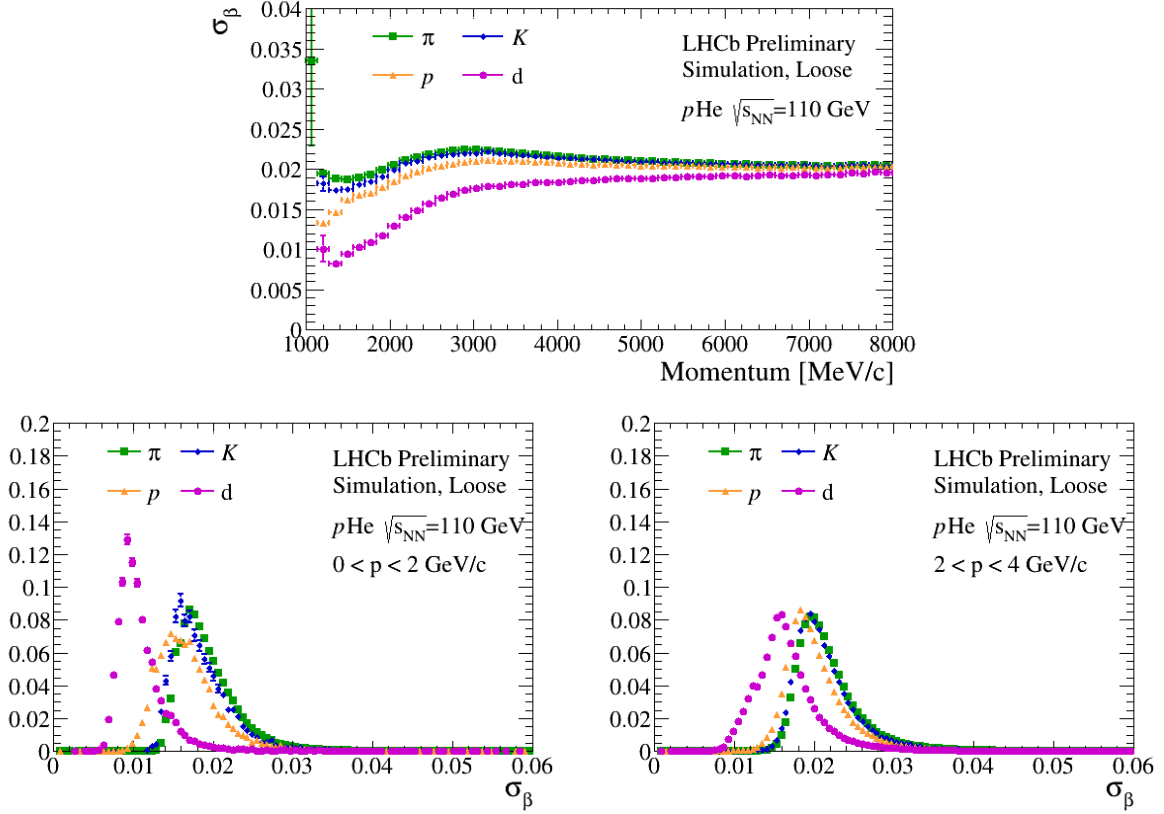
Figure II.3.4: Profile distribution of σ_β as a function of the particle p for four species in the simulated sample: pions (green square), kaons (blue diamond), protons (yellow triangle) and deuterons (purple dot). The distribution in two bins of momentum are also shown in the bottom row.

effect is independent of the species considered. The trajectory length considered calculating the time-of-flight for each track is obtained applying the magnetic field kick correction to the straight line hypothesis, which is demonstrated to be an over-approximation of the true value. A correction coefficient, obtained from simulations, is taken into consideration to compensate for it, but residual effects would bias the β reconstruction. Moreover, the time-of-flight correction is calculated considering a track originating from the nominal interaction point. While this approximation is in general valid for beam-beam interactions, in the case of beam-gas interactions this is not true since the gas is uniformly spread inside the whole beam pipe (Sec. I.4.2). The two effects coupled can be at the origin of the observed bias and they will require additional studies to be fully understood and corrected.

II.3.2.2 Performance on the pHe $\sqrt{s_{\mathrm{NN}}} =110$ GeV data sample

The TRACKBETATOOL has been tested on about 10% of the pHe $\sqrt{s_{\mathrm{NN}}} =110$ GeV data sample, reconstructed using the TOFFORWARD tool.

In order to check its performance on data, two clean samples of pions and protons are selected, respectively from $K_S^0 \to \pi^+\pi^-$ and from $\Lambda \to p\pi^- +$ cc (Fig. II.3.8, left and right), where the true beta β_{true} is known from the momentum.
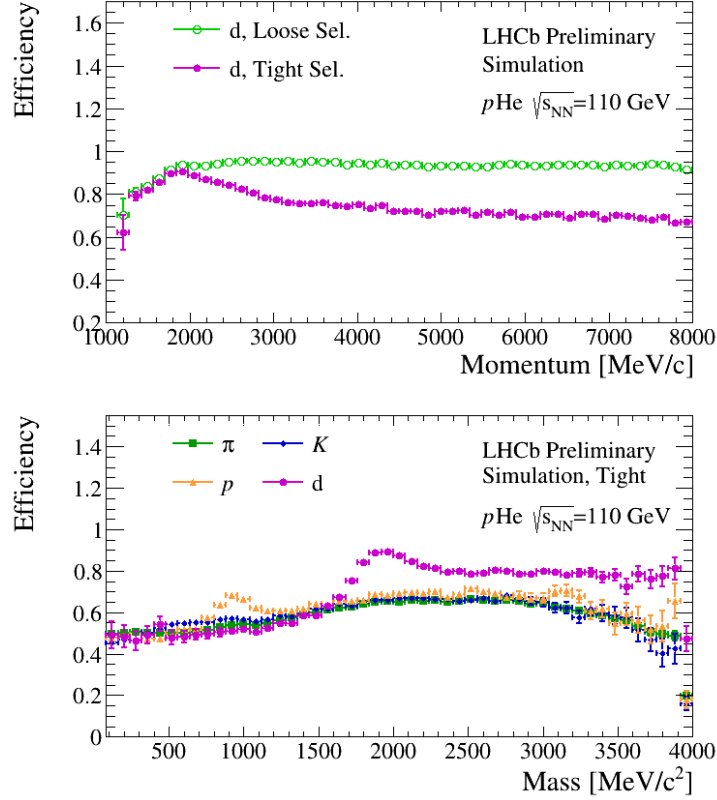
Figure II.3.5: Top: selection efficiency of the loose (empty green dot) and tight (full purple dot) cuts as a function of the momentum for deuterons in the simulation. Bottom: selection efficiency of the tight cuts as a function of the reconstructed mass for four particle species: pions (green square), kaons (blue diamond), protons (yellow triangle) and deuterons (purple dot).

Events with a reconstructed primary vertex in the $z \in [-700; 100]$ mm are considered. High quality reconstructed particles ($\chi^2_{Long}/ndof < 5$) are combined to form a Λ or a K^0_S if their χ^2_{DOCA} (*i.e.* their distance of closest approach divided by the uncertainty on its measurement) is lower than 10 and the quality of the decay vertex reconstructed from the pair is sufficient ($\chi^2_{\mathrm{vtx}} < 16$). The pair is then selected if the reconstructed invariant mass is within 50 MeV/c^2 from the nominal value. In order to eliminate the combinatorial background due to random association between two tracks, cuts on the final-state particles detachment with respect to the primary vertex are required ($\chi^2_{\mathrm{IP}} > 5$), to take into account the parent flight distance before the decay, as well as stringent requirements on the compatibility of the primary vertex with the beam line.

Due to kinematic constrains of the decay, only protons with momentum higher than 5 GeV/c are reconstructed and selected. Pions, on the other hand, cover the complete momentum range between 1 GeV/c and 40 GeV/c. The β_{true} for both particles is thus expected to be always higher than 0.98.

The distributions of β and its uncertainty as a function of p are compared to the results obtained on the simulation. As it can be seen in Fig. II.3.9, the bias observed in the simulation is accentuated in data both for pions and for protons. The effect is clearly visible in the momentum range of interest for the time-of-flight measurement ($p < 8$ GeV/c for protons and $p < 6$ GeV/c for pions) (Fig. II.3.10, left), while it gets negligible at
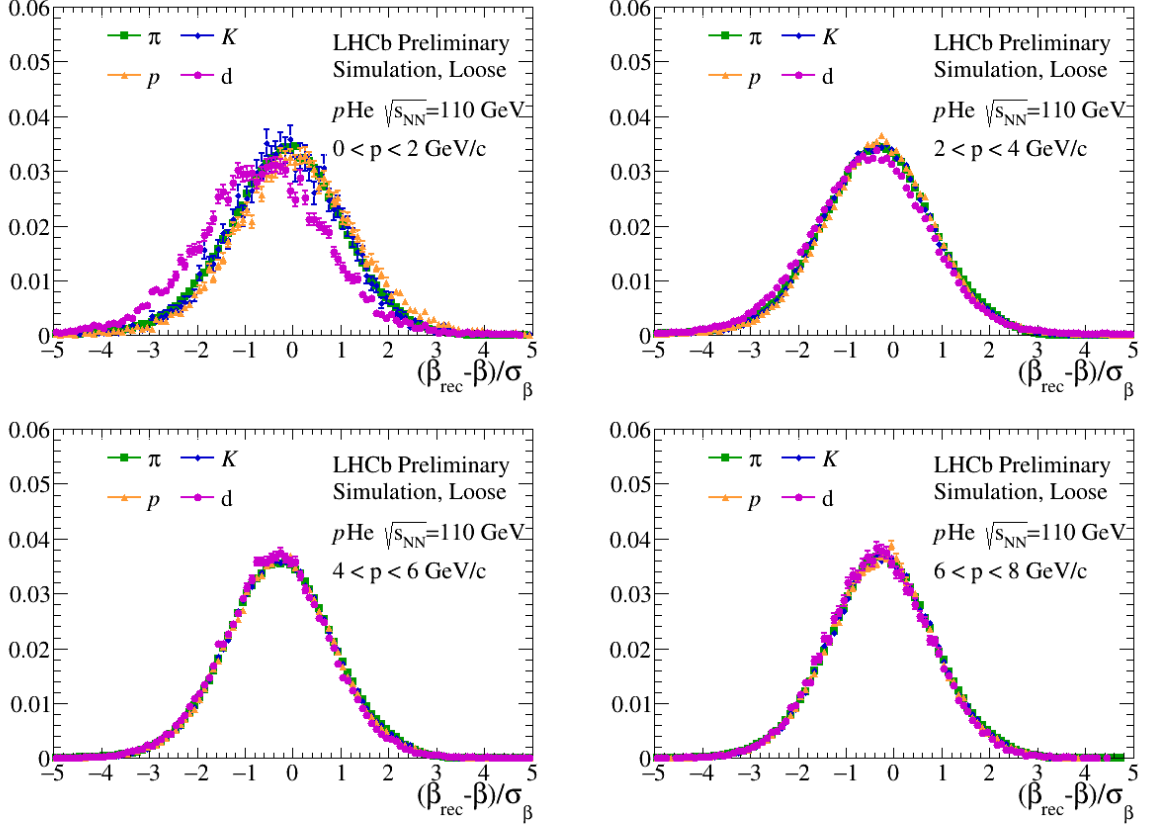
Figure II.3.6: Distribution of the pulls for β_{fit} in four bins of momentum for four species in the simulated sample: pions (green square), kaons (blue diamond), protons (yellow triangle) and deuterons (purple dot).

ultra-high momenta (20 GeV/$c < p < 40$ GeV/c) where no sensitivity to β is expected from the tool (Fig. II.3.10, right).

Considering σ_β distribution, a general lower fit quality is observed in data compared to the simulation, independently of the species and of the momentum considered (Fig. II.3.11). More detailed studies are needed to evaluate the systematics associated with the differences in the performance between simulation and data.

An empirical correction factor is obtained fitting the bias distribution of the pions. Since from the simulation it is clear that the bias is lower for lower value of β, the correction obtained from the fit is additionally multiplied by a power of β to suppress the correction where negligible effects are expected. The β_{fit} obtained from TrackBetaTool are thus corrected before analysing the final results.

II.3.3   Results

Finally, tracks passing the tight selection cuts defined in Sec. II.3.2.1 are considered. Figure II.3.12 shows the distribution of the reconstructed β as a function of the reconstructed momentum. The theoretical β-p relations for π, K, p and d are superimposed. Three different populations are distinguished: the uppermost is distributed around the theoretical curves for π and K, while the central one corresponds to the curves for p.
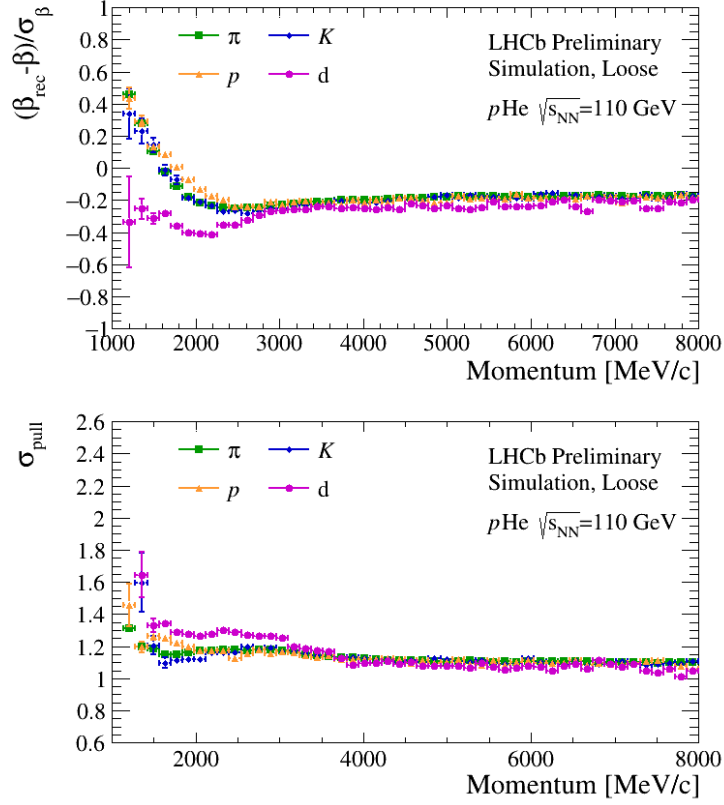
Figure II.3.7: Mean value (top) and standard deviation (bottom) of the pulls for β_{fit} as a function of the momentum for four species in the simulated sample: pions (green square), kaons (blue diamond), protons (yellow triangle) and deuterons (purple dot).
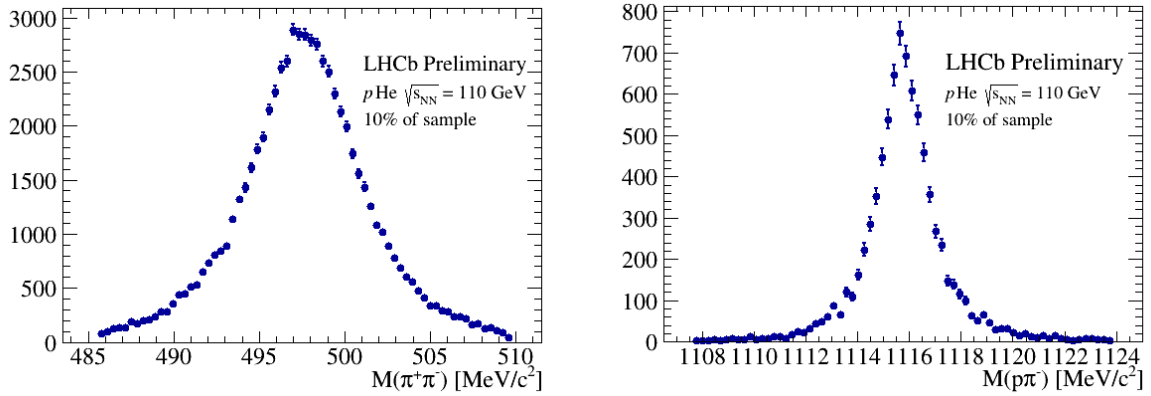

Figure II.3.8: Invariant mass distribution for the candidates K_S^0 (left) and Λ (right) reconstructed in 10% of the pHe $\sqrt{s_{NN}}$ =110 GeV data sample.
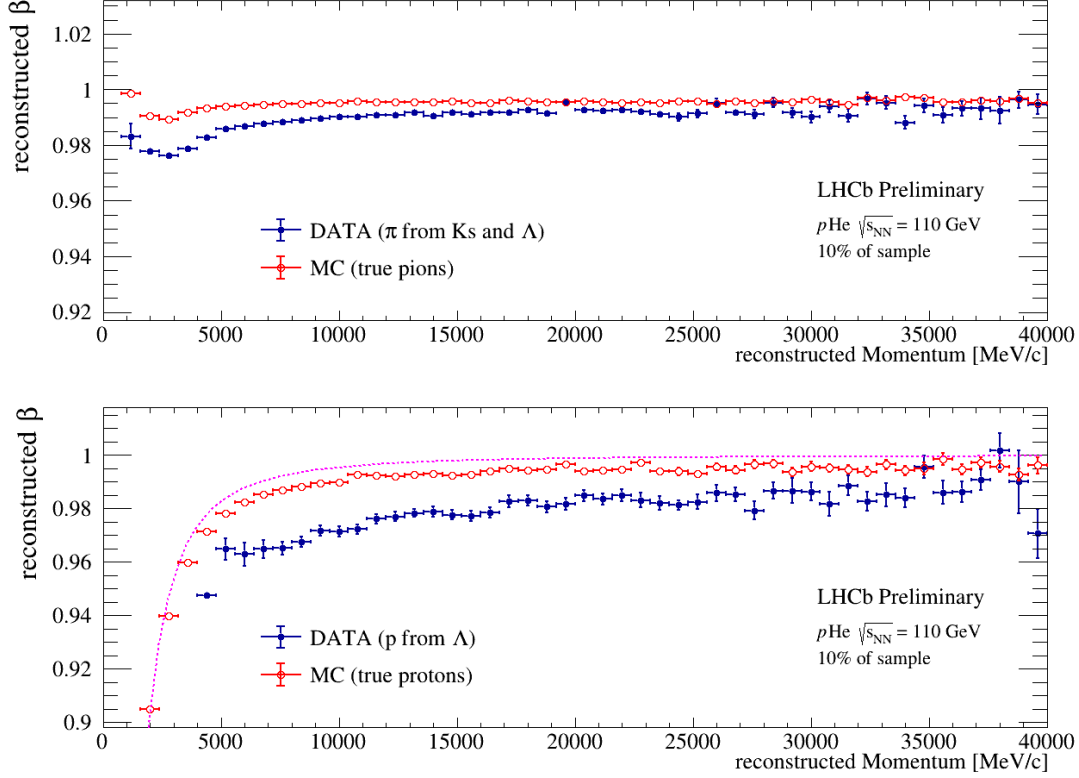
Figure II.3.9: Reconstructed β as a function of the momentum for pions (top) and protons (bottom) as a function of the reconstructed momentum. The distribution obtained for candidates in data (full blue dot) and for truth-matched particles in simulation (empty red dot) are both shown; the theoretical β-p relation for protons is also reported (pink dotted line).

Lastly, the lowermost follows the d theoretical curve and it identifies the first deuteron candidates observed in LHCb data. A clear separation is obtained for momentum lower than 2 GeV/c, as it can be seen in Fig. II.3.13, where the reconstructed β distribution in 4 bins of momentum, between 1.2 and 2.0 GeV/c, is shown: three peaks are clearly distinguished, corresponding to deuterons, protons and lighter particles.

The preliminary results presented in this thesis constitute the first evidence for an identified deuteron signal in the LHCb data, an unforeseen capability of the detector. The new technique presented in this work is proven to be able to identify (anti)deuteron in the momentum range below 2 GeV/c. Although $\mathcal{O}$ (1) antideuteron are expected to be reconstructed in this region, studies are ongoing to improve the background suppression through the implementation of a multivariate analysis-based filter, increasing the momentum coverage of the measurement. Other SMOG samples are also considered, in order to extend the search for (anti)deuterium notably to the pHe sample at $\sqrt{s_{\mathrm{NN}}} = 87$ GeV and the pNe sample at $\sqrt{s_{\mathrm{NN}}} = 68$ GeV. Recently, a new technique to identify He nuclei has been developed [172]. Exploiting the energy deposit in the silicon modules of the tracking system, charge 2 particles are identified. The potential of the technique has been demonstrated with the first observation in LHCb of the antihypertriton, through its decay $^{3}_{\bar{\Lambda}}\overline{\mathrm{H}} \rightarrow {}^{3}\overline{\mathrm{He}}\pi^{+}$ [173]. These two new techniques are the first step toward (anti)nuclei production measurements in LHCb, notably in its unique fixed-target regime.
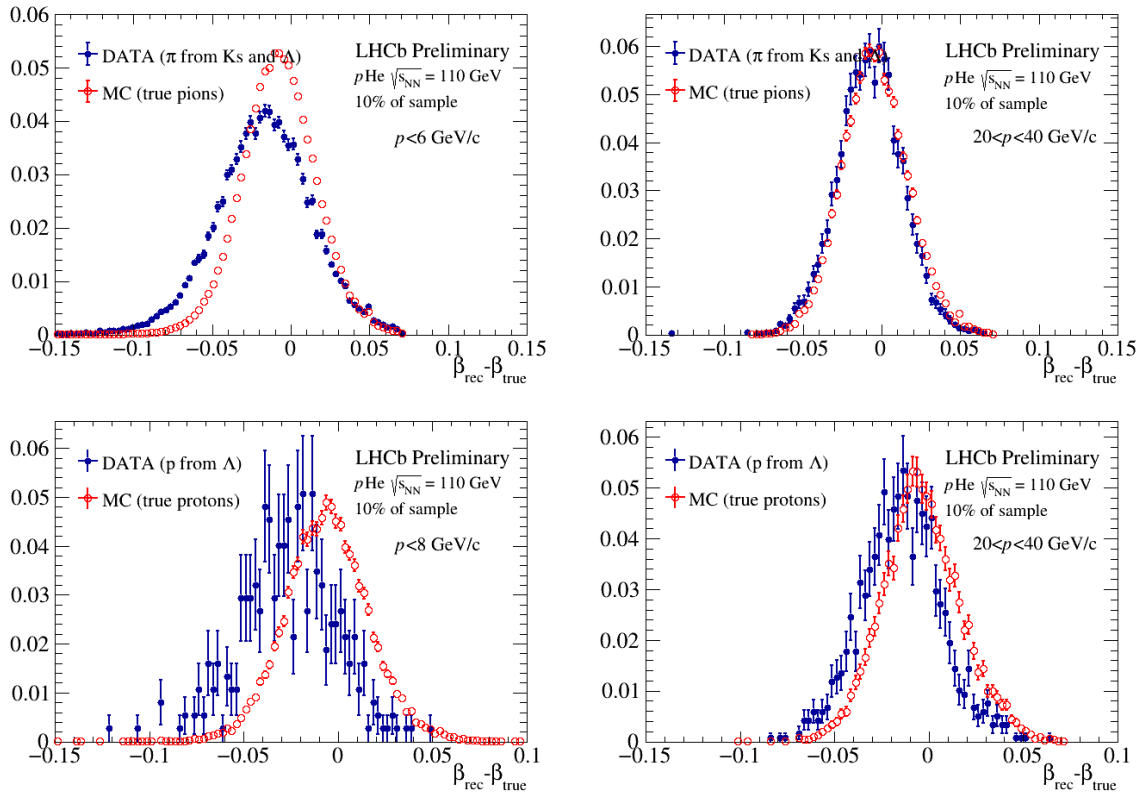
Figure II.3.10: Distribution of the reconstructed β for pions (top) and protons (bottom) in two bins of momentum. The distribution obtained for candidates in data (full blue dot) and for truth-matched particles in simulation (empty red dot) are both shown.
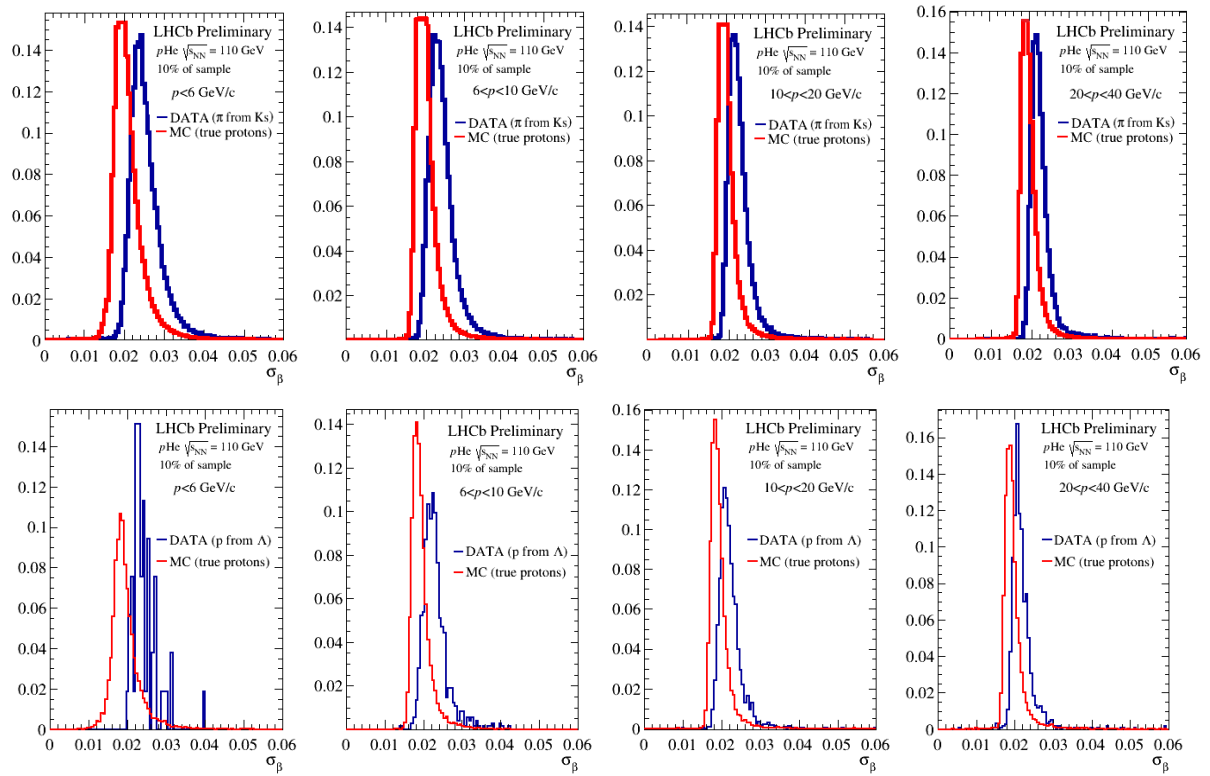
Figure II.3.11: Distribution of σ_β for pions (top) and protons (bottom) in four bins of momentum. The distribution obtained for candidates in data (blue line) and for truth-matched particles in simulation (red line) are both shown.
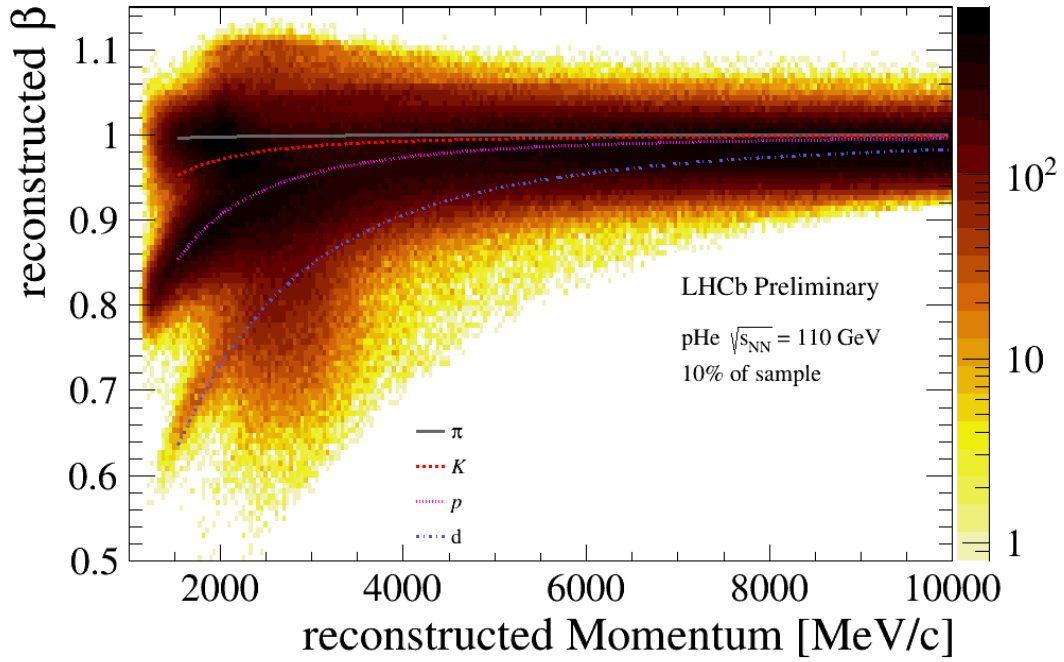
Figure II.3.12: Reconstructed β_{fit} as a function of the momentum for 10% of the 2016 pHe data sample, reconstructed with the TofForward algorithm and analysed with TrackBetaTool. The theoretical β-p relations for π (solid grey), K (dashed red), p (dotted pink) and d (dash dotted purple) are superimposed.
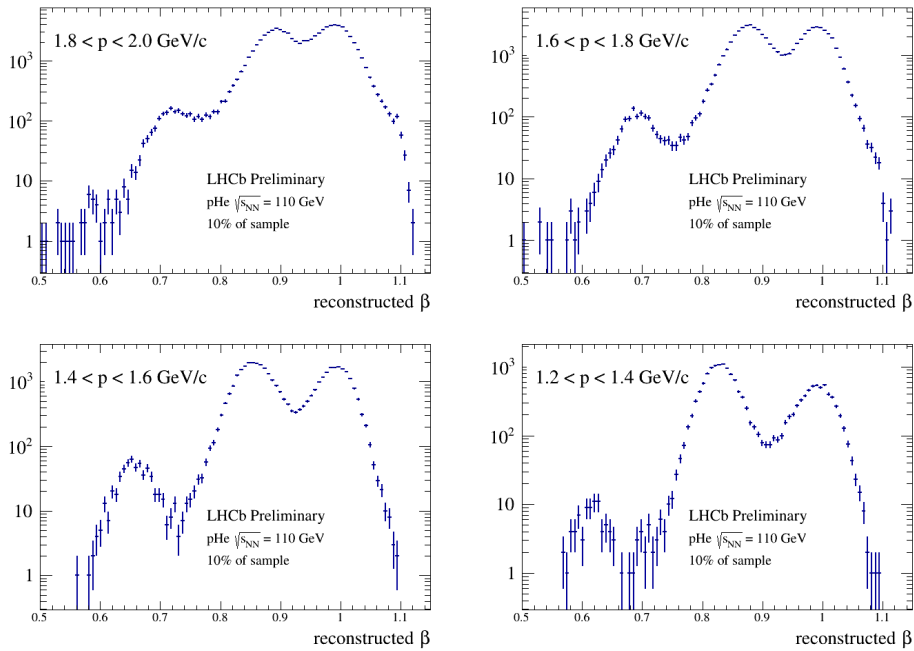
Figure II.3.13: Reconstructed β_{fit} distributions in four bins of momentum for 10% of the 2016 pHe data sample, reconstructed with the TofForward algorithm and analysed with TrackBetaTool.

Part III

SMOG2: preparatory studies and commissioning

III.1 SMOG2 storage cell operation

This chapter presents an introduction to the fluid dynamics (Section III.1.1) and coating technologies (Section III.1.2) principles that will be used in the next chapters. A description of the operation principles for the SMOG2 system is also presented in Section III.1.3.

III.1.1 Principles of fluid dynamics and vacuum technologies

Vacuum systems are characterised by a lower gas density than that obtained at the same temperature under atmospheric pressure. Based on the pressure level, vacuum can be divided in different degrees, characterised by specific gas flow properties and pumping strategies [174, 175]. In accelerator facilities, the ultra-high-vacuum regime is commonly adopted, with a typical pressure between 10^{-9} and 10^{-12} mbar.

The relation between the quantity of gas in the system and the state variables is described by the ideal gas law:

$$PV = Nk_BT, \tag{III.1.1}$$

being P the pressure, V the volume, N the number of particles in the system, k_B the Boltzmann constant and T the temperature.

The particles can be modelled as elastic hard spheres that move and collide in accordance with the laws of classical mechanics. Within these hypotheses, the velocities of the particles in an ideal gas follow the Maxwell-Boltzmann distribution, with a average speed of

$$\langle v \rangle = \sqrt{\frac{8k_b N_A T}{\pi M}}, \tag{III.1.2}$$

where N_A is the Avogadro constant and M is the molar mass of the gas. Under the hypothesis of a uniform molecular density, the impingement rate z, defined as the rate at which the gas molecules hit a unit surface area, can be expressed as $z = n\langle v \rangle/4$, where n is the numerical density of the gas defined as N/V.

The mean free path λ of a particle, corresponding to the mean distance it travels between two consecutive collisions, is

$$\lambda = \frac{1}{\sqrt{2}\pi d^2 n}, \tag{III.1.3}$$

with d the diameter of the ideal particle. When λ is of the order of the vacuum vessel dimensions, or higher, molecular collisions with the walls become predominant and the intermolecular interactions do not participate any longer in the gas dynamics. The Knudsen number K_n is used to separate the different flow regimes as described above and it is defined as the ratio between the gas mean free path and the characteristic dimension d_c of the vacuum vessel:

$$K_n = \frac{\lambda}{d_c}. \tag{III.1.4}$$

In the continuum flow regime ($K_n < 0.01$), the motion of particles is dominated by particle-particle collisions, resulting in viscous flow. On the other hand, in the molecular flow regime ($K_n > 5$), particles exhibit a random-walk and particle-wall collisions dominate. Considering typical beam pipes of $\mathcal{O}$ (10 cm) diameter, the molecular flow regime can be reached for pressure of the order of $10^{-4} - 10^{-3}$ mbar. As a consequence, accelerators vacuum systems only operate in the molecular flow regime and, as such, any instrumentations must act on single molecules since collective phenomena do not influence the gas dynamics.

The gas flow rate Q is the amount of gas, in units of pressure times volume, at a specified temperature, flowing per unit time across a specified cross-section. It characterises various gas transfer processes, such as leaking, outgassing and flow through an orifice. In the latter cases, it can be related to the pressure P of the gas contained in a volume V upstream of the aperture through the equation

$$Q = \frac{d(PV)}{dt}. \tag{III.1.5}$$

Given a defined flow rate Q, the equivalent particle flux Φ, is obtained from the ideal gas law:

$$\Phi = \frac{Q}{k_B T}. \tag{III.1.6}$$

In general, the gas flow rate can be defined between two points of a vacuum system and it is proportional to the pressure difference ΔP at the same points

$$Q = C\Delta P, \tag{III.1.7}$$

where C is the gas conductance of the system between the two points. The conductance is defined as the inverse of the resistance of a vacuum system section or orifice to the gas flow Q. It depends on T and M, through its average molecular speed, and, most importantly, on the geometrical shape of the section or orifice through the transmission probability τ

$$C \propto \sqrt{\frac{T}{M}}\tau. \tag{III.1.8}$$

For simple geometrical shapes, analytical formulas can be derived (see e.g. in Ref. [176]). For complicated shapes, generally numerical methods are used. In general, for gas molecules of different masses, the conductance scales as the square root of the inverse mass ratio

$$\frac{C_1}{C_2} = \sqrt{\frac{M_2}{M_1}}. \tag{III.1.9}$$

Given a system composed of n_{tot} different sections, the total conductance C_{tot} is obtained combining the conductances of the single sections C_i, similarly to electrical conductances. For conductances in parallel, which have the same pressure at the extremities, the total conductance is given by the sum of the single components: $C_{tot} = \sum_{i=1}^{n_{tot}} C_i$. In the case of a series of conductances, where the flow rate Q is conserved between the sections, the reciprocals of the conductances are summed to give the reciprocal of the total conductance: $1/C_{tot} = \sum_{i=1}^{n_{tot}} 1/C_i$.

In vacuum systems, a pump is any device that removes gas molecules from the system. In molecular regime, two families of pumps can be applied. Momentum transfer pumps work applying a momentum kick to the captured molecules in the direction of the pump outlet in order to increase the pressure up to the viscous regime, where mechanical pumps can be used to evacuate the gas. Capture pumps, on the other hand, sorb the molecules on the surface exposed to the vacuum, thus removing them from the system. In order to be efficient, the sojourn time, defined as the average time a molecule is blocked on the pump surface, must be longer than the typical running time of the accelerator. Long sojourn times can be achieved working the pumps at very low temperatures (cryogenic pumps) or choosing materials with high adsorption energies (chemical pumps).

Each pump is characterised by the pumping speed S, defined as the ratio of the pumped gas flow rate to the pressure P of the gas at a specific point near the inlet port of the pump

$$S = \frac{Q}{P}. \tag{III.1.10}$$

The pumping speed has the same unit of a conductance and it can, in fact, be alternatively defined as the conductance of the pump inlet multiplied by the probability that an impinging particle will be captured by it. The capture probability s, also known as sticking coefficient, is the appropriate quantity to describe distributed pumps like NEG coatings, where the molecules are removed from the vacuum system through sorption on the coated surfaces. Given the sticking coefficient of a distributed pump, the equivalent pumping speed can be obtained as

$$S = \frac{\langle v \rangle_{gas}}{4} A \cdot s, \tag{III.1.11}$$

where $\langle v \rangle_{gas}$ is the mean value of the gas speed given by the Maxwell-Boltzmann distribution and A is the area of the distributed the pump.

III.1.2 Principles of coating technologies

Getters are solid materials that are capable to chemically bind gas molecules to their surface, thus working as a chemical pump. Unlike momentum transfer pumps like the turbomolecular pumps (TMPs), they provide vibration-free pumping without continuous power consumption. In order to be able to chemically bind with gas molecules, getter surfaces must be clean from any contamination. A clean surface can be produced sublimating the getter directly in situ under vacuum (evaporable getters) or dissolving the surface contamination, mainly composed of oxygen, into the bulk by heating (non-evaporable getters). Compared to evaporable getters, non-evaporable getters (NEG) stand out thanks to their ability to regain pumping speed during an in-situ (under vacuum)

heating process known as activation, where the gettered species dissolve from the surface. Additionally, they avoid material deposition within the vacuum system [177]. Getter materials are not able to pump noble gases at room temperature, thus they must be always applied together with momentum transfer pumps to maintain stable vacuum conditions in accelerator facilities.

NEG pumps are composed of elements characterised by high solubility limit for oxygen, in order to favour the dissolution of the oxide layer during the activation process. The metals of the fourth group (Ti, Zr, Hf) are particularly favoured, thanks to their ability to dissolve more than 20% of oxygen in atomic concentration at room temperature. They can be combined with elements of the fifth group like vanadium that increase the oxygen diffusivity, in order to reduce the activation time and temperature [174]. The material, typically produced as powder, is then applied to the metallic substrate of the pump, which can be shaped as a filament or ribbon in order to achieve a linearly distributed pumping capacity. Among NEG pumps, NEG coatings on the beam pipes and other critical components are particularly useful at accelerator facilities because they allow for simpler vacuum vessel design and provide distributed pumping, which is essential in systems with limited space and narrow vacuum pipes. For the LHC beam pipe, a NEG coating composed by titanium, zirconium and vanadium (TiZrV), with a 0.3-0.3-0.4 relative composition, is adopted [178].

The operation of a NEG pump can be schematised in a three-step sequence:

Activation When NEG is exposed to air, its surface becomes saturated with oxide, carbide, and nitride formations, limiting its pumping capabilities. Therefore, an activation is required to make the NEG functional after its installation into a vacuum system. It usually takes place under vacuum conditions, after the bake-out of the rest of the system [179]. The bake-out is a heating process that accelerates the outgassing from the surfaces, in order to achieve low pressure levels in a shorter time using auxiliary pumps, compared to the time required for pumping at room temperature. While the non-coated stainless steel parts are being baked out at 250°C, the NEG pump is kept at an elevated temperature below the activation one. When the bake-out process is finished, the NEG pump is activated increasing the temperature of the NEG coated beam pipes. Although a temperature of 180°C was found to be sufficient to fully activate the TiZrV coating within 24 hours, a higher temperature of 230°C is employed in the LHC to ensure complete activation and a more uniform and sufficient dissolution of oxygen and carbon throughout the getter layer [178, 179]. Since H_2 is pumped by the NEG dissociating on the surface and monoatomically diffusing into the bulk in a thermally reversible process, during activation the hydrogen content may undergo outgassing from the getter, contrary to other gettered species, and it can be pumped away by an auxiliary pump.

Sorption After activation, the NEG transforms into a clean metallic surface able to pump different getterable gases, which can be classified based on their pumping process. They can be either chemisorbed, like CO, N_2 and O_2, or can undergo dissociation on the surface and then be absorbed individually, as is the case for H_2 and D_2. The sticking coefficient of homonuclear diatomic molecules are in general lower than that of molecules composed of dissimilar atoms. Noble gases, on the other hand, are inert and are not pumped by NEG at room temperature. While the pumping capabilities for chemisorbed gases are limited by the surface available sites,

the capacity for H_2-like gases is constrained by the bulk sorption capacity and, at a higher level, by the surface blocking caused by other gettered gases [180, 181].

Saturation As the pumping process progresses, the available surface sites on the getter are gradually occupied, leading to a decrease in the pumping speed due to the diminishing number of available sites for adsorption. The surface pumping capacity represents the maximum surface concentration of molecules that a NEG coating is able to pump before saturation. No theoretical model comprehensively describes the saturation process and predicts the sticking coefficient evolution, thus all models are based only on empirical data. A common characteristic observed in all NEG samples is that the pumping speed deteriorates most rapidly for N_2, followed by CO, while, when pumping H_2 alone, the pumping speed remains relatively unchanged for similar pumped values, thanks to its dissolution in the bulk [182].

In the case of H_2 exposition, an additional deterioration process can take place together with the surface saturation. The sorption of H_2 progresses through different consecutive steps: firstly, the H_2 molecules are physiosorbed on the getter surface and they are dissociated forming a metal-hydrogen bond. Then, the single atoms penetrate through the surface layer and diffuse into the bulk, where they occupy interstitial sites. The solubility at atmospheric pressure and room temperature of hydrogen, without the formation of hydride phases, is around the percent level for TiZrV mixture. For higher fractions, the hydride phase nucleation and growth [183, 184] is thermodynamically favoured, adding one more step to the sorption process. The value of H_2 solubility depends on the considered NEG sample and on the operational pressure and temperature. The hydride formation generates a strain in the surface that can finally lead to cracking, a general loss of ductility and peel-off of the coating, known as embrittlement [185]. The embrittlement limit in NEG refers to the point at which the quantity of sorbed hydrogen exceeds a critical threshold, leading to the formation of hydride phases and consequently to the mechanical disintegration of the getter material. Its value is obtained empirically and for the NEG coating used in LHC beam pipe it has been recently measured to be higher than 0.2 H/NEG (mol/mol) at 1 mbar and higher than 0.026 H/NEG (mol/mol) at 5×10^{-7} mbar [186].

III.1.3   Principles of SMOG2 operation

As presented in Sec. I.4.3.1, the SMOG2 system is mainly composed by a cylindrical storage cell installed at the upstream edge of the VELO detector, 34 cm away from the main interaction point, and by a GFS, positioned outside the detector 17 m away from the VELO vessel, that finely controls the gas injection.
The storage cell technique is the optimal choice for a gas target because it allows to maximise the areal density θ seen by the beam over a reduced longitudinal length given a fixed value of gas flow rate [141]. Given an isolated storage cell (Fig. III.1.1), the gas injected at the centre of the cell diffuses up to the extremities, where it can freely escape from the system. The density profile inside the cell is thus triangularly shaped with a maximum value ρ_0 at the centre that depends on the particle flux Φ and the conductance
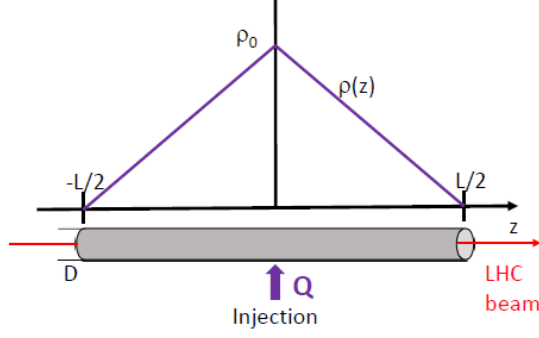
Figure III.1.1: Schematic representation of the ideal storage cell with the expected density profile superimposed. Figure taken from Ref. [141].

C of the cell from the centre outwards

$$\rho\left(z\right) = \rho_0 \left(1 - \frac{|z|}{L/2}\right) \tag{III.1.12.a}$$

$$\rho_0 = \frac{\Phi}{C}. \tag{III.1.12.b}$$

For a cylindrical cell of length L and diameter D, the conductance C is the parallel of the conductance of two tubes of length $L/2$:

$$C = 2 \times 3.81 \sqrt{\frac{T}{M}} \frac{D^3}{L/2 + 4D/3}. \tag{III.1.13}$$

The areal density, which is the defining parameter for fixed-target luminosity (Eq. I.4.1.a), thus depends on the gas flow rate Q and on the temperature T and it is given by

$$\theta = \frac{1}{2}\rho_0 L = \frac{Q}{k_b T} \sqrt{\frac{M}{T}} \frac{L/2 + 4D/3}{7.62D^3} \frac{L}{2} \tag{III.1.14}$$

Given the same gas flow rate used during the operation of SMOG2 and considering an operational temperature of 300 K, the areal density achieved with SMOG2 is at least 10 times higher than in SMOG2 for any given injected gas.

The gas is injected into the centre of the cell through a 0.5 mm capillary, connected to the GFS (Sec. I.4.3.1). The schematics of the injection system are shown in Fig. III.1.2. The GFS allows to inject a controlled and well known gas flow rate into the storage cell or the VELO vessel, when injecting in the same configuration as SMOG2, according to:

$$Q = \Delta P C_{inj}, \tag{III.1.15}$$

where C_{inj} is the conductance of the whole gas feed line and $\Delta P = P_{inj} - P_{out}$ is the difference between the pressure P_{inj} at the injection volume and the pressure P_{out} at the extraction point (storage cell or VELO vessel). Since the injection volume is kept at a pressure of around 10 mbar, the pressure at the extraction point, expected to be

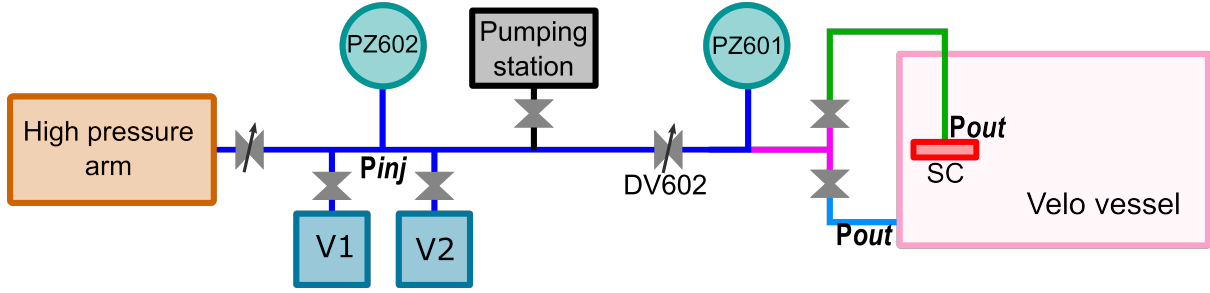Figure III.1.2: Schematic representation of the SMOG2 GFS; the same colour scheme as in Fig. I.4.12 has been used. The main elements relevant for the operation are indicated in the figure.

around 10^{-5} mbar during normal operation, can be disregarded. The conductance C_{inj} determines the time dependence of P_{inj}:

$$P_{inj}(t) = P_{inj}(0)e^{-\frac{C_{inj}}{V_{inj}}t}, \qquad \text{(III.1.16)}$$

therefore, the flow rate Q is measured from the derivative of the pressure during the injection:

$$\frac{dP_{inj}}{dt} = -\frac{C_{inj}}{V_{inj}}P_{inj}(t) \qquad \text{(III.1.17.a)}$$

$$Q = -\frac{dP_{inj}}{dt}V_{inj}. \qquad \text{(III.1.17.b)}$$

In general, the flow rate Q varies with time, but when the pressure drop is sufficiently small compared to the working pressure, the pressure dependence can be linearly approximate and the gas flow is constant, in the so-called linear regime.

A precise knowledge of the pressure and of the injection volume V_{inj} is needed to achieve the precision envisioned for the luminosity measurement. In particular, the injection volume V_{inj} is given by the sum of the calibration volumes V_1 and V_2 and the low pressure arm of the GFS, for a total volume of 0.378 l.

Technically, the system is based on precise absolute gauges to measure the pressure along the GFS line covering 6 order of magnitude variations. Two capacitance diaphragm gauges, PZ602 and PZ601, are installed respectively between the two calibration volumes and at the beginning of the feed line, with the aim of measuring and monitoring the pressure P_{inj} determining the stability of the injected flow. While PZ602 covers the range from 0.1 to 10 mbar, in order to be more sensitive to the pressure drop in the calibration volumes, PZ601 ranges between 10^{-5} to 0.1 mbar, in order to increase the precision on the line readout. The flow rate itself is regulated by a thermo-regulated valve, DV602, positioned between the calibration volumes and the feed line. The aperture can be modified, working as a tuneable conductance in series with the fixed one of the feed line, allowing to control and tune the total C_{inj}. The actual value of C_{inj} is not known *a priori* because, in viscous regime in which the GFS works, it depends on the working point pressure. It is also different for injection in the cell and injection in the VELO vessel because the feed lines in the two cases have different length and thus different fixed conductances. A calibration

campaign, in both injection configurations, is thus needed in order to understand the relation between the aperture of DV602 and the actual flow rate achieve. Long steady injections for different aperture values are being carried out and the drop in pressure is measured and fitted following Eq. III.1.17.a as a function of PZ602 readings. From the knowledge on V_{inj}, the calibration constant between PZ602 reading and the injected flow rate will be obtained for every aperture.

III.2 Dynamic gas flow simulations

In this chapter, the gas flow simulation studies performed to evaluate the impact of the injection of non-noble gases in the beam pipe are described. After a detailed presentation of the motivations in Section III.2.1, Section III.2.2 introduces the simulation software used as framework for the dynamic time-dependent algorithm that performs the simulation of the coating degradation with the injected dose, described in Section III.2.3. Finally, the results are shown in Section III.2.4, where their implications for the SMOG2 injection programme are detailed.

III.2.1 Motivations

The LHCb experiment at CERN, as presented in Sec. I.4.3, is equipped with an internal gas target called SMOG2 [131, 187], consisting of a 20-cm-long storage cell installed 34 cm upstream of the LHCb nominal interaction point and connected to the vertex locator detector (VELO) RF foil boxes. The gas confinement in a limited region could allow for more gases, even non-noble species such as H_2, D_2, N_2 and O_2, to be injected. Nevertheless, a fraction can still leak into the beam pipe and towards the VELO RF foil. Dedicated studies are thus needed to evaluate and minimise the impact on the LHC experiments and on the LHC machine [188], particularly with respect to the compatibility with the vacuum system and to the contribution to dynamic vacuum effects.

Both the strong electromagnetic field that accompany the beam and the surface bombardment by photons, electrons and ions, indeed, can induce desorption and emission phenomena from the surfaces exposed to the beam [189]. In order to mitigate these effects, most of the LHC beam pipes at room temperature and the VELO RF foil are coated with a non-evaporable getter (NEG), which helps in reducing the desorption and emission yields, in particular for SEY [190]. As it was presented in Sec. III.1.2, the NEG, working as a pump for getterable gases, can undergo degradation processes if exposed to a sufficient gas flow. As a consequence, an increase in the surface SEY and/or physical deterioration of the coating may occur. The quantity of gas that leaks toward the NEG-coated regions must be hence carefully estimated in order to determine the tolerable amount of injectable gas that will not compromise the machine operability. Being the impact on the NEG proportional to the sorbed dose of gas, and thus higher the closer to the gas injection point, the VELO RF foil, in front of the gas storage cell, is the most affected system. It has a corrugated surface in order to minimise the material budget, thus its geometry makes it

impossible to carry out an analytical extrapolation of the gas flow and of the quantity of gas sorbed by the coating. For this reason, the best approach is to use a simulation and, specifically, the Molflow+ software has been chosen thanks to its versatility and its embedded graphical interface that allows an easy manipulation of the geometry.

III.2.2 Molflow+ software for molecular flow simulations

Molflow+ [191] is a molecular flow Monte Carlo simulator that allows the pressure profile and the gas propagation to be computed in an arbitrarily complex geometry when ultra-high vacuum conditions are met. Since in the molecular flow regime the intermolecular collisions can be neglected, each particle can be treated individually and the test particle MC method can be applied. In this method, each particle is simulated separately and followed through its interactions with the walls of the system until it is pumped or exits the active volume. Compared to a direct simulation MC methods, where the active volume is divided into 3D cells, all the interacting particles are kept in memory and their positions are evolved with time, the test particle method presents several advantages:

- since intermolecular collisions are neglected, only a single test particle is kept in memory. Its trajectory in-between walls interactions can be considered a straight line and it can be determined by ray tracing;

- the simulation is event-driven: it looks for collisions with the walls and, based on the position and speed of the particle, it calculates the time of the hits;

- being all particles independent, the vacuum system behaviour is linear. This allows the simulation to be easily parallelised, only summing the hits when the results are evaluated;

- since only the collisions with the walls are considered, only the surfaces need to be simulated. In Molflow+ the geometry is described by polygons called facets, characterised by a unique temperature, opacity, sticking coefficient and other physical parameters.

III.2.2.1 Molflow+ algorithm

The main application of Molflow+ is for steady-state simulation, where the gas flow Q and the properties of the facets are constant. A source of gas, both in the case of desorption or injection, is represented by a facet f with a user-defined outgassing Q_f. The flow rate of physical particles $dN_{f,real}/dt$ is obtained from:

$$\frac{dN_{f,real}}{dt} = \frac{Q_f}{k_B T_f},\tag{III.2.1}$$

where T_f is the temperature of the gas source, k_B the Boltzmann constant and $N_{f,real}$ the number of particles injected in the system. If more than one outgassing facet is present, the total flow rate is given by the sum of all the contributions: $\frac{dN_{real}}{dt} = \Sigma \frac{dN_{f,real}}{dt}$.

As a proxy for N_{real}, only a smaller number of virtual particles $N_{virtual}$ is simulated according to a scale factor $K_{r/v}$

$$K_{r/v} = \frac{dN_{real}}{dt}/N_{virtual}. \qquad (\text{III.2.2})$$

Consequently, only quantities depending on rates, in particular the adsorption rate, pressure and particles density, are directly computed by the simulation.

For each generated virtual particle, a starting facet is chosen, with a probability proportional to the local flux $dN_{f,real}/dt$. The starting position is then chosen randomly on its surface. The particle direction, both at generation and at surface rebounds, is obtained applying Knudsen cosine law [192], which states that the probability dp of a gas molecule leaving a solid surface in a given direction within a solid angle $d\omega$ is:

$$dp = \pi \cos\theta d\omega, \qquad (\text{III.2.3})$$

where θ is the angle between the particle direction and the normal to the surface.

The particle speed v is regenerated after each collision with the walls, to reproduce the effect of the thermalisation that happens when the particle sojourns on the wall after the collision. In a real system at equilibrium, the speed distribution of particles is given by the Maxwell-Boltzmann distribution, hence the new speed depends on the temperature T_f of the hit facet. The mean value of the speed is

$$\langle v \rangle_{gas} = \sqrt{\frac{8k_b N_A T_f}{\pi M}}, \qquad (\text{III.2.4})$$

where N_A is the Avogadro constant.

Molflow+ only simulates the interaction with the walls, hence the speed distribution to be used for the test particles $f(v)_{coll}$ is different from the gas speed distribution $f(v)_{gas}$, because it takes into account the fact that fast particles hit the surface more frequently than slow ones: $f(v)_{coll} = vf(v)_{gas}/\langle v \rangle_{gas}$.

Once obtained the particle direction and speed, the next collision point is obtained through ray-tracing. If the particle exits the simulated volume, it is removed and a new one is generated. When a particle hits a facet with sticking coefficient s_f, a uniform random number n, following a uniform distribution in $[0, 1]$, is used to determine if the particle is re-emitted ($n > s_f$) or pumped away ($n \le s_f$, end of ray tracing).

Every facet has three counters in memory, incremented after each hit, that are needed to calculate physical quantities:

- N_{hit} is the number of MC hits, needed to calculate the impingement rate and evaluate the statistical accuracy of the results. Each of the facets also presents a counter for the number of adsorbed N_a and desorbed N_d test particles,

- $\Sigma I_\perp$ is the total orthogonal momentum change $mv_\perp = mv\cos\theta$, proportional to the pressure. In case of desorption, the outgoing component is added, while the incoming one is considered for adsorption,

- $\Sigma \frac{1}{v_\perp}$ is the sum of the reciprocals of the orthogonal speed components, that helps in the calculation of the particle density near the facet.

Using the counters above, the physical quantities are calculated, such as:

Impingement rate The impingement rate z_f on a facet is the rate of collisions per unit area $N_{hits,real}/dtdA$. Knowing for each facet the area A_f, the number of virtual hits $N_{hits,f}$ and the scale factor $K_{r/v}$

$$z_f = \frac{dN_{hits,real}}{dtdA} = \frac{N_{hits,f}K_{r/v}}{A_f}. \tag{III.2.5}$$

Pressure The pressure P is the force exerted on the wall divided by its area. It can be calculated from the rate of momentum change $dI/dtdA$

$$P_f = \frac{dI}{dtdA} = \frac{\Sigma I_{\perp,f}K_{r/v}}{A_f}. \tag{III.2.6}$$

Density The density n is the number of particles per unit volume, but in Molflow+ only information at surface level are accessible. Nevertheless, the density can be derived from the number of particles hitting a facet [193]. Considering a time Δt, only particles travelling at speed $v_\perp$ and within a distance $v_\perp \Delta t$ will hit the surface. The number of collisions for particle with speed $v_\perp$ $N_{hits,v_\perp}$ will be:

$$N_{hits,v_\perp} = nA\Delta t v_\perp. \tag{III.2.7}$$

The total number of collision N_{hits} will be the integral over the speed distribution function $f(v_\perp)$:

$$N_{hits} = nA\Delta t \int_0^\infty v_\perp f(v_\perp)_{gas}\, dv_\perp = nA\Delta t \langle v_\perp \rangle_{gas}, \tag{III.2.8}$$

being $\langle v_\perp \rangle_{gas}$ the average of the orthogonal speed components of the particles moving toward the surface, that can be obtained from the speed distribution of an adjacent facet:

$$\int_0^\infty f(v_\perp)_{gas}\, dv_\perp = 1$$

$$f(v_\perp)_{coll} = v_\perp f(v_\perp)_{gas}/\langle v_\perp \rangle_{gas}$$

$$\langle v_\perp \rangle_{gas} = \frac{\langle v_\perp \rangle_{gas}}{\int_0^\infty f(v_\perp)_{gas}\, dv_\perp}$$

$$\langle v_\perp \rangle_{gas} = \frac{1}{\int_0^\infty \frac{v_\perp f(v_\perp)_{gas}}{\langle v_\perp \rangle_{gas}} \frac{1}{v_\perp}\, dv_\perp} \tag{III.2.9}$$

$$\langle v_\perp \rangle_{gas} = \frac{1}{\int_0^\infty f(v_\perp)_{coll} \frac{1}{v_\perp}\, dv_\perp} = \frac{1}{\langle \frac{1}{v_\perp} \rangle_{coll}}.$$

The sum of the reciprocals of the orthogonal speed components is memorised for each facet, therefore the density can be obtained as:

$$n_f = \frac{N_{hits,real}}{A\Delta t}\frac{1}{\langle v_\perp \rangle_{gas}} = \frac{N_{hits,f}K_{r/v}}{A_f}\langle \frac{1}{v_\perp} \rangle_{coll} = \frac{N_{hits,f}K_{r/v}}{A_f}\frac{\Sigma \frac{1}{v_\perp}}{N_{hits,f}} = \frac{\Sigma \frac{1}{v_\perp}K_{r/v}}{A_f}. \tag{III.2.10}$$

125

All the physical quantities that can be directly obtained from the simulation are rate-dependent, while the absolute quantities (e.g. the number of adsorbed particles) can be calculated by multiplying the rates and the physical time of interest, thanks to the steady-state assumption that guarantees an equilibrium state for all the variables involved.

III.2.2.1.1 Time-dependent simulation

Molflow+ also presents a time-dependent configuration of the simulation, allowing the physical quantities introduced before to be studied out of steady-state conditions. The time of a hit can be defined as the sum of the time intervals between all previous couples of consecutive hits, calculated from the speed of the virtual particle and the length of the straight line trajectory connecting each couple. The physical quantities can thus be studied as a function of time.

In non-stationary conditions, both the gas flow and the properties of the surfaces vary with time. This is implemented in the simulation by defining the value of each parameter of interest for a set of time points and extrapolating the evolution function through a linear interpolation. The simulation results are then stored as independent set of counters for an *a priori* list of time intervals $[t_i - t_w/2, t_i + t_w/2]$, where t_w is the tolerance time window around the time t_i at which the parameters are evaluated.

The time feature is particularly interesting because it allows the injection of decaying gases to be simulated through the implementation of a decaying function associated to the injected particles. Nevertheless, the time-range that can be simulated is limited by the computational time needed to gather enough statistics for all the time points defined, that corresponds usually to time-ranges of hours. Moreover, while the time-dependent configuration allows to define a time evolution to the properties of the system, this must be set at the start of the simulation, thus the evolution cannot depend on the intermediate simulation results.

III.2.2.1.2 Post-processing embedded tools

In order to help in the post-processing of the results, Molflow+ provides some tools within the graphical user interface. The most relevant for the work presented in the next chapters are:

Profiles Each facet has a local 2D coordinate system corresponding to the bounding box delimiting it, with the origin usually on one of the vertices and the orthogonal axes named U and V.
The profile tool allows to split the facet along one of the axes into 100 slices, a fixed value, and samples the memorised counters for each slice. In this way, it is possible to easily plot the projection along the axis of interest of the physical quantity under study.

Textures Textures, similarly to profiles, allow to sample a physical quantity within a facet, through a mesh in U and V of the area. The cell size, corresponding to the UV resolution, can be chosen freely and both squared and rectangular cells are available. In case of cell close to the edges, the area can be extremely reduced with respect to the full cell, corresponding to a limited number of interactions with the virtual particles, thus the results are not reliable and should always be excluded

from further analysis. Each cell is provided with an independent set of counters and the results for pressure, impingement rate and density can be shown directly inside the graphical user interface through heat maps.

Both profiles and textures are powerful tools to help visualise results and study with finer details the behaviour of the physical quantities within a facet, but it is important to keep in mind that they share the same local properties (i.e. temperature, sticking coefficient, opacity) as the facet they are defined on. Defining smaller facets remains the only way to describe with finer details the spatial distribution of these quantities.

III.2.2.1.3 Command Line Interface

The graphical user interface is optimised to allow easy manipulation of the geometry and a first post-processing of the data through the provided tools, but only offers limited control over the simulation. In order to overcome these limitations, a command line interface has also been implemented, *MolflowCLI*. MolflowCLI allows to run simulations without the graphical user interface, thus running on computing clusters. Moreover, it gives the users the freedom to change the simulation parameters on demand, particularly through scripts implementation.

Starting from a geometry previously prepared with the Molflow+ graphical user interface, a simulation can be started providing the geometry file and a stopping condition, that can be either the number of desorbed virtual particles generated or the computational time of the simulation. A new geometry file will be produced as an output, with the counters updated to their values at the end of the simulation. A list of converted physical quantities and details for all the facets can also be saved in `csv` format. MolflowCLI is particularly suited for long simulations. An `autosave` interval can be set to regularly save the results, and it can therefore be reloaded through the `loadAutosave` command. Defining the number of desorbed particles for which an output is required, intermediate steps can also be recorded. A particularly interesting feature is the possibility to change the facets and simulation parameters directly from the command line or from a configuration file. In particular, the outgassing, the sticking coefficient, the temperature and the opacity can be modified, facet by facet, while the particle mass and its half life can be changed at simulation level. This degree of manipulation at command line level has been optimised to allow scripting, thus opening to easy and substantial customisation.

III.2.2.2 Statistical accuracy of the results

A MC simulator approximates a physical result by carrying out a given number of experiments and counting the number of positive outcomes. In Molflow+ case, each test particle can be considered an independent experiment and the positive outcome depends on the physical process of interest (e.g. a hit on the facet, absorption of the test particle, a test particle leaving the simulated volume). Translating to probability theory then, the binomial distribution can be applied to describe the yield of success of the MC simulation: if N is the total number of experiment and p is the probability of a success, the expected number of positive outcomes n is Np with a variance of $Np(1-p)$. Each physical quantities, barring normalising constants, can therefore be expressed as the probability of a positive outcome over the total number of tests: for the pressure, for example, it is proportional to the number of hits on the facet, so it can be expressed as a

function of $p = n/N$, where n is the number of hits on the facet and N the total number of hit in the simulation. The statistical relative uncertainty will be:

$$\sigma_{rel} = \sqrt{\frac{1}{n}\left(1 - \frac{1}{N}\right)} \qquad \text{(III.2.11)}$$

This result is valid only if the hypothesis of independent experiments can be considered true. In a real simulation this is generally not the case because the simulation traces the particle through consecutive hits, thus adjacent locations have correlated statistical fluctuations, highly influenced by the geometry taken in consideration. Nevertheless, this estimation remains a valid starting point for an order-of-magnitude evaluation of the statistical uncertainty and it remains true as a scaling law. For a more precise calculation, a case-by-case approach must be considered.

Considering the limitations of an analytical approach to the uncertainty estimation, a more qualitative approach can be a valuable workaround. When the geometry presents some degree of symmetry, one can estimate the statistical uncertainty as the deviation from the mean value over the symmetric surfaces. For this purpose, the texture feature can come in help, dividing the homogeneous regions in smaller cells and determining the uncertainty through a Gaussian fit of the values obtained. In case of known profile for the variable, on the other hand, the uncertainty can be extrapolated from the fit of the known model to the data. Finally, when none of these approaches are viable, repeating the simulation multiple times is still a reliable solution to estimate the fluctuations and the mean value.

III.2.3   Dynamic gas flow simulation strategy

In order to reliably simulate the evolution of the NEG sticking coefficient, a dynamical time-dependent simulation is needed to take into account the adsorbed dose of gas. As introduced in Sec. III.2.2, Molflow+ presents a time-dependent configuration, but it requires to know *a priori* the time evolution of the system. The command line interface is hence used instead, in order to implement in the steady-state configuration a script to iteratively control and automatise the sticking coefficient evolution. Required inputs to have reliable results are also a realistic model for the sticking coefficient evolution and a detailed geometry modelling of the SMOG2 storage cell and of the VELO RF foil.

III.2.3.1   Sticking coefficient saturation models

As discussed in Sec. III.1.2, there is no theoretical model describing the sticking coefficient evolution from first principles, especially because it greatly depends on the type of interacting gas and on the substrate. Any saturation model must thus be based on experimental data for a NEG type similar to the one under study and with the interesting gas. For TiZrV coating, comparable to the one used in LHC, only data for N_2, CO and H_2 are available. The H_2 sample has been chosen as a proxy for both H_2 and D_2, the N_2 one for all other getterable gases, since it is the species expected to have the fastest saturation evolution.

Considering the N_2 sample, an empirical model based on general assumptions

over the pumping mechanism [182, 194] can be applied. The NEG film can be modelled as a flat outer surface littered with circular holes. Each hole represents the end aperture of a straight cylindrical void, the inner surface of which has the same sticking coefficient as the flat outer surface. Initially, the molecules are adsorbed either on the flat surface or inside the voids. When the outer surface saturates, the adsorption persists in the voids. The sticking coefficient evolution in the two regions must be separately derived:

Saturation on the flat surface Under the assumptions that each molecule is adsorbed as a whole onto the defined adsorption sites, each site can accommodate only one molecule independently of the neighbour sites (single-site adsorption) and no desorption takes place. The Langmuir's adsorption isotherm model can be applied and the flat surface sticking coefficient evolution follows

$$s_f \sim s_{f,0} \left(1 - \frac{x}{x_0} \right), \tag{III.2.12}$$

where $s_{f,0}$ is the initial sticking coefficient of the flat surface in absence of any adsorption, x and x_0 are the concentration of pumped molecules and the maximum concentration of pumped molecules for the flat surface, respectively. Usually, for polyatomic molecules with same chemical elements, the single-site adsorption assumption is not true because the molecules undergo dissociation on the surface and occupy a higher number of adsorption sites. This can be taken into account introducing p, the number of sites that participate in the adsorption of a molecule

$$s_f \sim s_{f,0} \left(1 - \frac{x}{x_0} \right)^p. \tag{III.2.13}$$

Saturation on the voids The adsorption in the voids persists progressing gradually deeper inside them. The saturation depth will therefore be proportional to the quantity of gas pumped and the molecules will have to travel deeper in the void to be adsorbed. The pumping speed is thus proportional to the conductance of the saturated part of the voids, which is in turn inversely proportional to the saturated length

$$s_v \sim \frac{\alpha_v}{l}, \tag{III.2.14}$$

where α_v is the sticking coefficient at the entrance of the voids and l is the saturated length. Since both l and, mildly, α_v are proportional to x, a more generic model has been considered

$$s_v \sim \frac{s_{v,0}}{1 + \left(\frac{x}{k} \right)^h}, \tag{III.2.15}$$

being $s_{v,0}$ the initial sticking coefficient of the voids, h a factor taking into account the slight dependence of α_v to x, but it is expected to be near 1, and k an additional free parameter to help reproduce the data.

The final model is given by the composition of the two regions up to complete saturation of the flat surface, then by the voids model alone:

$$s(x) = \begin{cases} s_{f,0} \left(1 - \frac{x}{x_0} \right)^p + \frac{s_{v,0}}{1 + \left(\frac{x}{k} \right)^h} & x < x_0 \\ \frac{s_{v,0}}{1 + \left(\frac{x}{k} \right)^h} & x \geq x_0 \end{cases} \tag{III.2.16}$$
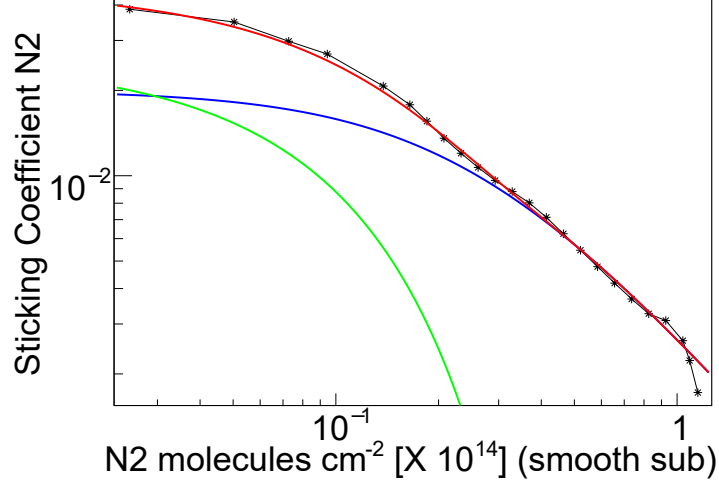
Figure III.2.1: Available experimental data [182, 194] for the N_2 sticking coefficient as a function of the N_2 surface concentration. The data points are modelled with a parametric model, as detailed on the text.

Table III.2.1: Fit results for the evolution of the N_2 sticking coefficient as a function of the N_2 surface concentration.

Parameter	Fitted value
$s_{f,0}$	0.0258 ± 0.0008
$x_0 \left[\, \text{cm}^{-2} \,\right]$	$(0.7 \pm 0.2) \cdot 10^{14}$
p	7 ± 2
$s_{v,0}$	0.020 ± 0.009
$k \left[\, \text{cm}^{-2} \,\right]$	$(0.26 \pm 0.16) \cdot 10^{14}$
h	1.4 ± 0.3

The free parameters are determined through a fit to the data. Being a complete scan of the sticking coefficient evolution as a function of the N_2 adsorbed concentration not available for LHC NEG samples, an older dataset, collected on a similar NEG sample, is used instead as a proxy to tune the parameters, and the final values for $s_{f,0}$ and $s_{v,0}$ are scaled in order to obtain the value of initial sticking coefficient s_0 measured on LHC NEG samples.

A first fit of the high coverage region ($x \geq x_0$) is carried out to determine $s_{v,0}$, k and h. The whole dataset is then fitted to the complete model in order to determine $s_{f,0}$, x_0 and p, keeping the already fitted parameters as fixed. Figure III.2.1 shows the result from the fit, while the final values for the parameters are reported in Tab. III.2.1. The results are compatible with expectations. In particular, the p parameter is compatible to those obtained in previous studies, while h is close to 1 as expected from the model.

Concerning H_2, the presented model is not applicable because the H_2 molecules pumped on the surface diffuse in the bulk, after dissociation, and the sticking coefficient depends more on the concentration in the bulk and on the rate of arrival of molecules on the surface. A new dataset was thus acquired on a NEG sample comparable to the one covering the LHC beam pipe and the VELO RF foil, in order to directly model on data [195]. The data were

acquired in a Fischer-Mommsen dome: a vacuum chamber is divided into two volumes by a wall with an orifice of known conductance C in the middle. Two pressure gauges are placed on the two sides of the orifice to measure the flux between the semi-volumes, according to Eq. III.1.7. A pump of known speed S_{pump} is positioned downstream of the orifice, in front of the NEG coated sample. Finally, a continuous influx of gas upstream of the orifice guarantees that the pressure upstream remains constant throughout the measurement. Since the dome constitutes a closed system, the flux from the orifice must be equal to the pumped away one:

$$Q = (P_1 - P_2)C$$
$$S = \frac{Q}{P_2} = \frac{P_1 - P_2}{P_2}C, \qquad \text{(III.2.17)}$$

being P_1 and P_2 the pressures values measured upstream and downstream of the orifice, respectively, and $S = S_{pump} + S_{NEG}$ the total pumping speed of the downstream semi-volume. The pumping speed of the NEG sample is then:

$$S_{NEG} = \frac{(P_1 - P_2)}{P_2}C - S_{pump}. \qquad \text{(III.2.18)}$$

The measured pumping speed is converted into the equivalent sticking coefficient and the H_2 concentration in the NEG bulk is obtained integrating over time the flux of pumped H_2. Experimentally, all NEG samples, minus a normalisation factor, have been observed to present the same evolution as a function of the relative atomic H concentration x_H in the NEG bulk. Hence, this is a convenient variable to model the sticking coefficient evolution, allowing the result to be applied to any new sample modulo just a normalisation factor depending on the appropriate starting value. The data have been fitted with an exponential function

$$s(x_H) = s_{sat} + s_0 e^{\lambda x_H}, \qquad \text{(III.2.19)}$$

where s_{sat} is the sticking coefficient residual at saturation, expected to be compatible with 0, s_0 is the starting sticking coefficient and λ is the sticking coefficient decay constant. The result of the fit is shown in Fig. III.2.2, while the obtained parameters are listed in Tab. III.2.2[1]. As for the previously discussed N_2 case, the obtained values are consistent with the expectations.

During Run3 SMOG2 operations, the NEG film is expected to interact with multiple getterable gas species, all of which can contribute to its saturation. Given that the cross-contamination with different gases can alter the pumping speed [196], even if the H_2 adsorption does not impact the pumping speed for the other species, thanks to its diffusion in the bulk, a partial saturation of the surface with O_2 or CO, desorbed from the walls, can highly reduce the sticking coefficient of H_2 and N_2. The implementation

---

[1]In a later reprocessing of the data used to obtain the evolution of the H_2 sticking coefficient as a function of the relative atomic H concentration in the NEG volume, an error in the data processing was found related to the atomic H concentration. The major difference corresponds to a decrease of around 85% of the sticking coefficient decay constant, that corresponds to an increase of a factor 4 of the atomic H concentration at saturation. This correction does not impact the conclusions of this simulations and, on the contrary, an even better performance of the NEG coating in terms of saturation can be expected, both as a decrease of the saturated area and of its spatial penetration.
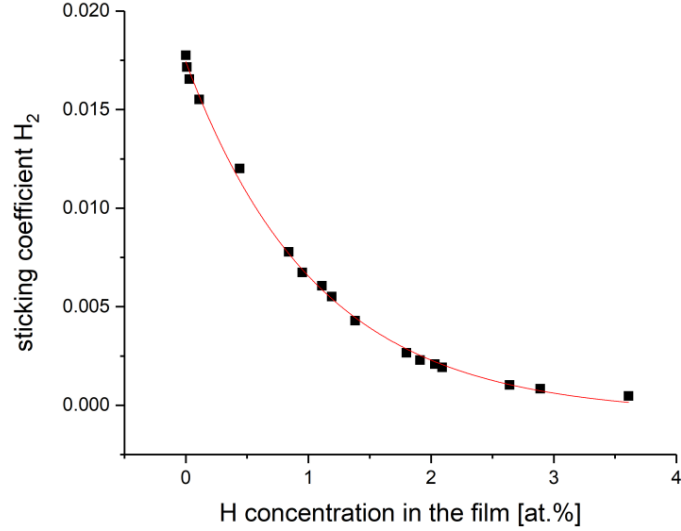
Figure III.2.2: Available experimental data for the H_2 sticking coefficient as a function of the relative atomic H concentration in the NEG volume. The data points are modelled with a parametric model, as detailed on the text.

Table III.2.2: Fit results for the evolution of the H_2 sticking coefficient as a function of the relative atomic H concentration in the NEG volume.

Parameter	Fitted value
s_{sat}	$(-4 \pm 2) \cdot 10^{-4}$
s_0	0.0179 ± 0.0002
λ	-0.94 ± 0.03

in a Molflow+ simulation of such a situation, though, is very challenging and has been discarded. Nevertheless, the cross-contamination effects will be taken into consideration in the planning of the timeline for the injections.

III.2.3.2 Dynamic gas flow simulation algorithm

A `python` script is implemented to simulate the sticking coefficient time evolution. For each short time interval, where the sticking coefficient can be assumed as stable, the simulation is executed and the parameters are updated.

In Fig III.2.3, the main algorithm steps are illustrated. Taking as an input the file with the initial geometry, generated using Molflow+ graphical interface, the script allows the user to define the simulation parameters directly from the command line. The MolflowCLI first step simulation is then configured and its outputs are used to update the sticking coefficient based on the considered model. If the stopping condition is satisfied, the simulation is concluded. Otherwise, the new starting configuration is generated and the output geometry of the step under consideration is used as input file for the next one. At each step, an `XML` summary file is updated with the relevant information for an offline analysis of the results. A more detailed description of the algorithm steps is presented in
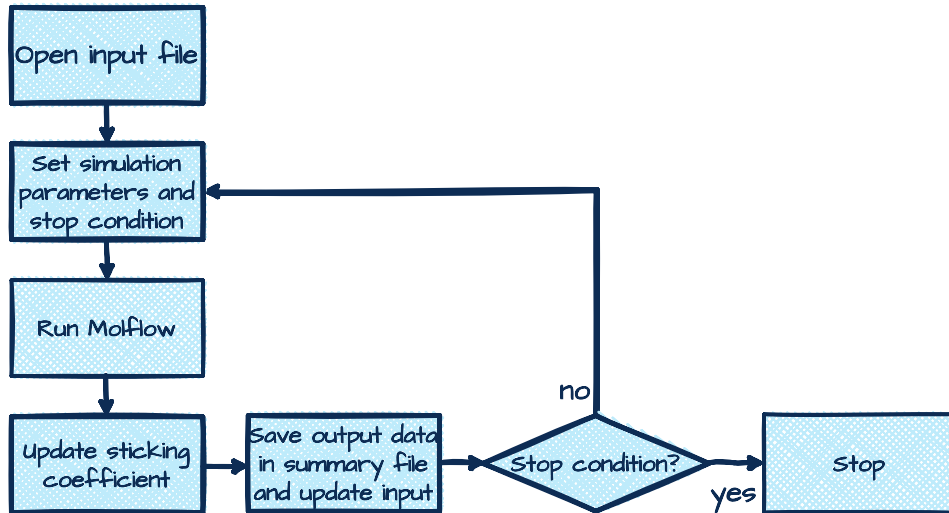
132

Figure III.2.3: Flow chart for the dynamic gas flow simulation algorithm.

the following sections.

III.2.3.2.1   Starting conditions

The starting conditions for the simulation can be fully controlled by the user through the command line interface. The configurable parameters can be separated into two categories:

Geometry configuration As an input, the geometry needs to be prepared by only defining the properties of the *inactive* facets, i.e. the ones that will remain unchanged throughout the whole simulation. All the *active* facets parameters (temperature, sticking coefficient, opacity), instead, can be selected at the command line level. Since the beam pipe and the RF foil are expected to be in the same starting conditions, for each parameter the same value will be applied to all the *active* facets, whose identification numbers (IDs) must be provided as input parameters. The injection conditions are set by providing the injected gas flow and the outgassing facet ID. A complete geometry definition can also be made through the graphical interface, with the only requirement to have the same type of NEG coating over the interesting volume. Indeed, different NEG coatings for different regions would require to apply different evolution models for each facet, as is not the case for this study, where a uniform NEG coating is expected over the whole surface.

Simulation flow configuration The main configuration needed to run the simulation is the saturation model to be used to update the sticking coefficient at the end of every step. For the following discussion, the models presented in Sec III.2.3.1 have been considered, but the code can be used to easily implement different models. Moreover, as discussed in Sec.III.2.2.1.3, MolflowCLI allows to choose the condition at which the simulation is interrupted, or in this case every step of it. Possible choices are the number of generated virtual particles, which fix the scale factor $K_{r/v}$, or the computational time of the simulation *CPUtime*. Since $K_{r/v}$ is directly connected to the statistical accuracy of the simulation, choosing the number of generated virtual particles gives a better control over the uncertainties on the results.

However, a new particle is generated only when the previous one is removed from the system, thus the simulation time required to obtained the same number of generated particles gets longer as the sticking coefficient decreases. Choosing the *CPUtime*, on the other hand, guarantees a total control over the time required to complete the simulation but the number of generated virtual particles will decrease with the sticking coefficient, for the same *CPUtime*, together with the statistical accuracy. A compromise between the two approaches is to consider the *CPUtime* as stopping condition, but allowing it to change during the simulation according to a defined evolution law in order to compensate for a lower adsorption rate.

The simulation can be started from any intermediate stage, which is particularly helpful when running very long simulations or when it is interesting to revisit previous results, without having to re-run the simulation from the beginning. In order to simplify the process, a file summarizing the condition at the end of the step, that would be used for the next one, is automatically saved and it can be provided as starting configuration.

III.2.3.2.2 Parameters update

For every step, parameters are updated, as a proxy for the continuous process in terms of space propagation and time evolution. While in reality, as the concentration of adsorbed molecules grows, the surface sticking coefficient continuously decreases, the discretisation is here required to accommodate for the steady-state regime under which each step is simulated, with the time interval to be determined balancing the computational time and the statistical accuracy of the results. Since the sticking coefficient cannot seamlessly descend the saturation curve, which would require infinitely small steps, a reasonable approach is to define the steps in order to have a fixed relative variation in the sticking coefficient. The magnitude of the variation allowed between steps determines the resolution of the simulation.

As discussed in Sec. III.2.2, the available variable from Molflow+ for each facet i is the adsorption rate Ra_i, which can be converted in concentration rate RC_i by dividing it by the area A_i. The concentration increase at each step is then obtained multiplying the rate for an arbitrary physical time, sufficiently short so that the steady-state hypothesis can be considered valid. The sum of the physical times defined at every step will also give the real time corresponding to the simulation.

The ideal physical time is such that the change in sticking coefficient is not higher than the desired resolution for any of the facets under study. For each facet, the increase in concentration ΔC_i needed to obtain the desired sticking coefficient is determined and the corresponding physical time t_i is obtained from the concentration rate. The physical time t_j for the step j is then chosen as the minimum between the physical times of the facets. This value is used to calculate the new concentrations and thus the new sticking coefficients at every facet.

In order to avoid micro-steps, which would inflate the computational time required for the simulation, a minimum physical time σ_t is defined, corresponding to the time resolution desired for the simulation. Moreover, the concentration rate resolution $\sigma_{RC;i,j}$ corresponds to the rate obtained when only one virtual particle is adsorbed during the step. Both

points contribute to the uncertainty $\sigma_{\Delta C;i,j}$ on $\Delta C_{i,j}$:

$$RC_{i,j} = \frac{Ra_{i,j}}{A_i} = \frac{Na_{i,j} \cdot K_{r/v,j}}{A_i}$$

$$\sigma_{RC;i,j} = \frac{K_{r/v,j}}{A_i}$$

$$\Delta C_{i,j} = RC_{i,j} \cdot t_j \qquad \text{(III.2.20)}$$

$$\frac{\sigma_{\Delta C;i,j}}{\Delta C_{i,j}} = \sqrt{\left(\frac{\sigma_{RC;i,j}}{RC_{i,j}}\right)^2 + \left(\frac{\sigma_t}{t_j}\right)^2} = \sqrt{\left(\frac{1}{Na_{i,j}}\right)^2 + \left(\frac{\sigma_t}{t_j}\right)^2}.$$

Appropriately choosing σ_t, the relative uncertainty on $\Delta C_{i,j}$ only depends on the number of adsorbed virtual particles:

$$\frac{\sigma_{\Delta C;i,j}}{\Delta C_{i,j}} = \frac{1}{Na_{i,j}}. \qquad \text{(III.2.21)}$$

The resolution on $\Delta C_{i,j}$ corresponds to the uncertainty $\sigma_{\Delta C;i,j}$ for a time step equal to σ_t, and it depends on the area of the facet and on the scale factor:

$$\sigma_{\Delta C;i,j,min} = \frac{K_{r/v,j}}{A_i} \cdot \sigma_t. \qquad \text{(III.2.22)}$$

$\sigma_{\Delta C;i,j,min}$ ultimately limits the minimum sticking coefficient variation that can be achieved in each facet and it should always be less than the minimum $\Delta C_{i,j}$ expected for the desired sticking coefficient resolution. When the facet reaches saturation, the uncertainty on $\Delta C_{i,j}$ at saturation $\sigma_{\Delta C;i,sat}$ also determine the maximum level of over-saturation that can be expected, where the over-saturation is the difference between the simulated concentration on the facet and the maximum capacity of the NEG coating.

III.2.3.2.3 Ending conditions

Considering that the goal of the iterative simulation is to study the degradation of the NEG coating and the onset and propagation of the saturation, it must be defined the condition at which the simulation loop can stop. The appropriate stopping condition can be chosen from:

Onset of saturation The simulation stops when at least one of the facets reaches saturation. This condition is recommended when the goal is to understand the conditions at which the saturation begins.

Saturation propagation The simulation stops when the saturation reaches a defined penetration in the geometry, being this defined as the maximum longitudinal coordinate of the centres of the saturated facets.

Total simulated time The simulations stops when the total real time simulated reaches the defined value. This condition allows to study the complete evolution of the system during the interesting time period.

At the end of the simulation, the summary file allows all the relevant data to be accessed without accessing the geometry files produced by MolflowCLI after each step. All the saved variables are reported in Tab. III.2.3 and can grouped as:

Table III.2.3: Variables stored in the summary file, divided per category

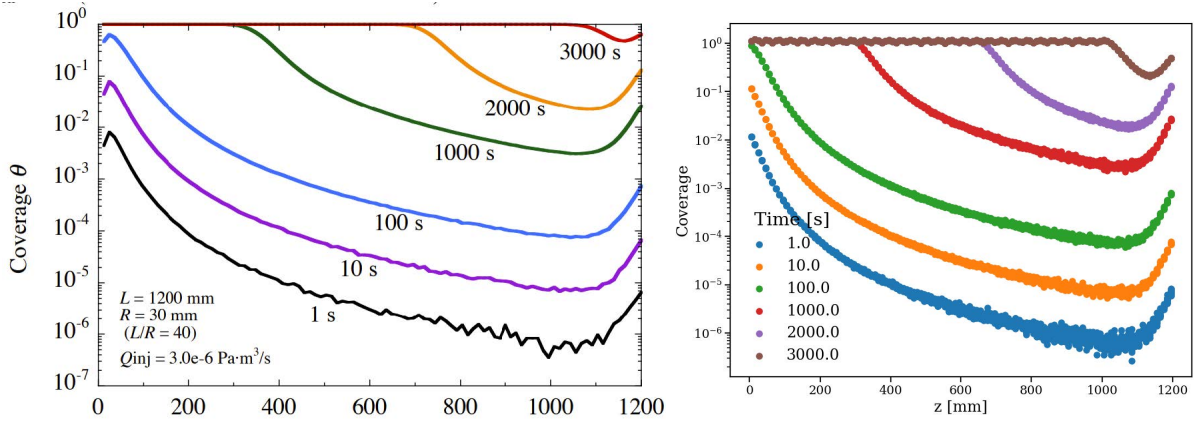| Global parameters	gas mass, injected gas flow
Facet parameters	facet id, temperature, area, centre coordinates
Iteration parameters	iteration id, physical time, CPUtime, scale factor
Facet-defined iteration variables	pressure, density, hits in iteration, adsorption rate, concentration variation, sticking coefficient

Figure III.2.4: Coverage (x/x_{max}) profiles as a function of the longitudinal position along the pipe z for different injection times for the reference simulation (left) and for the new algorithm (right)

- the parameters globally valid for the whole simulation,

- the parameters associated to each facet that are stable through the simulation;

- the variables characterising every step, valid for all the facets;

- the variables characterising every step that are uniquely defined for each facet.

The flow of the algorithm has been validated reproducing the results obtained on a simple test system with an independent simulation strategy [197], as illustrated in Fig. III.2.4. A geometry consisting of a pipe with constant gas flow from one extremity and constant pumping speed equal to 7 l/s from the opposite side has been considered. The same saturation model used in the reference has been implemented:

$$s\left(x\right) = 1 - \frac{x}{x_{max}},$$

where s is the sticking coefficient, x is the concentration of pumped particles and x_{max} is the adsorption capacity. The results obtained for an equivalent of 3000 hours of injection (right) show a good agreement with the reference values (left), validating the developed algorithm.
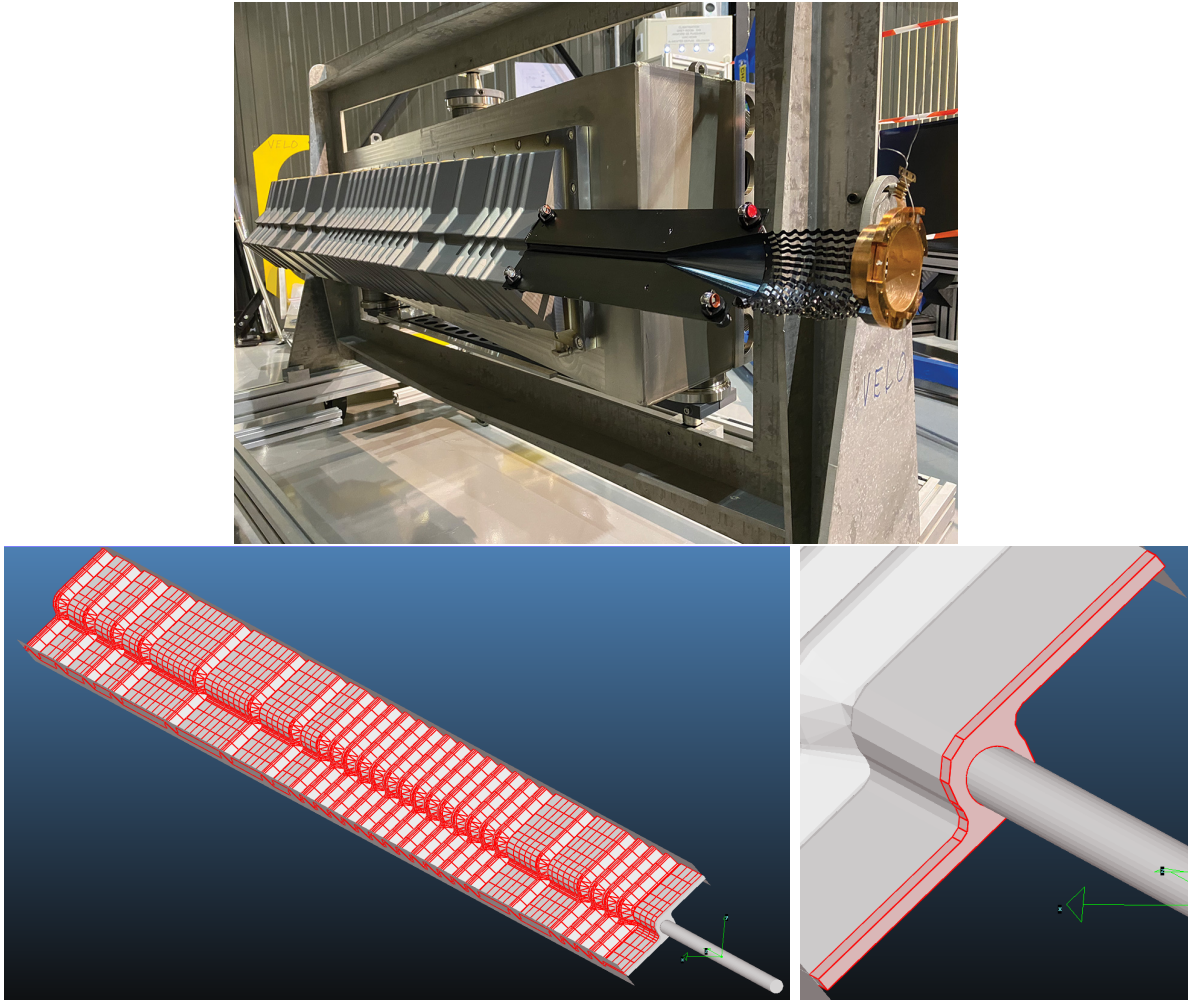
Figure III.2.5: Storage cell and RF foil geometry. On top, a picture of half storage cell connected to half RF foil, before the installation. On the bottom, the segmented geometry model obtained using Molflow+ graphical interface. The facets involved in the saturation studies (left) and the WFS (right) are outlined in red.

III.2.3.3 Storage cell and RF foil geometry

An accurate description of the geometry under study is essential to obtain reliable results: this can be directly created via the Molflow+ graphical interface, or, for more complex systems, can be imported as an `STL` file generated by CAD. For the discussed system, the storage cell and the RF foil must be considered (Fig. III.2.5, top). While the former can easily be modelled as an open pipe with a small injecting capillary in the middle, the RF foil is a corrugated surface, thus its geometry requires a careful study in order to reproduce its main features without putting a strain on the computation capabilities of the simulation.

Although the geometry obtained from the CAD model is the most accurate one, the RF foil region is composed by more than 90000 facets with areas ranging from around 10 cm^2 to 10^{-5} cm^2. While a 10 cm^2 surface does not allow the NEG evolution to be followed with enough space detail, the smallest facets, corresponding to around 90% of the total number (around 1% of total area), are prone to higher statistical fluctuations, limiting

the precision of the results and increasing the computational time. Moreover, due to the small area, the time resolution σ_t needed for the simulation would be of the order of the microseconds, prohibitively small. Choosing a σ_t of the order of the seconds would produce instant saturation of the small facets, with just one adsorbed virtual particle, limiting the validity of the results.

A solution has been found, starting from the CAD model and simplifying it through the Molflow+ graphical interface (Fig. III.2.5, bottom left). Exploiting the modular structure of the RF foil, a new geometry model has been created eliminating the small facets, without compromising the structural integrity of the system (i.e. without introducing leaking points and unphysical overlaps). A segmentation in both the longitudinal and transverse direction has also been introduced, in order to obtain the desired spatial resolution. A reduction factor of the number of facets of the order of 10 has been obtained, with an area ranging between 1 cm^2 and $0.5 \cdot 10^{-2}$ cm^2. A small fraction of facet with an area smaller than $0.5 \cdot 10^{-2}$ cm^2 (micro-facets) is still present and its impact on the final results will be taken into consideration.

Finally, the WFS that connects the cell to the RF foil must be modelled since it channels the gas towards the VELO limiting its dispersion at the interface and changing the final conductance of the system. The joint has been obtained as a box that follows the s-shaped profile of the RF foil (Fig. III.2.5, bottom right). The cell is connected to the box through a dedicated aperture on the face facing it, while the box is completely open on the RF foil side.

III.2.4   Simulation results

In this section, the results for the degradation of the NEG coating in the RF foil, in particular with respect to the saturation level and propagation, caused by SMOG2 injections in Run3, are discussed. The LHCb detector is characterised by a forward geometry that develops along the direction of the beams. The gas is injected into the storage cell from a capillary connected in the middle of its outer surface. Since the results presented in this section refer to the RF foil boxes, a system of reference with the longitudinal axis z aligned with the direction of the beams is considered, with its origin at the interface between the storage cell and the RF foil. The storage cell, thus, develops in the $[-20; 0]$ cm longitudinal interval with the injection point at $z = -10$ cm, while the RF foil boxes extend up to $z = 110$ cm.

The level of saturation can be defined according to different indicators:

- the fraction of total saturated area gives a general idea of the level of degradation, but it lacks any spatial information;

- the LHCb experiment is the maximum z with a saturated facet is ideal to evaluate the depth at which the saturation has propagated, but it is sensitive to spatial fluctuations since it does not factor the level of saturation at a given position.

The fraction of saturated area in z slices integrates the two approaches, giving an indication of the level of saturation at any longitudinal position. Finally, a picture of the NEG degradation temporal evolution can be obtained by mapping the sticking coefficient of each facet at different physical time. Three-dimensional heat maps, where each facet is

Table III.2.4: Parameters used to simulate H_2 (central column) and N_2 (left column) injection.

Parameters	H_2	N_2
Injected flux	1.5×10^{-4} mbar·l/s	4.05×10^{-5} mbar·l/s
s_0	0.0179	0.015
x_{max}	1.098×10^{17} cm^{-2}	1.5×10^{14} cm^{-2}
Simulation flow	Time evolving $CPUtime$	Time evolving $CPUtime$
Stop condition	96 hours of real simulated time	10 hours of real simulated time

represented as a point corresponding to its centre and the sticking value is shown through the point colour intensity, can be used. Alternatively, the sticking coefficient of each facet can be projected along the longitudinal direction z, to get a more immediate view of the sticking coefficient as a function of the depth in the geometry.

In order to monitor the stability and reliability performance of the algorithm, some additional distributions are taken into account. In particular, the number of adsorbed virtual particles at saturation for each facet monitors the impact of the micro-facets on the final results, while the number of hits for each facet can highlight regions in the geometry that are not tested during the simulation. The distribution of the resolution $\sigma_{\Delta C;i,j}$, normalised to the minimum $\Delta C_{i,j}$, can also be checked in order to verify that the approximations chosen during the simulation do not significantly impact the final result. In particular, the distribution of the over-saturation is a good indicator of the precision with which the saturation has been reached. The relative uncertainty on the concentration of each facet at the end of the simulation can also be used to assign a final uncertainty on the result.

III.2.4.1   Results for H_2

As presented in Sec. III.1.2, beside the loss of pumping speed, H_2 adsorption can bring to the embrittlement and, in extreme cases, to the flaking and peel off of the coating film. The simulation of the degradation of the NEG is thus also needed to understand the H_2 load that can be expected in the RF foil, to be compared to experimental results and to understand the limits of injection that can be reached. Now, while the functional dependence between the atomic concentration and the sticking coefficient is the same for all the NEG samples, the normalisation constant, corresponding to the starting sticking coefficient, is measured at constant injecting pressure and depends both on the type of substrate and the pressure value. Since the simulation only allows the injected flux in the storage cell to be configured, as it happens during SMOG2 operations, the corresponding pressure value in the RF foil must be checked to be compatible with the one considered for the sticking coefficient evolution model.

The simulation has been run by considering a total real simulated time comparable with the H_2 and D_2 injection time expected in one year of SMOG2 operation, 96 hours. For the injected flux, the expected highest value, 1.5×10^{-4} mbar·l/s, has been considered in order to monitor for saturation and embrittlement in the worst case scenario. A summary of the parameters chosen for the simulation can be found in Tab. III.2.4.

As shown in Fig. III.2.6, the onset of saturation begins at around 20 hours of injection. The fraction of saturated area (Fig. III.2.6, right) keeps increasing linearly throughout
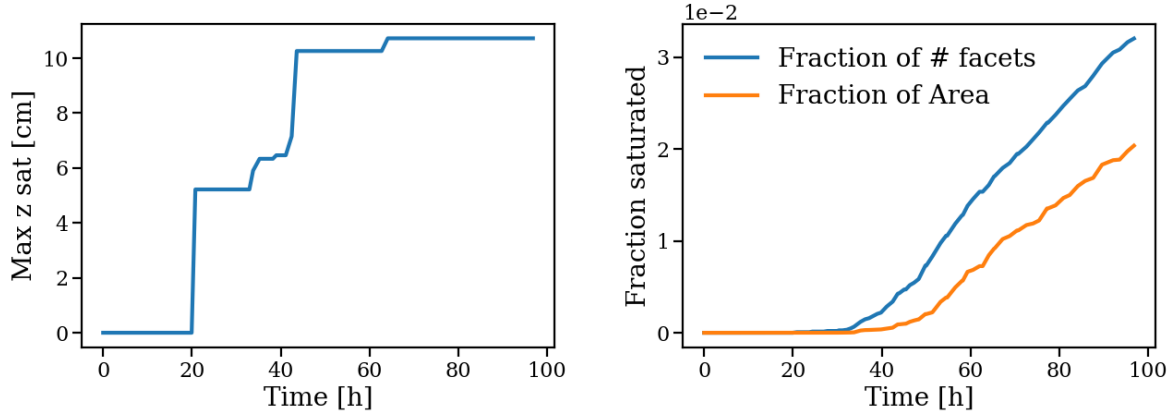
Figure III.2.6: Sticking coefficient simulation results as a function of H_2 injection time. Left: maximum longitudinal position z with a saturated facet in the RF foil as a function of the injection time. Right: fraction of saturated facets (blue) and fraction of saturated area (orange) of the RF foil as a function of the injection time.
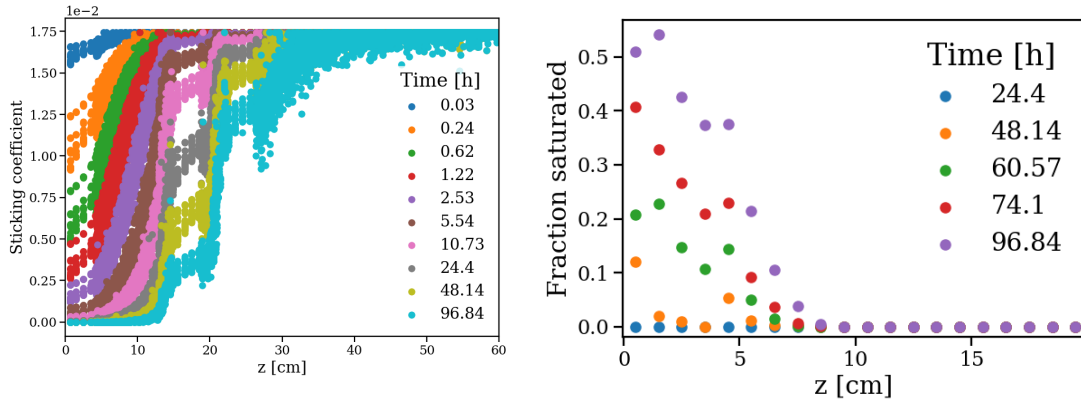

Figure III.2.7: Sticking coefficient simulation results for H_2 injection as a function of the longitudinal position z of the facets in the RF foil, for different time steps. Left: RF foil facets sticking coefficient as a function of z for different injection times. Right: fraction of saturated area of the RF foil as a function of z for different injection times.

the whole simulation, mainly concentrating in the central region of the foil. The fraction of saturated facets is also shown in the plot. The maximum penetration of the saturation is shown in Fig. III.2.6, left, as a function of time. After 48 hours the penetration of the saturation slows down due to the geometry conformation. When the gas reaches the first corrugated section, the conductance towards higher z is reduced and it is more difficult for the gas to reach and saturate the facets further away. The maximum penetration of the saturation thus progresses slowly, while the fraction of saturated area can keep increasing because the surface corresponding to the same Δz is higher. The same effect can be better appreciated from the sticking coefficient distribution as a function of z for different time steps (Fig. III.2.7, left), where a visible propagation in z of saturated facets, corresponding to the points aligned along 0, requires a progressively increased time. From the same plot, it can be also appreciated how the overall degradation of the sticking coefficient slows down progressively, due to the reduced sticking coefficient and thus the increased number of interactions required to have the adsorption of a particle.
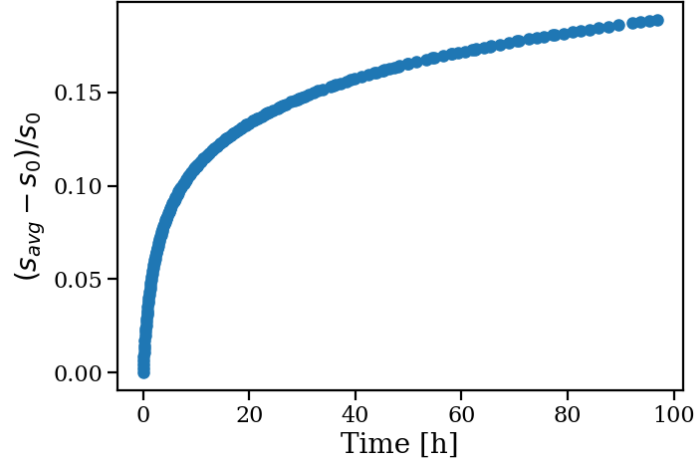
Figure III.2.8: Relative variation of the mean sticking coefficient as a function of time for H_2 simulation.
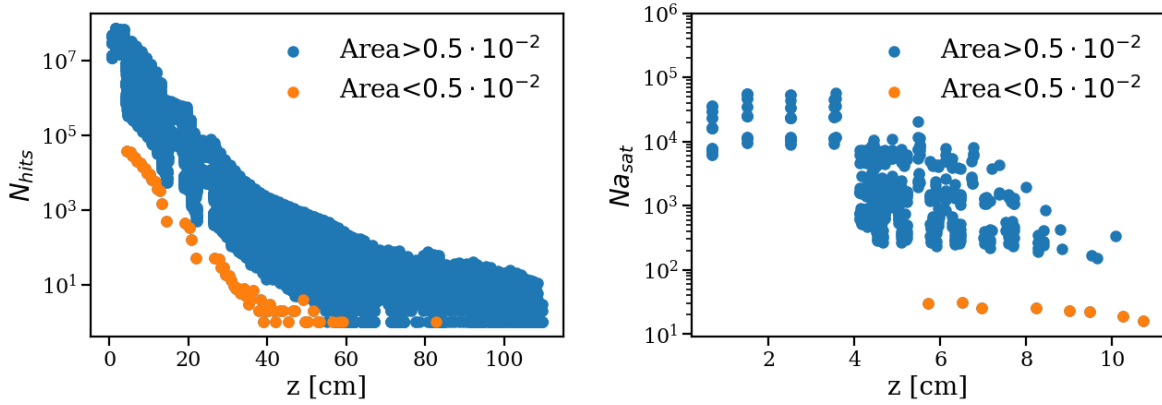

Figure III.2.9: Number of hits at the end of the H_2 simulation (left) and number of adsorbed virtual particles at saturation (right) as a function of the longitudinal position z of the facets in the RF foil. The orange dots correspond to facets with an area lower than $0.5 \cdot 10^{-2}$ cm^2, for which a lower interaction probability is expected.

After simulating 96 hours of continuos injection, only 2% of the RF foil is saturated (Fig. III.2.6, right), with a penetration of around 11 cm. Considering in more details the fraction of saturated area in z slices (Fig. III.2.7, right), the saturation is limited to at most 50% of each slice and only the first 7 cm presents a level of saturation higher than 10%. The total reduction of the sticking coefficient expected after one year of operation, defined as the relative difference between the starting sticking coefficient and the mean sticking coefficient of the RF foil at the end of the simulation, is around 20%, as shown in Fig. III.2.8.

In terms of atomic concentration, the level reached at the end of the simulation corresponds to around 3% for the first 20 cm of the RF foil, to around 0.55% considering the whole geometry. This value, limited by the pressure in the system, is well below the embrittlement threshold [186]. Hence, as confirmed from experimental data, no embrittlement is expected at the pressure scales which SMOG2 operates.
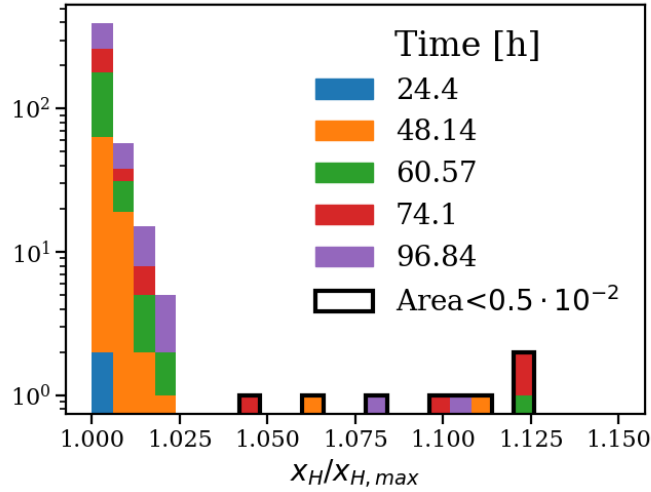
Figure III.2.10: Distribution of the over-saturation of the facets as a function of time for H_2 simulation. The distribution corresponding to facets with an area lower than $0.5 \cdot 10^{-2}$ cm^2 is superimposed as a solid black line.

Figure III.2.9, left, shows the final number of hits on the facets as a function of the longitudinal position, demonstrating that the complete geometry is probed during the simulation. The impact of the micro-facets can be seen in both Fig. III.2.9, right, and Fig. III.2.10, where it is shown that they reach saturation with around 10 adsorbed virtual particles with an average over-saturation of 9%. Since they only represent the 0.07% of the saturated area, their impact on the final results is negligible. For all the other facets, the saturation is reached on average after 10^4 adsorptions, with a maximum over-saturation of 2.5%, but it depends proportionally on the area of the facets, as shown in Fig. III.2.11, left. As expected from Eq. III.2.21, an inverse proportionality can be observed between the statistical uncertainty on the concentration and the area (Fig. III.2.11, right). The final uncertainty at saturation on the concentration is 4.7%, corresponding to an uncertainty on the sticking coefficient of 17.3%.

Finally, in order to check the validity of the evolution model applied, the maximum pressure in the RF foil, corresponding to the value at the interface with the cell, is considered as a function of time (Fig. III.2.12, left). After a steep increase at the beginning of the simulation, it stabilises around 2×10^{-6} mbar, corresponding to the pressure value considered for the sticking model applied. The pressure profile along the longitudinal direction z for the complete geometry is also shown in Figure III.2.12, right, where the corresponding profile for the isolated ideal cell is superimposed. While an overall agreement with the expected profile is observed, the ideal model does not reproduce the gas tail towards positive z values due to the gas flow towards the RF foil. A residual pressure inside the RF foil can be found up to around 40 cm, where the level due to the gas injected in the storage cell reaches values comparable to the nominal pressure inside the LHC primary vacuum.
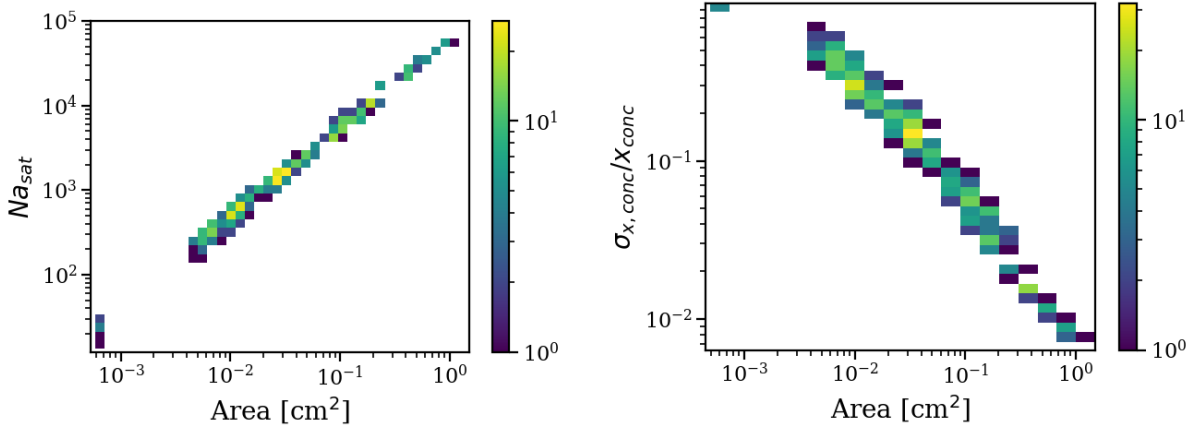
Figure III.2.11: Distribution of the number of adsorbed virtual particles (left) and of the relative statistical uncertainty on the concentration (right) at saturation as a function of the area of the facets, for H_2 simulation.
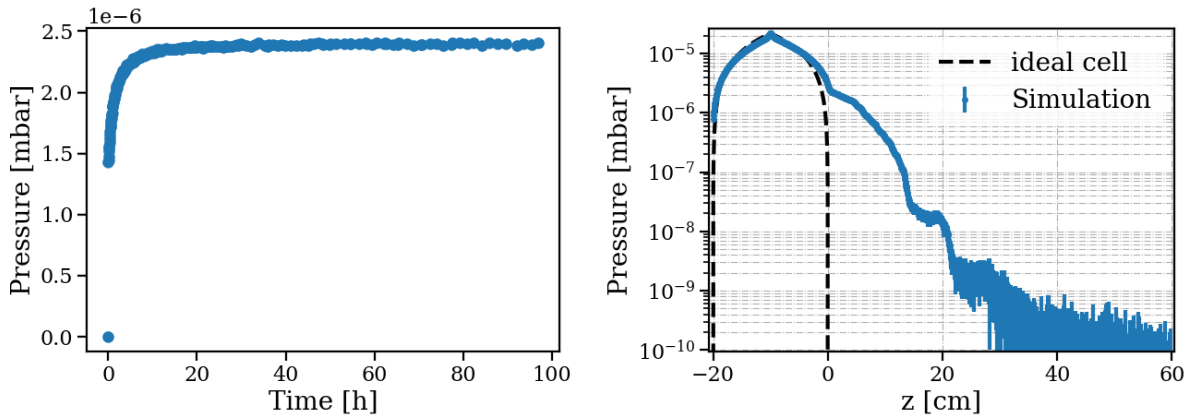

Figure III.2.12: Pressure at the interface between the storage cell and the RF foil as a function of time (left) and pressure profile along the longitudinal direction z at the end of the simulation (blue dots) and for the ideal cell (black dashed line).

III.2.4.2 Results for N_2

Similarly to H_2, the simulation parameters for N_2 have been chosen in order to reproduce one year of SMOG2 operation, corresponding to 10 hours of total real simulated time with an injected flux of 4.05×10^{-5} mbar·l/s. A summary of the parameters chosen for the simulation can be found in Tab. III.2.4.

The degradation of the sticking coefficient progresses much faster and spreads uniformly in the whole RF foil section (Fig. III.2.13). The saturation begins after around 3 minutes, and after 30 minutes the first 5 cm are completely saturated (Fig. III.2.14, right). After 10 hours, 13 cm of the RF foil are completely saturated, but a non-negligible fraction saturates up to 20 cm (Fig. III.2.13, left and Fig. III.2.14, right). Overall, more than 15% of the area is saturated. As in the H_2 simulation, the effect of the geometry configuration can be seen as a decrease in the degradation speed. For N_2, thanks to the faster and more uniform degradation, the effect is more clear, as illustrated by Fig III.2.13 and
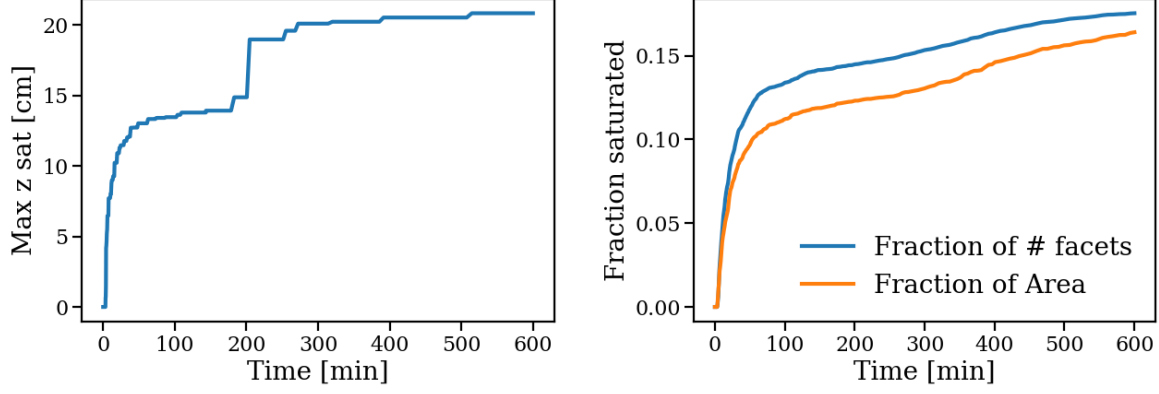
Figure III.2.13: Sticking coefficient simulation results as a function of N_2 injection time. Left: maximum longitudinal position z with a saturated facet in the RF foil as a function of the injection time. Right: fraction of saturated facets (blue) and fraction of saturated area (orange) of the RF foil as a function of the injection time.
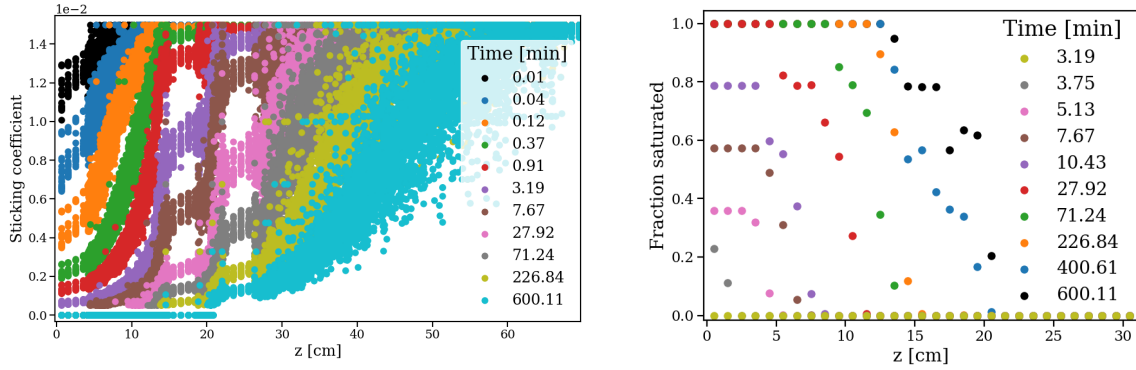

Figure III.2.14: Sticking coefficient simulation results for N_2 injection as a function of the longitudinal position z of the facets in the RF foil, for different time steps. Left: RF foil facets sticking coefficient as a function of z for different injection times. Right: fraction of saturated area of the RF foil as a function of z for different injection times.

Fig. III.2.14. The total reduction of the sticking coefficient expected after one year of operation is around 37%.

Similar quality checks as for the H_2 simulation are performed, confirming that the whole geometry is involved during the simulation (Fig. III.2.16, left). The average number of adsorbed virtual particle at saturation is around 10^3 (Fig. III.2.16, right), lower than for the H_2 as expected from the different sticking coefficient model. As for the micro-facets, thanks to the wider distribution of the saturation, their impact is reduced to 0.02% of the total saturated area. The over-saturation level reaches 4% (Fig. III.2.17), higher than the values reached for H_2. A similar decrease in the accuracy of the results can be observed also in Fig. III.2.18, left, where the number of adsorbed virtual particles at saturation present a broader distribution as a function of the area. This is propagated to the distribution of the statistical uncertainty on the concentration (Fig. III.2.18, right), giving a final uncertainty at saturation of 28% on the concentration and 39% on the sticking coefficient.

The results of these simulations, together with laboratory measurements on NEG sam-
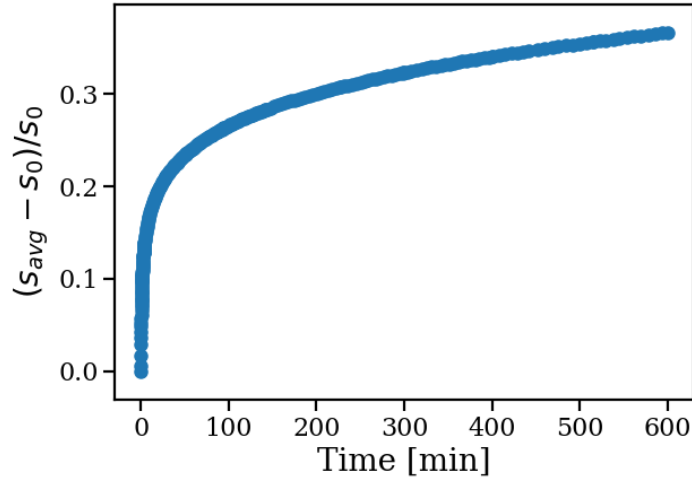
Figure III.2.15: Relative variation of the mean sticking coefficient as a function of time for N_2 simulation.
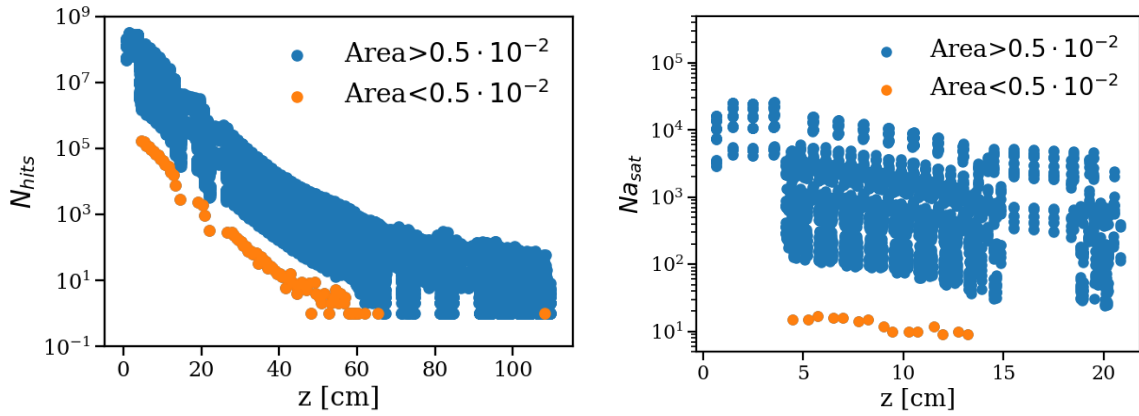

Figure III.2.16: Number of hits at the end of the N_2 simulation (left) and number of adsorbed virtual particles at saturation (right) as a function of the longitudinal position z of the facets in the RF foil. The orange dots correspond to facets with an area lower than $0.5 \cdot 10^{-2}$ cm^2, for which a lower interaction probability is expected.

ples [186], assured that the level of saturation prospected in the RF foil during Run 3 SMOG2 operation acceptable for LHC operation and the values of hydrogen concentration in the NEG bulk are not expected to cause the onset of embrittlement. These studies contributed to the final approval to the injection of both hydrogen-like and getterable gases. A first H_2 injection into the SMOG2 storage cell took place in November 2022.
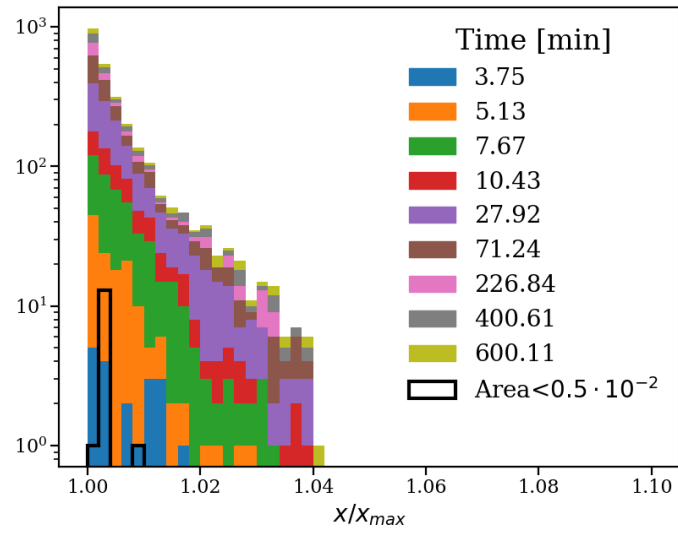
Figure III.2.17: Distribution of the over-saturation of the facets as a function of time for N_2 simulation. The distribution corresponding to facets with an area lower than $0.5 \cdot 10^{-2}$ cm^2 is superimposed as a solid black line.
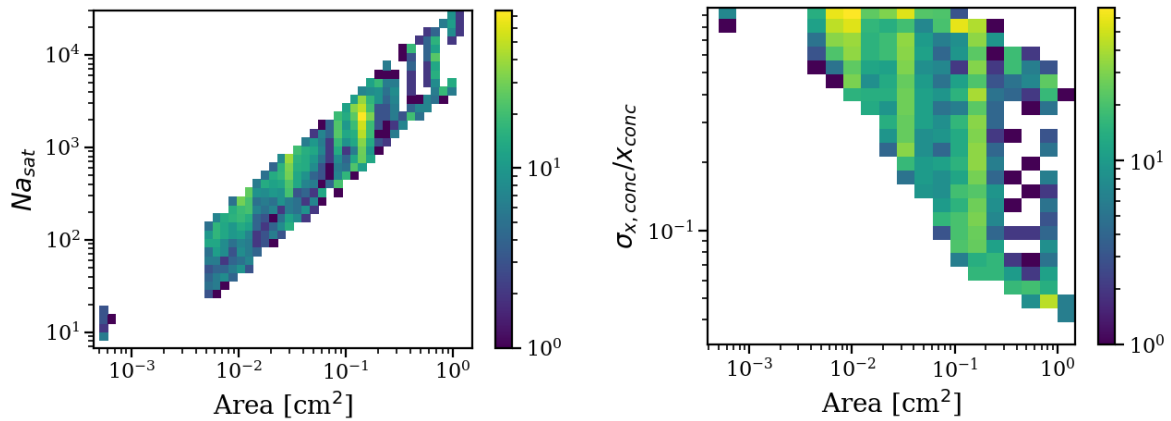

Figure III.2.18: Distribution of the number of adsorbed virtual particles (left) and of the relative statistical uncertainty on the concentration (right) at saturation as a function of the area of the facets, for N_2 simulation.

III.3 SMOG2 first data collection

The beginning of the LHC Run3 has been dedicated to the commissioning of the upgraded LHCb detector. In this chapter, the commissioning of the SMOG2 system is presented, focussing on its validation and integration into the LHCb control system. In Section III.3.1, the first data acquired while injecting argon or hydrogen gas in the SMOG2 storage cell are compared to the simulations to validate the models, in particular for the gas density profile. Section III.3.2 describes the operational steps required for injecting gas via the gas feed system, the acquisition of the operational data for monitoring purpose and their integration in the LHCb control system is presented.

III.3.1 Gas density profile validation on data

During the commissioning of the LHCb upgraded detector in 2022, data samples with different injected gases have been collected and used to validate the simulation results and the expected performance of the new injection system.

In particular, the validation of the gas density profile in the longitudinal direction z is crucial for a precise luminosity measurement: the luminosity calculation assumes an ideal isolated cylindrical cell with the gas injected from its centre. In these conditions, the longitudinal density profile would assume a triangular shape and the areal density is obtained as seen in Eq. III.1.14. These simplifying hypotheses are not met in the real implementation of the system. Firstly, the cell is positioned inside a complex geometry that modifies the gas distribution, as already illustrated in Fig. III.2.12, right. Moreover, the gas is injected from a capillary in the middle of the side surface, which creates a high density region in correspondence of the injection point. Detailed simulations are thus needed to understand the effects of the real cell implementation and evaluate a correction factor to be applied on the luminosity calculated in the ideal scenario. The results, first, must be validated on the data collected.

III.3.1.1 Luminosity correction factor from simulation

The Molflow+ software has been used to study the longitudinal density profile in the cell introducing the realistic conditions described in the previous paragraph. Three geometries have been taken into consideration:
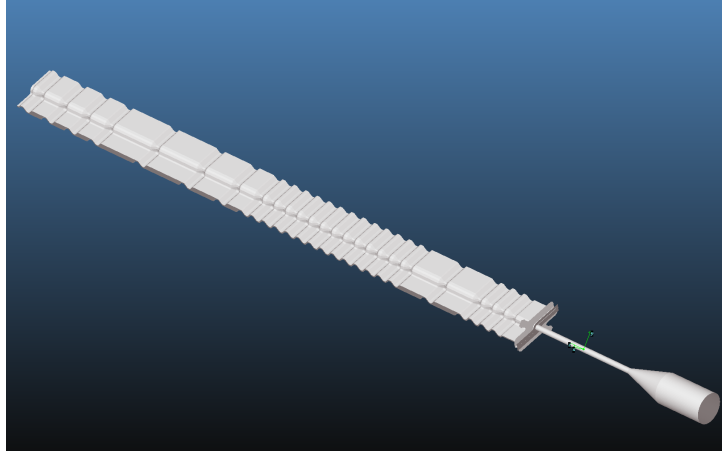
147

Figure III.3.1: Detailed geometry of the storage cell and the RF foil with the WFSs.

- An isolated cylindrical cell where the gas is injected from a circular opening in the middle of the lateral facets. The dimensions considered for the geometry correspond to the values measured on the cell using a coordinate measuring machine [198]: $L = 20.015$ cm, $D = 1.004$ cm, where the latter represents the average of the two extreme diameters, equal to 1.002 cm and 1.007 cm.

- The same cylindrical cell is considered interfaced to the RF foil, in the same geometry used for the dynamic simulation (Sec. III.2.3.3). The WFS upstream of the cell is not considered.

- A detailed description of the complete system is required to understand the effects at the edge of the cell. A further geometry is thus considered, where both the upstream and downstream wake filed suppressors (Sec. I.4.3.1) are precisely modelled starting from the available CAD model, as it is shown in Fig. III.3.1. The upstream WFS is modelled as an opaque cone and a semi-transparent cylinder, where the fraction of opacity is given by the ratio between the area of the CuBe strips and the total area of the tube. The downstream WFS is modelled following the profile of the RF foil and the opacity has been set following the same principle as for the upstream WFS.

The simulations have been generated considering the injection of 1.05×10^{-5} mbar·l/s of Ar, in order to reproduce the condition used for the data acquired during the first runs of 2022. Nonetheless, the same results are expected to be valid for all gas species and flow rates, up to a normalisation factor, since the density is proportional to the gas flow rate Q and the gas molar mass M.

In order to obtain a precise evaluation of the density profile along the longitudinal direction together with an estimation of the uncertainty associated to the statistical accuracy of the simulation, the texture tool available in Molflow+ is used. A transparent facet oriented orthogonal to the gas flow is used to evaluate the density distribution in the middle of the cell. The facet is 5 mm wide, in order to amply cover the region seen by the LHC beams, and it extends beyond the geometry extremes in length, in order to avoid spurious effects due to the cut-off at the edges. The facet is texturised considering a rectangular meshing with a resolution of 0.5 mm in the longitudinal direction and 0.1 mm in the transverse
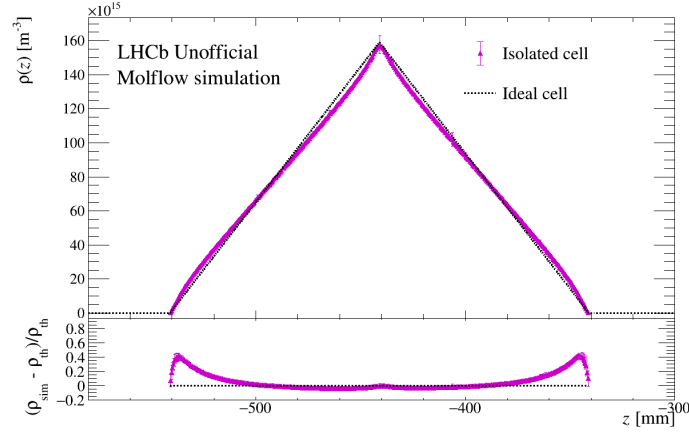
Figure III.3.2: Simulation of the gas density as a function of the longitudinal coordinate z for the isolated cell (pink); the ideal profile is superimposed (dotted black). In the bottom panel the residuals with respect to the ideal profile are shown.

direction. Under the hypothesis of a uniform gas distribution in the transverse direction, 100 independent measurements of the density are made available for each z position and the value for the profile is obtained from their average, with a statistical uncertainty given by their standard deviation.

In Fig. III.3.2, the density profile for the isolated cell is reported together with the density profile expected for the ideal cell. The residuals relative to the ideal model are also shown in the bottom box. While a general agreement is observed, the injection from the capillary on the side of the cell generates a deformation in the density profile, as clearly highlighted in the residuals plot. This deformation, however, does not impact the areal density, calculated integrating the profile between the cell extremes, which turns out to be compatible within the statistical uncertainty with the ideal one.

Considering the cell interfaced with the RF foil, the results for the density profile in Fig. III.3.3 confirms the deviation observed in Fig. III.2.12, right. The gas tail extending towards positive z values is due to the lower conductance of the RF foil compared to the cell. This obstructs the gas extraction and generates an accumulation towards the RF foil edge, right where the density is expected to go to 0. The increase in areal density corresponds to $\sim 7\%$, but largely depends on the conductance of the interface between the cell and the RF foil and, thus, it must be compared with the result for the complete geometry to understand the impact of the approximation in the geometry modelling. Figure III.3.4 shows distribution for the detailed geometry (left) and the comparison between the two geometries (right). A realistic modellisation of the downstream WFS suppresses the positive z tail but, at the same time, the introduction of the upstream WFS create a lower tail towards negative z values: while in the previous model the gas was free to expand to infinity out of the cell, giving a density equal to 0 at the extreme, the upstream WFS channels the gas extraction, generating the smooth transition towards negligible density. Overall, the two effects compensate each other and the areal density increase is compatible with 7%. Nevertheless, the detailed geometry allows to better understand the edge effects that can be expected during the data-taking, and it is thus favoured.

For completeness, in Tab. III.3.1 the values obtained for the areal density and the associated
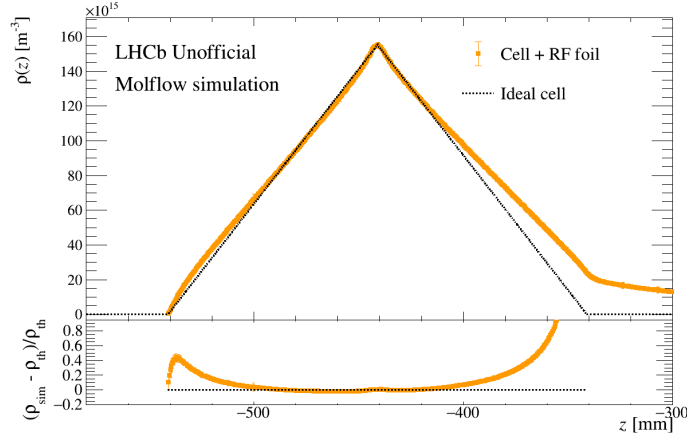
149

Figure III.3.3: Simulation of the gas density as a function of the longitudinal coordinate z for the cell and RF foil (orange); the ideal profile is superimposed (dotted black). In the bottom panel the residuals with respect to the ideal profile are shown.
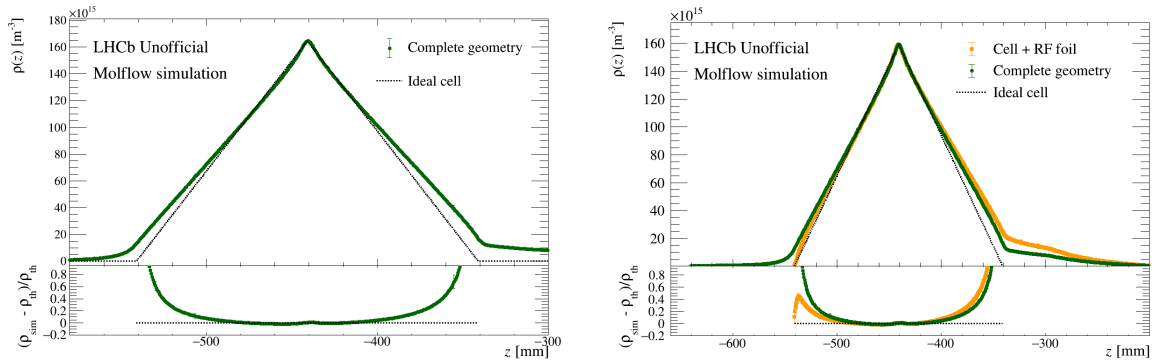

Figure III.3.4: Left: simulation of the gas density as a function of the longitudinal coordinate z for the detailed geometry (green); the ideal profile is superimposed (dotted black). Right: comparison of the simulated density profile for the detailed geometry (green) and the cell+RF foil geometry (orange); the ideal profile is superimposed (dotted black) In the bottom panels the residuals with respect to the ideal profile are shown.

correction factor K_θ, obtained as the ratio between the areal density obtained in a realistic model and the ideal value by Eq. III.1.14, are summarised.

III.3.1.2 Transverse gas density studies for BGI measurements

During Run3, the BGI technique [77, 130], used for the luminosity and ghost charge measurement, will benefit from the increase interaction rate and statistics provided by the SMOG2 cell injection system. A precise knowledge of the three-dimensional gas density distribution inside the cell is fundamental to understand possible disuniformities that would introduce systematics effects on the BGI results. While the longitudinal profile has been deeply studied for the fixed-target luminosity measurement, the transverse profile, in the $x - y$ plane, has never been studied and assumed to be uniform. The Molflow+ simulation samples obtained with the complete geometry have thus been considered to perform the first detailed study of the transverse density profile. A transparent facet in the

Table III.3.1: Simulated areal density obtained by injecting 1.05×10^{-5} mbar·l/s of Ar for the ideal model and for the three possible geometry implementations detailed in the text (middle column); the corresponding correction factor related to the ideal model are shown in the right column.

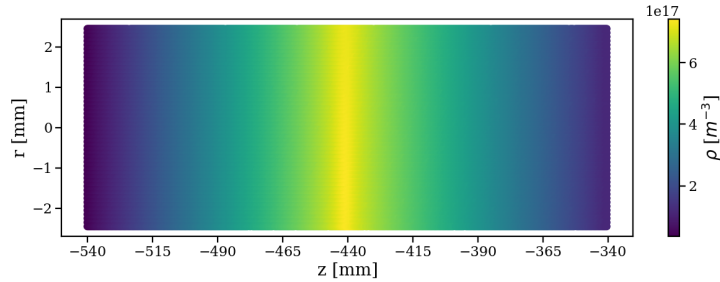| Model	$\theta \times 10^{12}$ [cm^{-2}]	K_θ
Theory	1.590	-
Isolated cell	1.590 ± 0.013	1.000 ± 0.008
Cell + RF foil	1.701 ± 0.017	1.070 ± 0.011
Complete	1.700 ± 0.009	1.069 ± 0.006

Figure III.3.5: Bidimensional density profile in the middle of the cell.

middle of the cell is considered to obtain a bi-dimensional maps of the density. While the longitudinal axis z is oriented parallel to the direction of the beam, the transverse axis r is chosen to be parallel to the gas flow injection direction (*i.e.* $45°$ in the $x - y$ plane). The facet is texturised considering a rectangular meshing with a resolution of 0.5 mm in the longitudinal direction and 0.1 mm in the transverse direction. The density distribution is shown in Fig. III.3.5, where the triangular longitudinal profile is clearly identified by the gradual density decrease from the centre to the extremes. The density disuniformity $\Delta\rho(r, z)$ in the transverse plane is evaluated as the relative difference between the density measured in the texture cell $\rho(r, z)$ with respect to the average density $\langle\rho\rangle(z)$ at the given longitudinal position z:

$$\Delta\rho(r, z) = \frac{\rho(r, z) - \langle\rho\rangle(z)}{\langle\rho\rangle(z)}. \tag{III.3.1}$$

As it is illustrated in Fig. III.3.6, top, the injection of gas through the capillary produces an increased density in the region under the injection point, which translates into a high disuniformity in the density distribution. When the region of ± 5 mm around the injection point is excluded, the density distribution results to be uniform at the 0.15% (Fig. III.3.6, middle and bottom), which is within the resolution limits of the BGI measurements.

III.3.1.3   Validation on data

A dataset consisting of around 20 minutes of Ar injection into the SMOG2 cell is considered for the following studies. A tomography of the cell [199], shown in Fig. III.3.7, is obtained reconstructing the vertices coming from beam collisions on the residual gas in LHC and
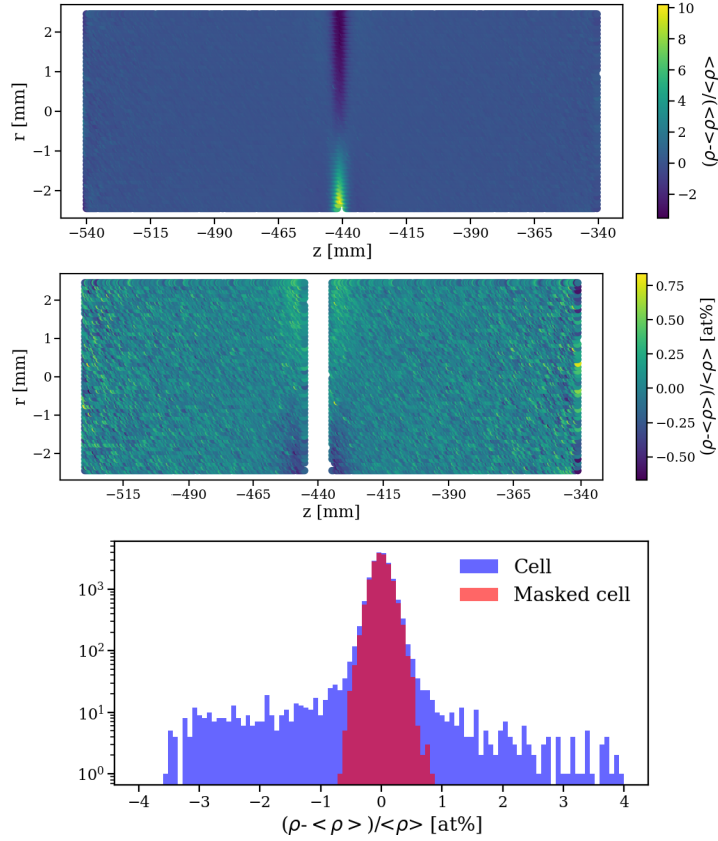
Figure III.3.6: Bidimensional map of the gas density disuniformity in the transverse plane in the middle of the cell (top); the disuniformity map excluding the central region in correspondence to the gas injection is also shown (middle). The disuniformity distribution in the two cases are reported in the bottom figure.

secondary interactions in the material. The closed cell with its wings and the injection capillary support are distinguished, confirming its position relative to the beam spot.

In order to obtain the gas density distribution from the acquired data, the distribution of the primary vertices longitudinal coordinate is considered. Indeed, the primary vertices reconstructed in $z \in [-541; -341]$ mm are generated from the collisions of the beam and the injected gas, thus their distribution follows the gas density. The primary vertices are reconstructed selecting VELO tracks with a low Distance Of Closest Approach (DOCA) to form seeds that are then fitted to determine the vertex position. The combinatorial background and secondary vertices are suppressed requiring a minimum of 3 tracks associated with the vertex, weighting the fit based on the χ^2_{IP}, which is the increase in the χ^2 of the primary vertex fit when a certain track is included, and selecting vertices within a maximum radial distance from the beam line. In Fig. III.3.8, the distribution over the whole interaction region is shown [199]: two clearly separated peaks can be seen, around the nominal interaction point and the SMOG2 cell confinement region, respectively. The LHCb detector is able to operate simultaneously with two separated interaction points, studying collisions in two different systems and with two energy scales.

The normalised distribution in $z \in [-600; -250]$ mm is compared to the normalised simulation obtained with the complete geometry, in Fig. III.3.9. A general agreement is observed, and in particular the simulation is able to well reproduce the tails towards
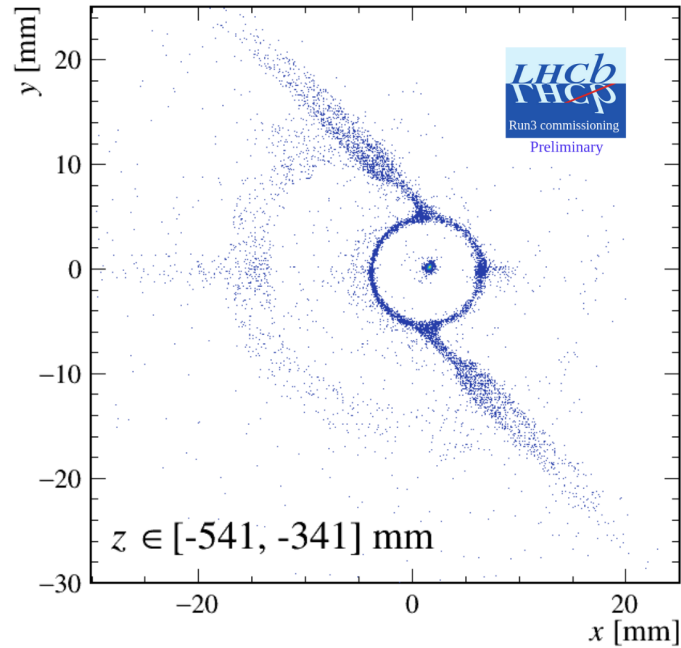
Figure III.3.7: Reconstructed vertices with $z \in [-541, -341]$ mm from beam collisions on the residual gas in LHC and secondary interactions in the material. The beamspot, the SMOG2 cell in its fully closed position and the support of the injection capillary (right side of the cell) can be clearly distinguished. Figure taken from Ref. [199]
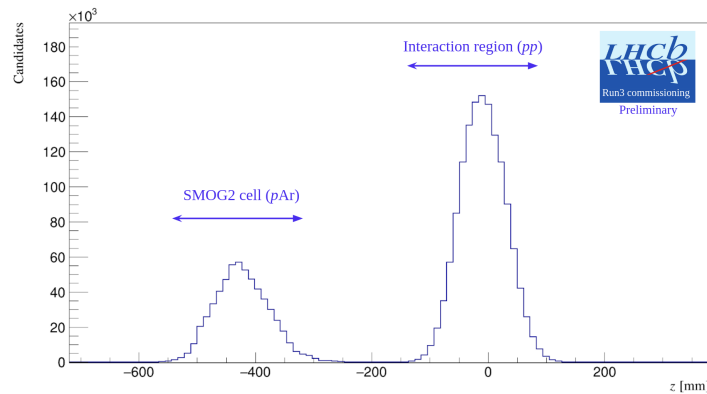

Figure III.3.8: Distribution of the primary vertex longitudinal coordinate. Figure taken from Ref. [199]

negative and positive value of z, outside the cell, confirming the reliability of the considered geometry. While some discrepancies are still present, it is worth to consider that the data have been acquired during the preliminary phase of commissioning of the whole detector and data chain, during which the performances were still under optimisation. The comparison will thus be repeated with data acquired with the commissioned detector, in order to understand if the effects are physical or associated with problems with the vertices reconstruction algorithm, such as errors in the real-time alignment of the VELO detectors.

Finally, the comparison of the normalised distributions of the primary vertices z for
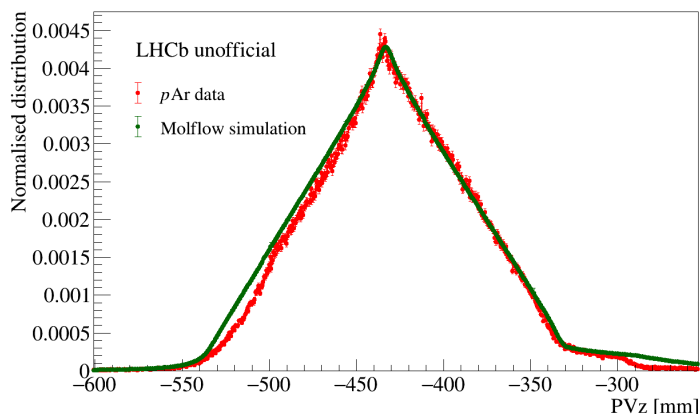
Figure III.3.9: Comparison between the normalised distribution of the primary vertex longitudinal coordinate reconstructed in the storage cell and the normalised gas density profile obtained with the detailed geometry in a Molflow+ simulation.
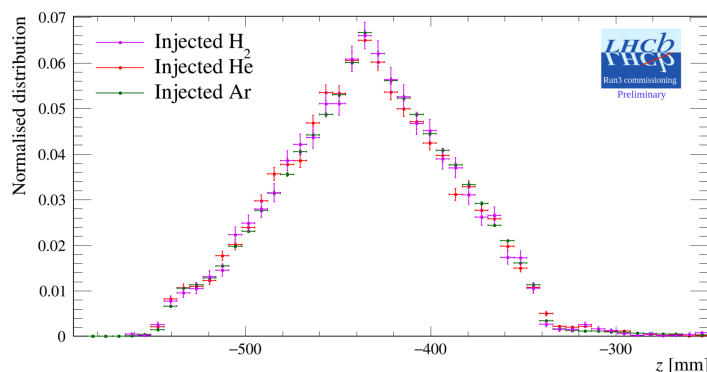

Figure III.3.10: Normalised distributions of the longitudinal coordinate for primary vertices in SMOG2 with injected hydrogen, helium and argon. Figure taken from Ref. [199]

datasets acquired injecting Ar, He and H_2 (Fig. III.3.10) confirms that the density profile is independent of the gas species considered, as expected from theory.

On the 10th of January 2023, a sequence of equipment failures in the LHC vacuum system around the VELO detector resulted in a build up pressure beyond specification between the VELO secondary vacuum inside the RF foils and the primary vacuum in the LHC beam volumes. As a consequence, while the VELO modules were not damaged, the RF foil boxes suffered a plastic deformation up to 14 mm (Fig. III.3.11) and will have to be replaced during the 2023-2024 winter technical stop. Due to the deformation, the VELO detector could not be closed during 2023 data-taking and, since the two halves of the SMOG2 cell move together with the RF foil, the SMOG2 cell remained open. No data in the SMOG2 configuration is thus available in 2023, but the SMOG2 gas injection system has been instrumental for the diagnosis of the situation, allowing to perform the tomography of the RF foils and detector material with a level of precision of the order of µm, and it has been consistently used for injections in the VELO vessel for the physics data samples.
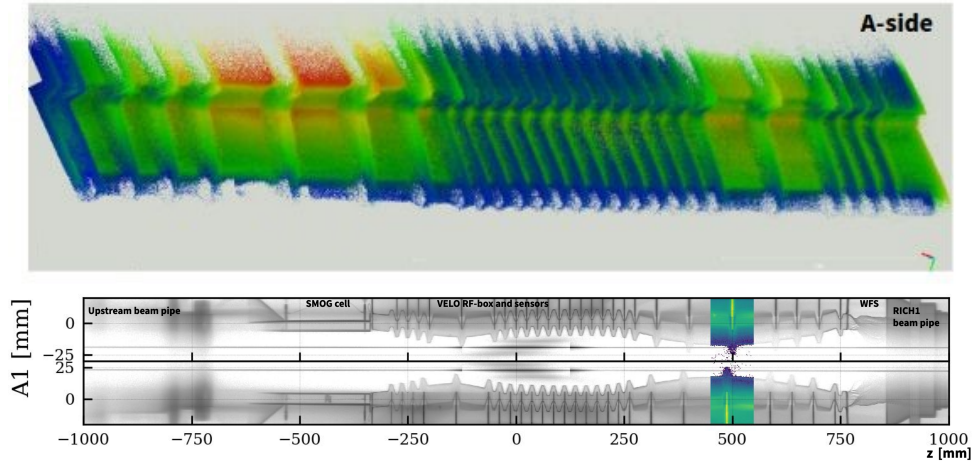
Figure III.3.11: Reconstructed vertices in the VELO RF foil from beam collisions on the SMOG2 injected gas and secondary interactions in the material. A three-dimensional reconstruction (top) and the transverse section (bottom) of the RF foil are shown where the deformation of the foil can be clearly distinguished.

III.3.2 SMOG2 real-time monitoring and integration in the LHCb control system

The operation of the SMOG2 system during the beginning of Run3 has been deferred to the LHC vacuum experts team, in order to safely carry out the commissioning and calibration of the injection probes. Several injection tests have been performed both in the SMOG2 cell and in the VELO vessel to set the optimal injection procedure and working point, finding a compromise between maximising the physical output and reducing the impact on LHC and LHCb operation.

Nevertheless, even though the gas feed system is completing its calibration, SMOG2 system has proven to be crucial to speed-up the overall commissioning of the detector as well as being fundamental for the luminosity measurement of all the four major experiment on the LHC ring, providing precise ghost charge measurement through the beam-gas imaging. It is thus fundamental to be able to monitor from the LHCb control system the status of SMOG2 system and to automatically propagate this information in order to make it accessible during data analysis. In particular, the information on the injected gas and the stability of the pressure is fundamental for the calculation of the luminosity in the fixed-target configuration. The integration of the SMOG2 subsystem into the LHCb control system can be organised into three targets:

- the injection controls must be integrated into the main LHCb operation panel in order to allow for a fast and efficient data acquisition. While the injected gas species, flow rate and injection mode should be set by the SMOG2 experts, the start and stop of the injection itself should be under the control of the LHCb operators;

- the injection conditions must be propagated to the condition database, where the acquisition conditions for each run are stored (*e.g.* the magnet polarity, filling scheme). In order for the information to be accurate, an automatic change of run when the status of SMOG2 system changes must be also implemented;
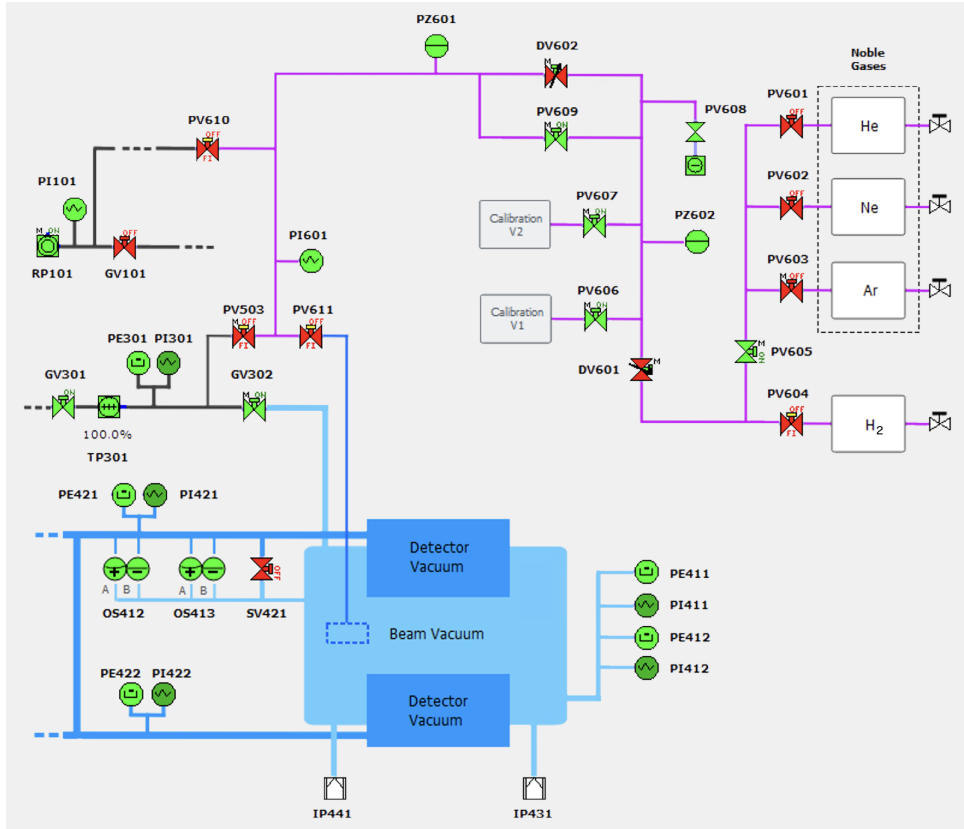
Figure III.3.12: Schematic representation of the GFS of the SMOG2 system.

- a monitoring panel is required to allow the experts to keep track of the operational status of the system and intervene promptly in case of problems. In particular, the temperature and pressure readings are fundamental, together with the status of the valves and gauges on the GFS.

The first point requires an automated injection procedure to be implemented, which in turn needs a fully commissioned and calibrated system. For this reason, its implementation is postponed and the injection controls, still manual, are maintained under the control of the LHC vacuum experts team. The understanding of the injection process is still crucial for the implementation of a functional monitoring interface and to define the fundamental status and conditions to be propagated in the database.

III.3.2.1 SMOG2 injection cycle

The SMOG2 GFS, as presented in Sec. I.4.3 and shown schematically in Fig. III.3.12, is a multi-gas injecting system composed of multiple remotely controlled valves and gauges that allows the injection flow rate to be controlled while operating in two different configurations. It is integrated within the complex LHC vacuum system at the LHCb experiment and it is interfaced with the VELO vacuum system. The injection procedure has been developed in order to maximise the physics output, in terms of both purity of the sample and acquisition time, ensuring at the same time the safety of the LHC and VELO vacuum systems. The process can be separated into five main steps:

Setting the vacuum configuration to the injection regime The VELO vessel is typically kept under the required vacuum regime via ion pumps. In order to safeguard their functionality, when injecting they are switched off and the pumping is moved to the auxiliary turbo pump positioned on the SMOG2 injection inlet and connected to the VELO vessel through the GV302 valve, which must be opened. Since changing the status of the vacuum equipments when the beams are circulating can cause pressure spikes and instabilities, the preparatory steps must be always carried out when no beam is in the LHC ring.

Preparation of the high pressure GFS arm The desired gas reservoir, filled at 1500 mbar, is opened to fill the high pressure arm of the GFS. The reservoir is then kept closed during the injection, to limit the gas consumption. The gas in the arm is sufficient to feed multiple injections, therefore the high pressure line is cleaned only during inactive periods or when a change in the injected species is required. This is achieved, completely opening the dosing valve DV601 to put the high pressure arm in communication with the pumping group at the PV608 valve. Considering the presence of two separated lines for noble gases and getterable gases, that must be kept separated at all times, the pumping proceeds in two steps and it is completed within a few hours.

Preparation of the low pressure GFS arm The low pressure arm of the GFS and the injection line are constantly pumped outside of operation, keeping the PV609 and PV608 valves open, in order to avoid contamination in the injected gas, mainly from N_2 degassing. When an injection is planned, the table is isolated from the line, closing PV609, and the pumping from PV608 is stopped. The dosing valve DV601 between the high pressure and low pressure arms is then opened to fill the calibrated volumes at 10 mbar, as it can be monitored from the PZ602 gauge, and it is closed again to preserve the gas from the reservoir. Keeping the high pressure arm always under pressure, the table preparation is completed in around 10 minutes.

Injection The injection is started when the valve connecting to the desired volume, the PV611 for the storage cell or the PV503 for the VELO vessel, is opened together with the dosing valve DV602, the aperture of which determines the injecting flow rate. For the SMOG2 regime, it is sufficient to open the PV503 valve, positioned on the inlet hosting the turbo pump, and the pressure in the VELO vessel stabilises in around 15 minutes. For the SMOG2 regime, on the other hand, an additional step is required: the gas feed line is preemptively filled, opening the DV602 valve, in order to reach the target injection pressure and reduce the stabilisation period to about 5 minutes during the injection. The injection is stopped by closing the relative valve, but it can also be put momentarily on hold by closing the DV602 valve.

Vacuum recovery after injection When the injection is stopped, the vacuum in the VELO vessel is recovered in around 10 minutes with the turbo pump. The line and the low pressure arm of the GFS, on the other hand, are cleaned opening again the PV608 and PV609, reverting to the stand-by configuration. When no injections are foreseen for the next days, the turbo pump is isolated closing the GV302 valve and the pumping of the VELO is reverted to the ion pumps.
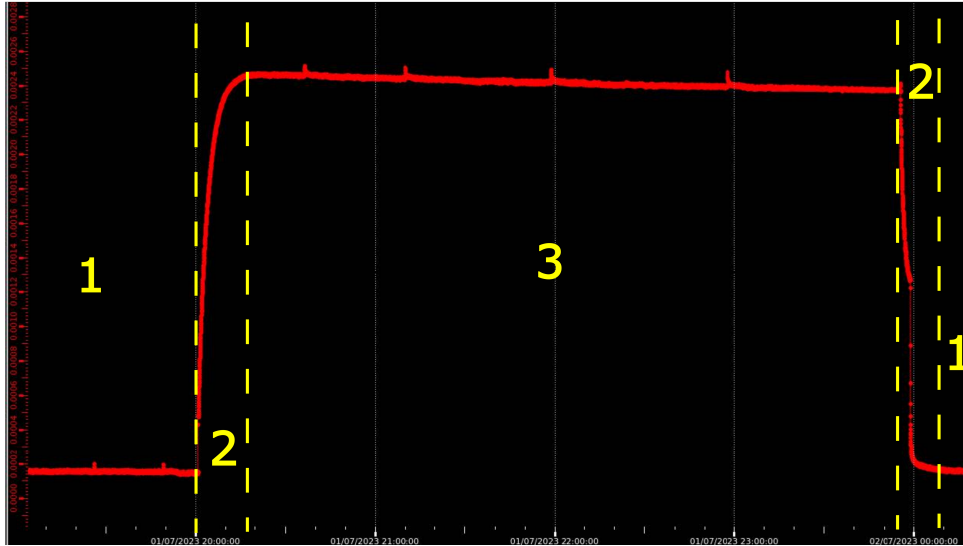
Figure III.3.13: Pressure readings in the VELO vessel as a function of time during a test injection in the VELO vessel; the three possible status are separated with a dashed line and identified with a number.

From a data analysis point of view, the injection process can thus be summarised into three possible status associated with the run, as it can be seen in Fig. III.3.13 where the pressure readings in the vacuum vessel is shown during an injection: no injection ongoing (1), unstable injection (2) (*i.e.* at the start and at the stop of the injection) and stable injection (3). Moreover, the injection regime (*i.e.* SMOG or SMOG2) and the injected gas are additional information to be added for the analyst.

Given the readings from the gauges and valves available, their decoding and elaboration is needed to obtain the high level information required.

III.3.2.2 The WinCC control framework

The interface between the operators and the complex system of hardware and software devices in the LHC ring is handled through a Supervisory Control And Data Acquisition (SCADA) system. A SCADA system is a distributed architecture for the remote supervision of machines and processes, and it can be schematised as:

- one or more field sensors and actuators that measure or apply changes to the physical machine or process;

- one or more programmable logic controller (PLC) that control and store the measurements carried out by the connected devices or implement the automation logic of the system to which they are connected;

- a communication network between the PLC and the supervising system;

- a supervising system, usually computer networks, that elaborates the information coming from the PLC to store and show the results, trigger alarms or issue commands to the PLC.

The LHC experiments employ the object-oriented SCADA platform WinCC-OA [200] that provides the software framework needed for the development of each individual systems. In particular, it presents a run time database, where the data coming from the devices are temporarily stored for further manipulation, an archiving tools, for long term storage of the data, and a graphical editor and parameterization tool, allowing the implementation of specific structures for the database and personalised user interfaces.

Each subsystem in the LHC infrastructure is managed by an individual project in the SCADA framework, with its independent database, set of control processes and user interfaces. A project cannot directly access the variables, called data-points, defined in the database of a different project. A publish-subscribe communication protocol (*data interchange protocol*, DIP [201]) has thus been developed to allow the exchange of real-time data between independent projects. In the DIP infrastructure, publishers and subscribers are located by a name server that acts as a directory. The publisher acts as the server, providing, or *publishing*, a set of data identified as unique paths in the name server directory. The subscriber, on the other hand, operates as the client, requesting the data, to be stored in its database: the subscription happens only once, when a transmission control protocol (TCP) communication is established, and the data-points are automatically updated by the publisher until the connection is terminated.

A new WinCC-OA project has been developed for the SMOG2 system. It gathers the monitoring interfaces and control scripts for the elaboration and communication of the data from the vacuum system to the LHCb control system. Its database is organised in three main data-point categories:

- input data-points coming from external projects via DIP, like the gauges and valves readings, or from sensors in the system, like the temperature readings;

- private data-points, which are associated with variables obtained from the manipulation of the input data-points or other intermediate variables. They are not of interest for external projects and they are not expected to be published via DIP;

- output data-points correspond to the data sent to the LHCb control system or that can be potentially published via DIP.

Since the gauges and valves in the GFS are part of the LHC or VELO vacuum system, they are acquired via DIP. The value available is the raw register coming from the associated PLC. Depending on the sensor considered, up to three 16 bits words, coding the status of the sensor, are published together with the pressure reading or the valve aperture for the pressure gauges and dosing valves. A dedicated control process, different for each of the sensor types, have been implemented to decode the key information:

- the status of the sensor, which can be open/active, closed/inactive, interlocked. The special unknown status is also considered for unidentified words or invalid readings;

- the possible warning or error status and associated code, to trigger an alarm in the project logbook;

- if available, the reading of the sensor (*i.e.* pressure or valve opening).

These decoded data-points are further used for the development of the SMOG2 SCADA project, as presented in the following sections.

Figure III.3.14: SMOG2 monitoring panel at the end of a test injection in the VELO vessel; the pressure readings in the VELO vessel (red) and in the PZ601 (light blue) and PZ602 (yellow) can be seen in the bottom left frame, while the temperature in the storage cell and in the VELO vessel can be seen in the bottom right frame.

III.3.2.3 SMOG2 monitoring panel and data propagation

A monitoring panel has been developed to help the experts keeping track of the status of the SMOG2 system. The target is to group in one intuitive interface all the relevant subsystems to be monitored, in order to speed up problem identification and intervention. The panel, shown in Fig. III.3.14, is divided in five logically independent sections, each controlled by a dedicated control process implemented as Finite-State Machine (FSM). A FSM represents a machine or a process that can be found in a finite number of states at any given time, which change in response to defined inputs. It is thus completely defined by the list of its states, the starting state and the input conditions that trigger each transition. The following sections can be found in the panel:

Table preparation status The first section is dedicated to the readiness of the calibration volumes to inject gas, as well as to the status of the high pressure arm. Keeping track of the last reservoir opened allows to determine which gas is ready to fill the calibration volumes on the line. A check on the DV601 dosing valve opening allows at the same time to identify the cleaning procedure and reset the status to NONE. The calibration volumes, during a typical injection, start EMPTY. They then go to FILLING when DV601 gets opened at the same time as PV608 get closed. When DV601 is closed again, the right pressure is reached and the state of the volumes is set to READY. After the injection, when the PV608 valve is opened again, the status goes to CLEANING, until the pressure on the PZ602 revert to stand-by values, at which point the status revert to EMPTY, completing the cycle. The status of the valves connected to the calibration volumes are also monitored through a dedicated colour-coded LED, in order to keep under control the reliability of the readings.

Gas feed line valves status The status of the valves on the gas feed line, which control the injection conditions, is monitored in the second section and specifically, four

160

valves are considered: GV302, which indicates when the system is in injection regime, PV503 and PV611, which fix the type of injection, and finally DV602 and its aperture, to determine the start and stop of the injection itself. The status of each valve (`OPEN`, `CLOSED`, `INTERLOCKED`) is written in a colour-coded box, while possible anomalous conditions, warnings or errors are highlighted via a dedicated colour-coded LED. Finally, the injection mode is clearly identified by a LED, signalling the active regime during the injection.

Luminosity monitor The central box is dedicated to the gas flow rate and luminosity measurement. Two field boxes allows to compare the targeted flow rate with the one measured on the line, from the pressure drop on the PZ602, and check that the values are compatible within a defined tolerance. A LED is also available to highlight the status, turning from green to yellow, orange and red as the measurement exceeds the tolerance thresholds. The measured flow is then used to calculate the instantaneous luminosity based on the Eq. I.4.1.a, when injecting in SMOG2 regime. For SMOG2 injections, an estimate of the instantaneous luminosity is provided from the pressure readings in the VELO vessel, based on Eq. I.4.1. Since no calibration is yet available, no value is published at the moment.

Pressure and temperature monitor The lower part of the panel is occupied by the pressure and temperature trending plots. They show, respectively, the temperature in the cell and in the VELO vessel and the pressure at different positions in the gas feed system and at the SMOG2 injection inlet, as a function of time. For the pressure, LEDs indicating the status of the measuring gauges are also present. In addition to allowing a real-time supervision of the injection progress, it also permits to immediately spot spikes or anomalous trends and intervene before any damage is done.

Throughout the panel, a colour convention is applied to simplify the identification of anomalous states. In particular, green, blue and grey colours are associated to the standard status (open, closed and interlocked), while yellow, orange and red are used to indicate anomalous conditions, in an increasing severity order.

The similar control processes to those applied for the monitoring panel are used to fill the output data-points that are sent to the LHCb control system and condition database. The aim of the database is to collect all relevant information on the conditions with which the data were acquired during a certain run. From the point of view of SMOG2 system, the analyst must be able to distinguish the runs where there was gas injected and to know which gas was injected. Moreover, the luminosity of the data sample is measured from a known relation with the gas flow rate or its pressure. It must therefore be possible to identify the runs where the relation is valid, which translates to runs with a stable pressure.

The injected gas and the injection type (`NONE`, `SMOG` or `SMOG2`) are identified using the information coming from the monitoring panel and stored in private data-points, updated in real time. A dedicated control process is instead developed to evaluate the stability of the pressure, also saved in real time as a private data-point: it must be able to indicate the stability status when and only if there is gas injected into the system. The process is automatically activated when the injection type changes from `NONE` to a different status. Since at the beginning of the injection the pressure is known to be unstable, the stability
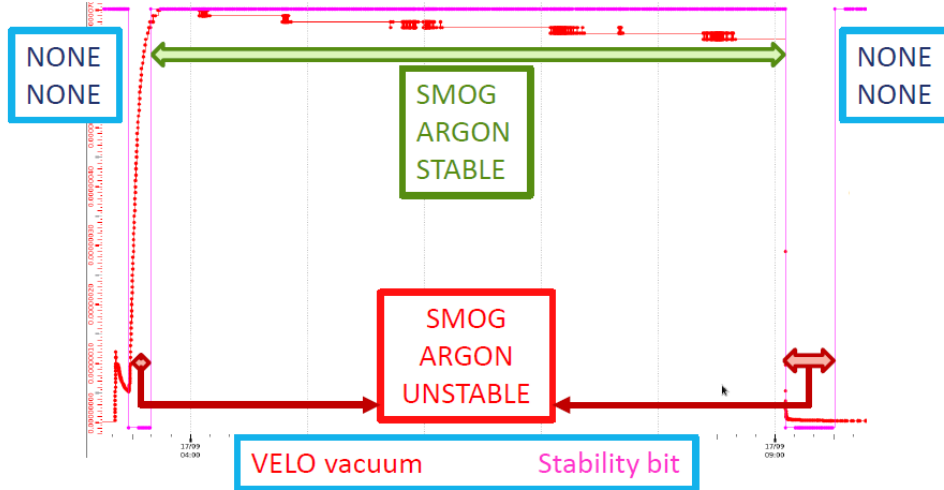
Figure III.3.15: Pressure readings in the VELO vessel (red) and value of the injection stability (pink) as a function of time during a test injection in the VELO vessel; the injection status sent to the LHCb control system are also reported.

variable is initialised to `UNSTABLE`. The pressure stability is then evaluated considering its moving average, calculated over 10 points. When the change in the moving average between two consecutive measurements is within 0.7%, the data-point is changed to `STABLE`, but it is changed back to `UNSTABLE` every time the condition is not satisfied. In this way, unexpected spikes or drastic variations in the pressure, associated with an unreliable data samples, will be correctly identified. The number of points for the moving average and the threshold value have been tuned during test injections, finding a compromise between the correct identification of the pressure plateau and the sensitivity to noise fluctuations: too few points or excessively low thresholds would trigger an unstable status solely based on noise fluctuations, while, on the opposite spectrum, too many points and a higher threshold are insensitive to real pressure variations and would identify as stable periods with changing pressure. When the injection is stopped, the pressure rapidly decreases until it returns to values compatible with normal conditions. The stability is thus automatically set to `UNSTABLE` again when the injection type changes from `SMOG` or `SMOG2` to `NONE` and a new moving average is started. When the `STABLE` status is reached, meaning that the nominal conditions have been recovered at the end of the injection, the process waits for a new injection to start. An example of an injection cycle is shown in Fig. III.3.15 where the pressure reading from the VELO vessel and the private data-point for the stability are shown. The equivalent status sent to the LHCb control system to be archived in the database are also reported.

The output data-points sent to the LHCb control system and database are a copy of the private ones previously defined, further modified to guarantee their stability. In particular, the output data-point for the stability is frozen for 5 minutes when it changes status to avoid fluctuations due to instabilities at the transient, and the output data-point for the injection type is changed back to `NONE` only when the pressure nominal conditions are recovered, since a few minutes are needed after the stop of the injection to pump out the gas still present inside the LHC beam pipe and the VELO vessel.

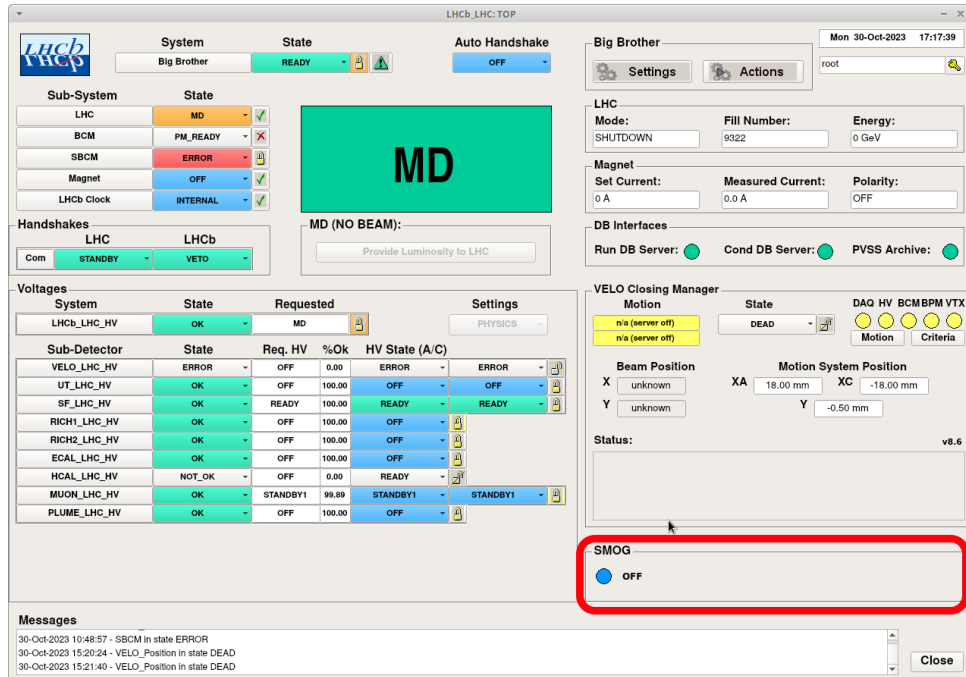At the beginning of each run, the values of the output data-points here defined are saved in

Figure III.3.16: Main LHCb control panel with the section indicating the status of the SMOG2 injection highlighted in red, outside injection.

Table III.3.2: Caption

	Start of injection	Stable injection	Stop of injection	Recovered vacuum
Mode	SMOG	SMOG	SMOG	NONE
Gas	ARGON	ARGON	ARGON	NONE
Stability	UNSTABLE	STABLE	UNSTABLE	-

the condition database. An automatic change of run has also been implemented whenever the overall SMOG2 status changes, in order for the saved information to be reliable and valid for the whole run. For every injection cycle, four run changes are expected:

- when the injection starts;

- when the injection reaches the pressure plateau;

- when the injection stops;

- when the vacuum in the VELO vessel is recovered.

For immediate access from the operators of other LHCb subsystems, the same information are also shown in the main control panel in the LHCb control room (Fig. III.3.16) and they are dumped in the official LHCb logbook, where relevant information related to the detector operations is saved. Table III.3.2 summarises the conditions expected in the database and in the logbook for each change of run associated to SMOG2, for an example injection of Ar in SMOG2 regime.

Part IV

Conclusions

Even though the Standard Model of Particle Physics has proved to be extremely successful in describing the fundamental constituents of matter and their interactions, it is still unable to explain 85% of the mass of the Universe, known as Dark Matter. Numerous space experiments such as AMS-02 aim to indirectly identify signatures of Dark Matter by precisely measuring the fraction of antimatter in Cosmic Rays. In particular, the positrons and antiprotons fractions have been measured and highlighted possible discrepancies with the expected spectra. Nevertheless, the interpretation of the results are limited by the uncertainty on the background production from known primary sources and secondary production in the collisions between the Cosmic Rays and the InterStellar Medium. Light antinuclei such as antideuterium and antihelium are expected to be sensitive probes to exotic contributions, being their secondary production suppressed, so that in some models its production could be dominated by a possible Dark Matter contribution. Recently, AMS-02 claimed to have observed both antideuterium and antihelium candidates. It is therefore of upmost importance to precisely understand the secondary production mechanism in order to clearly separate the possible exotic contributions from the background from known astrophysical processes. The coalescence model, used to describe the nuclei formation mechanism, is a phenomenological model whose free parameter is fitted on available data. Although in recent years great progresses have been made to reach a comprehensive description of the coalescence mechanism, still no theoretical model is able to take into account the observed variations associated with the interacting species and the collision energy. Direct measurements of antinuclei production in collision systems involving protons and helium nuclei and for projectile energies at the TeV scale are needed to improve the accuracy of the theoretical models.

The LHC accelerator at CERN provides beams in the TeV energy range, but no extraction lines are available for a high-energy fixed-target facility. The LHCb experiment, thanks to the forward geometry of its spectrometer, and the possibility to inject noble gases in the LHC beam pipe, is ideal to fill this gap. The SMOG injection apparatus, originally intended for precise luminosity measurements, has been exploited since 2015 in a pioneering fixed-target physics programme studying collisions between the LHC beams and gaseous targets. The unique possibilities offered by this setup have been demonstrated with the first measurements ever of prompt and detached antiproton production in pHe collisions at $\sqrt{s_{\mathrm{NN}}} = 110$ GeV. The results have contributed to the improvement of the secondary $\bar{p}$ flux prediction.

During my *Ph.D.* programme, I contributed to the extension of the LHCb fixed-target programme towards the measurement of light antinuclei production. Exploiting the accurate time calibration of the OT detector, it is possible to identify low-momentum hadrons with their time-of-flight with a track time resolution of about 1 ns. However, the standard LHCb reconstruction assumes that particles travel at the speed of light when correcting the OT drift times for the particle time-of-flight, producing a large tracking inefficiency for low-momentum deuterons and biasing the reconstructed trajectories of particles with velocity significantly smaller than c. I therefore developed a modified reconstruction algorithm that takes into account the larger time-of-flight of heavy particles. The reconstruction efficiency is recovered for low-momentum deuterons, in the region where the time-of-flight identification is expected to be more performing, and it is also improved for protons, maintaining a similar performance of momentum resolution and

fake track rejection. A new analysis tool has also been implemented to perform particle identification based on the time-of-flight information. In the final Kalman fit of the reconstructed tracks, the β of the particle is determined combining the time information from the OT detector and the M1 muon station. The performance has been tested on 10% of the pHe collisions recorded by LHCb in 2016 at $\sqrt{s_{\mathrm{NN}}} = 110$ GeV, privately reconstructed with the new algorithm, and showed promising separation power in the $p < 2$ GeV/c momentum region, where three clearly separated peaks, corresponding to deuterons, protons and lighter particles, are distinguished.

The preliminary results presented in this thesis constitute the first evidence for an identified deuteron signal in the LHCb data. It is the first step toward an (anti)deuteron production measurement in LHCb, notably in its unique fixed-target regime.

The LHCb fixed-target system has been upgraded in the context of the general upgrade of the LHCb detector, operational since 2022. A 20 cm-long storage cell, SMOG2, has been installed upstream of the nominal LHCb interaction point in order to confine the gas and increase the areal density up to two orders of magnitude for the same gas flow rate as in Run2. New non-noble gases, such as hydrogen, deuterium, nitrogen and oxygen, will be injected, further expanding the physics reach, with more precise quark-gluon plasma studies and the extension of the programme of Cosmic Ray interest. During my *Ph.D.* programme, as an active member of the LHC Physics Beyond Collider working group, I have been responsible for the simulation of the gas flow within the SMOG2 system. For such non-noble gases, such an activity is crucial to understand the impact on the LHC machine of their injection into the storage cell, in order to set realistic limits to the flux and injection time. In particular, I performed a detailed study on the deterioration of the NEG coating in the VELO RF foil, focussing on the level of saturation expected for getterable gases and the onset of embrittlement in the case of hydrogen-like gases. I developed a new dynamic time-dependent simulation in the framework of the Molflow+ software to characterise the time evolution of the degradation that can be expected during one year of SMOG2 operation in nominal conditions, considering N_2 and H_2. The results of the simulations, compared to laboratory measurement on NEG samples, demonstrated that the level of saturation prospected in the RF foil during Run3 is acceptable for LHC operation and no embrittlement is foreseen.

I also collaborated to the commissioning of the new SMOG2 system and at its integration in the LHCb control system. As expert in the luminosity working group for the fixed-target physics programme, I was responsible for the simulation studies to understand the systematics on the luminosity associated with the gas density profile. Exploiting the Molflow+ software, I studied the expected gas density profile taking into consideration the realistic geometry of the storage cell and its interfaces with the LHCb detector. I obtained a correction factor to the areal density obtained with an ideal isolated cell, to be considered in the fixed-target luminosity calculation. I also studied the gas density uniformity in the transverse plane with respect to the beam direction, in order to evaluate the systematics associated with the Beam Gas Imaging technique employed for the ghost charge measurement. I compared the simulated profiles with the primary vertex distribution obtained from the first data collected in the SMOG2 configuration during 2022. These commissioning data demonstrated the principle of the storage-cell-based gas target: beam-gas collison events could be reconstructed concurrently with beam-beam collisions. The longitudinal profile

of the gas target was reconstructed online and showed a good agreement with the simulation. Finally, I implemented the Supervisory Control And Data Acquisition system for the SMOG2 injection system based on Finite-State Machine to gather and elaborate the data coming from the vacuum system in order to allow the monitoring of the status of the system and to transmit the information to the LHCb control system.

The results presented in this thesis provided further steps in the development of the LHCb fixed-target programme. It was shown for the first time that the data collected during Run2 can be used to identify low-momentum antinuclei through their time-of-flight, an unforeseen capability in LHCb. This new technique, coupled with the dE/dx identification of He nuclei, also recently demonstrated, opens the way towards unique production studies of light (anti)nuclei at $\sqrt{s_{NN}} \sim 100$ GeV in LHCb. With the new SMOG2 target, I have demonstrated the feasibility of injecting non-noble gases, notably hydrogen. The empowerment of the LHCb fixed-target programme will contribute to broaden the physics capabilities of the LHC accelerator providing a unique laboratory for QCD studies.

Acknowledgements

Saying that these three years of my *Ph.D.* have been a peculiar experience doesn't even come close to capturing what it has been for me. My *Ph.D.*, especially in the first two years, was the *Ph.D.* of COVID, of coloured zones and remote work, of Zoom and virtual conferences. In this work, which is spent most of the time in front of a computer dealing with malfunctioning code and looming deadlines, I cannot deny feeling lost at times due to the absence of human interaction, so essential for the flourishing of ideas. At the end of this journey, filled with stress, uncertainties, and sleepless nights, though I can say that every effort and sacrifice made was worth it. I have gained a wealth of unique experiences, and much of it is owed to the people who, virtually or face-to-face, accompanied and guided me during these peculiar years. They contributed to my growth as a scientist and, above all, as a person, making these years unforgettable.

The first big thank you undoubtedly goes to Giacomo, who was my advisor. He introduced me to the unique world of SMOG physics when I was an undergraduate student facing my first thesis. He welcomed me back for my *Ph.D.*, proposing the challenge of researching nuclei in an experiment, LHCb, which was not originally designed for this kind of research. Over these years, he patiently guided me, always ready to clarify my countless doubts and consistently encouraging me to move forward. Knowing that I had someone behind me, ready to guide me if needed, helped me overcome even the moments of dejection that certainly occurred during these intense three years. Along with him, I thank the entire LHCb Florence group, which became my work family. They made me feel welcomed and comfortable from day one, as every best family knows how to do. Giovanni, who consistently showed great interest and confidence in what I was doing and always offered a smile and a good laugh. Michele, with whom I had the pleasure of working during my master thesis and has always been available for discussions and idea exchanges, even remotely. Lucio, who guided me during my master thesis and continued to do so during my *Ph.D.*. He never hesitated to offer help and support, both professionally and personally. From one pessimist to another, he never failed to restore my confidence when it was lacking. Matteo, my fellow in "misfortune", and Fabio, who had the honour/burden of keeping me company during the final months of this work. If I don't go blind before the age of 40, it will be mainly thanks to him. How can I not thank Saverio? We shared an office in Florence, and not even a fellow at CERN spared him from my presence. He was the first line of technical assistance, enduring my stupidest questions and always posing good ones to help me resolve doubts. Above all, he was a great human support, listening to my frustrations, sharing his own, and always committing, even when I didn't make his life easy, to immerse me more and more in the world of LHCb. I hope to be able to give back as much when I am on his side of the game. Finally, I cannot help but thank Antonio. I don't think I can ever repay him for all the coffees he has offered me over the years. Knowing that a coffee and some morning chatter awaited me when I arrived at the office made waking up at 7 a little less burdensome every day.

Just as in the Florence group, in the LHCb collaboration, I found colleagues, and in some cases, friends, who were willing to share ideas and results. Thanks to Pasquale, who gave me the opportunity to carve out my own space and collaborate first-hand on SMOG2, in its "daily" operation. The groups I collaborated with, Ions and Fixed Target and the Luminosity group, were always enthusiastic to hear about each new step and result, full of advice and suggestions to improve my work. I thank Matt, Jiayin, Elena, Vladik, Fabio,

and Elisabeth, as conveners of the groups, but my thanks go to all my colleagues, too many to name them all. Outside of LHCb, I had the opportunity to work within the Physics Beyond Colliders group for gas flow simulations. Here I found guidance and a reference in Massi, who supported me from start to finish in work that was entirely new to me. I was able to learn a lot thanks to his comments, doubts, and suggestions, as well as improve the final results.

Another special thank you goes to Oscar Adriani and the National Institute of Nuclear Physics for giving me the opportunity to spend my last year of *Ph.D.* at CERN. I had the chance to put a face to many of the people who accompanied me in these years of work, as well as to meet many new ones. Thanks to Shinichi and Federica, who opened the doors of their home to numerous dinners and bbqs, and to all the guys, LHCb and non-LHCb, who brighten them. Good meat, good beer, and lots of laughter coloured many evenings of this summer. Another even bigger thank you goes to Federica and Sara. They kept me company and supported me during the long working days, between a coffee (or tea), a "Che vita di merda", a few tears and lots of laughter. Thanks to Chiara and Giorgia, the first people I met from LHCb after the long isolation of COVID. If the first LHCb BBQ is unforgettable, they certainly contributed to making it as such; it's always a joy to be able to meet up again as often as possible. Thanks again to Irene, Sofia, Elena, Federica, and Laura. If my visits to Milan become frequent, it will primarily be their fault. Thanks to all the Pasta Pizza guys. Matteo, Paolo, Sara, Giusy, Rudy, Valerio, and Davide. We shared endless lunches and even more beers. If I can check climbing and downhill off my list of experiences, it's thanks to them (and I know they already have some more planned for when I will visit them again). I couldn't have found better friends to share an intense, at times difficult, but certainly the most beautiful year of my *Ph.D.*. Finally, thanks to Mom Andrea. With his calm and order, he kept the Allee des Bouleaux flat stable and floating, as well as my ability to live like a civilized woman and not a cave one. Our dinner chats and the endless Bang games made me reevaluate life with roommates (but only if they are like him).

The last thanks are all dedicated to lifelong friends and loved ones. Thanks to my family. After almost 30 years and in different homes (and sometimes countries), their support has always remained steadfast, whether it was offering an ear, a bed, or (more often than I'd like to admit) a ready meal. I hope life takes me around the world again, but home will always be home, and it's mainly thanks to them. Thanks to Edo, with whom I shared these 8 years of university and countless adventures. He supported me, endured my bad moods, and always encouraged me, believing in me more than I did myself. Thanks to Irene, my Spanish family. Adult life often gets in the way, and hearing from her is difficult, but I know I have her as a listener and a shelter to run to when I need it. All the girls and boys from judo. The evenings spent at Chiara or Claudia's homes warmed more than one winter night and always my heart. Spending time with them invariably makes me want to put on a judogi again. A special thank you to Claudia, because after all these years, she hasn't tired of answering the phone and listening to me talk for hours. Thanks to the Grigio, the E' tempo, Marg, Nicola, Riccardo, and Asia. Thanks to all those who, whether for a drink, a few words, or a simple Saturday night out, filled and coloured the most beautiful memories of these long years.

Acronyms

ALICE A Large Ion Collider Experiment. i, 26, 30, 75, 76, 80, 81

AMS-02 Alpha Magnetic Spectrometer. i, 13, 16–21, 27, 28, 76, 165

ATLAS A Toroidal LHC ApparatuS. i, 29, 32

BGI Beam Gas Imaging. vi, 57, 58, 150, 151, 166

CERN *Conseil europèen pour la recherche nuclèaire.* i, 2, 9, 26, 29, 31, 122, 165

CMB Cosmic Microwave Background. 8, 13

CMS Compact Muon Solenoid. i, 29, 32

CR Cosmic Ray. i, ii, iv, 9, 11–19, 21, 22, 25, 59, 62, 70, 74, 76, 165, 166

DM Dark Matter. i, ii, iv, 2, 6–11, 16–19, 21–23, 27, 28, 165

DOCA Distance Of Closest Approach. 106, 152

ECAL Electromagnetic Calorimeter. 44–46

ECs Electron Clouds. 67

FPGA Field Programmable Gate Array. 48

FSM Finite-State Machine. 160, 167

GAPS General AntiParticle Spectrometer. 13, 21, 27, 28

GEM Gas Electron Multipliers. 46

GFS Gas Feed System. v, 58, 64, 65, 67–69, 118–120, 156, 157, 159

GPU Graphic Processing Unit. 54

HCAL Hadronic Calorimeter. 44, 46

HLT High-Level Trigger. 48, 54, 55, 57, 85

HPDs Hybrid PhotoDetectors. 53

Bibliography

[1] G. S. Guralnik, C. R. Hagen, and T. W. B. Kibble, *Global conservation laws and massless particles*, Phys. Rev. Lett. **13** (1964) 585.

[2] F. Englert and R. Brout, *Broken symmetry and the mass of gauge vector mesons*, Phys. Rev. Lett. **13** (1964) 321.

[3] P. W. Higgs, *Broken symmetries, massless particles and gauge fields*, Physics Letters **12** (1964) 132.

[4] *Observation of a new boson at a mass of 125 GeV with the CMS experiment at the LHC*, Physics Letters B **716** (2012) 30.

[5] ATLAS collaboration, *Observation of a new particle in the search for the Standard Model Higgs boson with the ATLAS detector at the LHC*, Physics Letters B **716** (2012) 1.

[6] V. N. Gribov, *A reggeon diagram technique*, `http://jetp.ras.ru/cgi-bin/dn/e_026_02_0414.pdf`, 1968.

[7] Particle Data Group, *Review of Particle Physics*, PTEP **2022** (2022) 083C01.

[8] J. D. Bjorken, *Asymptotic sum rules at infinite momentum*, Phys. Rev. **179** (1969) 1547.

[9] G. Altarelli and G. Parisi, *Asymptotic freedom in parton language*, Nuclear Physics B **126** (1977) 298.

[10] S. Bailey *et al.*, *Parton distributions from LHC, HERA, Tevatron and fixed-target data: MSHT20 PDFs*, The European Physical Journal C **81** (2021) .

[11] J. H. Oort, *The force exerted by the stellar system in the direction perpendicular to the galactic plane and some related problems*, Bulletin of the astronomical institutes of Netherlands **6** (1932) 249, Provided by the SAO/NASA Astrophysics Data System.

[12] F. Zwicky, *The redshift of extragalactic nebulae*, `arXiv:1711.01693`.

[13] F. Zwicky, *On the masses of nebulae and of clusters of nebulae*, Astrophysical journal **86** (1937).

[14] V. Rubin, *Rotation of the Andromeda nebula from a spectroscopic survey of emission regions*, Astrophysical journal **15** (1979).

[15] M. Markevitch *et al.*, *Direct constraints on the Dark Matter self-interaction cross-section from the merging galaxy cluster 1e 0657-56*, The Astrophysical Journal **606** (2004) 819.

[16] NASA, *Nasa hubble space telescope detects ring of Dark Matter*, Multimedia Page, 2019.

[17] N. Sugiyama, *Cosmic background anisotropies in Cold Dark Matter cosmology*, The Astrophysical Journal Supplement Series **100** (1995) 281.

[18] WMAP collaboration, *Seven-year WMAP observations: cosmological interpretation*, The Astrophysical Journal Supplement Series **192** (2011) 18.

[19] P. A. R. Ade *et al.*, *Planck 2015 results*, Astronomy & Astrophysics **594** (2016) A13.

[20] N. Aghanim *et al.*, *Planck 2018 results*, Astronomy & Astrophysics **641** (2020) A6.

[21] S. Hannestad, A. Mirizzi, G. G. Raffelt, and Y. Y. Y. Wong, *Neutrino and axion Hot Dark Matter bounds after WMAP-7*, Journal of Cosmology and Astroparticle Physics **2010** (2010) 001.

[22] T. D. Brandt, *Constraints on macho Dark Matter from compact stellar systems in ultra-faint dwarf galaxies*, The Astrophysical Journal **824** (2016) L31.

[23] S. Dodelson and L. M. Widrow, *Sterile neutrinos as Dark Matter*, Phys. Rev. Lett. **72** (1994) 17.

[24] R. Bernabei *et al.*, *First results from DAMA/LIBRA and the combined results with DAMA/NaI*, The European Physical Journal C **56** (2008) 333.

[25] R. Bernabei *et al.*, *DAMA/LIBRA-phase2 results and implications on several Dark Matter scenarios*, International Journal of Modern Physics A **35** (2020) 2044023.

[26] A. Berlin and F. Kling, *Inelastic Dark Matter at the LHC lifetime frontier: ATLAS, CMS, LHCb, CODEX-b, FASER, and MATHUSLA*, Physical Review D **99** (2019) .

[27] K. Greisen, *End to the Cosmic Ray spectrum?*, Phys. Rev. Lett. **16** (1966) 748.

[28] G. T. Zatsepin and V. A. Kuz'min, *Upper Limit of the Spectrum of Cosmic Rays*, Soviet Journal of Experimental and Theoretical Physics Letters **4** (1966) 78, Provided by the SAO/NASA Astrophysics Data System.

[29] P. Picozza *et al.*, *PAMELA - a payload for antimatter matter exploration and light-nuclei astrophysics*, Astroparticle Physics **27** (2007) 296.

[30] A. Kounine, *The Alpha Magnetic spectrometer on the International Space Station*, International Journal of Modern Physics E **21** (2012) 1230005.

[31] S. Torii, *The CALorimetric Electron Telescope (CALET): a High-Energy Astroparticle Physics Observatory on the ISS*, PoS **ICRC2015** (2016) 581.

[32] Auger collaboration, *The Pierre Auger Cosmic Rays observatory*, Nucl. Instrum. Meth. Phys. Res. A **798** (2015) 172.

[33] R. A. Ong *et al.*, *The GAPS experiment to search for Dark Matter using low-energy antimatter*, `arXiv:1710.00452`.

[34] E. Fermi, *On the origin of the cosmic radiation*, 1949. doi: 10.1103/PhysRev.75.1169.

[35] M. Kachelriess, *Lecture notes on high energy Cosmic Rays*, `arXiv:0801.4376`.

[36] A. W. Strong and I. V. Moskalenko, *Propagation of Cosmic Ray nucleons in the galaxy*, The Astrophysical Journal **509** (1998) 212.

[37] Sun, X. H. , Reich, W. , Waelkens, A. , and Enßlin, T. A. , *Radio observational constraints on galactic 3d-emission models*, A&A **477** (2008) 573.

[38] F. Nozzoli and C. Cernetti, *A data-driven approach for the measurement of $^{10}Be/^{9}Be$ flux ratio in Cosmic Rays with magnetic spectrometers*, PoS **ICRC2021** (2021) 138.

[39] AMS collaboration, *Precision Measurement of the boron-to-carbon flux ratio in Cosmic Rays from 1.9 GV to 2.6 TV with the Alpha Magnetic Spectrometer on the International Space Station*, Phys. Rev. Lett. **117** (2016) 231102.

[40] N. Przybilla, M.-F. Nieva, and K. Butler, *A cosmic abundance standard: Chemical homogeneity of the solar neighborhood and the ISM dust-phase composition*, The Astrophysical Journal **688** (2008) L103.

[41] PAMELA collaboration, *Ten years of PAMELA in space*, Riv. Nuovo Cim. **40** (2017) 473, `arXiv:1801.10310`.

[42] L. Bonechi *et al.*, *Status of the PAMELA silicon tracker*, Nucl. Instrum. Meth. Phys. Res. A **570** (2007) 281.

[43] AMS collaboration, *High statistics measurement of the positron fraction in primary Cosmic Rays of 0.5–500 GeV with the Alpha Magnetic spectrometer on the International Space Station*, Phys. Rev. Lett. **113** (2014) 121101.

[44] A. Ibarra, D. Tran, and C. Weniger, *Indirect searches for decaying Dark Matter*, International Journal of Modern Physics A **28** (2013) 1330040.

[45] P.-F. Yin, Z.-H. Yu, Q. Yuan, and X.-J. Bi, *Pulsar interpretation for the AMS-02 result*, Phys. Rev. D **88** (2013) 023001, `arXiv:1304.4128`.

[46] D. Gaggero *et al.*, *Three-dimensional model of Cosmic Ray lepton propagation reproduces data from the Alpha Magnetic spectrometer on the International Space Station*, Phys. Rev. Lett. **111** (2013) 021102.

[47] S. Ting, *Latest results from AMS on the International Space Station*, `https://cds.cern.ch/record/2861432`, 2023. Presented at CERN Colloquium.

[48] PAMELA collaboration, *New measurement of the antiproton-to-proton flux ratio up to 100 GeV in the cosmic radiation*, Phys. Rev. Lett. **102** (2009) 051101.

[49] AMS collaboration, *Antiproton flux, antiproton-to-proton flux ratio, and properties of elementary particle fluxes in primary Cosmic Rays measured with the Alpha Magnetic spectrometer on the International Space Station*, Phys. Rev. Lett. **117** (2016) 091103.

[50] M. Aguilar *et al.*, *The Alpha Magnetic Spectrometer (AMS) on the International Space Station: Part II - Results from the first seven years*, Physics Reports **894** (2021) 1.

[51] G. Giesen *et al.*, *AMS-02 antiprotons, at last! Secondary astrophysical component and immediate implications for Dark Matter*, Journal of Cosmology and Astroparticle Physics **2015** (2015) 023.

[52] M. Boudaud *et al.*, *AMS-02 antiprotons' consistency with a secondary astrophysical origin*, Physical Review Research **2** (2020) .

[53] A. Aduszkiewicz *et al.*, *Measurements of $\pi^{\pm}$, $k^{\pm}$, p and $\overline{p}$ spectra in proton-proton interactions at 20, 31, 40, 80 and 158 GeV/c with the NA61/SHINE spectrometer at the CERN SPS*, The European Physical Journal C **77** (2017) .

[54] LHCb collaboration, R. Aaij *et al.*, *Measurement of antiproton production in pHe collisions at $\sqrt{s_{NN}} = 110$ GeV*, Phys. Rev. Lett. **121** (2018) 222001, `arXiv:1808.06127`.

[55] A. Cuoco, M. Kramer, and M. Korsmeier, *Novel Dark Matter constraints from antiprotons in light of AMS-02*, Phys. Rev. Lett. **118** (2017) 191102.

[56] P. De la Torre Luque, *Antinuclei with the DRAGON2 code and AMS-02 preliminary observation*, PoS **ICRC2023** (2023) 1369.

[57] ALICE collaboration, *Production of deuterons, tritons, ^{3}He nuclei, and their antinuclei in pp collisions at $\sqrt{s} = 0.9$, 2.76, and 7 TeV*, Phys. Rev. C **97** (2018) 024615.

[58] L. Csernai and J. I. Kapusta, *Entropy and cluster production in nuclear collisions*, Physics Reports **131** (1986) 223.

[59] S. T. Butler and C. A. Pearson, *Deuterons from high-energy proton bombardment of matter*, Phys. Rev. **129** (1963) 836.

[60] F. Donato, N. Fornengo, and P. Salati, *Antideuterons as a signature of supersymmetric Dark Matter*, Phys. Rev. D **62** (2000) 043003.

[61] N. Fornengo, L. Maccione, and A. Vittino, *Dark Matter searches with cosmic antideuterons: status and perspectives*, Journal of Cosmology and Astroparticle Physics **2013** (2013) 031.

[62] D. M. Gomez Coral, *Deuteron and antideuteron production in galactic Cosmic Rays*, PhD thesis, UNAM, Mexico, 2019, `https://cds.cern.ch/record/2673048`, Presented 26 Apr 2019.

[63] NA49 collaboration, *Production of deuterium, tritium, and ^{3}He in central pb + pb collisions at 20a, 30a, 40a, 80a, and 158a GeV at the cern super proton synchrotron*, Phys. Rev. C **94** (2016) 044906.

[64] A. Shukla, *Light nuclei and antinuclei production in proton-proton interactions*, PhD thesis, Hawaii U., 2023, https://cds.cern.ch/record/2859334, Presented 09 May 2023.

[65] S. Acharya *et al.*, *Measurement of the production of (anti)nuclei in p–Pb collisions at $\sqrt{s_{NN}} = 8.16$ TeV*, Physics Letters B **846** (2023) 137795.

[66] ALICE collaboration, *Production of (anti-)^{3}He and (anti-)^{3}H in p-Pb collisions at $\sqrt{s_{NN}} = 5.02$ TeV*, Phys. Rev. C **101** (2020) 044906.

[67] ALICE collaboration, *Enhanced deuteron coalescence probability in jets*, Phys. Rev. Lett. **131** (2023) 042301.

[68] C. Pinto, *Constraining (anti)nuclei measurements relevant for astrophysics with alice*, https://indico.cern.ch/event/1139644/contributions/5541492/. Quark Matter 2023.

[69] L. Evans and P. Bryant, *LHC machine*, Journal of Instrumentation **3** (2008) S08001.

[70] CMS collaboration, *The CMS experiment at the CERN LHC*, JINST **3** (2008) S08004.

[71] ATLAS collaboration, *The ATLAS experiment at the CERN LHC*, JINST **3** (2008) S08003.

[72] ALICE collaboration, *The ALICE experiment at the CERN LHC*, JINST **3** (2008) S08002.

[73] LHCb collaboration, *The LHCb detector at the LHC*, JINST **3** (2008) S08005.

[74] E. Lopienska, *The CERN accelerator complex, layout in 2022. Complexe des accélérateurs du CERN en janvier 2022*, , https://cds.cern.ch/record/2800984.

[75] J. Stirling, *Standard model cross sections as a function of collider energy*, https://www.hep.ph.ic.ac.uk/~wstirlin/plots/plots.html. 2022.

[76] C. Moller, *General properties of the characteristic matrix in the theory of elementary particles*, http://gymarkiv.sdu.dk/MFM/kdvs/mfm%2020-29/mfm-23-1.pdf, 1945.

[77] C. Barschel, *Precision luminosity measurement at LHCb with beam-gas imaging*, PhD thesis, RWTH Aachen U., 2014, https://cds.cern.ch/record/1693671, Presented 05 Mar 2014.

[78] LHCb collaboration, R. Aaij *et al.*, *LHCb detector performance*, Int. J. Mod. Phys. **A30** (2015) 1530022, arXiv:1412.6352.

[79] T. Sjöstrand, S. Mrenna, and P. Skands, *A brief introduction to PYTHIA 8.1*, Comput. Phys. Commun. **178** (2008) 852, arXiv:0710.3820.

[80] LHCb collaboration, *$b\bar{b}$ production angle plots*, https://lhcb.web.cern.ch/lhcb/speakersbureau/html/bb_ProductionAngles.html.

[81] LHCb collaboration, *LHCb magnet: Technical Design Report*, CERN-LHCC-2000-007, 2000.

[82] LHCb collaboration, *Performance of the LHCb Vertex Locator*, JINST **9** (2014) P09007, arXiv:1405.7808.

[83] LHCb collaboration, *LHCb VELO (VErtex LOcator): Technical Design Report*, CERN-LHCC-2001-011, 2001.

[84] T. Bird, *The upgrade of the LHCb Vertex Locator*, JINST **9** (2014) C12041, arXiv:1410.0812, Proceedings from PSD10 conference.

[85] LHCb collaboration, *Tracking and alignment plots for conferences*, https://twiki.cern.ch/twiki/bin/view/LHCb/ConferencePlots.

[86] LHCb collaboration, *Silicon tracker: material for publications*, https://lhcb.physik.uzh.ch/ST/public/material/index.php, 2016.

[87] LHCb collaboration, *LHCb inner tracker: Technical Design Report*, CERN-LHCC-2002-029, 2002.

[88] LHCb collaboration, *Tracking system*, https://lhcb-outreach.web.cern.ch/detector/tracking-system/.

[89] LHCb collaboration, *Tracking performance for long-lived particles at LHCb*, J. Phys. : Conf. Ser. **1525** (2019) 012095. 5 p, arXiv:1910.06171, Proceeding for Connecting the Dots and Workshop on Intelligent Trackers (CTD/WIT 2019).

[90] E. E. Bowen, B. Storaci, and M. Tresch, *VeloTT tracking for LHCb Run II*, LHCb-PUB-2015-024, 2016.

[91] LHCb collaboration, *LHCb Outer Tracker: Technical Design Report*, CERN-LHCC-2001-024, 2001.

[92] R. Arink *et al.*, *Performance of the LHCb Outer Tracker*, JINST **9** (2014) P01002, arXiv:1311.3893.

[93] P. d'Argent *et al.*, *Improved performance of the LHCb Outer Tracker in LHC Run 2*, JINST **12** (2017) P11016, arXiv:1708.00819.

[94] LHCb collaboration, *LHCb RICH: Technical Design Report*, CERN-LHCC-2000-037, 2000.

[95] S. Gambetta, *The LHCb RICH detectors: Operations and performance*, Nuclear Instruments and Methods in Physics Research Section A: Accelerators, Spectrometers, Detectors and Associated Equipment **952** (2020) 161882, 10th International Workshop on Ring Imaging Cherenkov Detectors (RICH 2018).

[96] H. Bichel, D. E. Groom, and S. R. Klein, *Passage of particles through matter*, Particle Data Group Review **32** (2019), https://pdg.lbl.gov/2019/reviews/rpp2018-rev-passage-particles-matter.pdf.

[97] M. Adinolfi *et al.*, *Performance of the LHCb RICH detector at the LHC*, Eur. Phys. J. **C73** (2013) 2431, `arXiv:1211.6759`.

[98] D. L. Perego, *The Ring Imaging CHerenkov Detectors of the LHCb Experiment*, Physics Procedia **37** (2012) 606, Proceedings of the 2nd International Conference on Technology and Instrumentation in Particle Physics (TIPP 2011).

[99] LHCb collaboration, *LHCbPreShower(PS) and Scintillating Pad Detector (SPD): Commissioning, calibration, and monitoring*, Journal of Physics: Conference Series **160** (2009) 012046.

[100] LHCb collaboration, *LHCb calorimeters: Technical Design Report*, CERN-LHCC-2000-036, 2000.

[101] C. Abellan Beteta *et al.*, *Calibration and performance of the LHCb calorimeters in Run1 and 2 at the LHC*, `arXiv:2008.11556`.

[102] LHCb collaboration, *LHCb muon system: Technical Design Report*, CERN-LHCC-2001-010, 2001.

[103] A. A. Alves Jr. *et al.*, *Performance of the LHCb muon system*, JINST **8** (2013) P02022, `arXiv:1211.1346`.

[104] F. Archilli *et al.*, *Performance of the Muon Identification at LHCb*, LHCB-DP-2013-001, 2013.

[105] LHCb collaboration, *LHCb online system, data acquisition and experiment control: Technical Design Report*, CERN-LHCC-2001-040, 2001.

[106] LHCb collaboration, *LHCb trigger system: Technical Design Report*, CERN-LHCC-2003-031, 2003.

[107] LHCb collaboration, *LHCb computing: Technical Design Report*, CERN-LHCC-2005-019, 2005.

[108] LHCb collaboration, *LHCb starterkit*, `https://lhcb.github.io/starterkit-lessons/first-analysis-steps/dataflow.html`.

[109] LHCb collaboration, *Design and performance of the LHCb trigger and full real-time reconstruction in Run2 of the LHC*, Journal of Instrumentation **14** (2019) 04013.

[110] *LHC computing grid web site*, `https://wlcg.web.cern.ch/`.

[111] M. Clemencic *et al.*, *The LHCb simulation application, Gauss: Design, evolution and experience*, J. Phys. Conf. Ser. **331** (2011) 032023.

[112] T. Pierog *et al.*, *EPOS LHC: test of collective hadronization with data measured at the CERN Large Hadron Collider*, Phys. Rev. **C92** (2015) 034906, `arXiv:1306.0121`.

[113] D. J. Lange, *The EvtGen particle decay simulation package*, Nucl. Instrum. Meth. **A462** (2001) 152.

[114] Geant4 collaboration, *Geant4: A simulation toolkit*, Nucl. Instrum. Meth. **A506** (2003) 250.

[115] Geant4 collaboration, *Geant4 developments and applications*, IEEE Trans. Nucl. Sci. **53** (2006) 270.

[116] LHCb collaboration, *The LHCb Upgrade I*, arXiv:2305.10515, to appear in JINST.

[117] LHCb collaboration, *Letter of Intent for the LHCb Upgrade*, CERN-LHCC-2011-001, LHCC-I-018, 2011.

[118] LHCb collaboration, *LHCb VELO Upgrade Technical Design Report*, CERN-LHCC-2013-021, 2013.

[119] LHCb collaboration, *LHCb Tracker Upgrade Technical Design Report*, CERN-LHCC-2014-001, 2014.

[120] LHCb collaboration, *LHCb PID Upgrade Technical Design Report*, CERN-LHCC-2013-022, 2013.

[121] J. Albrecht, V. V. Gligorov, and G. Raven, *Review Document: Full Software Trigger*, LHCb-PUB-2014-036, 2014, On behalf of the the HLT software group.

[122] LHCb collaboration, *LHCb Trigger and Online Upgrade Technical Design Report*, CERN-LHCC-2014-016, 2014.

[123] LHCb collaboration, *LHCb Upgrade Software and Computing*, CERN-LHCC-2018-007, 2018.

[124] LHCb collaboration, *LHCb Upgrade GPU High Level Trigger Technical Design Report*, CERN-LHCC-2020-006, 2020.

[125] LHCb collaboration, *Allen: A High-Level Trigger on GPUs for LHCb*, Computing and Software for Big Science **4** (2020) .

[126] LHCb collaboration, *Performance of the LHCb trigger and full real-time reconstruction in Run2 of the LHC*, JINST **14** (2019) P04013, arXiv:1812.10790.

[127] LHCb collaboration, *Precision luminosity measurements at LHCb*, Journal of Instrumentation **9** (2014) P12005.

[128] C. Rubbia, *Measurement of the luminosity of p-$\bar{p}$ collider with a (generalised) Van der Meer Method*, CERN-$p\bar{p}$-Note-38, 1977.

[129] V. Balagura, *Non factorization in LHCb VdM scans: experience in Run2, impact on luminosity calibration*, https://indico.cern.ch/event/813285/contributions/3406097/. LHC Lumi Days. 2019.

[130] M. Ferro-Luzzi, *Proposal for an absolute luminosity determination in colliding beam experiments using vertex detection of beam-gas interactions*, Nucl. Instrum. Methods Phys. Res. , A **553** (2005) 388.

[131] A. Bursche *et al.*, *Physics opportunities with the fixed-target programme of the LHCb experiment using an unpolarised gas target*, LHCb-PUB-2018-015, 2018.

[132] G. Graziani, *Results on heavy ion physics at LHCb*, J. Phys. : Conf. Ser. **1271** (2019) 012008. 10 p, arXiv:1904.04130, on behalf of the LHCb collaboration. Prepared for the fifth biennial Workshop on Discovery Physics at the LHC(Kruger2018), 3-7 December 2018, Hazyview (South Africa).

[133] LHCb collaboration, *First measurement of charm production in fixed-target configuration at the LHC*, Phys. Rev. Lett. **122** (2019) 132002, arXiv:1810.07907.

[134] LHCb collaboration, *J/ψ and D_2^0 production in $\sqrt{s_{NN}} = 68.5$ GeV PbNe collisions*, Eur. Phys. J. **C83** (2023) 658, arXiv:2211.11652.

[135] LHCb collaboration, *Charmonium production in pNe collisions at $\sqrt{s_{NN}} = 68.5$ GeV* , Eur. Phys. J. **C83** (2023) 625, arXiv:2211.11645.

[136] LHCb collaboration, *Open charm production and asymmetry in pNe collisions at $\sqrt{s_{NN}} = 68.5$ GeV*, Eur. Phys. J. **C83** (2023) 541, arXiv:2211.11633.

[137] M. Korsmeier, F. Donato, and M. Di Mauro, *Production cross-sections of cosmic antiprotons in the light of new data from the NA61 and LHCb experiments*, Physical Review D **97** (2018) .

[138] LHCb collaboration, *Measurement of antiproton production from antihyperon decays in pHe collisions at $\sqrt{s_{\mathrm{NN}}} = 110$ GeV*, Eur. Phys. J. **C83** (2023) 543, arXiv:2205.09009.

[139] S. Mariani, *Fixed-target physics with the LHCb experiment at CERN*, PhD thesis, Universita degli studi di Firenze, 2021, https://cds.cern.ch/record/2806641, Presented 08 Apr 2022.

[140] N. Caraban Gonzalez, *SMOG2 installation in the LHCb cavern*, https://cds.cern.ch/record/2727007, 2020.

[141] LHCb collaboration, *LHCb SMOG Upgrade*, CERN-LHCC-2019-005, 2019.

[142] C. De Angelis *et al.*, *SMOG2: temperature calibration and luminosity measurement* , CERN, Geneva, 2023. https://cds.cern.ch/record/2860194.

[143] M. W. Winkler, *Cosmic Rays in space*, https://agenda.infn.it/event/18734/contributions/98724/attachments/66188/80868/Winkler_lhcb.pdf, 2019. Presented at "Second LHCb Heavy Ion Workshop".

[144] M. W. Winkler, *Cosmic Ray antiprotons at high energies*, Journal of Cosmology and Astroparticle Physics **2017** (2017) 048.

[145] S. Ostapchenko, *QGSJET-II: towards reliable description of very high energy hadronic interactions*, Nuclear Physics B - Proceedings Supplements **151** (2006) 143.

[146] J. Albrecht *et al.*, *The muon puzzle in Cosmic Ray induced air showers and its connection to the large hadron collider*, arXiv:2105.06148.

[147] R. Duperray *et al.*, *Flux of light antimatter nuclei near earth, induced by Cosmic Rays in the galaxy and in the atmosphere*, Phys. Rev. D **71** (2005) 083013.

[148] M. Mahlein *et al.*, *Novel parameter-free coalescence model for deuteron production*, arXiv:2302.12696.

[149] NA61/SHINE collaboration, *The NA61/SHINE Experiment at the CERN SPS*, Nucl. Phys. A **830** (2009) 559C, arXiv:0907.4493.

[150] NA61/SHINE collaboration, *NA61/SHINE Detector Upgrade*, Acta Phys. Pol. B Proc. Suppl. **14** (2021) 579.

[151] P. Chardonnet, J. Orloff, and P. Salati, *The production of antimatter in our galaxy*, Physics Letters B **409** (1997) 313.

[152] A. Ibarra and S. Wild, *Determination of the cosmic antideuteron flux in a Monte Carlo approach*, Phys. Rev. D **88** (2013) 023014.

[153] M. Cirelli, N. Fornengo, M. Taoso, and A. Vittino, *Antihelium from Dark Matter annihilations*, Journal of High Energy Physics **2014** (2014) .

[154] J. Herms, A. Ibarra, A. Vittino, and S. Wild, *Antideuterons in Cosmic Rays: sources and discovery potential*, Journal of Cosmology and Astroparticle Physics **2017** (2017) 018.

[155] K. Blum, K. C. Y. Ng, R. Sato, and M. Takimoto, *Cosmic Rays, antihelium, and an old navy spotlight*, Phys. Rev. D **96** (2017) 103021.

[156] D.-M. Gomez-Coral *et al.*, *Deuteron and antideuteron production simulation in Cosmic Ray interactions*, Phys. Rev. D **98** (2018) 023012.

[157] H. Bethe, J. Ashkin, and E. Segre, *Experimental Nuclear Physics*, John Wiley and Sons, Inc., 1953.

[158] S. K. Baker, *Antideuteron sensitivity studies at LHCb*, PoS **LHCP2018** (2018) 078.

[159] LHCb collaboration, *Deuteron PID performance in LHCb simulation*, LHCb-FIGURE-2020-013, 2020.

[160] T. Pierog, C. Baus, and R. Ulrich, *CRMC library package*, web.ikp.kit.edu/rulrich/crmc.htm.

[161] M. De Cian, *Track Reconstruction Efficiency and Analysis of $B^0 \to K^{*0}\mu^+\mu^-$ at the LHCb Experiment*, PhD thesis, Zurich University, 2013, https://cds.cern.ch/record/1605179, Presented 14 Mar 2013.

[162] E. Rodrigues, *Dealing with clones in the tracking*, LHCb-2006-057, 2006.

[163] R. E. Kalman, *A new approach to linear filtering and prediction problems*, Transactions of the ASME–Journal of Basic Engineering **82** (1960) 35.

[164] W. D. Hulsbergen, *Decay chain fitting with a kalman filter*, Nuclear Instruments and Methods in Physics Research Section A: Accelerators, Spectrometers, Detectors and Associated Equipment **552** (2005) 566.

[165] E. Rodrigues, *Tracking definitions* , CERN, Geneva, 2007. `https://cds.cern.ch/record/1016937`.

[166] LHCb Computing group, *Track types*, `https://twiki.cern.ch/twiki/bin/view/LHCb/LHCbTrackingStrategies#TrackTypes`.

[167] O. Callot and S. Hansmann-Menzemer, *The Forward Tracking: Algorithm and Performance Studies*, LHCb-2007-015, CERN-LHCb-2007-015 (2007).

[168] P. V. C. Hough, *Machine Analysis of Bubble Chamber Pictures*, Conf. Proc. C **590914** (1959) 554.

[169] R. O. Duda and P. E. Hart, *Use of the hough transformation to detect lines and curves in pictures*, Commun. ACM **15** (1972) 11–15.

[170] M. De Cian, S. Farry, P. Seyfert, and S. Stahl, *Fast neural-net based fake track rejection in the LHCb reconstruction*, LHCb-PUB-2017-011, 2017.

[171] V. Zhukov. private communication.

[172] LHCb collaboration, *Helium identification with LHCb*, `arXiv:2310.05864`.

[173] LHCb collaboration, *Observation of antihypertriton in pp collisions with LHCb*, LHCb-CONF-2023-002 (2023).

[174] A. Chambers, *Modern Vacuum Physics*, Masters series in physics and astronomy, CRC Press, 2004. `https://books.google.ch/books?id=AnvMBQAAQBAJ`.

[175] D. J. Hucknall, A. Morris, and R. S. of Chemistry (Great Britain), *Vacuum Technology: Calculations in Chemistry*, EngineeringPro collection, RSC, 2003. `https://books.google.ch/books?id=HJLG-DtMYEEC`.

[176] A. Roth, *Vacuum Technology*, North-Holland, 1982. `https://books.google.ch/books?id=tR4sAAAAIAAJ`.

[177] C. Benvenuti, *Getter pumping*, doi: 10.5170/CERN-2007-003.313.

[178] P. Chiggiato and P. Costa Pinto, *Ti–Zr–V non-evaporable getter films: from development to large scale production for the Large Hadron Collider*, Thin Solid Films **515** (2006) 382.

[179] G. Bregliozzi *et al.*, *Achievement and Evaluation of the Beam Vacuum Performance of the LHC Long Straight Sections*, , `https://cds.cern.ch/record/1124067`.

[180] K. Welch, *Capture Pumping Technology*, Elsevier Science, 2001. `https://books.google.ch/books?id=56wANznvEA8C`.

[181] P. Manini and E. Maccallini, *Neg pumps: Sorption mechanisms and applications*, `arXiv:2006.01537`.

[182] C. Benvenuti and F. Francia, *Room-temperature pumping characteristics of a Zr-Al nonevaporable getter for individual gases*, Journal of Vacuum Science and Technology A **6** (1988) 2528.

[183] Y. Fukai, *The Metal-hydrogen System: Basic Bulk Properties*, Lecture Notes in Economic and Mathematical Systems, Springer-Verlag, 1993. https://books.google.ch/books?id=pelGAQAAIAAJ.

[184] P. Modi and K.-F. Aguey-Zinsou, *Room temperature metal hydrides for stationary and heat storage applications: A review*, Frontiers in Energy Research **9** (2021) .

[185] A. Efron, Y. Lifshitz, I. Lewkowicz, and M. H. Mintz, *The kinetics and mechanism of titanium hydride formation*, Journal of the Less Common Metals **153** (1989) 23.

[186] D. M. Parragh, *Hydrogen Embrittlement of TiZrV Non-Evaporable Getter Coating*, 2022. https://cds.cern.ch/record/2836903, Presented 26 Aug 2022.

[187] LHCb collaboration, *LHCb SMOG Upgrade* , CERN, Geneva, 2019. doi: 10.17181/CERN.SAQC.EOWH.

[188] PBC forum: C. Barschel *et. al.* , *LHC fixed-target experiments* , CERN, Geneva, 2019. doi: 10.23731/CYRM-2020-004.

[189] O. Grobner, *The LHC vacuum system*, in *Proceedings of the 1997 Particle Accelerator Conference (Cat. No.97CH36167)*, **3** 3542–3546 vol.3, 1997.

[190] P. Costa Pinto *et al.*, *Thin Film Coatings for Suppressing Electron Multipacting in Particle Accelerators*, , https://cds.cern.ch/record/1462768, 2011.

[191] R. Kersevan and M. Ady, *Recent Developments of Monte-Carlo Codes Molflow+ and Synrad+*, in *Proc. 10th International Particle Accelerator Conference (IPAC'19), Melbourne, Australia, 19-24 May 2019*, No. 10 in International Particle Accelerator Conference, (Geneva, Switzerland), 1327–1330, JACoW Publishing, 2019.

[192] J. J. Shea, *Foundations of vacuum science and technology*, Electrical Insulation Magazine, IEEE **14** (1998) 42 .

[193] M. Ady, *Monte Carlo simulations of ultra high vacuum and synchrotron radiation for particle accelerators*, PhD thesis, Ecole Polytechnique, Lausanne, 2016, https://cds.cern.ch/record/2157666, Presented 03 May 2016.

[194] A. E. Prodromides, *Non-Evaporable Getter Thin Film Coatings for Vacuum Applications*, PhD thesis, Ecole Polytechnique, Lausanne, 2002, https://cds.cern.ch/record/593236, Presented on 1 Sep 2002.

[195] P. Costa Pinto, H_2 *saturation of NEG thin films with 100 nm and 200 nm*, EDMS 2939325, CERN, 2023. https://edms.cern.ch/ui/#!master/navigator/document?D:101346282:101346282:subDocs.

[196] C. Benvenuti and F. Francia, *Room temperature pumping characteristics for gas mixtures of a Zr–Al nonevaporable getter*, Journal of Vacuum Science and Technology A **8** (1990) 3864.

[197] Tanimoto, Yasunori, *Vacuum properties of NEG and carbon coatings exposed to synchrotron radiation*, VSC Seminar, CERN, 2015.

[198] V. Carassiti. private communication.

[199] LHCb collaboration, *First LHCb upgrade reconstruction results on fixed-target data*, LHCb-FIGURE-2023-017, 2023.

[200] *SIMATIC WinCC Open Architecture*, `https://www.winccoa.com/`.

[201] C. B. Department, *DIP communication system*, `https://readthedocs.web.cern.ch/display/DIP/`.